

Dissertation
submitted to the
Combined Faculties for the Natural Sciences and for Mathematics
of the Ruperto-Carola University of Heidelberg, Germany
for the degree of
Doctor of Natural Sciences

Put forward by

M.Sc. Sören Schlichting
Born in: Frankfurt a.M.
Oral examination: 24.07.2013

**NON-EQUILIBRIUM DYNAMICS AND
THERMALIZATION OF WEAKLY COUPLED
NON-ABELIAN PLASMAS**

**Referees: Prof. Dr. Jürgen Berges
Prof. Dr. Jan Martin Pawłowski**

Abstract

We investigate several aspects of the non-equilibrium dynamics of non-abelian gauge theories, relevant to the problem of thermalization in relativistic heavy-ion collision experiments. We perform numerical simulations in the framework of classical-statistical lattice gauge theory as a first principle approach to study the non-equilibrium dynamics of weakly coupled yet strongly correlated non-abelian plasmas. The numerical studies are complemented by analytic considerations in the framework of kinetic theory and two-particle irreducible effective action techniques. Following a general introduction, the theoretical framework and the range of validity of the employed approximations is discussed.

The first main part of this thesis is concerned with the study of thermalization of non-abelian plasmas in Minkowski space. We establish by numerical studies, that the thermalization process is governed by a turbulent cascade towards the ultraviolet in the regime where quantum corrections can safely be neglected. The dynamics of the universal turbulent attractor is characterized by a self-similar evolution in time and we extract the universal scaling exponents and scaling functions. It is shown that the scaling exponents observed in numerical simulations agree with the ones extracted from a scaling analysis in the kinetic theory framework.

In the second main part of this thesis, we investigate the non-equilibrium dynamics of instabilities. We investigate analytically the unstable dynamics of coherent non-abelian gauge fields and compare our findings with the results from classical-statistical lattice simulations. The simulations demonstrate the phenomenon of non-linear self-amplification of the instability due to interactions of unstable modes. The non-linear dynamics of instabilities is discussed both analytically and numerically for the example of an anisotropically expanding scalar field theory, with a particular emphasis on the role of the anisotropic expansion of the system.

The third part of this work focuses on the non-equilibrium dynamics of anisotropically expanding non-abelian plasmas as encountered in heavy-ion collisions at ultra-relativistic energies. While our simulations indicate the importance of plasma instabilities and free streaming for the early stages of the evolution, we discover that the subsequent dynamics is again governed by a universal turbulent attractor. Most remarkably, the universal scaling exponents which characterize the self-similar evolution in the turbulent regime can be explained by elastic scattering processes.

Zusammenfassung

Diese Arbeit untersucht verschiedene Aspekte der Nichtgleichgewichtsdynamik nicht-abelscher Eichtheorien im Hinblick auf die Fragestellung der Thermalisierung in relativistischen Schwerionenkollisionen. Die Dynamik schwach gekoppelter jedoch stark korrelierter nicht-abelscher Plasmen wird mittels numerischer Rechnungen im Rahmen der klassisch-statistischen Gittereichtheorie in einem fundamentalen Zugang untersucht. Die numerischen Studien werden durch analytische Betrachtungen im Rahmen der kinetischen Theorie beziehungsweise der zwei-Teilchen-irreduziblen effektiven Wirkung ergänzt. Die theoretischen Grundlagen sowie die Anwendbarkeit der verwendeten Näherungen werden im Anschluss an eine allgemeine Einleitung diskutiert.

Der erste Hauptteil dieser Arbeit beschäftigt sich mit der Thermalisierung von nicht-abelschen Plasmen im Minkowski-Raum. Mit Hilfe numerischer Studien zeigen wir, dass der Thermalisierungsprozess im klassischen Bereich hoher Besetzungszahlen durch eine turbulente Kaskade ins Ultraviolette beschrieben wird. Die Dynamik des universellen turbulenten Attraktors ist hierbei durch eine selbstähnliche Zeitevolution charakterisiert, deren universelle Skalenexponenten und Skalierungsfunktionen numerisch bestimmt werden. Der Vergleich numerischer Simulationen mit Betrachtungen im Rahmen der kinetischen Theorie zeigt, dass die Skalenexponenten mit der kinetischen Theorie übereinstimmen.

Der zweite Hauptteil dieser Arbeit untersucht die Nichtgleichgewichtsdynamik von Instabilitäten. Wir analysieren zunächst die Dynamik kohärenter nicht-abelscher Eichfelder und vergleichen unsere analytischen Ergebnisse mit numerischen Simulationen. Die Simulationen demonstrieren das Phänomen der nicht-linearen Selbstverstärkung von Instabilitäten, welches als Konsequenz von Wechselwirkungen zwischen instabilen Moden auftritt. Die Dynamik des nicht-linearen Regimes wird am Beispiel einer anisotrop expandierenden Skalartheorie näher untersucht. Ein besonderes Augenmerk liegt hierbei auf dem Einfluss der longitudinalen Expansion.

Der dritte Teil dieser Arbeit behandelt die Nichtgleichgewichtsdynamik von anisotrop expandierenden Plasmen und ist daher von besonderer Relevanz im Hinblick auf ultra-relativistische Schwerionenkollisionen. Während die Frühzeitdynamik durch Plasma-Instabilitäten und freie Expansion dominiert ist, beobachten wir erneut das nachfolgende Auftreten eines universellen turbulenten Attraktors. Die universellen Skalenexponenten, welche die selbstähnliche Dynamik des turbulenten Plasmas charakterisieren, können hierbei bereits durch elastische Streuprozesse erklärt werden.

Contents

1	Introduction	1
1.1	Motivation	1
1.2	Outline of this work	5
2	Theoretical background	9
2.1	Basics of quantum chromodynamics	9
2.2	Non-equilibrium quantum field theory	14
2.3	Co-moving coordinates	21
2.4	Classical-statistical real-time lattice gauge theory	23
3	Thermalization in Minkowski space	35
3.1	Evolution in kinetic theory	37
3.2	Early times and transient phenomena	42
3.3	Non-thermal fixed points and perturbative scaling exponents	46
3.4	Late times and self-similarity	53
3.5	Turbulent thermalization	63
3.6	Discussion	66
4	Non-equilibrium dynamics of instabilities	67
4.1	Instabilities in SU(2) Yang-Mills theory in Minkowski space	68
4.2	Parametric resonance in expanding scalar field theories	79
4.3	Discussion	98
5	Heavy-ion collisions at ultra-relativistic energies	101
5.1	Non-equilibrium dynamics and the CGC framework	103
5.2	The unstable Glasma	110
5.3	Turbulent thermalization	120
5.4	Discussion	135
6	Conclusion	137

A Identities for the SU(2) gauge group	143
B Occupation numbers and generalized Coulomb gauge on the lattice	145
C Free field solutions in co-moving coordinates	149
D Hankel functions	157
E Perturbative calculation of hard scales	161
F Set-in and freeze-out times in the parametric resonance instability	167
G CGC initial conditions on the lattice	171
Bibliography	173

Chapter 1

Introduction

1.1 Motivation

The question “whatever holds the world together in its inmost folds”¹ is one of the most fundamental questions in physics and the philosophy of natural sciences. The most satisfactory answer today is given by the standard model of particle physics which provides a valid description of nature at energies at least up to the TeV scale. However, there is a variety of phenomena within the standard model, whose understanding can not be considered satisfactory at present. This concerns in particular many aspects of the theory of Quantum Chromo Dynamics (QCD). Moreover, there is presently a lack of theoretical understanding of heavy-ion collision experiments dedicated to study the properties of QCD under extreme conditions, which require a better insight into the non-equilibrium dynamics of these systems. Hence, the central motivation for this work is to contribute towards a better understanding of the out-of-equilibrium dynamics of QCD as encountered in ultra-relativistic heavy-ion collisions and we will briefly outline the most important aspects of this problem in the following.

In view of high energy processes in quantum chromodynamics, the property of asymptotic freedom [1, 2] renders the theory amenable to the methods of perturbation theory and theoretical predictions have successfully been tested for various processes in collider experiments [3]. In contrast, the properties of low energy QCD are such that the fundamental quark and gluon degrees of freedom can not exist as free objects and the theory determines the structure of hadronic bound states instead. While experimentally spectroscopic properties of hadrons are nowadays accessible [3], understanding the properties of low energy QCD and the mechanism underlying the confinement of quarks and gluons is a formidable task in theoretical physics. Besides the non-trivial structure of the QCD vacuum, open questions also concern the thermodynamic properties of QCD media. A popular version of the conjectured phase diagram of the

¹J. W. Goethe (1749-1832) - “*Faust*”

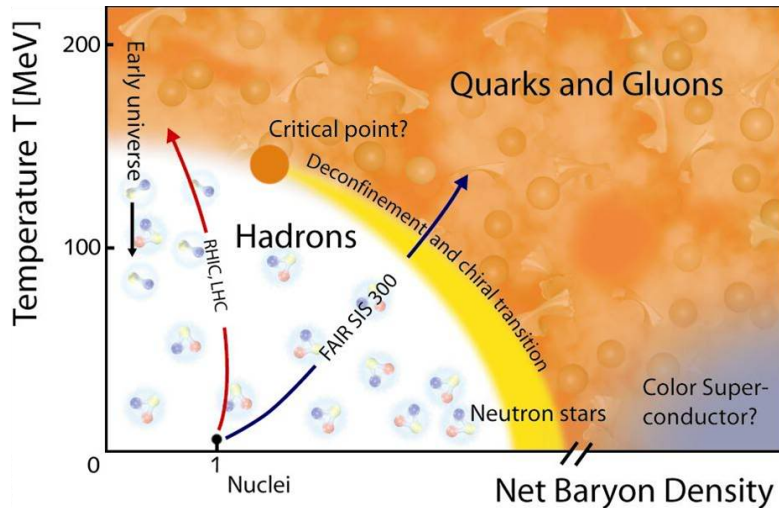


Figure 1.1: Illustration of a popular conjecture of the QCD phase diagram as a function of temperature and baryon chemical potential. The determination of the precise phase structure and the location of the phase boundaries is the subject of ongoing research. Figure taken from the GSI website (www.gsi.de).

theory is depicted in Fig. 1.1 in the plane of temperature and net baryon density. Theoretical progress from first principles in this field has mostly emerged from large scale numerical studies in the framework of lattice QCD. In particular, it has been established that at vanishing net baryon density, the theory exhibits a cross-over transition to a deconfined quark-gluon plasma phase at temperatures around 150 – 200 MeV [4–7]. However, even in thermal equilibrium the range of applicability of first principle lattice methods is presently limited to vanishing or at least small net baryon density [8]. Despite significant progress within different approaches [9, 10], which are able to study QCD thermodynamics also at finite baryon density, many aspects of the phase diagram such as e.g. the existence and location of a critical point have remained unsolved.

The experimental environment to study quantum chromodynamics under extreme conditions, such as high temperatures, large baryon densities or strong magnetic fields, can be realized in relativistic heavy-ion collision experiments presently carried out at the “Relativistic Heavy Ion Collider” (RHIC) at Brookhaven National Lab as well as at the “Large Hadron Collider” (LHC) at CERN. In the past, experiments have also been performed at the “Super Proton Synchrotron” (SPS) at CERN and in the future, the present facilities will be complemented by the “Facility for Antiproton and Ion Research” (FAIR) at GSI and the “Nuclotron-based Ion Collider Facility” (NICA) at JINR. The experiments at RHIC and LHC have indeed been able to provide striking evidence for the existence of a phase of deconfined QCD matter [11–15] and the common physics goal of future investigations is to explore the properties of the Quark Gluon Plasma (QGP) phase. However, the major challenge in the study of relativistic

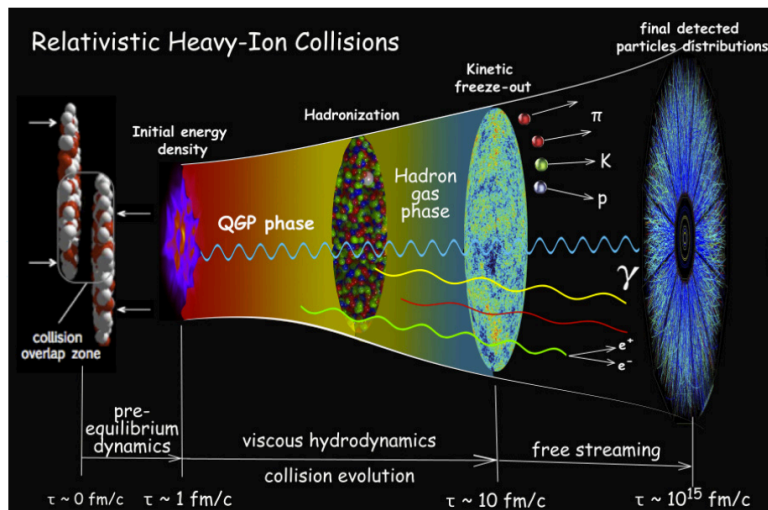


Figure 1.2: Standard model of the space-time evolution of relativistic heavy-ion collisions. The non-equilibrium plasma created immediately after the collision of heavy nuclei is conjectured to thermalize on a time scale of $\sim 1 \text{ fm}/c$. The subsequent evolution of the Quark Gluon Plasma is characterized by cooling due to the longitudinal expansion until the temperature drops below the confinement transition and the system re-enters the hadronic phase. This stage of the evolution is expected to be described by viscous hydrodynamics. Finally the system becomes a dilute gas of free streaming particles which can be observed in the detectors. Figure taken from Ref. [16].

heavy-ion collisions stems from the fact that experimental measurements are to a large extent only possible in the final state. Measured observables therefore contain information about the entire space-time evolution of the system and the extraction of properties of deconfined QCD matter from heavy-ion collision experiments inevitably requires a solid understanding of the dynamical space-time evolution.

From this point of view relativistic heavy-ion collisions should be regarded as a realization of an initial value problem in quantum chromodynamics rather than a probe of the QCD phase-diagram. However, the tremendous success of thermal models in terms of describing a vast amount of data at RHIC and LHC has led to the conjecture of a 'standard model of heavy-ion collisions', which generically features a local thermal equilibrium achieved shortly after the collision of heavy nuclei [16–20]. This standard scenario for relativistic heavy-ion collisions is portrayed in Fig. 1.2, which sketches the time evolution of the system in the transverse plane, i.e. perpendicular to the beam axis. Based on this description, the past decades of heavy-ion physics have indeed revealed remarkable properties of quark-gluon matter formed in collider experiments at RHIC and the LHC. Besides the in-medium energy loss of jets and the suppression and regeneration of quarkonia, one of the most striking observations is the apparent behavior of the Quark Gluon Plasma as a nearly perfect fluid [21, 22]. However, the question of

how these features emerge *ab initio* in a heavy-ion collision, and to what extent a thermalized Quark Gluon Plasma is achieved is an outstanding problem in theoretical physics [23].

In recent years there has been significant progress in a first principle understanding of this question from two limiting cases. The first case is the study of strongly coupled super-symmetric gauge theories via gauge-gravity duality. The results in this case qualitatively confirm the standard scenario, though the studies clearly show the importance of residual anisotropies at the transition to the hydrodynamic regime [24–26]. The other case that is amenable to first principle studies is the weak-coupling limit of quantum chromodynamics. In this case the colliding nuclei are described in the ‘Color Glass Condensate’ (CGC) framework [27, 28] and the non-equilibrium state created immediately after the collision is characterized by large gluon occupancies, such that the non-equilibrium plasma is strongly correlated even at weak coupling. In this framework, different scenarios of how thermalization proceeds have been developed based on kinetic descriptions of the non-equilibrium plasma [29–32]. While the original “bottom-up” thermalization scenario [29] emphasizes the role of elastic and inelastic scattering processes, recent works have identified plasma instabilities as a possible mechanism to speed up thermalization at weak coupling [31, 32]. However, no consensus has been reached concerning the relevant processes as well as the thermalization time and further progress crucially relies on the ability to identify the correct solution [23].

In this context, it is interesting to note that the non-equilibrium state created immediately after the collision of heavy nuclei shares important features with strongly correlated many-body systems at very different energy scales. These range from the reheating dynamics of the early universe to table-top experiments with cold atoms. Most remarkably, the non-equilibrium dynamics of such systems exhibits universal features. This universality is based on the existence of non-thermal fixed points which can be associated with the phenomenon of wave turbulence [33] and manifests itself in terms of a self-similar scaling behavior [34]. While turbulent phenomena have been subject to several studies at different energy scales [34–39], much less is known about wave turbulence in non-abelian gauge theories and it is an open question to what extent turbulent phenomena manifest themselves in the non-equilibrium dynamics of relativistic heavy-ion collisions.

From these motivations, the objective of this work is to explore the non-equilibrium dynamics of weakly coupled but highly occupied non-abelian plasmas. Since the dynamics may be governed by universal turbulent phenomena, we will focus on the theoretically clean case of weak coupling, large nuclei and high collider energies and study the space time evolution of non-abelian plasmas for a large range of different initial conditions, chosen to mimic the

situation in relativistic heavy-ion collisions. The central question in this context is to identify the mechanism underlying the thermalization process in this case.

1.2 Outline of this work

In this thesis we study several aspects of the non-equilibrium dynamics of non-abelian plasmas. Since the weak coupling dynamics of highly occupied plasmas can be accurately described within the framework of classical-statistical field theory [40, 41], we employ classical-statistical real-time lattice simulations as a first principle approach. The numerical studies are complemented by analytic considerations using kinetic theory as well as two-particle irreducible effective action techniques [42] to establish an understanding of the underlying non-equilibrium phenomena. The theoretical background and numerical techniques employed in this work are introduced in Chapter 2.

In the first part of this work we investigate the thermalization of non-abelian plasmas in Minkowski space. Besides theoretical interest, these systems provide an ideal testground for the concepts developed to understand the more complex dynamics of longitudinally expanding plasmas, phenomenologically relevant to relativistic heavy-ion collisions. We consider a class of systems, characterized by a large number of excitations up to a characteristic momentum scale, which is chosen to mimic the situation in relativistic heavy-ion collisions [30]. Since the final temperature of these systems is much larger than the typical momentum of hard excitations, one problem of thermalization is how energy is transported to higher momentum scales. While this process has been analyzed in the kinetic theory framework and different studies agree on the level of parametric estimates [30, 31], a rigorous answer from first principles can be obtained using classical-statistical lattice simulations. The central questions concern the role of inelastic (number-changing) versus elastic (number-conserving) scattering processes as well as the emergence of non-thermal fixed point solutions in the evolution of the system [23]. Since the total number of excitations is initially large compared to the final thermal state of the system, the initial over-occupation ultimately has to decrease due to inelastic processes. However, a suppression of inelastic processes at early times may result in the formation of a transient non-equilibrium condensate, which can absorb the surplus of hard excitations [30]. This observation has triggered related studies also in scalar field theories, where inelastic processes are parametrically suppressed and a transient Bose-Einstein condensate emerges quite naturally as a consequence of over-occupation [43]. However, this question becomes more involved in the context of non-abelian gauge theories, where elastic and inelastic processes are parametrically of the same order [30, 31]. In the context of scalar theories it is also well established that the evolution at late times is characterized by a non-thermal fixed point, which describes the

transport of energy towards the ultraviolet and particle number towards the infrared [33, 35]. This quasi-stationary state is characterized by a dual power law spectrum, with characteristic scaling exponents in the infrared and ultraviolet respectively [33, 35]. While the infrared fixed point features strongly enhanced long range correlations reminiscent of critical phenomena in thermal equilibrium, the spectral properties of the UV part are analogous to Kolmogorov wave turbulence [33, 35]. The dynamics of the energy transport towards the ultraviolet in these systems is characterized by a self-similar evolution in time, with universal scaling exponents [34]. The thermalization process in non-abelian gauge theories is investigated in Chapter 3, where we present results from classical-statistical lattice simulations in Minkowski space as well as analytic considerations. We first extend the kinetic theory analysis of Refs. [30, 31] to account for the presence of a non-thermal fixed point and establish an intuitive picture of the thermalization process. We then investigate the possibility of the emergence of a transient condensation phenomenon at early times, by considering the physical effects of a condensate on the interactions of hard excitations. Subsequently, we extend our numerical studies to later times, where the system exhibits the self-similar evolution characteristic of a non-thermal fixed point. We determine the universal scaling exponents in the turbulent regime and compare them to a scaling analysis based on a kinetic description. By studying a large range of different initial conditions, we are also able to identify the parametric dependencies of the non-universal amplitudes, which determine the thermalization time of the system.

The second part of this thesis is devoted to the non-equilibrium dynamics of instabilities, which are expected to play an important role in the early stages of relativistic heavy-ion collisions [44, 45]. It is well established that non-abelian gauge theories feature different types of instabilities, the most prominent examples of which are the (chromo-) Weibel instability, which occurs for momentum-space anisotropic plasmas [46], and the Nielsen-Olesen instability, associated to the unstable decay of coherent chromo-magnetic fields [47, 48]. Since the state created immediately after the collision of heavy nuclei is expected to be highly anisotropic, the (chromo-) Weibel instability has frequently been suggested as a possible mechanism that quickly drives the plasma towards an isotropic state [44, 45]. While the presence of Weibel-type instabilities has indeed been confirmed in classical-statistical lattice simulations of non-abelian gauge theories [49–52], the studies have also revealed the importance of non-linear correction to the linear instability regime [52]. More specifically, it has been shown that “secondary instabilities” arise as a consequence of the non-linear self-interaction of unstable modes, before ultimately the instability saturates and exponential growth can no longer be observed at late times [52]. A detailed understanding of these non-linear phenomena is thus inevitable to appraise the impact of plasma instabilities on the non-equilibrium dynamics of relativistic heavy-ion collisions. In Chapter 4, we investigate the non-equilibrium dynamics of instabili-

ties for two different systems. We first consider the out-of-equilibrium dynamics of coherent non-abelian gauge fields in Minkowski space and discover that in addition to a generalization of the Nielsen-Olesen instability these exhibit also a subleading parametric resonance instability. This emerges from analytic results as well as numerical simulations. We then discuss the non-linear stages of the evolution in more detail for the example of an expanding scalar theory. Since the non-linear dynamics of non-equilibrium instabilities manifests itself in a very similar way also in scalar field theories [52, 53], the discussion is directly relevant also to the study of longitudinally expanding non-abelian plasmas in Chapter 5.

The third part of this work is dedicated to the study of longitudinally expanding non-abelian plasmas and particularly relevant to the phenomenology of relativistic heavy-ion collisions. In the weak-coupling picture, the colliding nuclei are described in the color-glass condensate (CGC) framework, which provides the initial state immediately after the collision of heavy nuclei [27, 28]. The non-equilibrium initial state, referred to as the 'Glasma' [28], is characterized by strongly correlated gluon fields, which reflect the properties of the nuclear wave functions prior to the collision. The 'Glasma' is initially highly anisotropic and thus exhibits the (chromo-) Weibel instability, which is able to partially isotropize the system [49, 50]. However, the competition between interactions and the longitudinal expansion of the system renders the question of isotropization non-trivial at all times of the evolution. The question of how the subsequent thermalization proceeds in such a system has therefore been intensely debated in the literature and no consensus has been reached [23]. In Chapter 5, we address this problem by use of first principle lattice simulations. We first investigate the dynamics of plasma instabilities in the initial 'Glasma' stage and infer the associated time scales. We then study the dynamics at later times relevant to the thermalization process at weak coupling. We discover that ultimately the system exhibits the universal self-similar dynamics characteristic of wave turbulence and we obtain the universal scaling exponents and scaling functions. Most remarkably, the universal dynamics of the turbulent attractor can be described entirely in terms of elastic scattering as incorporated in the "bottom-up" thermalization scenario [29]. Since the turbulent attractor shows a significant anisotropy on large time scales, we finally speculate about the phenomenological consequences of our findings for heavy-ion collisions at RHIC and LHC energies.

Parts of this thesis have already been published in:

1. J. Berges, S. Scheffler, S. Schlichting and D. Sexty, “*Out of equilibrium dynamics of coherent non-abelian gauge fields*”, Phys. Rev. D **85**, 034507 (2012), arXiv:1111.2751 [hep-ph].
2. J. Berges, K. Boguslavski and S. Schlichting, “*Non-linear amplification of instabilities with longitudinal expansion*”, Phys. Rev. D **85**, 076005 (2012), arXiv:1201.3582 [hep-ph].
3. J. Berges, S. Schlichting and D. Sexty, “*Over-populated gauge fields on the lattice*”, Phys. Rev. D **86**, 074006 (2012), arXiv:1203.4646 [hep-ph].
4. S. Schlichting, “*Turbulent thermalization of weakly coupled non-abelian plasmas*”, Phys. Rev. D **86**, 065008 (2012), arXiv:1207.1450 [hep-ph].
5. J. Berges and S. Schlichting, “*The non-linear Glasma*”, Phys. Rev. D **87**, 014026 (2013), arXiv:1209.0817 [hep-ph].
6. J. Berges, K. Boguslavski, S. Schlichting and R. Venugopalan, “*Turbulent thermalization of the Quark Gluon Plasma*”, arXiv:1303.5650 [hep-ph] (submitted to Phys. Rev. Lett.).

Chapter 2

Theoretical background

In this chapter, we introduce the theoretical concepts on which the subsequent discussion is built upon. In Sec. 2.1, we summarize some basic facts about quantum chromodynamics and pure Yang-Mills theory, as they can be found in standard textbooks [54–58]. In Sec. 2.2, we give a short introduction to non-equilibrium dynamics of classical and quantum systems and motivate the classical-statistical approximation employed throughout this work. In Sec. 2.3, we introduce the coordinates used in Chapter 5 to study the non-equilibrium dynamics of ultra-relativistic heavy-ion collisions and we discuss the framework to perform classical-statistical real-time lattice simulations in Sec. 2.4.

2.1 Basics of quantum chromodynamics

Quantum Chromo Dynamics (QCD) is a non-abelian gauge theory coupled to fermions. The fermion fields $\Psi_f(x)$ and $\bar{\Psi}_f(x)$ carry the 'color' charge $A = 1, \dots, N_c$, which transforms according to the fundamental representation of the $SU(N_c)$ gauge group and the number of colors is $N_c = 3$ for QCD. The 'flavor' index $f = u, d, s, c, b, t$ distinguishes between different 'quark' species and characterizes the different masses and electroweak charges of the quarks. The quarks interact via the coupling to the bosonic 'gluon' fields $A_\mu(x)$, which in contrast to abelian gauge theories, such as Quantum Electro Dynamics (QED), carry an (adjoint) color charge $a = 1, \dots, N_c^2 - 1$ and are thus self-interacting.

The fermionic matter fields Ψ and $\bar{\Psi}$ transform under local gauge transformations $G(x)$ in the fundamental representation of the $SU(N_c)$ gauge group¹ according to

$$\psi^{(G)}(x) = G(x)\psi(x), \quad \bar{\psi}^{(G)}(x) = \bar{\psi}(x)G^\dagger(x), \quad (2.1)$$

¹This means $G(x)$ is a unitary $N_c \times N_c$ matrix with determinant equal to unity.

while the bosonic gauge fields A_μ transform under the adjoint representation of the $SU(N_c)$ gauge group according to

$$A_\mu^{(G)}(x) = G(x)A_\mu(x)G^\dagger(x) - \frac{i}{g}(\partial_\mu G(x))G^\dagger(x), \quad (2.2)$$

where g denotes the gauge coupling.² The gauge field A_μ can be decomposed in the basis of the $su(N_c)$ Lie algebra according to

$$A_\mu(x) = A_\mu^a(x)\Gamma^a, \quad (2.3)$$

with real expansion coefficients $A_\mu^a(x)$. The generators Γ^a of the $su(N_c)$ Lie algebra in the fundamental representation, are represented as traceless hermitian matrices and normalized such that $\text{tr}[\Gamma^a\Gamma^b] = \delta^{ab}/2$. For the gauge group $SU(3)$ the generators Γ^a are related to the Gell-Mann matrices λ^a by $\Gamma^a = \lambda^a/2$, whereas for the gauge group $SU(2)$, which we will consider in this work, the generators are related to the Pauli matrices by $\Gamma^a = \sigma^a/2$. The generators Γ^a satisfy the commutation relations

$$[\Gamma^a, \Gamma^b] = if^{abc}\Gamma^c, \quad (2.4)$$

where the structure constants f^{abc} are real and anti-symmetric in all indices. For the gauge group $SU(2)$ they are given by the Levi-Civita symbol $f^{abc} = \epsilon^{abc}$.³

The gauge covariant derivative D_μ acting on a fermion field Ψ is defined as

$$D_\mu\Psi = \partial_\mu\Psi - igA_\mu\Psi, \quad (2.5)$$

such that the covariant derivative transforms according to $D_\mu^{(G)}(x)\Psi^{(G)}(x) = G(x)D_\mu(x)\Psi(x)$ under local gauge transformations. By use of the decomposition in Eq. (2.3), the covariant derivative in the fundamental representation can be expressed as

$$D_\mu^{AB}(x)\Psi_B(x) = \partial_\mu\Psi^A(x) - igA_\mu^a(x)(\Gamma^a)^{AB}\Psi_B(x). \quad (2.6)$$

Introducing the notation $\not{D}_{AB}(x) = \gamma_\mu D_{AB}^\mu(x)$, where γ^μ denote the Dirac matrices, the matter part $\mathcal{L}_{\text{Matter}}$ of the QCD Lagrangian then takes the form

$$\mathcal{L}_{\text{Matter}}[A, \bar{\psi}, \psi](x) = \sum_f \bar{\psi}_f^A(x)(i\not{D}_{AB}(x) - m_f\delta_{AB})\psi_f^B(x), \quad (2.7)$$

²We will also use the notation $\alpha_S = g^2/4\pi$ for the coupling constant.

³We employ the convention $\epsilon^{123} = \epsilon^{312} = \epsilon^{231} = 1$, $\epsilon^{213} = \epsilon^{321} = \epsilon^{132} = -1$, whereas all other entries vanish.

which is manifestly invariant under local gauge transformations.

In addition to the matter sector, there is of course the Yang-Mills sector, which contains the dynamics of the non-abelian gauge fields. Since the gauge fields transform under the adjoint representation of the gauge group, we first note that the covariant derivative in the adjoint representation takes the form

$$D_\mu^{ab}(x) = \partial_\mu \delta^{ab} - ig A_\mu^c(x) (\tilde{\Gamma}_c)^{ab} = \partial_\mu \delta^{ab} + g f^{acb} A_\mu^c(x), \quad (2.8)$$

where $(\tilde{\Gamma}^a)_{bc} = -if^{abc}$ are the generators of the Lie algebra in the adjoint representation. The field strength tensor $\mathcal{F}_{\mu\nu}$ is then defined as

$$\mathcal{F}_{\mu\nu} = \frac{i}{g} [D_\mu, D_\nu] = \partial_\mu A_\nu - \partial_\nu A_\mu - ig [A_\mu, A_\nu], \quad (2.9)$$

and can be decomposed in the different components $\mathcal{F}_{\mu\nu}(x) = \mathcal{F}_{\mu\nu}^a(x) \Gamma^a$ according to

$$\mathcal{F}_{\mu\nu}^a(x) = \partial_\mu A_\nu^a(x) - \partial_\nu A_\mu^a(x) + g f^{abc} A_\mu^b(x) A_\nu^c(x). \quad (2.10)$$

We note that in contrast to QED, there is a non-linear term involved in Eq. (2.10), which is a manifestation of the non-abelian structure of the $SU(N_c)$ gauge group. By use of Eq. (2.2), it is straightforward to show that the field strength tensor transforms covariantly under local gauge transformations, i.e.

$$\mathcal{F}_{\mu\nu}^{(G)}(x) = G(x) \mathcal{F}_{\mu\nu}(x) G^\dagger(x). \quad (2.11)$$

The Yang-Mills part of the Lagrangian density $\mathcal{L}_{\text{Yang-Mills}}$ then takes the form

$$\mathcal{L}_{\text{Yang-Mills}}[A](x) = -\frac{1}{2} \text{tr}[\mathcal{F}_{\mu\nu}(x) \mathcal{F}^{\mu\nu}(x)], \quad (2.12)$$

which is invariant under local gauge transformations. Combining the gauge and matter sectors, the classical action of QCD is then given by

$$S[A, \bar{\psi}, \psi] = \int d^4x \left(\mathcal{L}_{\text{Yang-Mills}}[A](x) + \mathcal{L}_{\text{Matter}}[A, \bar{\psi}, \psi](x) \right). \quad (2.13)$$

In the remainder of this work, we will focus on the gluonic part and study the non-equilibrium dynamics of pure Yang-Mills theory, defined by the classical action

$$S_{YM}[A] = -\frac{1}{4} \int d^4x \mathcal{F}_{\mu\nu}^a(x) \mathcal{F}_a^{\mu\nu}(x). \quad (2.14)$$

Since the gluons are charged under the adjoint representation of the $SU(N_c)$ gauge group, they interact with each other and the classical action in Eq. (2.14) already contains cubic and quartic interaction terms. The simplification of neglecting fermionic degrees of freedom is motivated by several reasons of both physical and technical nature. First of all the non-equilibrium dynamics of heavy-ion collisions at weak coupling, as described in the color-glass condensate framework [27, 28], is characterized by large gluon occupations on the order of the inverse self-coupling. In contrast, since fermions obey the Pauli principle, their characteristic occupancy can not exceed unity, such that the gluonic contribution to bulk observables, as e.g. the energy density, is parametrically enhanced at weak coupling. One therefore expects the non-equilibrium plasma to be gluon dominated at sufficiently weak coupling and it is reasonable to neglect the quark degrees of freedom. The second, more technical reason, is related to the lattice discretization of fermionic degrees of freedom. First of all, since fermionic degrees of freedom can not exhibit occupation numbers larger than unity the classical-statistical approximation does not apply and one needs to consider a genuine quantum approach to study the non-equilibrium dynamics. While there has been significant progress concerning this problem [59–63], numerical simulations involving fermions are technically more involved and require larger computational resources. Hence it appears natural, to first study the non-equilibrium dynamics of pure Yang-Mills theory and include fermions later to study their effect on the evolution.

In addition to neglecting the fermionic degrees of freedom, we will in the following consider the gauge group $SU(2)$ rather than the $SU(3)$ gauge group of the QCD Yang-Mills sector. While this greatly simplifies the numerical studies, it has explicitly been checked that there are no qualitative differences in the non-equilibrium dynamics, for the different gauge groups $SU(2)$ and $SU(3)$ in classical-statistical lattice simulations [64] as well as for $SU(2)$, $SU(3)$, $SU(4)$ and $SU(5)$ in the discretized hard-loop approximation [65]. Hence, we expect no qualitative differences for the results presented in this work.

We close this short introduction with a discussion of the classical equations of motion. As we will argue shortly in Sec. 2.2, these capture the essence of the quantum field dynamics in the regime of large occupancies and weak coupling. The classical field equations follow from the principle of the stationary action

$$\frac{\delta S[A]}{\delta A_\mu^a(x)} = 0, \quad (2.15)$$

and form a set of $4 \times (N_c^2 - 1)$ coupled partial differential equations

$$D_\mu^{ab}(x) \mathcal{F}_b^{\mu\nu}(x) = -J_a^\nu(x), \quad (2.16)$$

which reduce to a set of free equations in the case of $g \rightarrow 0$, which correspond to the Maxwell equations in electrodynamics. The current in Eq. (2.16) is covariantly conserved and satisfies the continuity equation

$$D_\mu^{ab}(x)J_b^\mu(x) = 0. \quad (2.17)$$

In the case of full QCD the current is given by $J_a^\nu(x) = g\bar{\psi}\Gamma^a\gamma^\nu\psi$, whereas for pure Yang-Mills theory it vanishes in the absence of external sources.

We will frequently decompose the field strength tensor into the electric and magnetic components according to

$$E_a^i(x) = \mathcal{F}_a^{i0}(x), \quad B_i^a(x) = \frac{1}{2}\epsilon^{ijk}\mathcal{F}_{jk}^a(x), \quad (2.18)$$

such that the time-like component ($\nu = 0$) of the Yang-Mills equations (2.16) can also be rewritten as

$$D_i^{ab}(x)E_b^i(x) = -J_a^0(x). \quad (2.19)$$

This is the non-abelian version of the familiar Gauss law constraint. In the absence of sources $J_a^\nu(x) = 0$, which we will consider throughout this work, it can easily be shown that the left hand side of Eq. (2.19) is conserved by the dynamical evolution equations (2.16) for $\nu = 1, 2, 3$. The Gauss law in Eq. (2.19) therefore corresponds to a non-dynamical constraint, which once satisfied at initial time is conserved throughout the dynamical evolution.

Since the action in Eq. (2.14) is invariant under local gauge transformations, the stationary point is of course not unique and Eq. (2.15) is satisfied by all gauge copies. When solving the Yang-Mills equations (2.16), it is therefore more efficient to eliminate some of the redundancy by implementing a suitable gauge fixing condition. Here we will mostly employ temporal axial gauge ($A_t = 0$),⁴ which partially fixes the gauge freedom up to time independent gauge transformations. The latter will be left open and only be specified a posteriori, whenever we are interested in gauge dependent quantities.

⁴When simulating expanding systems, we will employ the Fock Schwinger gauge condition ($A_\tau = 0$), which is the co-moving analogue of temporal axial gauge.

2.2 Non-equilibrium quantum field theory

We will now introduce some of the basic concepts of non-equilibrium statistical mechanics of classical and quantum systems and subsequently outline a comparison between the two types of systems. We refer to Refs. [40–42, 66–69] for a more detailed discussion of many aspects.

The central problem of non-equilibrium statistical mechanics is to determine the time evolution of a given initial state. In a classical theory, defined by a (time-independent) Hamilton function $H(x, p)$ with canonical variables x and conjugate momenta p , such a state is determined by a (positive semi-definite) phase space function $W_0[x_0, p_0]$, which describes the distribution of initial conditions (x_0, p_0) at initial time t_0 and contains all information about physical observables. In particular the expectation value of any observable $\mathcal{O}(t)$, which is a function of the phase space variables x and p at any time $t \geq t_0$, can be calculated as an ensemble average over different realizations according to

$$\langle \mathcal{O}(t) \rangle = \int dx dp W[x, p; t] \mathcal{O}[x, p; t] , \quad (2.20)$$

such that the problem of non-equilibrium dynamics is to determine the time evolution of the phase space distribution $W[x, p; t]$. In classical-statistical mechanics, this is governed by the Liouville equation

$$\partial_t W[x, p; t] = \{H, W\}_{\text{PoissonBracket}} , \quad (2.21)$$

which describes the evolution of the phase space density in time. In view of systems with many degrees of freedom, Eq. (2.21) is in practice difficult to solve, since it is a partial differential equation of many variables. However, it is of course also possible to follow the individual phase space trajectories $(x_{\text{cl}}^0(t), p_{\text{cl}}^0(t))$, which solve the classical equations of motion

$$\dot{x}_{\text{cl}}^0(t) = \frac{\partial H}{\partial p}(x_{\text{cl}}^0(t), p_{\text{cl}}^0(t)) , \quad \dot{p}_{\text{cl}}^0(t) = -\frac{\partial H}{\partial x}(x_{\text{cl}}^0(t), p_{\text{cl}}^0(t)) , \quad (2.22)$$

for the initial condition $(x_{\text{cl}}^0(t_0), p_{\text{cl}}^0(t_0)) = (x_0, p_0)$, and subsequently average over all trajectories according to the initial phase space distribution. The phase space density $W[x, p; t]$ can then equivalently be expressed as [68]

$$W[x, p; t] = \int dx_0 dp_0 W_0[x_0, p_0] \delta(x - x_{\text{cl}}^0(t)) \delta(p - p_{\text{cl}}^0(t)) , \quad (2.23)$$

which is more useful for practical purposes. Since the classical evolution maps every point (x_0, p_0) in phase space at initial time t_0 , to exactly one point $(x_{\text{cl}}^0(t), p_{\text{cl}}^0(t))$ at any time $t > t_0$,

the corresponding transition amplitude is the point measure given by the delta functions in Eq. (2.23) and it is straightforward to prove that Eq. (2.23) solves the Liouville equation.⁵ In particular, the extension of Eq. (2.23) to systems with many degrees of freedom is straightforward, and we will use this formulation to calculate expectation values in classical-statistical field theories by a standard Monte-Carlo procedure as discussed in Sec. 2.4. We will now discuss the general properties of non-equilibrium quantum systems and motivate the classical-statistical approximation.

In a general quantum theory in the Schrödinger picture, defined by a (time-independent) Hamiltonian H , the properties of a state are determined by the density operator ρ , which contains the information about all physical observables. The expectation value of observables \mathcal{O} can be calculated as the trace over the Hilbert space according to

$$\langle \mathcal{O} \rangle = \text{tr}[\mathcal{O}\rho] , \quad (2.24)$$

and the time evolution of the density operator is governed by the quantum analogue of the Liouville equation, the von-Neumann equation

$$i\hbar \partial_t \rho = [H, \rho] . \quad (2.25)$$

Since solving the operator equation (2.25) is impractical to study the non-equilibrium dynamics of quantum many-body systems, alternative functional techniques have been developed to study initial value problems in quantum field theories (see e.g. Refs. [42, 66]). The general strategy is to perform a path integral quantization and compute observables from correlation functions. However, the functional quantization of non-abelian gauge theories is complicated by the appearance of gauge equivalent copies, which need to be eliminated by a suitable gauge fixing procedure in order to extract meaningful correlation functions. Since this is not of direct relevance to this work, we will omit a further discussion and assume the existence of a gener-

⁵By exponentiating the delta functions and performing the partial derivative one immediately obtains

$$\begin{aligned} \partial_t W[x, p; t] &= - \int \frac{d\alpha}{2\pi} \frac{d\beta}{2\pi} \int dx_0 dp_0 W_0[x_0, p_0] [i\alpha \dot{x}_{\text{cl}}^0(t) + i\beta \dot{p}_{\text{cl}}^0(t)] e^{i\alpha(x-x_{\text{cl}}^0(t))} e^{i\beta(p-p_{\text{cl}}^0(t))} \\ &= - \frac{\partial}{\partial x} \int dx_0 dp_0 W_0[x_0, p_0] \frac{\partial H}{\partial p}(x_{\text{cl}}^0, p_{\text{cl}}^0) \delta(x - x_{\text{cl}}^0(t)) \delta(p - p_{\text{cl}}^0(t)) \\ &\quad + \frac{\partial}{\partial p} \int dx_0 dp_0 W_0[x_0, p_0] \frac{\partial H}{\partial x}(x_{\text{cl}}^0, p_{\text{cl}}^0) \delta(x - x_{\text{cl}}^0(t)) \delta(p - p_{\text{cl}}^0(t)) \\ &= \left(\frac{\partial H}{\partial x} \right) \left(\frac{\partial W}{\partial p} \right) - \left(\frac{\partial W}{\partial x} \right) \left(\frac{\partial H}{\partial p} \right) = \{H, W\}_{\text{PoissonBracket}} , \end{aligned}$$

where we used Hamilton's equations of motion (2.22) to express the time derivatives and in the last step we evaluated the expressions at $(x_{\text{cl}}^0(t), p_{\text{cl}}^0(t)) = (x, p)$ according to the delta functions. We also used that the second derivatives cancel due to the relative minus sign.

ating functional in the following. We refer the interested reader to the literature instead (see e.g. [56, 57, 70, 71]).

2.2.1 Generating Functional and 2PI effective action

The central object in functional approaches is the non-equilibrium generating functional [42, 66, 72, 73]

$$\begin{aligned}
 Z[J, R] = & \underbrace{\int [dA^{(1)}][dA^{(2)}] \langle A^{(1)} | \rho_0 | A^{(2)} \rangle}_{\text{Initial conditions}} \int_{A^{(1)}}^{A^{(2)}} \mathcal{D}A \exp \left[i \left(S_{\text{eff}}^{\mathcal{C}}[A] + \int_x^{\mathcal{C}} J_a^\mu(x) A_\mu^a(x) \right. \right. \\
 & \left. \left. + \frac{1}{2} \int_{xy}^{\mathcal{C}} A_\mu^a(x) R_{ab}^{\mu\nu}(x, y) A_\nu^b(y) \right) \right], \\
 & \underbrace{\hspace{15em}}_{\text{Non-equilibrium dynamics}}
 \end{aligned} \tag{2.26}$$

from which correlation functions can be obtained by functional differentiation with respect to the sources J and R . The functional integrals over the initial conditions $[dA^{(1/2)}]$ are taken at initial time t_0 , whereas the integration over the dynamical gauge fields $\mathcal{D}A$ extends along the Schwinger-Keldysh contour shown in Fig. 2.1.⁶ Similarly, the space-time integrals $\int_x^{\mathcal{C}}$ are to be understood as integration along the closed time path, such that the time ordering on the lower branch is reversed, while any time on the lower part of the contour is considered later than any time on the upper part of the contour. Also, the contour action $S_{\text{eff}}^{\mathcal{C}}[A]$ in Eq. (2.26) is taken along the closed time path and in general contains additional gauge fixing and ghost contributions [72, 73]. However, we will only consider axial gauges, in particular temporal axial gauge ($A_t = 0$), for which the contour action is given by⁷

$$S_{\text{eff}}^{\mathcal{C}}[A] = \int_x^{\mathcal{C}} \left[\frac{1}{2} (\partial_t A_i^a(x))^2 - \frac{1}{4} \mathcal{F}_{ij}^a(x) \mathcal{F}_a^{ij}(x) \right]. \tag{2.27}$$

In order to obtain connected correlation functions, it is more suitable to consider the Schwinger functional $W[J, R]$, which similar to vacuum or thermal equilibrium quantum field theory is defined as

$$W[J, R] = -i \log Z[J, R]. \tag{2.28}$$

The field expectation value is then given by functional differentiation with respect to J according

⁶The super- and subscripts of the functional integral represent the fact that the fields match $A^{(1)}$ and $A^{(2)}$ at the beginning and respectively the end of the closed time contour.

⁷Note that we did not fix the residual gauge freedom to perform time-independent gauge transformations. However, this can be done at initial time t_0 , such that only the initial conditions are affected.

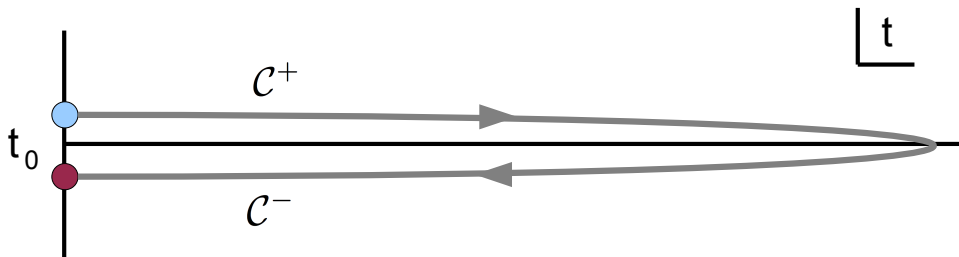


Figure 2.1: Closed time contour.

to

$$\mathcal{A}_\mu^a(x) = \langle A_\mu^a(x) \rangle = \left. \frac{\delta W[J, R]}{\delta J_\mu^a(x)} \right|_{J, R} \quad (2.29)$$

and vanishes in the absence of sources.⁸ The propagator $G_{\mu\nu}^{ab}(x, y)$ is defined as the connected two-point correlation function

$$G_{\mu\nu}^{ab}(x, y) = \langle \mathcal{T}_C A_\mu^a(x) A_\nu^b(y) \rangle - \mathcal{A}_\mu^a(x) \mathcal{A}_\nu^b(y) = 2 \left. \frac{\delta W[J, R]}{\delta R_{ab}^{\mu\nu}(x, y)} \right|_{J, R} - \mathcal{A}_\mu^a(x) \mathcal{A}_\nu^b(y), \quad (2.30)$$

where \mathcal{T}_C denotes time ordering along the closed time path as illustrated in Fig. 2.1. The time ordered propagator can be decomposed in terms of the spectral and statistical components according to

$$G_{\mu\nu}^{ab}(x, y) = F_{\mu\nu}^{ab}(x, y) - \frac{i}{2} \text{sign}_C(x^0 - y^0) \rho_{\mu\nu}^{ab}(x, y), \quad (2.31)$$

where sign_C denotes the sign function on the closed time contour. The statistical two-point function is given by the anti-commutator

$$F_{\mu\nu}^{ab}(x, y) = \frac{1}{2} \langle \{A_\mu^a(x), A_\nu^b(y)\} \rangle - \mathcal{A}_\mu^a(x) \mathcal{A}_\nu^b(y) = \frac{1}{2} [G_{\mu\nu}^{ab}(x, y) + G_{\nu\mu}^{ba}(y, x)], \quad (2.32)$$

while the spectral function is given by the commutator⁹

$$\rho_{\mu\nu}^{ab}(x, y) = i \langle [A_\mu^a(x), A_\nu^b(y)] \rangle. \quad (2.33)$$

The spectral function ρ determines the structure of excitations of the system, while the statistical propagator F contains the information about how often these states are occupied. In thermal equilibrium there is only one independent two point correlation function, since the two

⁸We will also consider non-vanishing background fields $\mathcal{A}_\mu^a(x)$, as an effective description of very soft excitations of the system, for which a description in terms of two-point correlation functions is more involved.

⁹Note that these can also be obtained by functional derivatives with respect to the sources, when the distinction between the upper branch C^+ and lower branch C^- of the contour is made explicit (see e.g. [41, 66]).

are related by the Kubo-Martin-Schwinger (KMS) condition [74, 75], sometimes also referred to as fluctuation-dissipation relation. Of course, this is no longer true out-of-equilibrium and we will need to consider F and ρ as independent objects.

The quantum evolution equations, for the connected one and two-point correlation functions can be derived from the two particle irreducible (2PI) effective action, which is defined as the Legendre transform of the Schwinger functional according to

$$\Gamma_{2\text{PI}}[\mathcal{A}, G] = W[J, R] - \int_x^{\mathcal{C}} \mathcal{A}_\mu^a(x) J_a^\mu(x) - \frac{1}{2} \int_{xy}^{\mathcal{C}} (G_{\mu\nu}^{ab}(x, y) + \mathcal{A}_\mu^a(x) \mathcal{A}_\nu^b(y)) R_{ab}^{\mu\nu}(x, y), \quad (2.34)$$

which is frequently expressed as [42, 72, 76, 77]

$$\Gamma_{2\text{PI}}[\mathcal{A}, G] = S[\mathcal{A}] + \frac{i}{2} \text{tr} \log G^{-1} + \frac{i}{2} \text{tr} G_0^{-1}[\mathcal{A}]G + \Gamma_2[\mathcal{A}, G]. \quad (2.35)$$

In a diagrammatic language, the 2PI effective action contains all two-particle irreducible diagrams, with propagator lines associated to the self-consistently resummed propagators. The vertices are the standard tree level ones in the presence of the background field \mathcal{A} , which is in contrast to different functional approaches such as the Functional Renormalization Group [78, 79], Dyson-Schwinger equations [79, 80] or higher n -PI effective actions [72, 79], where the vertices also receive corrections.

In analogy to the classical equations of motion, the quantum evolution equations follow from the stationarity of the 2PI effective action

$$\left. \frac{\delta \Gamma_{2\text{PI}}[\mathcal{A}, G]}{\delta \mathcal{A}_\mu^a(x)} \right|_{J,R=0} = -J_a^\mu(x), \quad \left. \frac{\delta \Gamma_{2\text{PI}}[\mathcal{A}, G]}{\delta G_{\mu\nu}^{ab}(x, y)} \right|_{J,R=0} = 0, \quad (2.36)$$

and form a closed set of coupled integro-differential equations for the connected one and two-point correlation functions [42, 72]. These are analogous to the Dyson-Schwinger equations, with the difference that the self-energies in this approach contain the tree-level vertices only and the hierarchy of equations is closed at the propagator level. In turn, the Eqns. (2.36) contain an infinite set of self-energy diagrams, which for any practical purpose requires a suitable truncation. While for some purposes it is sufficient to employ an expansion up to a fixed loop order [42], this typically fails in situations where the suppression of higher loops due to the small coupling constant is compensated by large statistical fluctuations (see e.g. [53]). However, as we will discuss now, the framework of classical-statistical field theory provides a robust approximation for the quantum field dynamics in these situations [40, 41].

2.2.2 Classical aspects of quantum dynamics

In order to highlight the classical aspects of the quantum dynamics, we follow a standard procedure [40, 41, 68] and perform some manipulations of the generating functional in Eq. (2.26). In the first step, we split the closed time contour \mathcal{C} into the upper branch \mathcal{C}^+ and lower branch \mathcal{C}^- as illustrated in Fig. 2.1 and introduce the field variables A^+ and A^- , which have support only on the respective branches. This allows us to make the time ordering on the contour explicit, and the contour action in Eq. (2.27) can then be expressed as

$$S_{\text{eff}}^{\mathcal{C}}[A^+, A^-] = S[A^+] - S[A^-], \quad S[A^\pm] = \int_x \mathcal{L}_{YM}[A^\pm](x), \quad (2.37)$$

where the $\int_x = \int d^4x$ and the time integration now extends along the real time axis only. In the next step, we introduce the field variables A_{cl} and \tilde{A} , which correspond to the average and the difference of the fields on the different branches of the contour according to

$$A_{cl,\mu}^a(x) = [A_\mu^{a,+}(x) + A_\mu^{a,-}(x)] / 2, \quad \tilde{A}_\mu^a(x) = A_\mu^{a,+}(x) - A_\mu^{a,-}(x). \quad (2.38)$$

In terms of the new field variables, the contour action then takes the form

$$S_{\text{eff}}^{\mathcal{C}}[A_{cl}, \tilde{A}] = S[A_{cl} + \tilde{A}/2] - S[A_{cl} - \tilde{A}/2], \quad (2.39)$$

which can be evaluated explicitly according to

$$S_{\text{eff}}^{\mathcal{C}}[A_{cl}, \tilde{A}] = \int_x \frac{\delta S[A]}{\delta A_\mu^a(x)} \Big|_{A=A_{cl}} \tilde{A}_\mu^a(x) + \frac{1}{24} \int_{x,y,z} \frac{\delta^{(3)} S[A]}{\delta A_\gamma^c(z) \delta A_\nu^b(y) \delta A_\mu^a(x)} \Big|_{A=A_{cl}} \tilde{A}_\gamma^c(z) \tilde{A}_\nu^b(y) \tilde{A}_\mu^a(x). \quad (2.40)$$

The functional Taylor series on the right hand side of Eq. (2.40) contains only odd power of \tilde{A} and terminates at fourth order, since the classical action $S[A]$ contains only terms up to cubic order in the fields. One immediately observes that if one drops the second term in Eq. (2.40), the auxiliary field \tilde{A} can be integrated out, since it appears only linearly in the contour action. The integration over the exponential $\exp[i \delta S / \delta A \tilde{A}]$ then enforces the action principle and one recovers the classical equations of motion for the A_{cl} field [68].¹⁰ The difference between the quantum field dynamics and the classical field dynamics is therefore entirely contained in the second term in Eq. (2.40). One also observes, that at the level of a Gaussian approximation, i.e. keeping only terms quadratic in the fields, this term does not contribute, since it contains already three powers of the \tilde{A} field. The difference between the classical and quantum field

¹⁰Note that one can also construct the corresponding path integral from the classical-statistical field theory (see e.g. Refs. [40, 41, 68]).

dynamics is therefore the appearance of additional quantum vertices, which are absent in the dynamics of classical fields.

In order to work out the difference between the classical and quantum vertices, we follow Refs. [40, 41] and consider the diagrammatic contributions of the different terms in Eq. (2.40). We first note that, in terms of the field variables A_{cl} and \tilde{A} , one finds that for physical sources $J^+ = J^- = J$ and $R = 0$, the one point functions are given by [41, 66]

$$\langle A_{cl,\mu}^a(x) \rangle = \mathcal{A}_\mu^a(x), \quad \langle \tilde{A}_\mu^a(x) \rangle = 0, \quad (2.41)$$

and the two-point correlation functions take the form [41, 66]

$$\begin{aligned} \langle \mathcal{T}_C A_{cl,\mu}^a(x) A_{cl,\nu}^b(y) \rangle &= F_{\mu\nu}^{ab}(x, y) + \mathcal{A}_\mu^a(x) \mathcal{A}_\nu^b(y), \quad \langle \mathcal{T}_C \tilde{A}_\mu^a(x) \tilde{A}_\nu^b(y) \rangle = 0, \\ \langle \mathcal{T}_C \tilde{A}_\mu^a(x) A_{cl,\nu}^b(y) \rangle &= -G_{\mu\nu}^{(R),ab}(x, y), \quad \langle \mathcal{T}_C A_{cl,\mu}^a(x) \tilde{A}_\nu^b(y) \rangle = -G_{\mu\nu}^{(A),ab}(x, y). \end{aligned} \quad (2.42)$$

Here we introduced the retarded $G^{(R)}$ and advanced $G^{(A)}$ correlation functions, which are given by¹¹

$$G_{\mu\nu}^{(R),ab}(x, y) = i\theta(x_0 - y_0) \langle [A_\mu^a(x), A_\nu^b(y)] \rangle \quad (2.43)$$

$$G_{\mu\nu}^{(A),ab}(x, y) = -i\theta(y_0 - x_0) \langle [A_\mu^a(x), A_\nu^b(y)] \rangle \quad (2.44)$$

and are related to the spectral function by $\rho = G^{(R)} - G^{(A)}$.

Since the classical and quantum vertices in Eq. (2.40) have the same general structure, it is clear that they give rise to the same topology of self-energy diagrams. However, since the quantum vertex contains powers of \tilde{A} instead of A_{cl} , the additional quantum diagrams contain retarded and advanced propagators $G^{(R/A)}$ instead of the statistical two-point function F . This feature has been exploited in Refs. [40, 41] to formulate the 'classicality condition'

$$|F_{\mu\nu}^{ab}(x, y) F_{\gamma\delta}^{cd}(z, w)| \gg \frac{3}{4} |\rho_{\mu\nu}^{ab}(x, y) \rho_{\gamma\delta}^{cd}(z, w)|, \quad (2.45)$$

and states that the statistical fluctuations have to be large compared to the spectral function for the system to exhibit classical-statistical dynamics. Neglecting the quantum vertices in Eq. (2.40), then amounts to dropping terms proportional to the spectral function, whenever they appear in combination with terms containing the statistical two-point function instead.

¹¹Again, we refrain from giving the formal definition of the correlation functions via the introduction of appropriate contour source terms (see e.g. Refs. [41, 66]).

Of course, a one to one mapping of the generating functional in Eq. (2.26) on to a classical-statistical theory also involves a mapping of the initial conditions [68]. The classical-statistical theory will therefore contain characteristic properties of the quantum system, such as vacuum fluctuations of the initial state. However, the subsequent dynamics is entirely classical and described by the Yang-Mills field equations discussed in Sec. 2.1. Finally, we note that in situations where spectral and statistical two-point functions are related by an occupation number, the classicality condition states that the characteristic occupation of modes has to be much larger than unity. This condition will be met in all physical systems under consideration in this work.

2.3 Co-moving coordinates

Before we discuss the implementation of the classical-statistical framework, we will introduce a different set of coordinates, which are more suitable to describe the dynamics of longitudinally expanding non-abelian plasmas as they appear in the context of relativistic heavy-ion collisions. We will therefore introduce the longitudinal rapidity coordinate η and the longitudinal proper time τ according to

$$\tau = \sqrt{t^2 - z^2}, \quad \eta = \operatorname{atanh}(z/t), \quad (2.46)$$

and we will also need the inverse transformation, given by

$$t = \tau \cosh(\eta), \quad z = \tau \sinh(\eta). \quad (2.47)$$

The covariant metric tensor $g_{\mu\nu}(x)$ in $x^\mu = (\tau, x^1, x^2, \eta)$ coordinates follows from its counterpart $\eta_{\mu\nu} = \operatorname{diag}(1, -1, -1, -1)$ in Minkowski space, with coordinates $\tilde{x}^\mu = (t, x^1, x^2, z)$ according to [81]

$$g_{\mu\nu}(x) = \frac{\partial \tilde{x}^\alpha}{\partial x^\mu} \eta_{\alpha\beta} \frac{\partial \tilde{x}^\beta}{\partial x^\nu} = \operatorname{diag}(1, -1, -1, -\tau^2), \quad (2.48)$$

and we will denote the metric determinant as $g(x) = \det[g_{\mu\nu}(x)] = -\tau^2$, such that $\gamma(x) = \sqrt{-g(x)} = \tau$. In contrast the contravariant metric tensor $g^{\mu\nu}(x)$ is defined by the inverse of the covariant metric tensor $g_{\mu\nu}(x)$, according to [81]

$$g^{\mu\alpha}(x) g_{\alpha\nu}(x) = \delta_\nu^\mu, \quad (2.49)$$

where δ_{ν}^{μ} denotes the Kronecker symbol, such that

$$g^{\mu\nu}(x) = \text{diag}(1, -1, -1, -1/\tau^2) . \quad (2.50)$$

Similarly, the classical gauge fields $A_{\mu}^a(x)$ transform as Lorentz co-vectors under general coordinate transformations [81]

$$A_{\mu}^a(x) = \frac{\partial \tilde{x}^{\alpha}}{\partial x^{\mu}} \tilde{A}_{\alpha}^a(x) , \quad (2.51)$$

such that the (τ, η) components of the gauge fields are given by

$$A_{\tau}^a(x) = \cosh(\eta) A_t^a(x) + \sinh(\eta) A_z^a(x) , \quad A_{\eta}^a(x) = \tau [\sinh(\eta) A_t^a + \cosh(\eta) A_z^a(x)] . \quad (2.52)$$

The classical Yang-Mills action in $x = (\tau, x^1, x^2, \eta)$ coordinates can then be expressed as (see e.g. [50])

$$S[A] = -\frac{1}{4} \int d^4x \sqrt{-g(x)} \mathcal{F}_{\mu\nu}^a(x) g^{\mu\alpha}(x) g^{\nu\beta}(x) \mathcal{F}_{\alpha\beta}^a(x) , \quad (2.53)$$

where the Lorentz indices take the values $\mu, \nu, \alpha, \beta = \tau, 1, 2, \eta$ and $\int d^4x \sqrt{-g(x)} = \int \tau d\tau d\eta d^2\vec{x}_T$ denotes the space-time integral in the new coordinate system. We note that the covariant field strength tensor $\mathcal{F}_{\mu\nu}^a(x)$ is still given by Eq. (2.10), whereas the contravariant field strength tensor $\mathcal{F}_a^{\mu\nu}(x)$ follows as

$$\mathcal{F}_a^{\mu\nu}(x) = g^{\mu\alpha}(x) g^{\nu\beta}(x) \mathcal{F}_{\alpha\beta}^a(x) . \quad (2.54)$$

We will in the following denote the electric components of the field strength tensor as

$$E_a^{\eta}(x) = \tau \mathcal{F}_a^{\eta\tau}(x) , \quad E_a^i(x) = \tau \mathcal{F}_a^{i\tau}(x) , \quad (2.55)$$

such that in Fock-Schwinger ($A_{\tau} = 0$) gauge, which provides the co-moving analogue of the temporal axial ($A_t = 0$) gauge, the electric fields are given by

$$E_a^{\eta}(x) \stackrel{(A_{\tau}=0)}{=} \tau^{-1} \partial_{\tau} A_{\eta}^a(x) , \quad E_a^i(x) \stackrel{(A_{\tau}=0)}{=} \tau \partial_{\tau} A_i^a(x) , \quad (2.56)$$

and correspond to the conjugate momentum variables of the spatial gauge fields.

The classical Yang-Mills equations follow from the action principle in Eq. (2.15) and take

the form

$$D_\mu^{ab}(x) \sqrt{-g(x)} g^{\mu\alpha}(x) g^{\nu\beta}(x) \mathcal{F}_{\alpha\beta}^b(x) = 0, \quad (2.57)$$

where the (gauge) covariant derivative $D_\mu^{ab}(x)$ is still given by Eq. (2.8). We emphasize that this change of coordinates simply amounts to a re-parametrization, which does not affect the physical properties of the theory, such that the above equations still describe the dynamics of Yang-Mills theory in 3+1 space-time dimensions. However, since the typical initial conditions employed to study the non-equilibrium dynamics of relativistic heavy-ion collisions are defined at a fixed proper time $\tau = \tau_0$ and exhibit a translation invariance in longitudinal rapidity η as well as in the transverse coordinates $\vec{x}_T = (x^1, x^2)$, a formulation in terms of (τ, η) coordinates is indeed beneficial. Since the study of longitudinally expanding systems is a central topic of this work, we will also discuss the lattice discretization in the co-moving (τ, η) coordinates. The reduction to Minkowski space is straightforward and also discussed below.

2.4 Classical-statistical real-time lattice gauge theory

In the remainder of this chapter we will describe the framework to perform classical-statistical real-time simulations of $SU(2)$ Yang-Mills theory. Since the classical Yang-Mills equations can in general not be solved analytically, this requires the use of a numerical method which is based on the discretization of the theory on a space-time lattice. The lattice discretization proceeds along similar lines as in standard vacuum or thermal equilibrium lattice QCD (see e.g. [82]), where in general there are several ways to discretize the Yang-Mills action, which differ in the level of accuracy in spatial and temporal lattice spacings [83–85]. Here we will employ a Wilsonian lattice formulation [84] in Fock-Schwinger ($A_\tau = 0$) gauge, which is particularly well suited to describe the dynamics of longitudinally expanding non-abelian plasmas. In this approach we consider points (\vec{x}_\perp, η) on a cubic lattice of spatial size $N_T \times N_T \times N_\eta$ separated by the lattice spacing a_\perp in the transverse and a_η in the longitudinal directions respectively. The temporal τ direction remains continuous in the first place and will be discretized in the second step. We employ periodic boundary conditions in the spatial directions and we will collectively label the spatial and temporal coordinates as $x = (\tau, \vec{x}_\perp, \eta)$.

In this framework, the continuum gauge fields $A_\mu^a(x)$ are represented in terms of the gauge link variables $U_\mu(x)$ which are given by

$$U_i(x) = \exp[iga_\perp A_i^a(x + \hat{i}/2)\Gamma^a], \quad U_\eta(x) = \exp[iga_\eta A_\eta^a(x + \hat{\eta}/2)\Gamma^a], \quad (2.58)$$

where $\Gamma^a = \sigma^a/2$ are the generators of the $su(2)$ Lie algebra in the fundamental representation

and the symbol $\hat{\mu} = \hat{x}^1, \hat{x}^2, \hat{\eta}$ denotes the neighboring lattice site in the μ direction. The gauge link variables can be intuitively understood as an approximation of the path-ordered Wilson line $\mathcal{P} \exp[ig \int_x^y A]$, connecting adjacent lattice sites x and y along a straight line path. In particular, the gauge link variables transform as the Wilson lines according to

$$U_\mu^{(G)}(x) = G(x)U_\mu(x)G^\dagger(x + \hat{\mu}), \quad U_\mu^{\dagger(G)}(x) = G(x + \hat{\mu})U_\mu(x)G^\dagger(x), \quad (2.59)$$

under time-independent local gauge transformations $G(x) \in SU(2)$. The lattice action and the classical evolution equations for the gauge link variables can be formulated in terms of the spatial plaquette variables $V_{\mu\nu}(x)$ and $W_{\mu\nu}(x)$, which are defined as usual as

$$\begin{aligned} V_{\mu\nu}(x) &= U_\mu(x)U_\nu(x + \hat{\mu})U_\mu^\dagger(x + \hat{\nu})U_\nu^\dagger(x), \\ W_{\mu\nu}(x) &= U_\mu(x)U_\nu^\dagger(x + \hat{\mu} - \hat{\nu})U_\mu^\dagger(x - \hat{\nu})U_\nu(x - \hat{\nu}), \end{aligned} \quad (2.60)$$

such that $W_{\mu\nu}(x) = U_\nu^\dagger(x - \hat{\nu})V_{\mu\nu}^\dagger(x - \hat{\nu})U_\nu(x - \hat{\nu})$. The plaquette variables can be related to the continuum expression of the non-abelian field strength tensor $\mathcal{F}_{\mu\nu}^a(x)$ by virtue of

$$V_{\mu\nu}(x) = \exp[iga_\mu a_\nu \mathcal{F}_{\mu\nu}^a(x + \hat{\mu}/2 + \hat{\nu}/2)\Gamma^a + \mathcal{O}(ga^3)] \quad (2.61)$$

$$W_{\mu\nu}(x) = \exp[-iga_\mu a_\nu \mathcal{F}_{\mu\nu}^a(x + \hat{\mu}/2 - \hat{\nu}/2)\Gamma^a + \mathcal{O}(ga^3)] \quad (2.62)$$

for sufficiently small lattice spacings a_\perp, a_η . We note that the plaquette variables are defined in the center of the respective Wilson loop as indicated in Fig. 2.2. In this sense the phase of the plaquette $V_{\mu\nu}(x)$ and $W_{\mu\nu}(x)$ corresponds to the magnetic flux through the area spanned by the Wilson loop to leading order in the lattice spacing.

In order to construct the lattice gauge action, we will now also discretize the time direction, however keeping the temporal lattice spacing $a_\tau \ll (a_\perp, \tau, \tau a_\eta)$ sufficiently close to the continuum limit. We can then also introduce the time-like plaquette variables $U_{\tau\mu}(x)$, which take the general form

$$U_{\tau\mu}(x) = U_\tau(x)U_\mu(x + \hat{\tau})U_\tau^\dagger(x + \hat{\mu})U_\mu^\dagger(x), \quad (2.63)$$

where $\hat{\tau}$ denotes the neighboring lattice site in the temporal direction. In Fock-Schwinger ($A_\tau = 0$) gauge, where the temporal links are trivial ($U_\tau = \mathbb{1}$), the time-like plaquette variables have a simpler structure

$$U_{\tau\mu}(x) = U_\mu(x + \hat{\tau})U_\mu^\dagger(x). \quad (2.64)$$

Similar to Eqns. (2.61) and (2.62), the temporal plaquette variables can be related to the

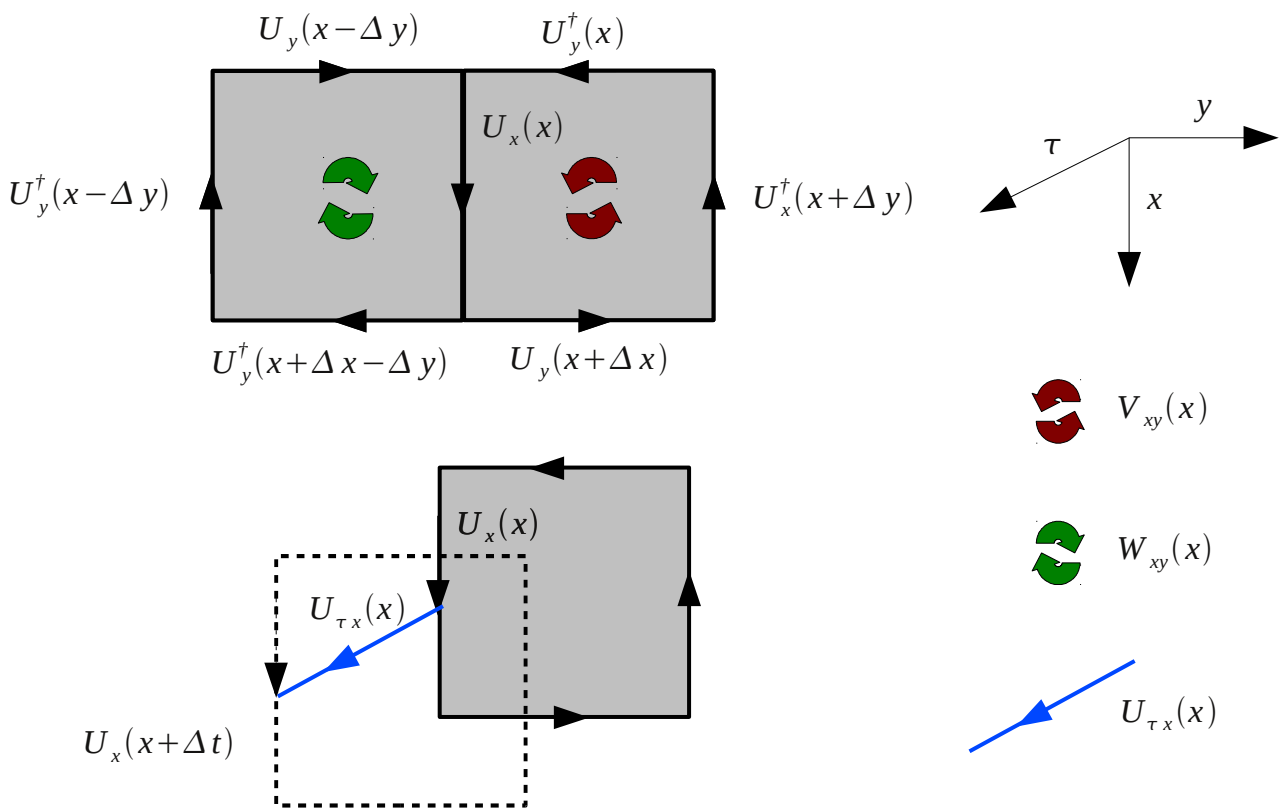


Figure 2.2: Illustration of the lattice link and plaquette variables.

(dimensionless) electric field variables $\tilde{E}_a^\mu(x)$ on the lattice according to

$$\tilde{E}_a^i(x) = -2\frac{\tau}{a_\tau}\text{tr}[i\Gamma^a U_{\tau i}(x)] , \quad \tilde{E}_a^\eta(x) = -2\frac{a_\perp^2}{\tau a_\tau a_\eta}\text{tr}[i\Gamma^a U_{\tau\eta}(x)] , \quad (2.65)$$

for the transverse components $U_{\tau i}(x)$ and longitudinal components $U_{\tau\eta}(x)$ respectively. In the limit of small temporal lattice spacing ($a_\tau \rightarrow 0$), they are then related to the corresponding continuum fields $E_a^i(x)$ by

$$\tilde{E}_a^i(x) = ga_\perp E_a^i(x + \hat{i}/2 + \hat{\tau}/2) , \quad \tilde{E}_a^\eta(x) = ga_\perp^2 E_a^\eta(x + \hat{\eta}/2 + \hat{\tau}/2) . \quad (2.66)$$

In analogy to the spatial plaquette variables $V_{\mu\nu}(x)$ and $W_{\mu\nu}(x)$, the time-like plaquette variables $U_{\tau\mu}(x)$ are defined at half-integer time-steps $x + \hat{\mu}/2 + \hat{\tau}/2$, as indicated by blue arrows in Fig. 2.2. We will see shortly that this choice corresponds to the so called leap-frog discretization scheme employed in the discretized version of the evolution equations.

An important feature of the plaquette variables is the fact that these objects transform covariantly under time-independent gauge transformations, i.e.

$$V_{\mu\nu}^{(G)}(x) = G(x)V_{\mu\nu}(x)G^\dagger(x) , \quad W_{\mu\nu}^{(G)}(x) = G(x)W_{\mu\nu}(x)G^\dagger(x) , \quad U_{\tau\mu}^{(G)}(x) = G(x)U_{\tau\mu}(x)G^\dagger(x) . \quad (2.67)$$

In particular this implies that the trace of a plaquette variable or in general any closed Wilson loop is gauge invariant. This property can be used to construct a gauge invariant lattice action as well as gauge invariant observables as discussed below.

2.4.1 Equations of motion and Gauss law

The lattice evolution equations can be derived from the Wilsonian lattice action, which for the $SU(2)$ gauge group can be expressed as (see e.g. [52, 86, 87])

$$S[U] = \frac{2}{g^2} \sum_x \left\{ \left(\frac{a_\perp^2}{a_\tau \tau a_\eta} \right) \text{tr}[\mathbb{1} - U_{\tau\eta}(x)] - \left(\frac{a_\tau \tau a_\eta}{a_\perp^2} \right) \text{tr}[\mathbb{1} - V_{xy}(x)] \right. \\ \left. + \left(\frac{\tau a_\eta}{a_\tau} \right) \sum_i \text{tr}[\mathbb{1} - U_{\tau i}(x)] - \left(\frac{a_\tau}{\tau a_\eta} \right) \sum_i \text{tr}[\mathbb{1} - V_{i\eta}(x)] \right\} , \quad (2.68)$$

where the sum over $x = \tau, \vec{x}_\perp, \eta$ includes all sites of the space-time lattice. Since the lattice action in Eq. (2.68) contains only traces of plaquette variables it is manifestly gauge-invariant. The classical equations of motion can then be obtained as usual by variation of the action with

respect to the gauge links

$$\frac{\delta S}{\delta U} = 0. \quad (2.69)$$

Since the gauge link variables are group elements, the variation has to be performed within the $SU(2)$ gauge group according to $U_\mu(x) \rightarrow (1 + i\alpha_\mu^a(x)\Gamma^a)U_\mu(x)$.¹² Since according to Eq. (2.64) the time-like plaquette variables connect two neighboring sites in the temporal direction, the variation of the electric components of the action is given by

$$\left. \frac{\delta}{\delta \alpha_\mu^a(y)} \right|_{\alpha=0} \sum_x \text{tr}[U_{\tau\alpha}(x)] = -\delta_{\mu\alpha} \text{tr} [i\Gamma^a(U_{\tau\alpha}(y) - U_{\tau\alpha}(y - \hat{\tau}))]. \quad (2.70)$$

Similarly one finds that the variation of the magnetic components of the gauge action can be expressed as

$$\left. \frac{\delta}{\delta \alpha_\mu^a(y)} \right|_{\alpha=0} \sum_x \text{tr}[V_{\alpha\beta}(x)] = \delta_{\mu\alpha} \text{tr} [i\Gamma^a(V_{\alpha\beta}(y) + W_{\alpha\beta}(y))] + \delta_{\mu\beta} \text{tr} [i\Gamma^a(V_{\beta\alpha}(y) + W_{\beta\alpha}(y))]. \quad (2.71)$$

By use of Eq. (2.65) the expression on the right hand side of Eq. (2.70) can be rewritten in terms of the electric field variables. The evolution equations for the electric field variables then take the form

$$\begin{aligned} \tilde{E}_a^i(x) - \tilde{E}_a^i(x - \hat{\tau}) &= 2\frac{a_\tau}{\tau a_\eta^2} \text{tr} [i\Gamma^a(V_{i\eta}(x) + W_{i\eta}(x))] + 2\frac{a_\tau\tau}{a_\perp^2} \sum_{j \neq i} \text{tr} [i\Gamma^a(V_{ij}(x) + W_{ij}(x))], \\ \tilde{E}_a^\eta(x) - \tilde{E}_a^\eta(x - \hat{\tau}) &= 2\frac{a_\tau}{\tau a_\eta} \sum_i \text{tr} [i\Gamma^a(V_{\eta i}(x) + W_{\eta i}(x))]. \end{aligned} \quad (2.72)$$

Similarly one can invert Eq. (2.65), such that, in the limit of small temporal lattice spacing ($a_\tau \rightarrow 0$), the time-like plaquette variables can equivalently be expressed in terms of the electric field variables according to¹³

$$U_{\tau i}(x) = \exp \left[i\frac{a_\tau}{\tau} \tilde{E}_a^i(x)\Gamma^a \right], \quad U_{\tau\eta}(x) = \exp \left[i\frac{a_\tau\tau a_\eta}{a_\perp^2} \tilde{E}_a^\eta(x)\Gamma^a \right]. \quad (2.73)$$

Since the time plaquettes connect the gauge link variables on adjacent lattice sites in the time direction, Eqns. (2.64) and (2.73) can be used to construct the evolution equation for the link

¹²Note that this automatically implies the variation of $U_\mu^\dagger(x) \rightarrow (1 - i\alpha_\mu^a(x)\Gamma^a)U_\mu^\dagger(x)$ for the adjoint gauge links.

¹³We note that, while strictly speaking, the relation in Eq. (2.73) is only accurate to next-to-leading order in the temporal lattice spacing $\mathcal{O}(a_\tau^2)$, the stability of the numerical solution typically requires very small values of $a_\tau \ll (a_\perp, \tau, \tau a_\eta)$, such that in practice we observe no difference between Eq. (2.73) and the exact inversion of Eq. (2.65).

variables as

$$U_i(x + \hat{\tau}) = \exp \left[i \frac{a_\tau}{\tau} \tilde{E}_a^i(x) \Gamma^a \right] U_i(x), \quad U_\eta(x + \hat{\tau}) = \exp \left[i \frac{a_\tau \tau a_\eta}{a_\perp^2} \tilde{E}_a^\eta(x) \Gamma^a \right] U_\eta(x). \quad (2.74)$$

We note that the electric field variables are defined at half-integer time steps according to Eq. (2.66), such that the gauge force on the right hand side of Eq. (2.72) is effectively calculated at the mid-point of the considered time interval. Similarly the time-like plaquettes $U_{\tau\mu}(x)$ on the right hand side of Eq. (2.74) are defined at the mid-point $x + \hat{\mu}/2 + \hat{\tau}/2$ of the considered time interval. This realization of the evolution equation corresponds to the so called leap-frog discretization scheme.

In addition to the evolution equations (2.72) and (2.74), a further constraint can be derived from the lattice action, by performing a variation with respect to the temporal links $U_\tau(x)$.¹⁴ This yields the discretized version of the Gauss law constraint

$$\begin{aligned} & \left(\frac{a_\perp^2}{a_\tau \tau a_\eta} \right) \text{tr} [i \Gamma^a (U_{\tau\eta}(x) - U_\eta^\dagger(x - \hat{\eta}) U_{\tau\eta}(x - \hat{\eta}) U_\eta(x - \hat{\eta}))] \\ & + \left(\frac{\tau a_\eta}{a_\tau} \right) \sum_i \text{tr} [i \Gamma^a (U_{\tau i}(x) - U_i^\dagger(x - \hat{i}) U_{\tau i}(x - \hat{i}) U_i(x - \hat{i}))] = 0 \end{aligned} \quad (2.75)$$

which needs to be satisfied separately for all color components a at each position x in space-time. Since the current on the left hand side of Eq. (2.75) is conserved by the equations of motion in the continuum limit, the Gauss law constraint is a non-dynamical constraint, which physically meaningful initial conditions have to satisfy. However, during the course of numerical lattice simulations, Eq. (2.75) will be violated due to rounding and discretization errors. In practice, the Gauss law constraint is therefore implemented at initial time and the violation of Eq. (2.75) is then monitored throughout the subsequent time evolution to ensure that discretization errors are sufficiently small.

Before we discuss the implementation of the above lattice setup, we briefly note that the evolution equations in Minkowski space time (see e.g. [52, 86, 87]) can easily be recovered by the replacement $\tau \rightarrow a_\perp$, $a_\eta \rightarrow 1$ in the above evolution equations.¹⁵ This is particularly convenient for testing the numerical implementation and will further enable us to perform simulations also in the so called 'static box' in Minkowski space time as discussed in Chapter 3.

¹⁴Note that the lattice action is invariant also under time dependent gauge transformations. We can therefore consider also variations with respect to the temporal gauge links fix the Fock-Schwinger gauge ($U_\tau = \mathbb{1}$) only after taking derivatives.

¹⁵Of course a reinterpretation of the rapidity coordinate η as the longitudinal coordinate z and the proper time coordinate τ as the Minkowski time t is implied. Similarly, the simulations in Minkowski space time are performed in temporal axial gauge ($A_t = 0$) instead of Fock-Schwinger gauge ($A_\tau = 0$).

2.4.2 Classical-statistical averages and numerical implementation

In order to calculate the expectation value of an observable $\mathcal{O}(x)$ in the classical-statistical approximation one needs to evaluate the expression

$$\langle \mathcal{O}(x) \rangle = \int \mathcal{D}A_0 \mathcal{D}E_0 W_0[A_0, E_0] \mathcal{O}[A_{\text{cl}}^0, E_{\text{cl}}^0; x], \quad (2.76)$$

where $W_0[A_0, E_0]$ is the initial phase-space density and the functional integral extends over all possible field configurations at initial time τ_0 . Here the notation $\mathcal{O}[A_{\text{cl}}^0, E_{\text{cl}}^0; x]$ implies that the observable of interest is to be evaluated as a functional of the classical field solutions A_{cl}^0 and E_{cl}^0 at the point x in space time. While the discretization on a space-time lattice renders the integration in Eq. (2.76) finite dimensional, the remaining high dimensional integral is evaluated by the following Monte Carlo procedure:

We first generate an ensemble of initial conditions according to the initial phase space density $W_0[A_0, E_0]$. For each configuration, the evolution equations (2.72) and (2.74) can then be solved numerically in a straightforward fashion. The electric field variables at the next time step can be calculated from the initial ones by use of Eq. (2.72). In order to construct the gauge links at the next step in time, one subsequently solves Eq. (2.74). The matrix valued exponential involved in Eq. (2.74) can be calculated explicitly for the $SU(2)$ gauge group by use of the relations in Appendix A. By iterating the update procedure multiple times, one obtains the solution of the classical field equations at any time of interest. The classical-statistical expectation value of any observable can then be calculated by evaluating the observable separately for each configuration and subsequently averaging over the ensemble of initial conditions.

In view of the numerical efficiency of the algorithm it is important to realize, that the problem exhibits a high degree of parallelizability, since the time evolution of different initial configurations can be computed independently. Moreover, since the individual updates in Eqns. (2.72) and (2.74) only require the information from up to next-to-nearest neighbor sites, the updates of electric field and gauge link variables can be computed in parallel, with a subsequent exchange of information with nearest and next-to-nearest neighboring sites. In practice, we exploit this feature by dividing the lattice into several slices in the longitudinal direction, which are then all updated in parallel.

2.4.3 Observables

All physical information about the time evolution of the system is contained in gauge invariant observables, which can be calculated in a straightforward way within the framework of classical-

statistical lattice simulations. A central quantity in this context is the energy momentum tensor, which in the continuum takes the form [50]

$$T^{\mu\nu}(x) = -g^{\nu\alpha}(x)\mathcal{F}_a^{\mu\delta}(x)\mathcal{F}_{\alpha\delta}^a(x) + \frac{1}{4}g^{\mu\nu}(x)\mathcal{F}_a^{\gamma\delta}(x)\mathcal{F}_{\gamma\delta}^a(x). \quad (2.77)$$

In particular, we will be interested in the diagonal components of the energy momentum tensor, which can be associated with the energy density ϵ and the longitudinal and transverse pressure densities P_L and P_T according to [50]

$$\epsilon(x) = \langle T^{\tau}_{\tau}(x) \rangle, \quad P_T(x) = -\frac{1}{2}\langle T^x_x(x) + T^y_y(x) \rangle, \quad P_L(x) = -\langle T^{\eta}_{\eta}(x) \rangle. \quad (2.78)$$

The above definitions are normalized such that for locally isotropic systems one obtains the relation $P_L = P_T = \epsilon/3$, whereas for anisotropic systems, the ratio P_L/P_T can be used to quantify the bulk anisotropy of the plasma. The corresponding lattice expressions can be written compactly in terms of the electric and magnetic components as¹⁶

$$\begin{aligned} (g^2 a_{\perp}^4) \epsilon(x) &= \frac{1}{2} [\langle \mathcal{B}_{\eta}^2(x) \rangle + \langle \mathcal{E}_{\eta}^2(x) \rangle + \langle \mathcal{B}_T^2(x) \rangle + \langle \mathcal{E}_T^2(x) \rangle], \\ (g^2 a_{\perp}^4) P_T(x) &= \frac{1}{2} [\langle \mathcal{B}_{\eta}^2(x) \rangle + \langle \mathcal{E}_{\eta}^2(x) \rangle], \\ (g^2 a_{\perp}^4) P_L(x) &= \frac{1}{2} [\langle \mathcal{B}_T^2(x) \rangle + \langle \mathcal{E}_T^2(x) \rangle - \langle \mathcal{B}_{\eta}^2(x) \rangle - \langle \mathcal{E}_{\eta}^2(x) \rangle], \end{aligned} \quad (2.79)$$

where the individual electric and magnetic components can be obtained as

$$\begin{aligned} \mathcal{B}_{\eta}^2(x) &= 4 \operatorname{tr}[\mathbb{1} - V_{xy}(x)], & \mathcal{B}_T^2(x) &= 4 \left(\frac{a_{\perp}^2}{\tau^2 a_{\eta}^2} \right) \sum_i \operatorname{tr}[\mathbb{1} - V_{i\eta}(x)], \\ \mathcal{E}_{\eta}^2(x) &= \sum_{a=1}^{N_c^2-1} [\tilde{E}_a^{\eta}(x)]^2, & \mathcal{E}_T^2(x) &= \left(\frac{a_{\perp}^2}{\tau^2} \right) \sum_i \sum_{a=1}^{N_c^2-1} [\tilde{E}_a^i(x)]^2. \end{aligned} \quad (2.80)$$

Since the different plaquette variables are formally defined at different half-integer positions on the space time lattice, a higher order accurate expression can be obtained by interpolation of the result with the neighboring plaquette variables. However, since we will primarily be interested in volume averages of the energy density $\epsilon(t)$ according to

$$\epsilon(\tau) = \frac{1}{N_T^2 N_{\eta}} \sum_{\vec{x}_{\perp}, \eta} \epsilon(x), \quad (2.81)$$

¹⁶Note that all expressions are given in lattice units. The conversion to physical units is discussed at the end of this section.

and similarly for the longitudinal and transverse pressures $P_{T/L}$, there is no need to apply this procedure in practice.

Besides the energy momentum tensor, additional gauge invariant observables can be constructed by considering higher dimensional operators such as e.g. the covariant derivatives of the field strength tensor [88]

$$\mathcal{H}_\mu^\mu(\tau) = \frac{1}{V_\perp L_\eta} \int d^2 \vec{x}_\perp d\eta D_\alpha^{ab}(x) \mathcal{F}_b^{\alpha\mu}(x) D_{ac}^\beta(x) \mathcal{F}_{\beta\mu}^c(x), \quad (2.82)$$

(no summation over μ) where summation over *spatial* Lorentz indices $\alpha, \beta = x, y, \eta$ and color indices $a, b, c = 1, \dots, N_c^2 - 1$ is implied.¹⁷ The corresponding expression on the lattice can be obtained in a straightforward way according to

$$\begin{aligned} (g^2 a_\perp^6) \mathcal{H}_x^x(\tau) &= \frac{4}{N_T^2 N_\eta} \sum_{\vec{x}_\perp, \eta} \sum_{a=1}^{N_c^2-1} \left[\text{tr}[i\Gamma^a(V_{xy}(x) + W_{xy}(x))] + \frac{a_\perp^2}{\tau^2 a_\eta^2} \text{tr}[i\Gamma^a(V_{x\eta}(x) + W_{x\eta}(x))] \right]^2, \\ (g^2 a_\perp^6) \mathcal{H}_y^y(\tau) &= \frac{4}{N_T^2 N_\eta} \sum_{\vec{x}_\perp, \eta} \sum_{a=1}^{N_c^2-1} \left[\text{tr}[i\Gamma^a(V_{yx}(x) + W_{yx}(x))] + \frac{a_\perp^2}{\tau^2 a_\eta^2} \text{tr}[i\Gamma^a(V_{y\eta}(x) + W_{y\eta}(x))] \right]^2, \\ (g^2 a_\perp^6) \mathcal{H}_\eta^\eta(\tau) &= \frac{4}{N_T^2 N_\eta} \sum_{\vec{x}_\perp, \eta} \frac{a_\perp^2}{\tau^2 a_\eta^2} \sum_{a=1}^{N_c^2-1} \left[\text{tr}[i\Gamma^a(V_{\eta x}(x) + W_{\eta x}(x))] + \text{tr}[i\Gamma^a(V_{\eta y}(x) + W_{\eta y}(x))] \right]^2. \end{aligned} \quad (2.83)$$

In particular, we will be interested in the quantities Λ_L^2 and Λ_T^2 , which are defined as the longitudinal and transverse projections of \mathcal{H}_μ^μ according to

$$\Lambda_T^2(\tau) = \frac{\langle \mathcal{H}_\eta^\eta(\tau) \rangle}{\epsilon(\tau)}, \quad \Lambda_L^2(\tau) = \frac{\langle \mathcal{H}_x^x(\tau) \rangle + \langle \mathcal{H}_y^y(\tau) \rangle - \langle \mathcal{H}_\eta^\eta(\tau) \rangle}{\epsilon(\tau)}. \quad (2.84)$$

The observables Λ_L and Λ_T correspond to the characteristic longitudinal and transverse momentum scales of hard excitations and therefore contain additional information about the microscopic evolution. While this correspondence follows immediately from a dimensional analysis, it is nevertheless insightful to evaluate also the perturbative expressions for Λ_T^2 and Λ_L^2 – considering only the abelian part of the field strength tensor – as

$$\Lambda_T^2(\tau) \simeq \frac{\int d^2 \vec{p}_T dp_z \vec{p}_T^2 / 2 \omega_p f(\vec{p}_T, p_z, \tau)}{\int d^2 \vec{p}_T dp_z \omega_p f(\vec{p}_T, p_z, \tau)}, \quad \Lambda_L^2(\tau) \simeq \frac{\int d^2 \vec{p}_T dp_z p_z^2 \omega_p f(\vec{p}_T, p_z, \tau)}{\int d^2 \vec{p}_T dp_z \omega_p f(\vec{p}_T, p_z, \tau)}, \quad (2.85)$$

¹⁷Note that by virtue of the equations of motion, we can equivalently express the left hand side of Eq. (2.82) in terms of time derivatives of the electric fields.

where $f(\vec{p}_T, p_z, \tau)$ denotes the gluon distribution function as a function of longitudinal and transverse momenta, and $\omega_p \simeq p_T$ is the relativistic quasi-particle energy in the limit $p_T \gg \nu/\tau$. The details of this calculation are presented in Appendix E.

In addition to the gauge invariant observables outlined above, it will prove to be insightful to consider also a specific set of gauge-dependent quantities. In this context it is important to recall that by employing the Fock-Schwinger gauge condition ($A_\tau = 0$), we have so far not specified the residual gauge freedom to perform time independent gauge transformations. In order to eliminate this residual gauge freedom, we fix the Coulomb type gauge condition

$$\tau^{-2} \partial_\eta A_\eta(x) + \sum_i \partial_i A_i(x) = 0 \quad (2.86)$$

at any time τ when we extract gauge dependent observables. This can be achieved by use of standard lattice gauge-fixing techniques (see e.g. [89]), as discussed in Appendix B.

In particular, we will be interested in the gluon distribution function $f(\vec{p}_T, p_z, \tau)$, which describes the occupation number of gluons per momentum mode averaged over spin and color degrees of freedom. Since this quantity has a direct analogue in the kinetic theory framework, it is particularly useful to establish a direct comparison between the different methods. The gluon distribution function $f(p_\perp, p_z, \tau)$ can be extracted from equal-time (two-point) correlation functions in Coulomb gauge and different definitions have been employed in the literature [88, 90, 91]. Here we use a projection on Fock states according to

$$f(\vec{p}_T, p_z, \tau) = \frac{\tau^2}{N_g V_\perp L_\eta} \sum_{a=1}^{N_c^2-1} \sum_{\lambda=1,2} \left\langle \left| g^{\mu\nu} \left[(\xi_\mu^{(\lambda)\vec{p}_T\nu+}(\tau))^* \overset{\leftrightarrow}{\partial}_\tau A_\nu^a(\tau, \vec{p}_T, \nu) \right] \right|^2 \right\rangle_{\text{Coul. Gauge}}, \quad (2.87)$$

where $A \overset{\leftrightarrow}{\partial}_\tau B = A \partial_\tau B - B \partial_\tau A$, the index $\lambda = 1, 2$ counts the two transverse polarizations and $N_g = 2(N_c^2 - 1)$ is the number of transversely polarized gluon degrees of freedom. Here we identify the longitudinal momenta as $p_z = \nu/\tau$, and $\xi_\mu^{(\lambda)\vec{p}_T\nu+}(\tau)$ denotes the two time-dependent transverse polarization vectors in the free theory, whose explicit form in Fock-Schwinger gauge is derived in Appendix C. The gauge field $A_\nu^a(\tau, \vec{p}_T, \nu)$ in Eq. (2.87) is computed from the plaquette variables by inversion of Eq. (2.58) and subsequently performing a fast Fourier transformation to obtain the result in momentum space. Similarly, we obtain the time derivative of the gauge field from the fast Fourier transform of the electric field variables. We note that the definition in Eq. (2.87) is such that in the absence of interactions $f(\vec{p}_T, p_z, \tau)$ is, up to the red shift of longitudinal momenta, exactly conserved by the equations of motion.

In view of the physical interpretation of our results it is important to realize that, since classical Yang-Mills theory is a scale invariant theory, there is no natural scale a priori involved in the problem. Similarly the coupling constant g can be scaled out of the classical evolution equations and absorbed into a redefinition of the observables.¹⁸ However a characteristic momentum scale Q , as well as a measure of the gauge coupling g arise naturally when specifying physically well motivated 'quantum' initial conditions. It is therefore natural to express all dimensionful observables in appropriate units of the dimensionful scale Q and the gauge coupling g . The conversion to physical units is then straightforward by specifying the appropriate values of Q and g for the considered physical situation.¹⁹

¹⁸Note that this is not the case for the corresponding quantum theory, where the gauge coupling g explicitly enters in the amplitude of the phase factor $e^{iS[A]}$ in the non-equilibrium generating functional.

¹⁹Of course, one needs to respect the range of validity of the classical-statistical approximation such that this procedure only applies in situations where the characteristic occupancies are much larger than unity.

Chapter 3

Thermalization of weakly-coupled non-abelian plasmas in Minkowski space

In view of the discussion of the non-equilibrium dynamics and thermalization process in relativistic heavy-ion collisions, it is useful to first address the problem of thermalization from a more general point of view, by considering a class of simpler systems which share important features with the one created in nucleus-nucleus collisions at ultra-relativistic energies. In this chapter, we will study the thermalization of non-abelian plasmas in Minkowski space and develop an intuitive understanding of the thermalization process at weak coupling. The major simplification in this discussion is the fact that by neglecting the longitudinal expansion, we can restrict our analysis to systems, which are isotropic at all times of the evolution. In contrast, since the longitudinal expansion explicitly breaks the rotational symmetry of the system, we will always have to consider the influence of anisotropies in the longitudinally expanding case. Despite this important difference, we emphasize that the concepts developed in this chapter apply in a very similar way also to the longitudinally expanding case.

We will consider a class of homogeneous, isotropic systems within the weak coupling scenario ($\alpha_S(Q) \ll 1$), which initially have a parametrically large occupancy

$$f(\mathbf{p}) \sim \alpha_S^{-c} \text{ for } |\mathbf{p}| < Q, \quad f(|\mathbf{p}| > Q) \ll 1, \quad (3.1)$$

where $0 < c < 1$, and are characterized by a single momentum scale Q . As discussed in Sec. 5.3, this represents an idealized version of the situation encountered in heavy-ion collisions at times $\tau \sim Q^{-1} \log^2(\alpha_S^{-1})$ after the collision of heavy nuclei, where the characteristic momentum scale Q can be related to the saturation scale Q_s of nuclear wave functions in the framework of the

color-glass condensate effective field theory [30–32].

Since the typical occupancies are large $f(|\mathbf{p}| \simeq Q) \gg 1$, the plasma exhibits classical-statistical dynamics as long as the occupation numbers of hard excitations remain much larger than unity. In this regime, we can study the non-equilibrium dynamics from first principles using the classical-statistical lattice gauge-theory techniques introduced in Sec. 2.4. In the regime where the characteristic occupancies are $f(|\mathbf{p}| \simeq Q) \ll \alpha_s^{-1}$, we will employ a kinetic description and use resummed perturbation theory as a complementary approach. Since the different methods have an overlap in the range of validity for $1 \ll f(\mathbf{p} \simeq Q) \ll \alpha_s^{-1}$, our strategy will be to combine the different approaches in order to provide an intuitive understanding based on the perturbative description, while at the same time having full control over genuinely non-perturbative and non-equilibrium effects.

The discussion in this chapter is largely based on Refs. [90, 91] and organized in the following way: We start with a kinetic theory analysis in Sec. 3.1, where we review the previous discussion in Refs. [30, 31] and extend it to account for the presence of a non-thermal fixed point. In Sec. 3.2, we study the dynamics at early times using classical-statistical lattice simulations. We investigate the possibility of the dynamical formation of a Bose-Einstein condensate and discuss our findings using resummed perturbative techniques in Sec. 3.3. We then extend our lattice studies to later times in Sec. 3.4, where we analyze the emergence of a turbulent cascade. The numerical results are complemented by a turbulent scaling analysis in Sec. 3.5. We conclude this chapter in Sec. 3.6 with a discussion of the turbulent thermalization mechanism, which is found to drive the thermalization process.

3.1 Evolution in kinetic theory

The kinetic evolution of systems characterized with an initial distribution as in Eq. (3.1) has been studied in Refs. [30, 31] and we will adopt the notation of Ref. [30] to analyze the evolution of the system. Since we will consider closed systems, the energy density $\epsilon \sim \int d^3\mathbf{p} \omega_{\mathbf{p}} f(\mathbf{p})$ is conserved and one can immediately infer the final state temperature as ¹

$$T_{\text{Final}} \sim \alpha_S^{-c/4} Q. \quad (3.2)$$

Since we will be interested in over-occupied systems ($0 < c < 1$) one immediately observes that $T_{\text{Final}} \gtrsim Q$, such that the characteristic momentum of hard excitations has to increase during the thermalization process. This is illustrated in Fig. 3.1, where we sketch the different regimes of the kinetic evolution. The left panel of Fig. 3.1 shows the initial state, characterized by large occupancies up to the momentum scale Q , in comparison with the thermal final state, indicated by the red dashed line. One also observes, that the typical occupancy of initially hard excitations

$$n_{\text{Hard}}(t) = f(t, |\mathbf{p}| \simeq Q), \quad (3.3)$$

decreases during the time evolution from the initial value $n_{\text{Hard}}^{\text{Initial}} \sim \alpha_S^{-c}$ to the final value $n_{\text{Hard}}^{\text{Final}} \sim \alpha_S^{-c/4}$. Interestingly, the decrease in occupancy is accompanied by a change of the overall particle number density $n(t) \sim \int d^3\mathbf{p} f(t, \mathbf{p})$. Since the particle number density in the final state is parametrically smaller than initially

$$n_{\text{Final}} \sim T_{\text{Final}}^3 \sim \alpha_S^{-3c/4} Q^3 \lesssim n_{\text{initial}} \sim \alpha_S^{-c} Q^3, \quad (3.4)$$

this means that ultimately number-changing inelastic interactions, will reduce the total number of excitations, which in contrast to the energy density is not a conserved quantity. However, there are situations where inelastic processes are highly suppressed as compared to elastic scattering, such that the total number of excitations is approximately conserved for a transient regime of the evolution. In this situation, the surplus of hard excitations due to initial over-occupation may be absorbed in the soft sector and result in the formation of a transient Bose-Einstein condensate [30]. This non-equilibrium condensation mechanism has previously been observed in relativistic scalar field theories [43, 92, 93] and is well understood in the context of non-relativistic scalar field theories, where evaporative cooling techniques are widely used experimentally to trigger the formation of a Bose-Einstein condensate [94, 95].² The ques-

¹Note that, in this section, we only provide parametric estimates and the notation $A \sim B$ is to be understood as 'A is parametrically equal to B'. Similarly, $A \gtrsim B$ denotes the fact that 'A is parametrically larger than B'.

²Note that, in contrast to relativistic systems, in the non-relativistic case the particle number is exactly conserved by the equations of motion. The system may therefore develop a chemical potential associated to the

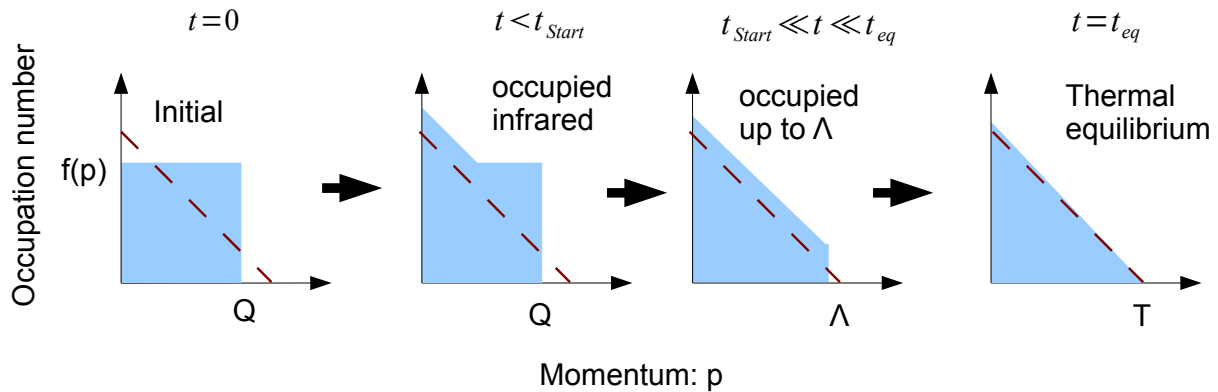


Figure 3.1: Sketch of the thermalization process in the kinetic theory description. The different graphs represent the different stages of the evolution. The red dashed line indicates the final thermal state. After the time $t \sim t_{\text{start}}$, when initially hard excitations start to be strongly affected by elastic scattering a dynamical scale Λ develops. The time evolution of the hard scale Λ then characterizes the transport of energy towards higher momentum scales.

tion whether such a transient behavior is realized also in non-abelian gauge theories, crucially depends on the time scales under consideration: On the level of parametric estimates one can already argue, that since both elastic and inelastic processes show the same parametric dependencies, no condensation occurs on large time scales [31]. However, on shorter time scales, elastic scattering may indeed be more efficient as compared to inelastic interactions and we will investigate the possibility of such a transient regime in more detail in Sec. 3.2.

In order to describe the thermalization process in the kinetic theory framework, one has to take into account the effects of elastic and inelastic scattering, as well as the interaction of hard and soft excitations. We start with a discussion of elastic scattering, which in this case is dominated by scattering of hard particles with small momentum transfer [30, 31]. In the small angle approximation, where the average momentum of hard excitations is much bigger than the average exchanged momentum, the process appears as a 'random walk' in momentum space, controlled by the momentum diffusion parameter (c.f. Ref. [30, 31])

$$\hat{q}_{\text{el}} \sim \alpha_S^2 \int \frac{d^3 \mathbf{p}}{(2\pi)^3} f(\mathbf{p}) [1 + f(\mathbf{p})]. \quad (3.5)$$

Similarly one can estimate the effects of inelastic processes. The important observation is that for over-occupied, isotropic systems all processes are parametrically as efficient as elastic

conserved particle number, which ultimately results in the formation of a Bose-Einstein condensate.

scattering [30, 31] such that

$$\hat{q} \sim \hat{q}_{el} \sim \hat{q}_{inel} . \quad (3.6)$$

This greatly simplifies the discussion of the kinetic evolution of the system, since we do not have to distinguish different regimes where either of the processes dominates. From Eq. (3.5) we can also obtain the rate at which a particle with momentum \mathbf{p} exhibits a momentum transfer of the same order. This rate is parametrically given by

$$\Gamma_{el}(\mathbf{p}) \sim \frac{\hat{q}_{el}}{\mathbf{p}^2} , \quad (3.7)$$

such that soft particles experience large angle scatterings at a higher rate as compared to hard particles. Given the enhanced scattering rates of soft excitations, we expect that the soft tail of the distribution can always 'equilibrate' to a distribution which is dictated by the dynamics of the hard modes. We will assume in the following that this distribution is described by a power law, where

$$f(\mathbf{p}) \sim \alpha_S^{-c} \left(\frac{\Lambda_s}{\omega_{\mathbf{p}}} \right)^\kappa \quad \text{for } p < \Lambda , \quad (3.8)$$

up to a momentum cutoff Λ above which occupancies are negligible. Here the exponent c characterizes parametrically the occupation number of the system, and we will only consider the case $0 < c < 1$ of initially over-occupied systems.³ The exponent κ characterizes the shape of the distribution. While $\kappa = 1$ corresponds to a thermal-like shape, the values $\kappa = 3/2$ (c.f. Ref. [90]) and $\kappa = 4/3, 5/3$ (c.f. Ref. [87]) are known to appear for systems which exhibit Kolmogorov wave turbulence.⁴

The scales Λ and Λ_s in Eq. (3.8) both depend on time and determine the dynamical evolution of the system. At initial time $t = 0$ the two scales coincide and one finds $\Lambda \sim \Lambda_s \sim Q$. In order to extract the time evolution of the scales Λ and Λ_s , we first note that for $\kappa < 3/2$ the momentum diffusion parameter is parametrically given by

$$\hat{q} \sim \alpha_S^{2-2c} \left(\frac{\Lambda_s}{\Lambda} \right)^{2\kappa} \Lambda^3 . \quad (3.9)$$

In contrast, if one considers $\kappa > 3/2$ the integral in Eq. (3.5) is dominated by infrared contribu-

³For a study of dilute systems with $c < 0$, we refer to Ref. [31].

⁴The appearance of the exponent $\kappa = 3/2$ can be explained with the existence of a classical background field [33, 35, 66, 90, 96] as discussed in more detail in Sec. 3.3. We note that in this situation, one needs to consider a different interaction to determine the time evolution of the scales Λ and Λ_s . This analysis is analogous to the one in scalar theories and we refer to Ref. [34] for more details.

tions indicating a breakdown of the kinetic description. We will therefore limit our discussion to the case $\kappa < 3/2$, where we expect a kinetic description to apply. As we will see shortly in Sec. 3.2, this situation will also be realized in our lattice simulations. From Eq. (3.7) we can infer the time scale t_{start} on which the momentum of initially hard excitations changes appreciably as

$$t_{\text{start}} \sim \Gamma_{el}^{-1}(Q) \sim Q^{-1} \alpha_S^{2c-2}. \quad (3.10)$$

Before the time t_{start} the system will develop its soft tail, which then moves out towards higher momenta until at times $t \sim t_{\text{start}}$ changes in the distribution of hard excitations start to take place. This behavior is illustrated in the second and third panel of Fig. 3.1. In the regime $t \gtrsim t_{\text{start}}$ one can find a self-consistent scaling solution by requiring the evolution of the hard scale to be governed by momentum diffusion such that (c.f. Ref. [30, 31])

$$\frac{d}{dt} \Lambda^2 \sim \hat{q} \sim \alpha_S^{2-2c} \left(\frac{\Lambda_s}{\Lambda} \right)^{2\kappa} \Lambda^3. \quad (3.11)$$

We note that for closed systems the evolution of the ratio of soft and hard scale $(\Lambda_s/\Lambda)^\kappa$ is fixed by energy conservation

$$\epsilon \sim \alpha_S^{-c} \left(\frac{\Lambda_s}{\Lambda} \right)^\kappa \Lambda^4 \sim \alpha_S^{-c} Q^4, \quad (3.12)$$

such that the relation

$$\left(\frac{\Lambda_s}{\Lambda} \right)^\kappa \sim \left(\frac{Q}{\Lambda} \right)^4, \quad (3.13)$$

holds at all times of the evolution. Combining the above conditions then yields the evolution of the scales Λ and Λ_s for times $t \gtrsim t_{\text{start}}$ to be

$$\Lambda \sim Q \left(\frac{t}{t_{\text{start}}} \right)^{1/7}, \quad \Lambda_s \sim Q \left(\frac{t}{t_{\text{start}}} \right)^{(1-4/\kappa)/7}, \quad (3.14)$$

which agrees with the results obtained in Refs. [30, 31] for the case $\kappa = 1$ of a (quasi-)thermal distribution. We note that the evolution of the hard scale Λ as well as the evolution of the occupancies of hard modes $(\Lambda_s/\Lambda)^\kappa$ turn out to be independent of the spectral exponent κ . This behavior is a direct consequence of energy conservation.

The evolution of the scales Λ and Λ_s proceeds in this way until at some points the occupancies of hard modes become $\mathcal{O}(1)$, where quantum effects become important. These will

have the effect of driving the system towards its unique thermal fixed point, and hence complete the thermalization process. We therefore expect thermalization of the system to occur as a two-step process, where the first regime is characterized by the above scaling solutions. The time scale t_{change} for entering the quantum regime, is then parametrically given by

$$t_{\text{change}} \sim Q^{-1} \alpha_S^{-2+c/4}, \quad (3.15)$$

and independent of the value of the spectral exponent κ . However, for $\kappa \neq 1$ the system still deviates significantly from a thermal state even at times $t \sim t_{\text{change}}$ and one has to take into account also the time for the approach to thermal equilibrium in the quantum regime. Only if the latter is assumed to be parametrically faster than our previous estimate, one obtains $t_{\text{eq}} \sim t_{\text{change}}$ as the final result. In this situation one recovers the estimate of Refs. [30, 31] for the overall thermalization time.

3.2 Early times and transient phenomena

Having established an intuitive picture of the thermalization process, we will now turn to the results of classical-statistical lattice simulations. We will first focus on the early time dynamics and investigate in particular the possibility that the initial over-occupation may result in large infrared occupancies at a transient stage of the evolution. The evolution at later times and the thermalization process are discussed in more detail in Sec. 3.4.

In order to make contact with the previous discussions, we first need to extract suitably gauge-fixed distribution functions. These can be related to equal-time correlation functions, in a gauge with a clear physical interpretation of the degrees of freedom. Since the dynamics is solved in temporal axial gauge in Minkowski space, we choose to fix the residual gauge freedom such that the Coulomb type gauge condition $\partial_i A_i^a(x) = 0$ is satisfied at each read-out time. In practice, this can be achieved by use of standard lattice gauge fixing techniques and we employ the overrelaxation method described in Ref. [89] and with typically 10^5 overrelaxation steps, which results in a very good convergence for the employed lattice sizes. The associated distribution functions can then safely be extracted for momenta where perturbation theory is useful, although it may be unclear how to interpret the most infrared modes in this context. However, we will see that important lessons can already be learned for not too low momenta, such that a characterization of the physics in terms of distribution functions is indeed useful.

In this section, we will compute the distribution function with the help of time-dependent field momentum modes, which are obtained as the Fourier transform of the gauge fields according to $A_i^a(t, \mathbf{p}) = \int d^3x A_i^a(t, \mathbf{x}) \exp(i\mathbf{p} \cdot \mathbf{x})$. By averaging over color and Lorentz indices according to

$$|A(t, \mathbf{p})|^2 = \frac{1}{(N_c^2 - 1)(d - 1)} \sum_i \sum_a |A_i^a(t, \mathbf{p})|^2, \quad (3.16)$$

to improve the statistics, the occupation number can be defined as

$$f(t, \mathbf{p}) = \frac{1}{V} \sqrt{\langle |E(t, \mathbf{p})|^2 \rangle_{\text{Coul. Gauge}} \langle |A(t, \mathbf{p})|^2 \rangle_{\text{Coul. Gauge}}}, \quad (3.17)$$

where $N_c = 2$ is the number of colors, $d = 3$ is the number of spatial dimensions and $V = (Na)^3$ denotes the lattice volume. We perform typically five to ten runs on $N = 128$ and $N = 256$ lattices with $Qa = 0.25, 0.5$ and compute classical-statistical averages $\langle \dots \rangle_{\text{Coul. Gauge}}$ of the correlation functions with the residual gauge freedom fixed by the Coulomb type gauge condition. Similarly to the distribution function, we will also consider the effective “dispersion

relation”

$$\omega_{\mathbf{p}}(t) = \sqrt{\frac{\langle |E(t, \mathbf{p})|^2 \rangle_{\text{Coul. Gauge}}}{\langle |A(t, \mathbf{p})|^2 \rangle_{\text{Coul. Gauge}}}}, \quad (3.18)$$

which in this gauge should only deviate from a free, linear behavior in the regime of large occupancies at low momenta.

Since we are interested in the time-evolution starting from initial over-population, we choose the initial conditions such that the distribution function at early times has a non-perturbatively large occupancy $f(|\mathbf{p}| \simeq Q) \sim 1/g^2$ at the characteristic momentum scale Q . Here we employ Gaussian initial conditions, with vanishing electric fields $E_i^a = 0$ at initial time $t = 0$ to fulfill the Gauss law constraint exactly. In Fig. 3.2 we show the occupation number distribution as a function of spatial momentum for different times in units of the characteristic momentum scale Q . The (red) dashed-dotted line shows the approximate initial distribution as it is shortly after the electric field components built up. Relatively quickly we observe the evolution towards a distribution, which for an intermediate time range can be well described by a power-law for momenta $|\mathbf{p}| \lesssim 2Q$. The (blue) dashed curve at $Qt = 315$ and the (black) solid one at $Qt = 730$ indicate that the power-law behavior is rather well described by the dashed-dotted fit curve $f(\mathbf{p}) \sim |\mathbf{p}|^{-3/2}$. Once this power-law behavior is established, the subsequent evolution becomes rather slow or quasi-stationary. In this regime one observes from Fig. 3.2, that the UV part of the spectrum is very slowly filled up, moving the breakdown of the power-law dependence in the direction of higher momenta. As time proceeds, at some point deviations from a simple power become visible. The (grey) dotted curve for $Qt = 1575$ shows already a somewhat steeper behavior at lower momenta and a diminished slope at higher momenta. At times $Qt = 4410$ the curve is clearly not described by a simple power.

Before we analyze the power-law behavior in more detail below, we present in Fig. 3.3 the dispersion relation. For sufficiently high momenta the considered quantity is always close to the free expression $\omega_{\mathbf{p}} = |\mathbf{p}|$ as expected. We find that discrepancies from the massless dispersion are present only below $\mathbf{p}^2 \lesssim 0.1Q^2$, with decreasing amplitude as the time grows. In the infrared the point where the dispersion starts to deviate from the free dispersion is roughly at the same momenta, where the breakdown of the power-law dependence of the spectrum occurs.

In order to characterize the transition to and the evolution away from the $f(\mathbf{p}) \sim |\mathbf{p}|^{-3/2}$ behavior observed in Fig. 3.2, we extract the scaling exponent κ by fitting a power-law dependence. The resulting scaling exponent as a function of time is shown in Fig. 3.4. The error bars correspond to the change of the power as the fitting region is varied by choosing the lower

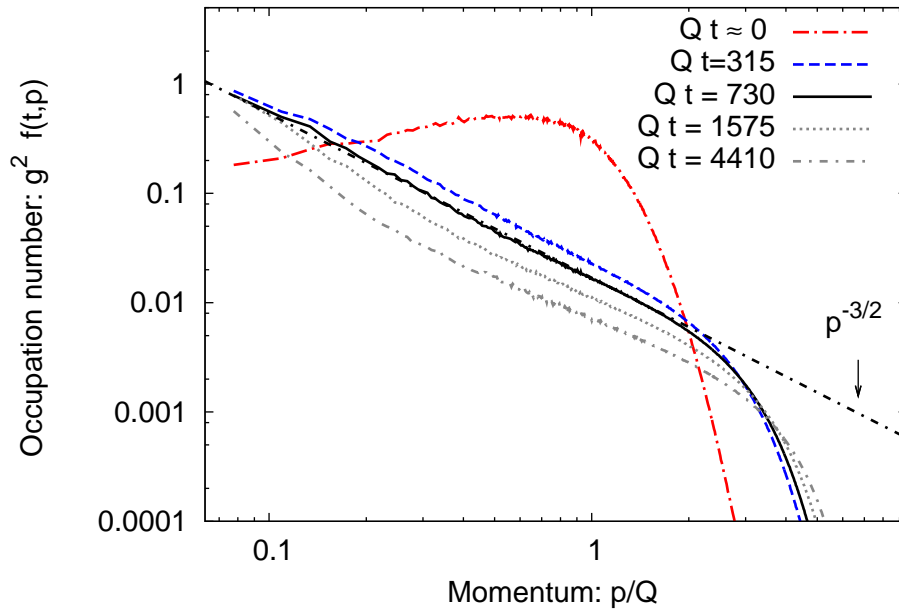


Figure 3.2: Occupation number distribution as a function of momentum for different times Qt of the evolution. Starting from a distribution characterized by initial over-occupation, one observes the quick buildup of a power-law distribution, with $f(\mathbf{p}) \sim |\mathbf{p}|^{-3/2}$ up to times $Qt \simeq 1000$.

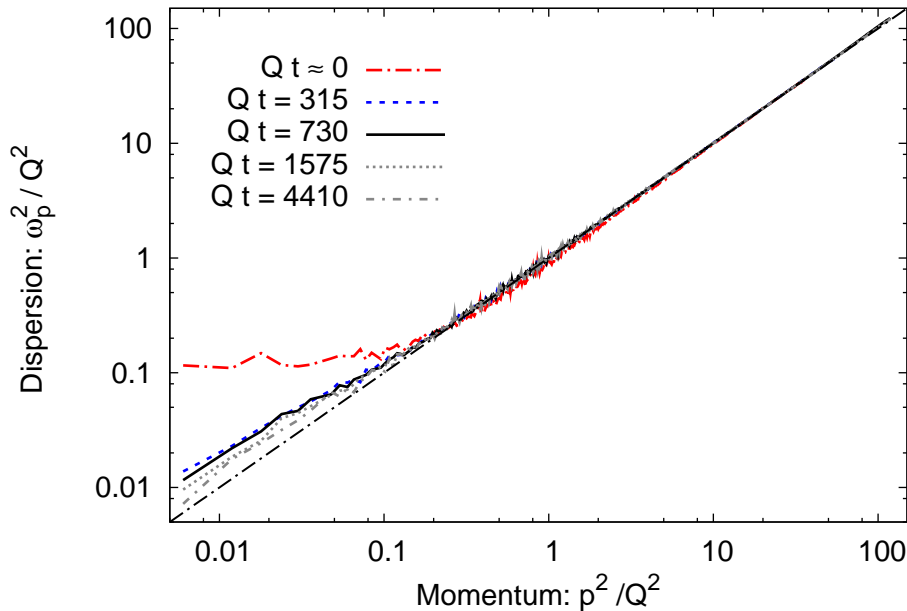


Figure 3.3: Dispersion relation as a function of momentum for different times Qt of the evolution. The dispersion relation at large momenta is identical with the one for massless relativistic particles.

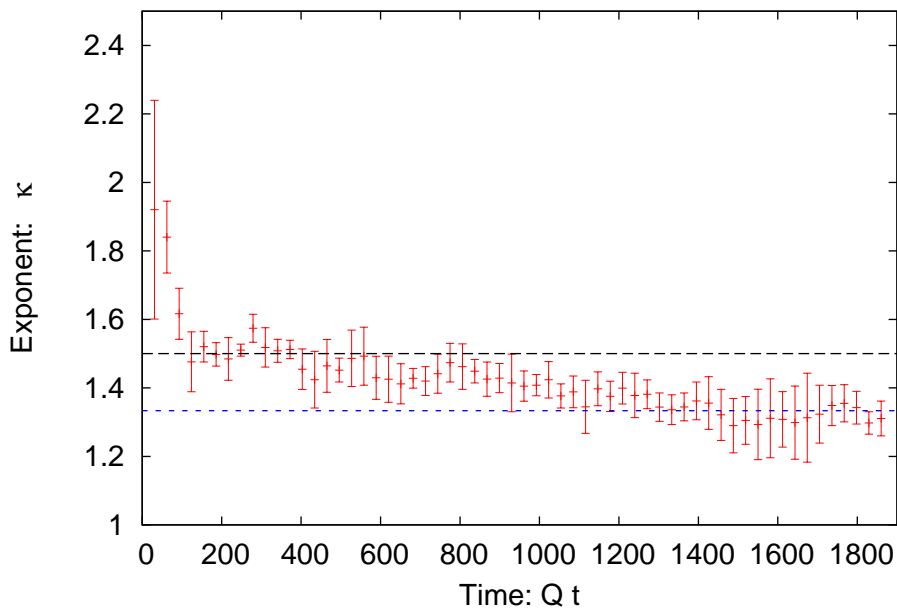


Figure 3.4: Scaling exponent κ as a function of time, extracted from a power-law fit of the occupation number distribution displayed in Fig. 3.2. The error bars are extracted from a variation of the range of momenta included in the fit. One observes that the exponent quickly approaches the value $3/2$ indicated by the black dashed line. The exponent remains approximately $\kappa = 3/2$ until at times $Qt \simeq 1000$ a transition to $\kappa = 4/3$, as indicated by the blue dashed line, occurs.

bound from $(0.3 - 0.6)Q$ and the upper bound from $(0.9 - 1.3)Q$. The results indicate that initially the system evolves rapidly to $\kappa = 3/2$ (long-dashed curve) and spends a relatively long time around that value, before it slowly evolves to lower values. Of course, this evolution towards lower values is partly expected since the system will thermalize classically to a distribution $f(\mathbf{p}) \sim |\mathbf{p}|^{-1}$ at sufficiently late times (which in general happens rather quickly once the occupied high-momentum modes reach the lattice cut-off).⁵ However, a non-trivial observation is the fact that this intermediate evolution of the exponent is very slow and stays also a significant amount of time around the value $\kappa = 4/3$ at later times. Most remarkably, this observation is consistent with earlier investigations starting from very different, anisotropic initial conditions [87] and will be subject to further investigations in Sec. 3.4.

Before we turn to a more detailed discussion of the late time regime, where the scaling exponent $\kappa = 4/3$ is realized, we will first perform a perturbative fixed-point analysis explaining the occurrence of the scaling exponent $\kappa = 3/2$ at early times. Interestingly, this explanation requires the presence of a parametrically large background field $\mathcal{A}_\mu^a(x) \sim 1/g$, such that the

⁵For a recent study of equal time correlation functions in classical thermal equilibrium we refer to Ref. [88].

observation of the scaling exponent $\kappa = 3/2$ may also be interpreted as an indication of a transient condensation phenomenon.

3.3 Non-thermal fixed points and perturbative scaling exponents

In view of the interpretation of our lattice results presented in the previous section, we first note that there is an interesting analogy to previous observations in scalar field theories in the context of early universe dynamics [34, 35]. In these scenarios, the over-occupation is build up dynamically by an instability of the inflaton field, which results in occupation numbers on the order of the inverse self-coupling up to a characteristic momentum scale (e.g. associated to the initial field amplitude) [53]. The subsequent quasi-stationary time evolution shows the scaling exponent $\kappa = 3/2$ as the high momentum part of a dual turbulent cascade. This ultraviolet cascade is associated to an energy flux towards the high momentum regime, which drives the thermalization process [34, 35]. In contrast, the infrared counterpart of this cascade is described by a $f(\mathbf{p}) \sim |\mathbf{p}|^{-4}$ power law, which can be associated to a particle flux towards the infrared, catalyzing the formation of a non-equilibrium condensate [43].

The emergence of a dual cascade in scalar field theories is a consequence of the parametric suppression of inelastic processes at weak coupling, such that both the energy density and the particle number are (approximately) conserved during the evolution. Since the ultraviolet cascade can not account for two conservation laws, the surplus particle number is transported towards the infrared, ultimately leading to the formation of a Bose-Einstein condensate [35, 43]. While the physics of the infrared regime is intrinsically non-perturbative and manifests itself in a similar way as critical phenomena in thermal equilibrium [33, 35, 96] the evolution of the ultraviolet cascade and the appearance of the scaling exponent $\kappa = 3/2$ is analogous to Kolmogorov wave turbulence and can already be understood on the perturbative level [37–39]. In the context of scalar field theories, it is well understood, that the appearance of such a non-thermal fixed point with the scaling exponent $\kappa = 3/2$ is due to an effective $2 \leftrightarrow (1 + \text{soft})$ interaction, which appears at leading order of (resummed) perturbation theory in the presence of a soft ‘background field’ [34, 35]. Despite the important differences between scalar theories and gauge theories, which of course become evident at later times of the evolution, we will see shortly that the emergence of a transient regime with a scaling exponent $\kappa = 3/2$ in our simulations can be attributed to a similar phenomenon.

In order to analyze the possible values of the scaling exponent κ , our strategy will be to investigate the non-thermal fixed point solutions, which correspond to stationary solutions of

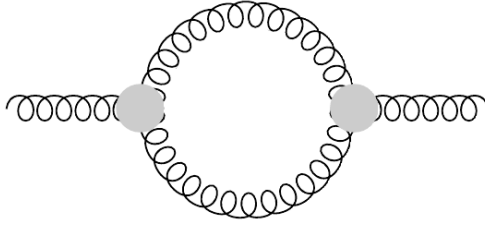


Figure 3.5: Gluon part of the one-loop contribution to the self-energy with (2PI) resummed propagator lines. The grey circles indicate an effective three-vertex in the presence of a background gauge field potential.

the equations of motion characterized by a non-zero flux of conserved quantities [37–39]. We follow here the approach of Ref. [87] and analyze the fixed point structure at leading order $\mathcal{O}(g^2)$ contribution, within (2PI) resummed perturbation theory.

We first recall from Sec. 2.2 that, for quantum fields $A_\mu^a(x)$, one can define two independent connected two-point correlation functions out of equilibrium, which may be associated to the anti-commutator and the commutator respectively,

$$\begin{aligned} F_{\mu\nu}^{ab}(x, y) &= \frac{1}{2} \langle \{A_\mu^a(x), A_\nu^b(y)\} \rangle - \mathcal{A}_\mu^a(x) \mathcal{A}_\nu^b(y), \\ \rho_{\mu\nu}^{ab}(x, y) &= i \langle [A_\mu^a(x), A_\nu^b(y)] \rangle. \end{aligned} \quad (3.19)$$

Here we also took into account a possible expectation value or ‘background field’

$$\mathcal{A}_\mu^a(x) = \langle A_\mu^a(x) \rangle, \quad (3.20)$$

which should be understood as an effective description of very soft excitations of the system, for which a purely perturbative treatment is clearly inadequate [31, 97].

As discussed in Sec. 2.2, the spectral function ρ determines the structure of excitations of the system, while the statistical propagator F contains the information about how often these states are occupied. In thermal equilibrium, a tremendous simplification is that the spectral and statistical functions are related by the fluctuation-dissipation relation, which is not assumed here since we are considering a non-equilibrium situation [42]. We also recall, that the spectral function is related to the retarded propagator $G^{(R)}$ and the advanced one $G^{(A)}$ as $\rho = G^{(R)} - G^{(A)}$, which we will use below to simplify the expressions.

The one-loop self-energy correction to two-point correlation functions in the presence of a background gauge potential is shown diagrammatically in Fig. 3.5. To avoid problems of secu-

larity in standard perturbation theory, here the lines are meant in the two-particle irreducible (2PI) effective action scheme, where self-energies are expressed in terms of self-consistently dressed propagators [42]. This includes also the background-field dependence of the propagators. The grey circles indicate an effective three-gluon vertex $gV_{\mu\nu\gamma}^{abc}$, which is appearing at one loop in the presence of the background gauge field potential [98]. This effective three-vertex consists of the conventional tree-level vertex and an \mathcal{A} -dependent term,

$$V_{\mu\nu\gamma}^{abc} = V_{0,\mu\nu\gamma}^{abc} + V_{\mathcal{A},\mu\nu\gamma}^{abc} . \quad (3.21)$$

The standard tree-level part reads in Fourier space

$$V_{0,\mu\nu\gamma}^{abc}(p, q, k) = f^{abc} \left(g_{\mu\nu}(p - q)_\gamma + g_{\nu\gamma}(q - k)_\mu + g_{\gamma\mu}(k - p)_\nu \right) , \quad (3.22)$$

where f^{abc} are the structure constants of the non-abelian gauge group. Finally, we will be interested in a situation where the background field has a residual (space-) time dependence. Then the corresponding part of the interaction in Eq. (3.21) reads in configuration space

$$V_{\mathcal{A},\mu\nu\gamma}^{abc}(x, y, z) = \left(C_{ac,bd} g_{\mu\nu} \mathcal{A}_\gamma^d(x) + C_{ab,dc} g_{\nu\gamma} \mathcal{A}_\mu^d(x) + C_{ab,cd} g_{\gamma\mu} \mathcal{A}_\nu^d(x) \right) g \delta^{d+1}(x - y) \delta^{d+1}(x - z) , \quad (3.23)$$

with

$$C_{ab,cd} = f^{abe} f^{cde} + f^{ade} f^{cbe} . \quad (3.24)$$

In order to understand the importance of a non-constant background field, it is instructive to consider first the case of a *homogeneous* field $\mathcal{A}_\mu^i(x) = \bar{\mathcal{A}}_\mu^i$, with $\bar{\mathcal{A}}_\mu^i \sim \mathcal{O}(1/g)$. Since we are interested only in fixed-point solutions of the evolution equations, we will consider time and space translation invariant correlators in Eq. (3.19) and express them in terms of their Fourier transform $\tilde{F}(p)$ and $\tilde{\rho}(p)$. We introduce a factor of $(-i)$ in the Fourier transforms of the spectral (ρ) and retarded/advanced components, such that

$$\tilde{\rho}(p) = -i \int d^4x e^{ip_\mu x^\mu} \rho(x) , \quad (3.25)$$

while

$$\tilde{F}(p) = \int d^4x e^{ip_\mu x^\mu} F(x) . \quad (3.26)$$

Similar to the two-point correlation functions in Eq. (3.19) we introduce statistical, $\tilde{\Pi}_{(F)}$, and

spectral, $\tilde{\Pi}_{(\rho)}$, components of self-energies defined as [42]

$$\begin{aligned}\tilde{\Pi}_{(F)ab}^{\mu\nu}(p) &= \tilde{G}_{(R)ac}^{-1\mu\gamma}(p) \tilde{F}_{\gamma\delta}^{cd}(p) \tilde{G}_{(A)db}^{-1\delta\nu}(p), \\ \tilde{\Pi}_{(\rho)ab}^{\mu\nu}(p) &= \tilde{G}_{(R)ab}^{-1\mu\nu}(p) - \tilde{G}_{(A)ab}^{-1\mu\nu}(p),\end{aligned}\quad (3.27)$$

where summation over repeated Lorentz and color indices is implied. The translation invariant propagators in Eq. (3.19) and self-energies in Eq. (3.27) then obey the identity [96]

$$\tilde{\Pi}_{(F)ab}^{\mu\nu}(p) \tilde{\rho}_{\nu\mu}^{ba}(p) - \tilde{\Pi}_{(\rho)ab}^{\mu\nu}(p) \tilde{F}_{\nu\mu}^{ba}(p) = 0, \quad (3.28)$$

which can be directly verified by plugging in the above definitions. Equation (3.28) is well-known in non-equilibrium physics and will be the starting point of our calculation. In the language of Boltzmann dynamics it states that "gain terms" equal "loss terms" for which stationarity is achieved [42]. Thermal equilibrium trivially solves Eq. (3.28), and we will not consider this solution in the following. Instead, we will look for possible non-thermal scaling solutions.

Decomposing the one-loop self-energy shown in Fig. 3.5 into its statistical (real) and spectral (imaginary) part, one obtains

$$\begin{aligned}\tilde{\Pi}_{(F)ef}^{\mu\nu}(p; \bar{\mathcal{A}}) &= \frac{g^2}{2} \int_{qk} (2\pi)^4 \delta^{(4)}(p+q+k) V_{eac}^{\mu\alpha\gamma}(p, q, k; \bar{\mathcal{A}}) \\ &\quad \times \left[\tilde{F}_{\beta\alpha}^{ba}(q) \tilde{F}_{\delta\gamma}^{dc}(k) + \frac{1}{4} \tilde{\rho}_{\beta\alpha}^{ba}(q) \tilde{\rho}_{\delta\gamma}^{dc}(k) \right] V_{fbd}^{\nu\beta\delta}(-p, -q, -k; \bar{\mathcal{A}}), \\ \tilde{\Pi}_{(\rho)ef}^{\mu\nu}(p; \bar{\mathcal{A}}) &= -\frac{g^2}{2} \int_{qk} (2\pi)^4 \delta^{(4)}(p+q+k) V_{eac}^{\mu\alpha\gamma}(p, q, k; \bar{\mathcal{A}}) \\ &\quad \times \left[\tilde{F}_{\beta\alpha}^{ba}(q) \tilde{\rho}_{\delta\gamma}^{dc}(k) + \tilde{\rho}_{\beta\alpha}^{ba}(q) \tilde{F}_{\delta\gamma}^{dc}(k) \right] V_{fbd}^{\nu\beta\delta}(-p, -q, -k; \bar{\mathcal{A}}),\end{aligned}\quad (3.29)$$

with the notation $\int_q \equiv \int d^4q/(2\pi)^4$ and the symmetry property of the anti-commutator and commutator functions

$$\tilde{F}_{\mu\nu}^{ab}(-p) = \tilde{F}_{\nu\mu}^{ba}(p), \quad \tilde{\rho}_{\mu\nu}^{ab}(-p) = -\tilde{\rho}_{\nu\mu}^{ba}(p). \quad (3.30)$$

Following similar steps as in Refs. [33, 87], scaling solutions can be efficiently identified by integrating Eq. (3.28) over external spatial momentum \mathbf{p} and applying suitable scaling transformations. In this way the problem can be reduced to simple algebraic conditions for scaling exponents. Non-thermal scaling solutions may be obtained in the classical regime, where expectation values of anti-commutators are much larger than commutators, $F^2 \gg \rho^2$. This is analogous to what is done in the context of weak Kolmogorov wave turbulence using kinetic

equations in the regime of sufficiently large occupation numbers [37–39]. In contrast, for lower occupancies of order one, dissipative or quantum corrections will obstruct scaling.

Dropping the genuine quantum contributions in Eq. (3.29), the stationarity condition then reads

$$\begin{aligned}
 0 &= \frac{g^2}{2} \int_{\mathbf{p}qk} (2\pi)^4 \delta^{(4)}(p+q+k) V_{eac}^{\mu\alpha\gamma}(p, q, k; \bar{\mathcal{A}}) V_{fbd}^{\nu\beta\delta}(-p, -q, -k; \bar{\mathcal{A}}) \\
 &\times \left[\underbrace{\tilde{F}_{\beta\alpha}^{ba}(q) \tilde{F}_{\delta\gamma}^{dc}(k) \tilde{\rho}_{\nu\mu}^{fe}(p)}_{\text{(I)}} + \underbrace{\tilde{F}_{\beta\alpha}^{ba}(q) \tilde{\rho}_{\delta\gamma}^{dc}(k) \tilde{F}_{\nu\mu}^{fe}(p)}_{\text{(II)}} + \underbrace{\tilde{\rho}_{\beta\alpha}^{ba}(q) \tilde{F}_{\delta\gamma}^{dc}(k) \tilde{F}_{\nu\mu}^{fe}(p)}_{\text{(III)}} \right], \tag{3.31}
 \end{aligned}$$

where $\int_{\mathbf{p}} \equiv \int d^3p/(2\pi)^3$. We are looking for scaling solutions which behave as

$$\tilde{F}_{\mu\nu}^{ab}(sp) = |s|^{-(2+\kappa)} \tilde{F}_{\mu\nu}^{ab}(p) \quad , \quad \tilde{\rho}_{\mu\nu}^{ab}(sp) = |s|^{-2} \text{sgn}(s) \tilde{\rho}_{\mu\nu}^{ab}(p) \quad , \tag{3.32}$$

under rescaling with the real parameter s . This behavior reflects the scaling of the spectral function with the canonical dimension and takes into account a possible occupation number exponent κ for the statistical function. This is equivalent to what is obtained from using a kinetic approach. We emphasize that no explicit gauge fixing has to be applied here and the calculation goes through for all gauges which admit scaling solutions of the form in Eq. (3.32). The scaling properties of the three-gluon vertex in Eq. (3.21) are different for the standard tree-level part in Eq. (3.22) and the background-field part in Eq. (3.23). To parametrize this behavior in a compact way, we write

$$V_{\mu\nu\gamma}^{abc}(sp, sq, sk) = s^v V_{\mu\nu\gamma}^{abc}(p, q, k) \quad , \tag{3.33}$$

where $v = 1$ for the standard tree-level vertex and $v = 0$ for the background field part.

We now map the terms (II) and (III) in Eq. (3.31) using scaling transformations such that they have the same form as (I) up to momentum dependent prefactors. First, we apply for (II) the transformation

$$q \rightarrow \frac{p^0}{k^0} q \quad , \quad k \rightarrow \frac{p^0}{k^0} p \quad , \quad p \rightarrow \frac{p^0}{k^0} k. \tag{3.34}$$

The absolute value of the Jacobian for the frequency part of this transformation is $|p^0/k^0|^3$. The same procedure applies to the term (III) where the roles of $(k, \gamma, \delta, c, d)$ and (q, α, β, a, b) are interchanged. Taking also into account the symmetry of the three-gluon vertex under exchange

of combined momentum, color and Lorentz index leads us to

$$\begin{aligned}
 0 &= \frac{g^2}{2} \int_{\mathbf{p}qk} (2\pi)^4 \delta^{(4)}(p+q+k) V_{eac}^{\mu\alpha\gamma}(p, q, k; \bar{\mathcal{A}}) V_{fbd}^{\nu\beta\delta}(-p, -q, -k; \bar{\mathcal{A}}) \\
 &\times \tilde{F}_{\beta\alpha}^{ba}(q) \tilde{F}_{\delta\gamma}^{dc}(k) \tilde{\rho}_{\nu\mu}^{fe}(p) \left[1 + \left| \frac{p^0}{k^0} \right|^\Delta \operatorname{sgn} \left(\frac{p^0}{k^0} \right) + \left| \frac{p^0}{q^0} \right|^\Delta \operatorname{sgn} \left(\frac{p^0}{q^0} \right) \right]. \quad (3.35)
 \end{aligned}$$

Here the exponent Δ is given by

$$\Delta = \underbrace{3 \cdot 3 + 3}_{\text{measure}} \underbrace{-4}_{\delta\text{'s}} \underbrace{-2(2 + \kappa)}_{FF} \underbrace{-2}_{\rho} \underbrace{+ v^{(1)} + v^{(2)}}_{VV}, \quad (3.36)$$

and $v^{(1)}, v^{(2)}$ are the scaling exponents of the respective parts of the two vertex functions appearing in the one-loop self-energy.

As is well known, the above analysis in the presence of a homogeneous background field is complicated by the fact that to order g^2 the individual terms in Eq. (3.31) vanish, since the corresponding processes are kinematically suppressed on-shell, i.e. for $p^0 = \pm|\mathbf{p}|$. Only if the background field has a residual (space-) time dependence, $\mathcal{A}(t)$, the phase space is opened up by the associated (momentum) frequency contribution of the field and it becomes kinematically allowed. In this sense, the background field should be understood as an effective description for soft excitations of the system, rather than an actual condensate. Since all contributions not involving the background field are phase space suppressed, we need to consider only the situation where both vertices are associated with the background field, which implies $v^{(1)} = v^{(2)} = 0$ for the above scaling analysis. After taking this into account, the subsequent analysis is analogous to the discussion in scalar field theories, where the corresponding dynamics has been analyzed in great detail [33, 34, 43]. Therefore, it is also not surprising that the gauge theory in the presence of a (space-) time background may exhibit the same scaling exponents as a scalar field theory with quartic self-interaction in the presence of a time-dependent condensate [43].

Indeed, if we set $\Delta = -1$ in Eq. (3.35) then the energy conservation constraint $\delta(p^0 + q^0 + k^0)$ in the integrand of Eq. (3.35) ensures the vanishing of $(1 + k^0/p^0 + q^0/p^0)$, using $|k^0/p^0| \operatorname{sgn}(p^0/k^0) = k^0/p^0$ with nonzero p^0 . One can then directly read off the scaling solution by use of Eq. (3.36) as

$$\Delta = -1 \quad \Rightarrow \quad \kappa = \frac{3}{2}. \quad (3.37)$$

In analogy to the situation in scalar theories, this solution is associated to an energy cascade towards higher momenta [33, 34, 37–39, 87].

Since the above analysis requires the presence of a parametrically large background field $\mathcal{A}_\mu^a(x) \sim 1/g$, it is important to consider also the situation where this background field is absent. In this case, the leading order g^2 contributions to the self-energies is phase space suppressed for massless on-shell excitations and one needs to consider the next to leading order g^4 contributions. This analysis has been performed within the same framework in Ref. [87]. Since the elastic scattering processes, which appear at order g^4 are both particle number and energy conserving, there are two non-trivial fixed point solutions. The corresponding scaling exponents are given by $\kappa = 4/3$ and $\kappa = 5/3$ for the particle and energy cascade respectively.

The above discussion suggests a clear interpretation of our lattice results presented in the previous section. Since at early times we clearly observe the emergence of a $|\mathbf{p}|^{-3/2}$ power law, this can be interpreted as the consequence of an effective $2 \leftrightarrow (1 + \text{soft})$ interaction in the presence of a parametrically large background field, associated to a large number of very soft excitations of the system. This particular aspect is very similar to what is observed for scalar theories, where an effective $2 \leftrightarrow (1 + \text{soft})$ interaction arises due to the presence of a time-dependent Bose condensate. However a clear difference between scalar and non-abelian gauge theories emerges on longer time scales, since in the gauge theory these soft excitations decay and one observes a transition to a $|\mathbf{p}|^{-4/3}$ power law regime, which is governed by elastic $2 \leftrightarrow 2$ scattering processes. We note that, in this regime one should in principle also consider inelastic processes which naively appear only at order g^6 . However, due to soft-collinear singularities of the corresponding scattering matrix elements, these processes contribute already at order g^4 [99]. Since the kinematics of these processes is rather involved [100], the corresponding fixed point analysis has not yet been performed and it remains an open question to what extent these are compatible with the scaling exponent $\kappa = 4/3$.

3.4 Late times and self-similarity

We now turn to a detailed analysis of the dynamics of the late time regime. In particular, we will investigate whether the system remains at the non-thermal fixed point and to what extent the kinetic scaling behavior in time, as discussed in Sec. 3.1, is realized within classical-statistical lattice simulations. We will see shortly, how the emergence of self-similarity in our simulations suggests to extend the previous kinetic analysis in Sec. 3.1, leading to a unified description in the theory of turbulent thermalization [34] discussed in Sec. 3.5.

We employ the same setup as in Sec. 3.2 and study the evolution of the electric and magnetic two-point correlation functions⁶

$$\langle BB \rangle(t, \mathbf{p}) = \int_{\mathbf{x-y}} \frac{\langle B_i^a(t, \mathbf{x}) B_i^a(t, \mathbf{y}) \rangle_{\text{Coul. Gauge}}}{(N_c^2 - 1)(d - 1)} e^{-i\mathbf{p}(\mathbf{x-y})}, \quad (3.38)$$

$$\langle EE \rangle(t, \mathbf{p}) = \int_{\mathbf{x-y}} \frac{\langle E_i^a(t, \mathbf{x}) E_i^a(t, \mathbf{y}) \rangle_{\text{Coul. Gauge}}}{(N_c^2 - 1)(d - 1)} e^{-i\mathbf{p}(\mathbf{x-y})}, \quad (3.39)$$

here written in terms of continuum variables, where $N_c = 2$ is the number of colors, $d = 3$ is the number of spatial dimensions and $\langle \cdot \rangle_{\text{Coul. Gauge}}$ denotes classical-statistical averaging with the residual gauge freedom fixed by the Coulomb type gauge condition as in Sec. 3.2.⁷

The initial conditions are chosen to mimic the quasi-particle picture in Eq. (3.1) as a superposition of transversely polarized modes $a^{\lambda\mathbf{p},a}(x)$ labeled by the color index $a = 1, \dots, N_c^2 - 1$, the polarization index $\lambda = 1, 2$ and spatial momentum \mathbf{p} . The mode functions $a^{\lambda\mathbf{p},a}(x)$ are determined in the free theory, and satisfy the gauge-condition $\mathbf{p}^i a_i^{\lambda\mathbf{p},a}(x) = 0$ as well as the abelian part of the Gauss law constraint $\mathbf{p}^i \partial_t a_i^{\lambda\mathbf{p},a}(x) = 0$ individually for each mode. The initial occupation of these modes is determined by the distribution function

$$f_0(\mathbf{p}) = \alpha_s^{-c} \theta(Q - |\mathbf{p}|), \quad (3.40)$$

where the parameter $0 < c < 1$ characterizes the initial over-occupation. Since we are interested in the dynamics at late times, the simulations are performed on relatively small $N = 64, 96, 128$ lattices with three different values of the lattice spacing $Qa = 0.33, 0.66, 1.0$ to gain systematic control over lattice spacing and finite volume effects. If not stated otherwise the results presented in this section are obtained from simulations with $N = 96$ and $Qa = 0.66$ lattices.

⁶The normalization factor $(N_c^2 - 1)(d - 1)$ corresponds to the number of transversely polarized gluons. This normalization implicitly assumes that the contributions from longitudinal (plasmon) excitations are small compared to the transverse ones. This has also been studied in terms of the individual projections in Ref. [88].

⁷In this section, we use the so-called 'Los Alamos' procedure to perform the gauge-fixing [89].

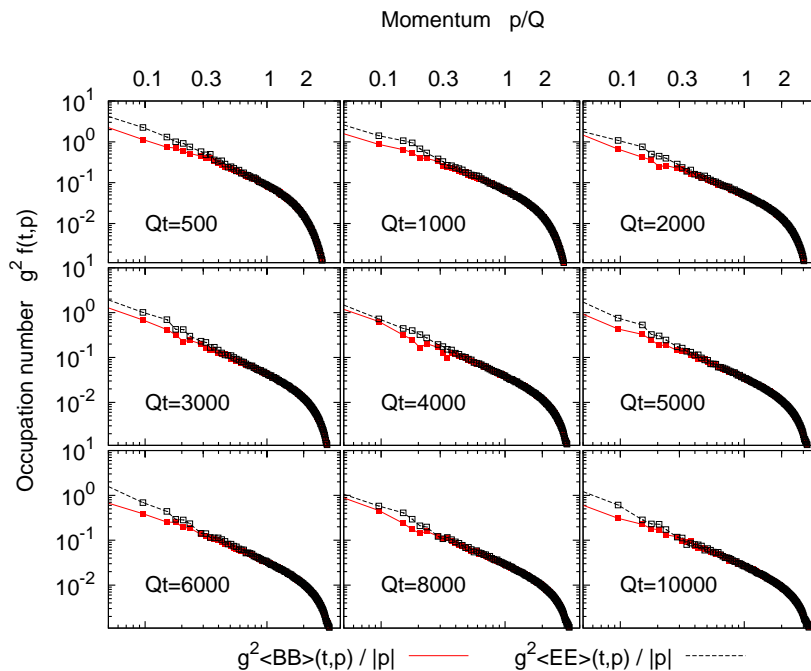


Figure 3.6: Spectrum of excitations obtained from the correlation functions, $\langle EE \rangle / |\mathbf{p}|$ and $\langle BB \rangle / |\mathbf{p}|$ at different times Qt of the evolution. One observes a clear power-law dependence for the correlation functions $\langle EE \rangle$ and $\langle BB \rangle$, which extends over approximately one decade. As time proceeds the tail of the power law propagates towards the ultraviolet, while the amplitude of the distribution decreases.

3.4.1 Highly over-occupied systems - $f_0(p) \sim \alpha_S^{-1}$

We first study the time evolution of the correlation functions defined in Eq. (3.38) and (3.39). The results are presented in Fig. 3.6, where we show the spectrum of the correlation functions $\langle EE \rangle(t, \mathbf{p}) / |\mathbf{p}|$ and $\langle BB \rangle(t, \mathbf{p}) / |\mathbf{p}|$ at different times Qt of the evolution. The factor $1/|\mathbf{p}|$ is chosen to produce dimensionless quantities, which can be interpreted as an occupation number. From Fig. 3.6 one clearly observes the emergence of a power law spectrum, which subsequently decreases in amplitude while slowly moving out towards higher momenta. We observe that towards later times the electric and magnetic correlation functions $\langle EE \rangle / |\mathbf{p}|$ and $\langle BB \rangle / |\mathbf{p}|$ show a consistent scaling behavior over a wide range of momenta. In order to establish a more direct comparison with the kinetic theory discussion we extract the effective occupation number from the electric field correlation function as

$$f(t, \mathbf{p}) = \frac{\langle EE \rangle(t, \mathbf{p})}{|\mathbf{p}|}, \quad (3.41)$$

which we will use in the following to further analyze the evolution.

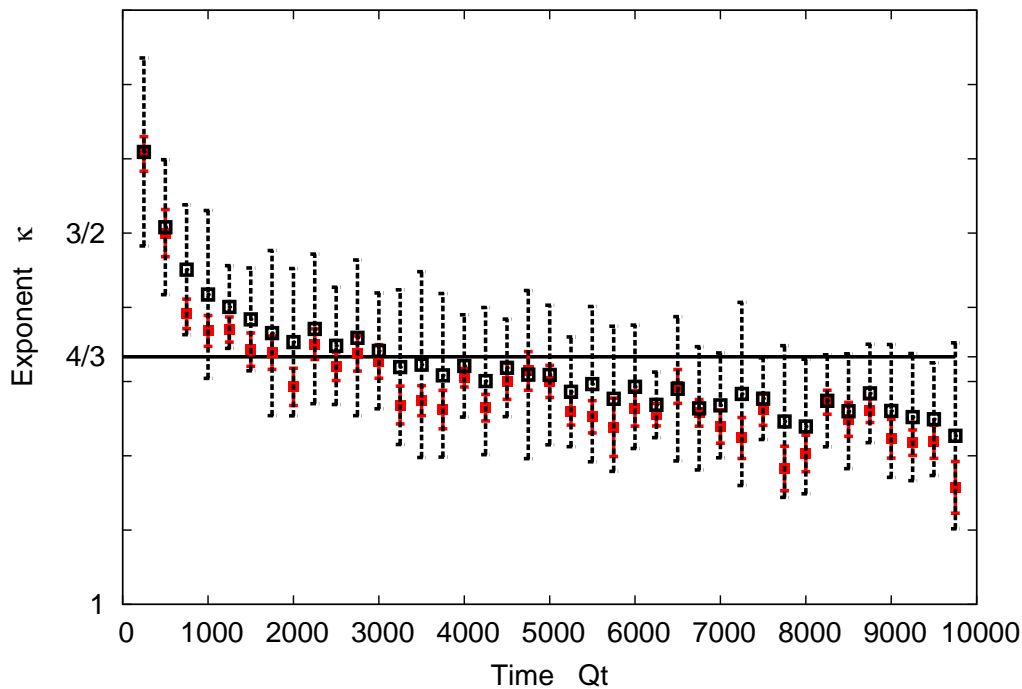


Figure 3.7: Scaling exponent κ extracted from the spectrum of the correlation function $f(t, \mathbf{p}) \sim \langle EE \rangle / |\mathbf{p}|$ at different times of the evolution. The different symbols correspond to the two different extraction methods. The red filled squares correspond to a global fit in the momentum range $p = 0.3 - 1.0 Q$, whereas the black empty squares correspond to averages of local fits as described in the text. Over a large time scale the exponent is consistent with the Kolmogorov turbulence exponent $\kappa = 4/3$ [87].

While the power law dependence of the distribution function $f(t, \mathbf{p})$ can already be observed from Fig. 3.6 we are interested also in the exponent κ of the power law. This is important to distinguish the cases where the observed spectrum corresponds to a quasi-thermal evolution ($\kappa = 1$) or a turbulent Kolmogorov cascade ($\kappa = 4/3, 5/3; 3/2$). To extract the exponent from the data we perform a series of least-square fits at each time slice, with a distribution function of the form

$$f(t, \mathbf{p}) = \alpha_S^{-c} \left(\frac{\Lambda_s(t)}{|\mathbf{p}|} \right)^{\kappa(t)}. \quad (3.42)$$

This procedure yields the two parameters $\kappa(t)$ and $n_{\text{Hard}}(t) = (\Lambda_s/Q)^{\kappa(t)}$ which are shown in Fig. 3.7 and 3.8 respectively. To estimate the error of this procedure we perform the analysis in two different ways: In the first case we simply consider the result of a global fit along with its error in the momentum range $p/Q = 0.3 - 1.0$, where scaling is observed. The results of this procedure are shown as red squares in Fig. 3.7. In the second case we divide the data in momentum bins and perform a separate fit for each bin. We then extract the average exponent and its error in the scaling region. The results correspond to the black points in Fig. 3.7. One

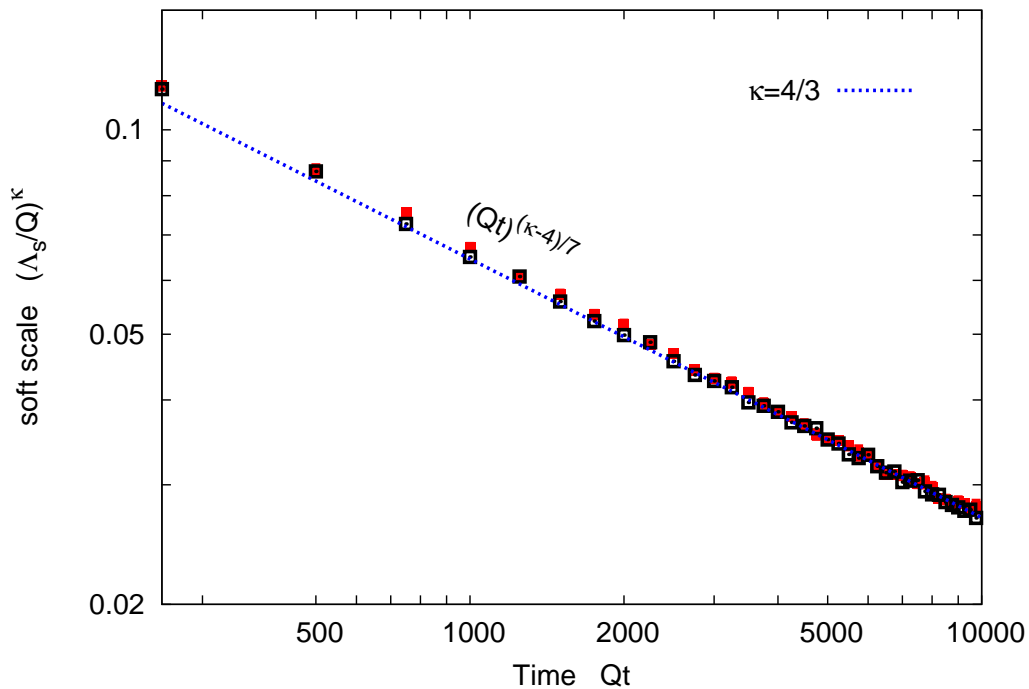


Figure 3.8: Time evolution of the soft scale $(\Lambda_s/Q)^\kappa$ extracted from fits of the spectra at different times (red squares) and from the time evolution of the occupation number for modes with $p \simeq Q$ (black squares). The blue dashed line corresponds to a power-law behavior $(Qt)^{(\kappa-4)/7}$ as expected from the kinetic theory analysis, where we assumed $\kappa = 4/3$ as a constant in time.

observes that the results for κ of the two procedures agree, while the second method provides a more reliable estimate of the error. We find that at early times the spectrum features a power law exponent of $\kappa \simeq 3/2$, in agreement with the result presented in Sec. 3.2. At later times one observes a hardening of the spectrum where the data is in favor of $\kappa \simeq 4/3$ over a large time scale. As discussed in Sec. 3.3, the appearance of the exponent $\kappa = 3/2$, can be attributed to a transient condensation phenomenon, which does not persist on parametrically large time scales [43, 90]. The thermal value $\kappa = 1$ is clearly ruled out by the data over the entire simulation time.

As discussed in Sec. 3.1 in the kinetic theory framework, the appearance of a non-thermal fixed point characterized by the non-trivial scaling exponent $\kappa \neq 1$ has an immediate impact on the evolution of the soft scale Λ_s , which is expected to display a slower evolution for larger values of κ . To investigate whether this is supported by the lattice data, we extract the time evolution of the soft scale $(\Lambda_s/Q)^\kappa(t)$ by two different procedures. The results are on display in Fig. 3.8. In the first case we use the results of the previous fit procedure to directly obtain the quantity $(\Lambda_s/Q)^\kappa$ as a function of time. This corresponds to red squares in Fig. 3.8. In the second case we investigate the evolution of modes with $|\mathbf{p}| \simeq Q$, where $f(t, |\mathbf{p}| \simeq Q) \sim \alpha_S^{-c} (\Lambda_s/Q)^\kappa$ according to Eq. (3.42). This is shown by black squares in Fig. 3.8. The results from both methods

agree and one observes a clear power law dependence. The blue dashed line corresponds to the kinetic theory estimate (c.f. Sec. 3.1)

$$\left(\frac{\Lambda_s(t)}{Q}\right)^\kappa \sim (Qt)^{(\kappa-4)/7}, \quad (3.43)$$

where we assumed $\kappa = 4/3$ to be independent of time. One observes good overall agreement with the data. We also performed fits to extract the scaling exponent from the time evolution of $(\Lambda_s/Q)^\kappa$. Using the same methods as introduced previously and assuming the evolution in Eq. (3.43) this yields $\kappa \simeq 1.3 \pm 0.1$, which is consistent with the values shown in Fig. 3.7.

So far we have only analyzed the behavior of the spectrum in a momentum region where it shows a clear power law dependence. However one of the key features of the evolution is the propagation towards higher momenta, which ultimately leads to thermalization of the system. As discussed in Sec. 3.1 the kinetic theory framework provides a strong prediction of how this evolution proceeds, which is insensitive also to the scaling exponent κ .

To extract the evolution of the cut-off scale $\Lambda(t)$ from the lattice data, we exploit the fact that the spectrum shown in Fig. 3.6 exhibits a self-similar behavior. To illustrate this we first note that we can parametrize the entire spectrum as

$$f(t, \mathbf{p}) = \alpha_s^{-c} \left(\frac{\Lambda_s(t)}{|\mathbf{p}|}\right)^\kappa C(t, |\mathbf{p}|/\Lambda(t)), \quad (3.44)$$

where the first part corresponds to the infrared power-law and the second part regulates the ultraviolet behavior such that $C(t, |\mathbf{p}|/\Lambda(t)) = 1$ for $|\mathbf{p}| < \Lambda(t)$, whereas it drops off quickly for $|\mathbf{p}| > \Lambda(t)$ as observed in Fig. 3.6. Here $\kappa \simeq 4/3$ is assumed to be constant in time. If we assume further that the shape of the cut-off function is independent of time, i.e.

$$C(t, |\mathbf{p}|/\Lambda(t)) \simeq C(|\mathbf{p}|/\Lambda(t)), \quad (3.45)$$

and the scales $\Lambda(t)$ and $\Lambda_s(t)$ evolve according to a power law in time, i.e.

$$\Lambda(t) \sim Q (t/t_{\text{Start}})^\alpha, \quad (3.46)$$

$$\Lambda_s(t) \sim Q (t/t_{\text{Start}})^\beta, \quad (3.47)$$

we find that the distribution function is self-similar in the sense that for $s > 0$ one finds

$$f(st, s^\alpha \mathbf{p}) = s^{(\beta-\alpha)\kappa} f(t, \mathbf{p}). \quad (3.48)$$

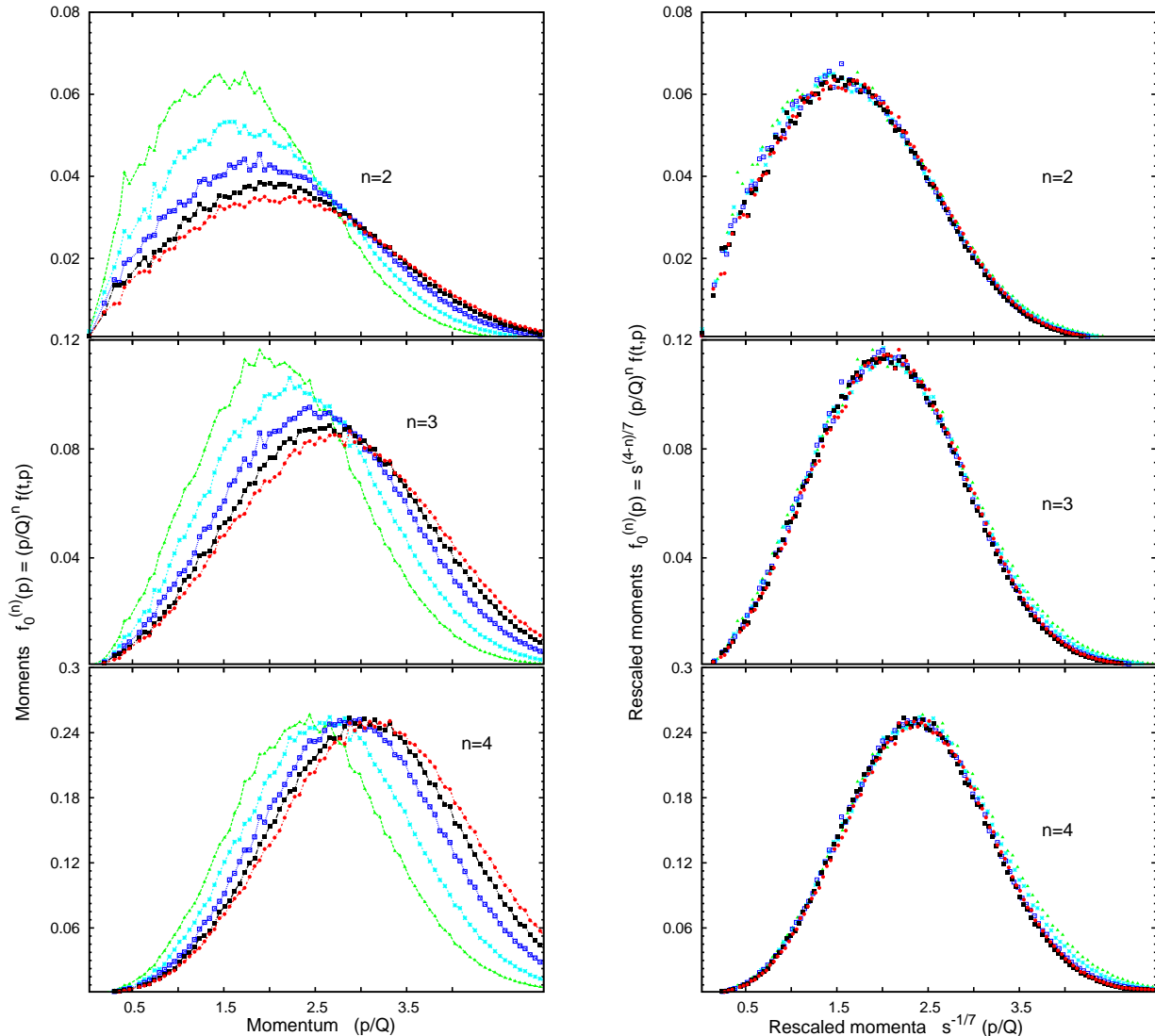


Figure 3.9: **(left)** Moments of the distribution function as a function of momentum. The different colors and symbols correspond to different evolution times. **(right)** Rescaled moments of the distribution function as a function of the rescaled momentum variable. The scale factor is $s = t/t_0$, where we chose $Qt_0 = 1000$ as normalization. As a striking manifestation of self-similarity, one observes that after the appropriate rescaling all data collapses onto a single curve. The scaling exponents are sensitive to the evolution of the hard scale $\Lambda(t)$ and we used the values from the kinetic theory analysis in Sec. 3.1. The results were obtained on $N = 96$ lattices with $Qa = 0.33$.

Here it is crucial to rescale momenta according to s^α , whereas the evolution time scales with s in order to reproduce the correct cut-off behavior. Therefore Eq. (3.48) is particularly sensitive to the scaling of the hard scale $\Lambda(t)$ and can be used to extract the scaling exponent α . We note that the assumption (3.45) only concerns the behavior of $p > \Lambda(t)$, while for $p < \Lambda(t)$ this property is satisfied by construction. Hence the condition (3.45) reflects the assumption that the fall-off above the cut-off scale is universal and we will turn back to this point when we contrast the above analysis with lattice data. We also note that the scaling behavior of $\Lambda_s(t)$ readily emerges from Fig. 3.8, where we confirmed $\beta\kappa = (\kappa - 4)/7$ in agreement with the analysis in Sec. 3.1, where we obtained the exponents $\alpha = 1/7$ and $\beta = (1 - 4/\kappa)/7$.

In order to investigate to which degree this self-similarity is featured by the lattice data, we invert Eq. (3.48) such that we expect the spectra at different times to collapse onto a single curve. As we are particularly interested in the evolution of the hard scale $\Lambda(t)$, we find it convenient to consider moments of the distribution function

$$f^{(n)}(t, \mathbf{p}) = |\mathbf{p}|^n f(t, \mathbf{p}), \quad (3.49)$$

which are more sensitive to hard modes than the distribution function itself. Setting $s = t/t_0$ the scaling relation for the moments $f^{(n)}(t, \mathbf{p})$ then takes the form

$$f_0^{(n)}(\mathbf{p}) = (t/t_0)^{(4-n)/7} f^{(n)}(t, (t/t_0)^{1/7} \mathbf{p}), \quad (3.50)$$

where we used the values of α, β from Sec. 3.1 and abbreviated $f_0^{(n)}(\mathbf{p}) = f^{(n)}(t_0, \mathbf{p})$ for an arbitrary time $t_0 > t_{\text{start}}$. The rescaled moments of the lattice data are shown in Fig. 3.9 for $n = 2, 3$ and 4 and times $Qt = 1000 - 8000$, where we used $Qt_0 = 1000$ as the normalization. As the moments are more sensitive to the hard tail of the distribution, we used $N = 96$ and $Qa = 0.33$ in our simulations to achieve a larger momentum cut-off. One observes that the rescaled data collapses onto a single curve to very good accuracy. This provides strong evidence that the hard scale $\Lambda(t)$ indeed follows a power law behavior with $\Lambda(t) \sim Q (Qt)^{1/7}$ as discussed in Sec. 3.1. In particular the position and amplitude of the peak, which are very sensitive to $\alpha = 1/7$, coincide for all curves. Above the peak we observe minor deviations from the universal behavior. This can be attributed to a non-universal fall-off of the cutoff function for $p > \Lambda(t)$, however we can also not completely rule out the presence of lattice artifacts in the high momentum region.

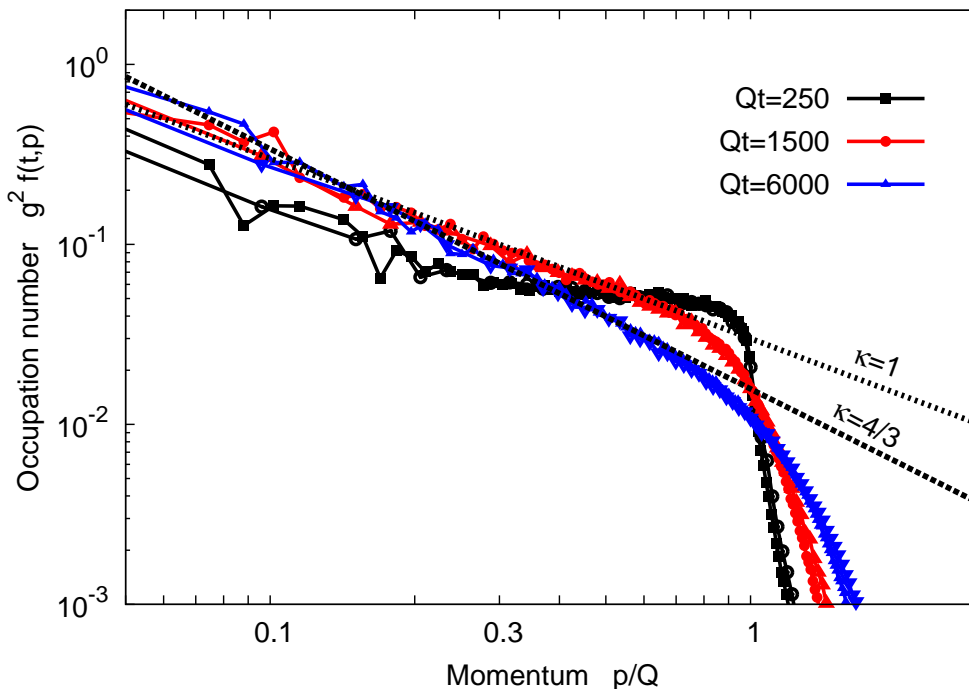


Figure 3.10: Spectrum of excitations for initial occupancies $n_0 = 0.05$ at different times of the evolution. In addition to $N = 96$ and $Qa = 0.66$ data (open symbols) we also show results with reduced statistics for $N = 128$ and $Qa = 1$ (filled symbols). One observes that the evolution of modes with $p \simeq Q$ is much slower as compared to the $n_0 = 1$ case. As a consequence only the soft sector is subject to changes due to interactions at early times, while at later times hard modes are also affected. In the transition region the spectrum shows a thermal shape $\kappa \simeq 1$ at some point of the evolution. Nevertheless the evolution at late times proceeds via a turbulent cascade with $\kappa \simeq 4/3$. This behavior is indicated by the black dashed lines.

3.4.2 Over-occupied systems - $f_0(p) \sim \alpha_S^{-c}$, $0 < c < 1$

We now extend our previous analysis to systems with initial occupancies which are still parametrically large but now smaller than α_S^{-1} . We will in the following denote the initial occupancy by $n_0 = \alpha_S^{1-c}$ and we study systems with $n_0 = 0.05, 0.1, 0.2, 0.5$ for a fixed value of the strong coupling constant $\alpha_S = 10^{-6}$ such that the classicality condition $n_0 \gg \alpha_S$ is always satisfied. We will first discuss the case $n_0 = 0.05$ as an example and then turn to a global analysis of all data. We note that the qualitative behavior on large time scales is very similar for all values of n_0 considered here.

We proceed as previously and first study the evolution of the spectrum of the correlation functions. In Fig. 3.10 we present snapshots of the spectrum of $f(t, \mathbf{p})$ as defined in Eq. (3.41) for different times Qt and initial occupation $n_0 = 0.05$. At early times we observe an increase of occupancies in the soft sector, whereas the occupation for modes with $p \simeq Q$ remains almost unaffected. This is in accordance with our expectations from the kinetic theory analysis

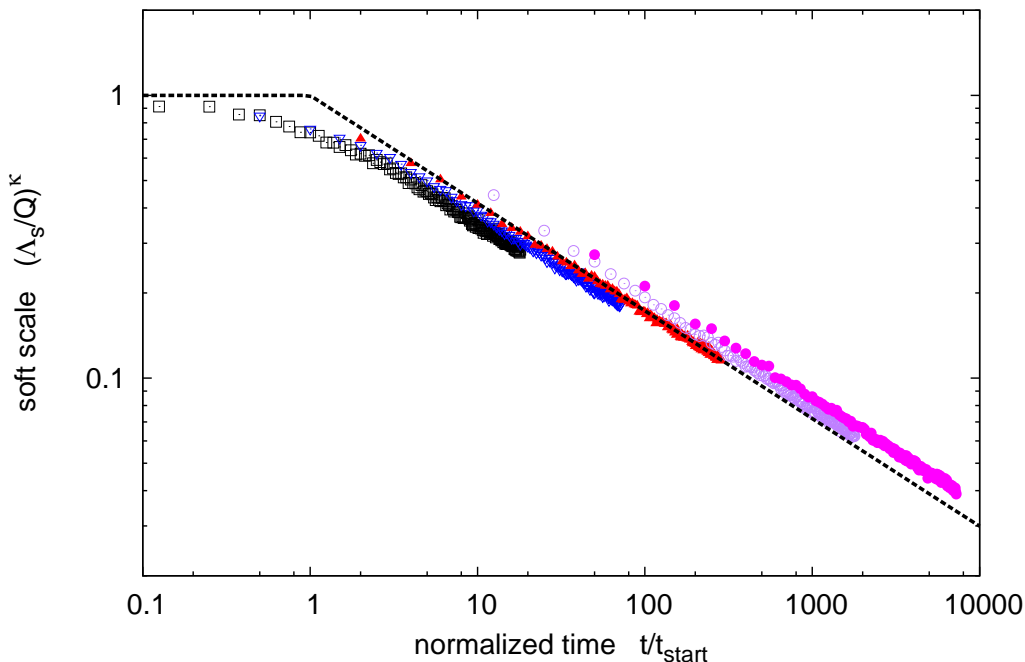


Figure 3.11: Evolution of the soft scale $(\Lambda_s/Q)^\kappa$ normalized by the initial occupation n_0 as a function of the normalized time t/t_{start} for different initial occupations $n_0 = 0.05, 0.1, 0.2, 0.5$ and 1 (bottom to top). The quantity $(\Lambda_s/Q)^\kappa$ is obtained from the occupation of modes with $p \simeq 0.9Q$. The black dashed line portraits the result of the kinetic theory analysis (c.f. Sec. 3.1). At late times $t \gg t_{\text{start}}$ one observes a power law dependence independent of the choice of n_0 in the considered range of parameters.

(c.f. Sec. 3.1), where at times $t < t_{\text{start}}$ only soft modes are affected by small angle elastic scattering. The evolution at late times proceeds, similarly to the case $n_0 = 1$, as a turbulent cascade ($\kappa \simeq 4/3$) towards the ultraviolet. The transition region between early and late times is characterized by a softening of the spectrum, where the initially flat distribution changes its shape to a power-law distribution with exponent $\kappa \simeq 4/3$. Even though the classical thermal value $\kappa \simeq 1$ is featured at some time during this transition, the system subsequently continues to evolve towards $\kappa \simeq 4/3$ at later times. This provides yet another strong piece of evidence that a non-thermal exponent $\kappa \neq 1$ is indeed favored during the far from-equilibrium evolution.

Interestingly, we find that by lowering the initial occupancy n_0 , the transient regime discussed in Sec. 3.2 and characterized by the scaling exponent $\kappa = 3/2$ disappears for initial occupancies $n_0 \lesssim 0.2$ and one observes the direct buildup of a $\kappa = 4/3$ instead. In view of the discussion in Sec. 3.3, this feature can be understood quite naturally: Since the initial over-occupation is significantly reduced for smaller values of n_0 , a much smaller fraction of excitations is absorbed into the very soft sector, such that a parametrically large ‘background field’ is no longer build up dynamically. The effective $2 \leftrightarrow (1 + \text{soft})$ interaction is therefore

less relevant and hard modes interact predominantly by ordinary elastic and inelastic scattering.

When comparing the results in Fig. 3.10 with the evolution in the case $n_0 = 1$, one immediately observes that the evolution proceeds significantly slower in the case of reduced occupancy. This is expected given the smaller interacting rates for lower occupancies. The kinetic theory analysis presented in Sec. 3.1 makes a strong statement about the occupancy dependence, based on the parametric dependence of the momentum diffusion parameter $\hat{q} \sim n_0^2 Q^3$, which controls the rate of interactions at the hard scale. Accordingly the natural time scale for the system to evolve is therefore no longer set by Q^{-1} but rather by the initial 'scattering time' $t_{\text{start}} \sim Q^{-1} n_0^{-2}$ which initially controls the rate of interactions at the hard scale (see also Ref. [31]). In order to analyze whether this behavior is displayed by the lattice data, we chose to investigate the time evolution of the soft scale $(\Lambda_s/Q)^\kappa$ for different initial occupancies. This quantity can be obtained from the occupation of modes with $p \simeq 0.9 Q$ and is shown in Fig. 3.11 as a function of time in units of the 'scattering time'. One observes that around $t \simeq t_{\text{start}}$ the transition from an approximately constant behavior to a power-law decay takes place. The time dependence at late times $t \gg t_{\text{start}}$ is well described by a power law, where $(\Lambda_s/Q)^\kappa \sim (t/t_{\text{start}})^{(\kappa-4)/7}$ with $\kappa \simeq 4/3$ as indicated by the black dashed line in Fig. 3.11. Concerning the dependence on the initial occupancy n_0 , we find that the expected scaling holds approximately as the data shown in Fig. 3.11 nearly collapses on a single curve. However one does observe a residual dependence of the overall amplitude of $(\Lambda_s/Q)^\kappa$ on the initial occupancy, which we found to be rather sensitive to the details of the initial conditions.

3.5 Turbulent thermalization

In view of the results presented in the previous section, it appears intuitive to directly investigate the possibility of self-similar scaling solutions in the kinetic theory framework. The analysis is analogous to the discussion of turbulent thermalization in scalar field theories, investigated in the context of early universe cosmology in Ref. [34]. Here we follow the same procedure and search for self-similar fixed-point solutions for the gluon distribution function $f(t, \mathbf{p})$ according to

$$f(t, \mathbf{p}) = t^\gamma f_S(t^{-\alpha} \mathbf{p}) , \quad (3.51)$$

where $f_S(\mathbf{p})$ denotes a stationary distribution, which characterizes the shape of the attractor and does not depend on time. The factor $t^{-\alpha}$ in the argument describes the evolution of the hard momentum scale $\Lambda(t) \propto t^\alpha$ as in Eq. (3.46), whereas the prefactor t^γ characterizes the overall decrease in amplitude, as previously parametrized by the soft scale $\Lambda_s(t)$. The kinetic evolution is described in terms of a Boltzmann equation of the generic form

$$\partial_t f(t, \mathbf{p}) = C[f](t, \mathbf{p}) , \quad (3.52)$$

where $C[f](t, \mathbf{p})$ denotes the collision integral including the relevant $n \leftrightarrow m$ scattering processes and we will focus on elastic $2 \leftrightarrow 2$ and inelastic $2 \leftrightarrow 3$ scattering processes, which are expected to drive the evolution in the self-similar regime [31]. The collision integral for elastic scattering takes the form [101]

$$\begin{aligned} C[f](t, \mathbf{p}) = & \frac{1}{2} \int_{\mathbf{q}, \mathbf{k}, \mathbf{l}} \frac{|M(\mathbf{p}, \mathbf{q}, \mathbf{k}, \mathbf{l})|^2}{2\omega_p 2\omega_q 2\omega_k 2\omega_l} (2\pi)^4 \delta(\omega_q + \omega_k - \omega_l - \omega_p) \delta^{(3)}(\mathbf{q} + \mathbf{k} - \mathbf{l} - \mathbf{p}) \\ & \times \left[(1 + f_p)(1 + f_l) f_q f_k - f_p f_l (1 + f_q)(1 + f_k) \right] , \end{aligned} \quad (3.53)$$

where the scattering matrix element in the non-relativistic normalization is given by [101]

$$|M(\mathbf{p}, \mathbf{q}, \mathbf{k}, \mathbf{l})|^2 = 128\pi^2 \alpha_s^2 N_c^2 \left(3 - \frac{tu}{s^2} - \frac{su}{t^2} - \frac{ts}{u^2} \right) , \quad (3.54)$$

for non-abelian $SU(N_c)$ gauge theories. We then follow the standard turbulence analysis [34] and insert the scaling ansatz in Eq. (3.51) into the Boltzmann equation (3.52). The left hand side of the Boltzmann equation is then given by

$$\partial_t f(t, \mathbf{p}) = t^{\gamma-1} [\gamma f_S(\tilde{\mathbf{p}}) - \alpha \tilde{\mathbf{p}} \cdot \nabla_{\tilde{\mathbf{p}}} f_S(\tilde{\mathbf{p}})]_{\tilde{\mathbf{p}}=t^{-\alpha} \mathbf{p}} . \quad (3.55)$$

Similarly, one finds that in the classical regime ($f(t, \mathbf{p}) \gg 1$), the collision integral in Eq. (3.53) can be expressed as

$$\begin{aligned}
 C[f](t, \mathbf{p}) &= \frac{1}{2} \int d\Omega^{2\leftrightarrow 2}(\mathbf{p}, \mathbf{q}, \mathbf{k}, \mathbf{l}) f_{\mathbf{p}} f_{\mathbf{l}} f_{\mathbf{q}} f_{\mathbf{k}} \left[f_{\mathbf{p}}^{-1} + f_{\mathbf{l}}^{-1} - f_{\mathbf{q}}^{-1} - f_{\mathbf{k}}^{-1} \right], \\
 &\quad (\text{ Use Eq. (3.51) to re-express } f(t, \mathbf{p}) \text{ in terms of } f_S(t^{-\alpha} \mathbf{p})) \\
 &= t^{3\gamma} \frac{1}{2} \int d\Omega^{2\leftrightarrow 2}(\mathbf{p}, \mathbf{q}, \mathbf{k}, \mathbf{l}) f_S(t^{-\alpha} \mathbf{p}) f_S(t^{-\alpha} \mathbf{l}) f_S(t^{-\alpha} \mathbf{q}) f_S(t^{-\alpha} \mathbf{k}) \\
 &\quad \times \left[f_S^{-1}(t^{-\alpha} \mathbf{p}) + f_S^{-1}(t^{-\alpha} \mathbf{l}) - f_S^{-1}(t^{-\alpha} \mathbf{q}) - f_S^{-1}(t^{-\alpha} \mathbf{k}) \right], \\
 &\quad (\text{ Use Eq. (3.57) to transform the differential cross-section}) \\
 &= t^{3\gamma+\alpha} \frac{1}{2} \int d\Omega^{2\leftrightarrow 2}(t^{-\alpha} \mathbf{p}, t^{-\alpha} \mathbf{q}, t^{-\alpha} \mathbf{k}, t^{-\alpha} \mathbf{l}) f_S(t^{-\alpha} \mathbf{p}) f_S(t^{-\alpha} \mathbf{l}) f_S(t^{-\alpha} \mathbf{q}) f_S(t^{-\alpha} \mathbf{k}) \\
 &\quad \times \left[f_S^{-1}(t^{-\alpha} \mathbf{p}) + f_S^{-1}(t^{-\alpha} \mathbf{l}) - f_S^{-1}(t^{-\alpha} \mathbf{q}) - f_S^{-1}(t^{-\alpha} \mathbf{k}) \right], \\
 &\quad (\text{ Identify with the first line}) \\
 &= t^{3\gamma+\alpha} C[f_S](t^{-\alpha} \mathbf{p}), \tag{3.56}
 \end{aligned}$$

where we used the relation

$$\begin{aligned}
 \int d\Omega^{2\leftrightarrow 2}(\mathbf{p}, \mathbf{q}, \mathbf{k}, \mathbf{l}) &= \int_{\mathbf{q}, \mathbf{k}, \mathbf{l}} \frac{|M(\mathbf{p}, \mathbf{q}, \mathbf{k}, \mathbf{l})|^2}{2\omega_p 2\omega_q 2\omega_k 2\omega_l} (2\pi)^4 \delta^{(4)}(q + k - l - p), \\
 &\quad (\text{ Substitute: } \tilde{\mathbf{q}} = t^{-\alpha} \mathbf{q}, \tilde{\mathbf{k}} = t^{-\alpha} \mathbf{k}, \tilde{\mathbf{l}} = t^{-\alpha} \mathbf{l} \mid \text{ Express : } \mathbf{p} = t^\alpha(t^{-\alpha} \mathbf{p}) \mid \text{ Use: } \omega_{sp} = |s|\omega_p), \\
 &= t^{9\alpha} \int_{\tilde{\mathbf{q}}, \tilde{\mathbf{k}}, \tilde{\mathbf{l}}} \frac{|M(t^\alpha(t^{-\alpha} \mathbf{p}), t^\alpha \tilde{\mathbf{q}}, t^\alpha \tilde{\mathbf{k}}, t^\alpha \tilde{\mathbf{l}})|^2}{2\omega_p 2\omega_{t^\alpha \tilde{\mathbf{q}}} 2\omega_{t^\alpha \tilde{\mathbf{k}}} 2\omega_{t^\alpha \tilde{\mathbf{l}}}} (2\pi)^4 \delta^{(4)}(t^\alpha(\tilde{q} + \tilde{k} - \tilde{l} - t^{-\alpha} p)), \\
 &\quad (\text{ Use: } \omega_{sp} = |s|\omega_p, \delta(sx) = |s|^{-1} \delta(x), |M(sp, sq, sk, sl)|^2 = |M(p, q, k, l)|^2) \\
 &= t^\alpha \int_{\tilde{\mathbf{q}}, \tilde{\mathbf{k}}, \tilde{\mathbf{l}}} \frac{|M(t^{-\alpha} \mathbf{p}, \tilde{\mathbf{q}}, \tilde{\mathbf{k}}, \tilde{\mathbf{l}})|^2}{2\omega_{t^{-\alpha} p} 2\omega_{\tilde{q}} 2\omega_{\tilde{k}} 2\omega_{\tilde{l}}} (2\pi)^4 \delta^{(4)}(\tilde{q} + \tilde{k} - \tilde{l} - t^{-\alpha} p), \\
 &\quad (\text{ Rename: } \tilde{\mathbf{q}} \rightarrow t^{-\alpha} \mathbf{q}, \tilde{\mathbf{k}} \rightarrow t^{-\alpha} \mathbf{k}, \tilde{\mathbf{l}} \rightarrow t^{-\alpha} \mathbf{l} \mid \text{ Identify with the first line}) \\
 &= t^\alpha \int d\Omega^{2\leftrightarrow 2}(t^{-\alpha} \mathbf{p}, t^{-\alpha} \mathbf{q}, t^{-\alpha} \mathbf{k}, t^{-\alpha} \mathbf{l}). \tag{3.57}
 \end{aligned}$$

By use of Eqns. (3.55) and (3.56), the Boltzmann equation (3.52) can be decomposed into a condition for the fixed point solution $f_S(\mathbf{p})$

$$\gamma f_S(\mathbf{p}) - \alpha \mathbf{p} \cdot \nabla_{\mathbf{p}} f_S(\mathbf{p}) = C[f_S](\mathbf{p}) , \quad (3.58)$$

and the scaling relation

$$\gamma - 1 = 3\gamma + \alpha . \quad (3.59)$$

The non-trivial solutions of Eq. (3.58) characterize the functional form of the fixed point solutions $f_S(\mathbf{p})$, whereas the scaling relation (3.59) constraints the evolution of the system on the fixed point trajectory. Since Eq. (3.59) does not uniquely determine the scaling exponents, a further constraint can be derived from energy conservation. By use of

$$\epsilon = \int_{\mathbf{p}} \omega_p f(t, \mathbf{p}) = t^\gamma \int_{\mathbf{p}} \omega_p f_S(t^{-\alpha} \mathbf{p}) = t^{\gamma+3\alpha} \int_{\tilde{\mathbf{p}}} \omega_{t\alpha\tilde{\mathbf{p}}} f_S(\tilde{\mathbf{p}}) = t^{\gamma+4\alpha} \epsilon_S , \quad (3.60)$$

one then obtains the scaling relation

$$\gamma + 4\alpha = 0 . \quad (3.61)$$

We note that if one considers only elastic scattering the overall particle number is also conserved. However, this is no longer the case when inelastic (number-changing) interactions are also taken into account. Since in non-abelian gauge theories, inelastic processes exhibit the same parametric dependencies as elastic scattering,⁸ taking inelastic processes into account does not affect the scaling properties of the collision integral in Eq. (3.56). Hence, the above scaling analysis still applies while particle number conservation does not have to be considered due to inelastic interactions [31, 88]. Combining the scaling relations obtained from the analysis of the Boltzmann equation in Eq. (3.59) and the energy conservation constraint in Eq. (3.61), then yields the set of scaling exponents

$$\alpha = 1/7 , \quad \gamma = -4/7 , \quad (3.62)$$

which are in excellent agreement with the lattice results presented in Sec. 3.4. Of course, the above scaling exponents also agree with the discussion in Sec. 3.1, where instead of searching for self-consistent solutions of the Boltzmann equation, we considered the parametric dependencies only.

⁸In this case the additional factor of α_S as well as the additional momentum integration and the additional factor of the gluon distribution function are canceled by the soft-collinear singularity of the $2 \leftrightarrow 3$ matrix element [101].

3.6 Discussion

We close this chapter with a brief summary of our findings and a comparison to similar observations at very different energy scales.

We established in Sec. 3.2 and 3.4 that thermalization of initially over-occupied systems proceeds as a turbulent cascade towards the ultraviolet, which continues as long as the typical occupancies are much larger than unity. Turbulent behavior emerges after a short period of time, controlled by the initial occupation number, when the system exhibits a (non-thermal) power-law spectrum and the dynamics becomes quasi-stationary, indicating the presence of a non-thermal fixed point [87, 88, 90, 91].

In Sec. 3.2 we observed that highly over-occupied systems exhibit a transient regime, where the spectral index of this power law is described by $\kappa = 3/2$ and we explained this behavior in Sec. 3.3 by an effective $2 \leftrightarrow (1 + \text{soft})$ interaction appearing in the presence of an excess of very soft excitations [90]. However, at later times, these excitations decay due to inelastic interactions and the scaling exponent becomes $\kappa = 4/3$, indicative of wave turbulence governed by ordinary elastic scattering processes [87].

Strikingly, we discovered in Sec. 3.4 that the dynamics at late times is characterized by a self-similar evolution, which describes the energy transport towards the ultraviolet and drives the thermalization process. The scaling exponents characterizing the self-similar evolution in time can be obtained from a kinetic theory analysis, when taking properly into account the presence of a non-thermal fixed point as discussed in Sec. 3.5.

Most remarkably, these scaling exponents are universal in the sense that they are sensitive only to the parametric dependencies of the underlying evolution equations. In particular, one obtains the same result also for relativistic scalar field theories [34], such that the two theories belong to the same universality class. This notion of universality far from equilibrium manifests itself in the fact that similar phenomena can be observed across very different energy scales, ranging from early universe cosmology [34] to the dynamics of ultra-cold quantum gases [36, 102, 103]. In this sense, our results may after all not appear very surprising, since they are shared by a large variety of strongly correlated many-body systems out of equilibrium.

Chapter 4

Non-equilibrium dynamics of instabilities

In this chapter we explore the physics of plasma instabilities, which governs the early stages of the non-equilibrium state formed in ultra-relativistic heavy-ion collisions [49–51]. While several studies have focused on QCD plasma instabilities of momentum space anisotropic media [44–46, 49–51, 104–113], we explore here a class of models characterized by large homogeneous background fields, which can be studied analytically. These can be understood as an idealization of the state created immediately after the collision of heavy nuclei, where an approximately boost invariant plasma with a characteristic transverse correlation length $\sim Q^{-1}$ is expected to be formed at high collider energies [27, 28].

We will first explore the physics of plasma instabilities in non-abelian gauge theories in Minkowski space, by studying the out-of-equilibrium dynamics of coherent non-abelian gauge fields. We employ homogeneous gauge field configurations, which can be studied analytically and compare our findings with the results of classical-statistical lattice simulations. We discover that, in addition to a generalization of the Nielsen-Olesen instability [47, 48], the coherent gauge-field configurations also exhibit a (subleading) parametric resonance instability. The characteristic non-equilibrium dynamics of instabilities ultimately leads to a decoherence of the background field and creates an over-occupied state, similar to the ones discussed in the previous chapter.

Since the dynamics of non-equilibrium instabilities manifests itself in a very similar way in scalar quantum field theories as well as in non-abelian gauge theories [52, 53], we will also consider the example of a parametric resonance instability in a scalar expanding field theory. While the dynamics of the parametric resonance instability in non-expanding scalar theories is comparatively well understood within previous studies [42, 53], we find that the dynamics

of instabilities in the expanding case is qualitatively similar, though some interesting features emerge due to the interplay of instabilities and the longitudinal expansion. The scalar model therefore provides an ideal testground for the theoretical concepts and methods employed in the study of the non-equilibrium dynamics of relativistic heavy-ion collisions. Most remarkably, we find that the techniques previously developed to study the dynamics of the parametric resonance instability in Minkowski space [42, 53] apply in a similar fashion also to longitudinally expanding systems, once the anisotropic expansion of the system is accounted for by the introduction of a generalized conformal time. In particular, this renders the different effects of the longitudinal expansion transparent and important lessons with regard to anisotropically expanding non-abelian plasmas can be learned.

The discussion in this chapter is largely based on Refs. [114, 115] and organized in the following way: In Sec. 4.1, we study the unstable dynamics of coherent field configurations in $SU(2)$ Yang-Mills theory in Minkowski space. We then turn to a detailed discussion of the dynamics of the parametric resonance instability in longitudinally expanding scalar field theories in Sec. 4.2. We conclude this chapter in Sec. 4.3 with a summary of our results and a brief discussion of related studies.

4.1 Instabilities in $SU(2)$ Yang-Mills theory in Minkowski space

In this section, we investigate the classical dynamics of coherent non-abelian gauge fields. As outlined above, this is motivated by the notion of 'color flux tubes' that may form after the collision of heavy nuclei at ultra-relativistic energies. These are characterized by intense color-magnetic as well as color-electric field configurations in the longitudinal direction, which are correlated over a transverse size associated to the inverse of the characteristic momentum scale Q in the saturation scenario [27, 28]. To understand the time evolution of these configurations in QCD is a formidable task, which is further complicated by the longitudinal expansion of the system. In order to approach this complex question of non-linear gauge field dynamics, it is very instructive to consider first an extreme simplification for which analytic insights can be gained. We will therefore neglect the longitudinal expansion of the system for a moment and employ a constant color-magnetic field configuration in the longitudinal direction. For the ease of a later numerical treatment we study the $SU(2)$ gauge theory, for which the homogeneous background field can always be arranged to point in the $a = 1$ direction in color space, such that

$$B_i^a(t_0, \mathbf{x}) = \delta^{1a} \delta_{zi} B. \quad (4.1)$$

Such field configurations have been extensively discussed in the literature [116–118], where the field in the infinite volume limit is taken to be generated from the time independent vector potential $A_\mu^a(x)$ as

$$\mathcal{A}_x^1(x) = -\frac{1}{2}yB, \quad \mathcal{A}_y^1(x) = \frac{1}{2}xB, \quad (4.2)$$

with all other spatial components vanishing. Such a field configuration is known to exhibit a Nielsen-Olesen instability [47, 48] characterized by an exponential growth of fluctuations with maximum growth rate

$$\gamma_{\text{NO}} = \sqrt{gB}, \quad (4.3)$$

where the effective amplitude \sqrt{gB} may be taken to be of order Q in the context of relativistic heavy-ion collisions. This exponential growth leads to a production of gluons which is much faster than any conventional production process and the consequences for the question of thermalization in a heavy-ion collision can be significant. Of course, in this context a single constant color-magnetic background field is certainly not a realistic option and it is important to understand the robustness of the underlying physical processes against suitable generalizations. In a first step, we will therefore allow for temporal modulations of the color magnetic background field by studying homogeneous gauge field configurations

$$\mathcal{A}_x^2(t_0, \mathbf{x}) = \mathcal{A}_y^3(t_0, \mathbf{x}) = \sqrt{\frac{B}{g}}, \quad (4.4)$$

with all other components equal to zero. It can be directly verified that this vector potential configuration yields the same form of the longitudinal magnetic field in Eq. (4.1), however generated entirely by the non-abelian part of the field strength tensor. Most remarkably, this model can still be studied analytically and we will now discuss analytic solutions for the classical time evolution of the configuration in Eq. (4.4) in temporal axial ($A_t = 0$) gauge and study the behavior of linear perturbations on top of the oscillating background. The model can also be extended to include spatial modulations in the transverse plane and we refer the interested reader to Ref. [114] for a detailed numerical study.

4.1.1 Linear instability regime

To study the classical evolution of small perturbations $\delta A_\mu^a(x)$ in the presence of a homogeneous gauge field configurations $\mathcal{A}_\mu^a(t)$, we decompose the classical gauge potentials $A_\mu^a(x)$ according to

$$A_\mu^a(x) = \mathcal{A}_\mu^a(t) + \delta A_\mu^a(x). \quad (4.5)$$

We can then compute the time evolution in an expansion of the classical Yang-Mills equation

$$D_\mu^{ab}(x)\mathcal{F}_b^{\mu\nu}(x)\Big|_{A_\mu^a(x)=\mathcal{A}_\mu^a(t)+\delta A_\mu^a(x)}=0, \quad (4.6)$$

in powers of the perturbation $\delta A_\mu^a(x)$. This can efficiently be achieved by decomposing the covariant derivative and the field strength tensor into a δA independent and a δA dependent part according to

$$D_\mu^{ab}(x) = D_\mu^{ab}[x; \mathcal{A}] + \delta D_\mu^{ab}(x), \quad \mathcal{F}_{\mu\nu}^a(x) = \mathcal{F}_{\mu\nu}^a[x; \mathcal{A}] + \delta \mathcal{F}_{\mu\nu}^a[x; \mathcal{A}]. \quad (4.7)$$

The individual parts of the covariant derivative are given by

$$D_\mu^{ab}[x; \mathcal{A}] = \partial_\mu^x \delta^{ab} + g f^{acb} \mathcal{A}_\mu^c(x), \quad \delta D_\mu^{ab}(x) = g f^{acb} \delta A_\mu^c(x), \quad (4.8)$$

and the individual contributions to the field strength tensor take the form

$$\mathcal{F}_{\mu\nu}^a[x; \mathcal{A}] = \partial_\mu \mathcal{A}_\nu^a(x) - \partial_\nu \mathcal{A}_\mu^a(x) + g f^{abc} \mathcal{A}_\mu^b(x) \mathcal{A}_\nu^c(x), \quad (4.9)$$

$$\delta \mathcal{F}_{\mu\nu}^a[x; \mathcal{A}] = D_\mu^{ab}[x; \mathcal{A}] \delta A_\nu^b(x) - D_\nu^{ab}[x; \mathcal{A}] \delta A_\mu^b(x) + g f^{abc} \delta A_\mu^b(x) \delta A_\nu^c(x). \quad (4.10)$$

At zeroth order in δA one obtains the classical Yang-Mills equations as the evolution equation for the background field

$$D_\mu^{ab}[x; \mathcal{A}] \mathcal{F}_b^{\mu\nu}[x; \mathcal{A}] = 0. \quad (4.11)$$

The next order corresponds to the linearized equations of motions for the fluctuations δA and takes the form [119]

$$D_\mu^{ab}[x; \mathcal{A}] D_{bc}^\mu[x; \mathcal{A}] \delta A_c^\nu(x) - D_\mu^{ab}[x; \mathcal{A}] D_{bc}^\nu[x; \mathcal{A}] \delta A_c^\mu(x) + g f^{abc} \delta A_\mu^b(x) \mathcal{F}_c^{\mu\nu}[x; \mathcal{A}] = 0, \quad (4.12)$$

where we neglected all terms quadratic in the small perturbations δA . The initial conditions for the non-vanishing components of the background field $\mathcal{A}_\mu^a(t)$ are given by Eq. (4.4) and we chose the time derivative $\partial_t \mathcal{A}_\mu^a(t)$ to vanish at initial time $t = t_0 = 0$. The structure of the evolution equations (4.11) then ensures, that the background field can always be expressed as

$$\mathcal{A}_i^a(t) = \mathcal{A}(t) (\delta^{a2} \delta_{ix} + \delta^{a3} \delta_{iy}), \quad (4.13)$$

and the equation of motion for the background field (4.11) then takes the form

$$\partial_t^2 \mathcal{A}(t) + g^2 \mathcal{A}(t)^3 = 0. \quad (4.14)$$

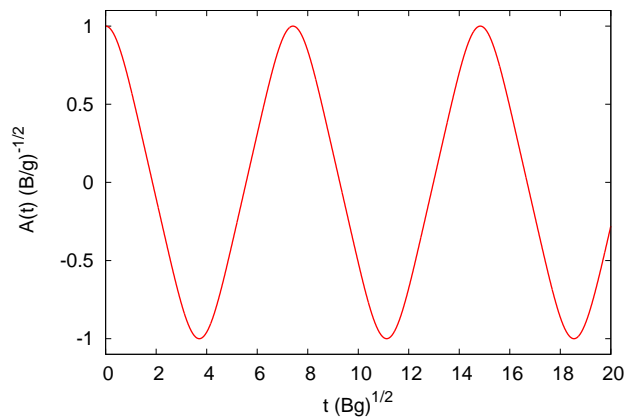


Figure 4.1: Time evolution of the background field $\mathcal{A}(t)$ normalized to its initial value. The functional form is described by the Jacobi elliptic function $\sqrt{B/g} \operatorname{cn}(\sqrt{Bg}t, 1/2)$ as a function of time t in units of the characteristic scale \sqrt{gB} .

The solution to Eq. (4.14) is given in terms of a Jacobi elliptic function

$$\mathcal{A}(t) = \sqrt{\frac{B}{g}} \operatorname{cn}\left(\sqrt{gB}t, \frac{1}{2}\right). \quad (4.15)$$

for the considered initial conditions. The Jacobi cosine $\operatorname{cn}(\sqrt{gB}t, 1/2)$ is an oscillatory function in time such that $\mathcal{A}(t) = \mathcal{A}(t + \Delta t_B)$ with period

$$\Delta t_B = \frac{4K(1/2)}{\sqrt{gB}} \simeq \frac{7.42}{\sqrt{gB}}, \quad (4.16)$$

where $K(1/2)$ denotes the complete elliptic integral of the first kind [120]. Similar behavior has been discussed e.g. in the context of classical chaos [121], or for parametric resonance in scalar field theories [122]. The solution in Eq. (4.15) is plotted in Fig. 4.1. For later use we note that the corresponding characteristic frequency is $\omega_B = 2\pi/\Delta t_B \simeq 0.847\sqrt{gB}$.

We will now study the dynamics of the fluctuations by use of linearized evolution equations in Eq. (4.12) and discuss the solutions for modes δA_i^a in (spatial) Fourier space

$$\delta A_i^a(t, \mathbf{p}) = \int d^3x e^{-ip_j x^j} \delta A_i^a(t, \mathbf{x}). \quad (4.17)$$

We concentrate on momenta p_z along the z -direction, i.e. we evaluate the modes of $\delta A_i^a(t, \mathbf{p})$ at $p_x = p_y = 0$. The evolution equations (4.12) for the different components of $\delta A_i^a(t, p_z)$ can

then be written as the following independent sets of coupled differential equations

$$\begin{pmatrix} \delta \ddot{A}_x^1 \\ \delta \ddot{A}_z^3 \end{pmatrix} = - \begin{pmatrix} g^2 \mathcal{A}^2(t) + p_z^2 & ig\mathcal{A}(t)p_z \\ -ig\mathcal{A}(t)p_z & g^2 \mathcal{A}^2(t) \end{pmatrix} \begin{pmatrix} \delta A_x^1 \\ \delta A_z^3 \end{pmatrix}, \quad (4.18)$$

where we introduce the shorthand notation $\delta \dot{A}_i^a(t, p_z) \equiv \partial_t \delta A_i^a(t, p_z)$ for the time derivative. The complex conjugates of the components $(\delta A_y^1, \delta A_z^2)$ obey the same equation, which is obtained from Eq. (4.18) with the replacement $(\delta A_x^1, \delta A_z^3) \rightarrow (\delta A_y^{1*}, \delta A_z^{2*})$. Similarly, one finds

$$\begin{pmatrix} \delta \ddot{A}_x^2 \\ \delta \ddot{A}_y^3 \end{pmatrix} = - \begin{pmatrix} g^2 \mathcal{A}^2(t) + p_z^2 & 2g^2 \mathcal{A}^2(t) \\ 2g^2 \mathcal{A}^2(t) & g^2 \mathcal{A}^2(t) + p_z^2 \end{pmatrix} \begin{pmatrix} \delta A_x^2 \\ \delta A_y^3 \end{pmatrix}, \quad (4.19)$$

and

$$\begin{pmatrix} \delta \ddot{A}_x^3 \\ \delta \ddot{A}_y^2 \\ \delta \ddot{A}_z^1 \end{pmatrix} = - \begin{pmatrix} p_z^2 & -g^2 \mathcal{A}^2(t) & -ig\mathcal{A}(t)p_z \\ -g^2 \mathcal{A}^2(t) & p_z^2 & ig\mathcal{A}(t)p_z \\ ig\mathcal{A}(t)p_z & -ig\mathcal{A}(t)p_z & 2g^2 \mathcal{A}^2(t) \end{pmatrix} \begin{pmatrix} \delta A_x^3 \\ \delta A_y^2 \\ \delta A_z^1 \end{pmatrix}. \quad (4.20)$$

Each of the linear differential equations (4.18)-(4.20) with time dependent background field $\mathcal{A}(t)$ may be further analyzed by diagonalization. The time-dependent eigenvalues of the matrices read for Eq. (4.18)

$$\omega_{1\pm}^2(p_z) = g^2 \mathcal{A}^2 + \frac{p_z^2}{2} \pm \frac{1}{2} \sqrt{4g^2 \mathcal{A}^2 p_z^2 + p_z^4}, \quad (4.21)$$

for Eq. (4.19)

$$\omega_2^2(p_z) = 3g^2 \mathcal{A}^2 + p_z^2, \quad \omega_3^2(p_z) = -(g^2 \mathcal{A}^2 - p_z^2), \quad (4.22)$$

and for Eq. (4.20)

$$\omega_4^2(p_z) = -(g^2 \mathcal{A}^2 - p_z^2), \quad \omega_{5\pm}^2(p_z) = \infty 2 \left(3g^2 \mathcal{A}^2 + p_z^2 \pm \sqrt{g^4 \mathcal{A}^4 + 6g^2 \mathcal{A}^2 p_z^2 + p_z^4} \right). \quad (4.23)$$

The corresponding eigenvectors depend, in general, on $\mathcal{A}(t)$ and thus on time. However, the eigenvectors associated to $\omega_2^2(p_z)$, $\omega_3^2(p_z)$ and $\omega_4^2(p_z)$ are time-independent and given by $(1, 1)/\sqrt{2}$, $(-1, 1)/\sqrt{2}$, and $(1, 1, 0)/\sqrt{2}$, respectively. These include, in particular, the only *negative* eigenvalues $\omega_3^2(p_z) = \omega_4^2(p_z) < 0$ for momenta $p_z^2 < g^2 \mathcal{A}(t)$. These will play a particularly important role in the following since they turn out to govern the fastest time scales. It is very instructive to consider the example of Eq. (4.19) in diagonalized form

$$\delta \ddot{A}_+ = -(3g^2 \mathcal{A}^2 + p_z^2) \delta A_+, \quad (4.24)$$

$$\delta \ddot{A}_- = (g^2 \mathcal{A}^2 - p_z^2) \delta A_-, \quad (4.25)$$

where $\delta A_+ = \delta A_x^2 + \delta A_y^3$ and $\delta A_- = \delta A_y^3 - \delta A_x^2$. The same equation for δA_- would also be obtained from Eq. (4.20) by associating δA_- to $\delta A_x^3 + \delta A_y^2$ in this case. The equations (4.24) and (4.25) are of the Lamé-type [123]: Since the squared background field appearing in Eqns. (4.24) and (4.25) has periodicity $\Delta t_B/2$, each solution can be written as a linear combination of the form

$$\delta A_{\pm}(t + \Delta t_B/2, p_z) = e^{iC_{\pm}(p_z)t} \delta A_{\pm}(t, p_z), \quad (4.26)$$

such that

$$\delta A_{\pm}(t, p_z) = e^{2iC_{\pm}(p_z)t/\Delta t_B} \Pi_{\pm}(t, p_z), \quad (4.27)$$

with periodic functions $\Pi_{\pm}(t + \Delta t_B/2, p_z) = \Pi_{\pm}(t, p_z)$. The Floquet indices $C_{\pm}(p_z)$ are time-independent and lead to oscillating behavior if $C_{\pm}(p_z)$ is purely real or to exponentially growing or decaying solutions if $C_{\pm}(p_z)$ has a non-zero imaginary part. The dominant exponentially growing solutions arise for δA_- modes because of the appearance of the time-dependent negative eigenvalues $\omega_3^2(p_z) = \omega_4^2(p_z)$ and we will concentrate on them in the following.

Before we discuss the approximate solution to the evolution equation (4.25), it is instructive to consider first the situation, where we neglect the time dependence of the background field by replacing $\mathcal{A}(t) \rightarrow \sqrt{B(t=0)/g}$. In this case one recovers the well-known Nielsen-Olesen result for the growth rate of modes with $p_z^2 \leq gB(t=0)$:

$$\gamma_{\text{NO}}(p_z) = \sqrt{gB(t=0) - p_z^2}. \quad (4.28)$$

This is in accordance with the fact that the value for the maximum growth rate for constant fields, as stated in Eq. (4.3), is obtained for vanishing momenta. In contrast, since the background field is oscillatory in our case there will be deviations from the Nielsen-Olesen result in Eq. (4.28). However, it turns out that to rather good accuracy the growth rates follow the Nielsen-Olesen estimate if the temporal average of the oscillating magnetic background field is used in Eq. (4.28). The time average over one period $\Delta t_B/2$ of the square of the time-dependent background field in Eq. (4.15), which enters the evolution equation (4.25) for the fluctuations $\delta A_-(t, p_z)$, is given by

$$g\bar{B} \equiv \frac{gB(t=0)}{2K(1/2)} \int_0^{2K(1/2)} dx \operatorname{cn}^2\left(x, \frac{1}{2}\right) = \underbrace{\frac{\Gamma(3/4)^2}{\Gamma(5/4)\Gamma(1/4)}}_{\approx 0.457} gB(t=0). \quad (4.29)$$

Replacing $gB(t=0)$ in Eq. (4.28) by the average value in Eq. (4.29) indeed reproduces the full numerical results in the linear instability regime to good accuracy.

Before we discuss our numerical results, we will now turn back to Eq. (4.25) and consider

a different approximation, which maps the evolution equation onto the Jacobian form of the Lamé equation. By use of the solution of the background field in Eq. (4.15), the evolution equation for $\delta A_-(t, p_z)$ takes the form

$$\left[\partial_t^2 + p_z^2 - gB \operatorname{cn}^2 \left(\sqrt{gB} t, \frac{1}{2} \right) \right] \delta A_-(t, p_z) = 0, \quad (4.30)$$

which closely resembles the Jacobian form of the Lamé equation. The crucial difference here is the negative sign in front of the oscillating term, which gives rise to the Nielsen-Olesen type instability discussed above. Our strategy for solving the above evolution equation consists of approximating

$$\operatorname{cn}^2(x, m) = 1 - \operatorname{cn}^2(x - K(m), m) + \mathcal{O}(m^2), \quad (4.31)$$

for $m = 1/2$ as in Eq. (4.30), in order to reduce it to the well-known Lamé equation. While this approximation captures all qualitative features of Eq. (4.30), it has the shortcoming that the average field strength $g\bar{B}$ according to Eq. (4.29) is overestimated by a factor of

$$\frac{g\bar{B}}{g\bar{B}_{\text{app}}} = \frac{c}{1-c} \approx 0.841, \quad c = \frac{\Gamma(3/4)^2}{\Gamma(5/4)\Gamma(1/4)} \simeq 0.457. \quad (4.32)$$

Consequently, we expect the approximation to yield slightly enhanced growth rates which extend to somewhat higher momenta.¹

In order to obtain the solutions for $\delta A_-(t, p)$ within the above approximation, we follow similar steps as in Ref. [124] and recast the evolution equation to the Weierstrass form by use of the identity [120, 123, 124]

$$\operatorname{cn}^2 \left(x, \frac{1}{2} \right) = -2 \wp \left(x + iK \left(\frac{1}{2} \right) \right), \quad (4.33)$$

where $\wp(x)$ is the Weierstrass elliptic function with roots $e_1 = 1/2$, $e_2 = 0$ and $e_3 = -1/2$. The evolution equation in Weierstrass form then reads

$$\left[\partial_t^2 + p_z^2 - gB - 2gB \wp \left(\sqrt{gB} t - \tau \right) \right] \delta A_-(t, p_z) = 0, \quad (4.34)$$

where $\tau = (1-i)K(1/2)$. By introducing the dimensionless time variable $\theta = \sqrt{gB} t$ and expressing the time independent contribution in Eq. (4.34) in terms of the Weierstrass elliptic

¹Note that one can account for this shortcoming by simply rescaling the field amplitude by the factor in Eq. (4.32).

function according to

$$\wp(z) = 1 - \frac{p_z^2}{gB}, \quad (4.35)$$

where $z = z(p_z)$ contains the momentum dependence, the two independent fundamental solutions $U_{p_z}^1(\theta)$ and $U_{p_z}^2(\theta)$ to Eq. (4.34) read [123]

$$U_{p_z}^{1/2}(\theta) = e^{\mp(\theta-\tau)\zeta(z)} \frac{\sigma(\theta - \tau \pm z)}{\sigma(\theta - \tau)}, \quad (4.36)$$

where the functions $\sigma(x)$ and $\zeta(x)$ represent the corresponding Weierstrass functions and the momentum dependence of the solutions is encoded in z defined by Eq. (4.35). In order to obtain the growth rate $\gamma(p)$ and the oscillation frequency $\omega(p)$ we perform a Floquet analysis of the fundamental solutions according to

$$U_{p_z}^{1/2}(\theta + 2K(1/2)) = e^{iC_-^{1/2}(p_z)} U_{p_z}^{1/2}(\theta), \quad (4.37)$$

with the Floquet index $C_-^{1/2}(p_z)$ as introduced above. Using the quasi periodicity of the Weierstrass σ -function [120, 124]

$$\sigma(x + 2K(1/2)) = -\sigma(x) \exp[2(x + K(1/2))\zeta(K(1/2))], \quad (4.38)$$

one finds

$$C_-^{1/2}(p_z) = \pm 2i [K(1/2)\zeta(z) - z \zeta(K(1/2))]. \quad (4.39)$$

The growth rate $\gamma(p_z)$ and the oscillation frequency $\omega(p_z)$ are then related to the real and imaginary parts of the Floquet index by²

$$\gamma(p_z) = \sqrt{gB} \frac{|\text{Im}[C_-(p_z)]|}{2K(1/2)}, \quad \omega(p_z) = \sqrt{gB} \frac{|\text{Re}[C_-(p_z)]|}{2K(1/2)}. \quad (4.40)$$

In order to evaluate the expressions in Eq. (4.40) we follow Ref. [124] to evaluate the mapping

²We note that in this way the oscillation frequency is only defined up to constants of $2\omega_B$.

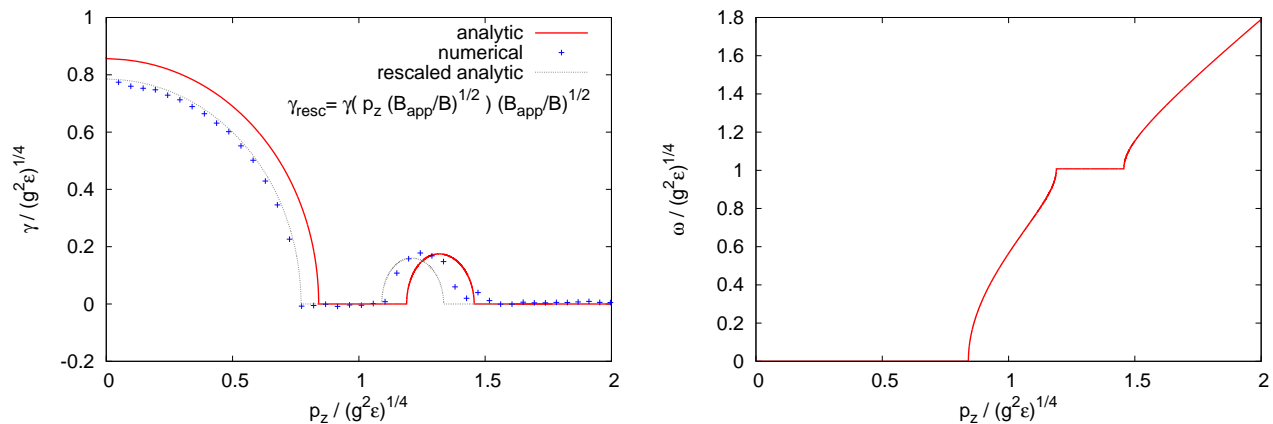


Figure 4.2: **(left)** Growth rates and **(right)** oscillation frequencies in the linear instability regime. The red lines correspond to the analytic result in Eq. (4.40). The growth-rates extracted from classical-statistical lattice simulations are shown as blue crosses.

of z in Eq. (4.35). We find that there are four different regimes described by

$$z = \beta_1(p_z) \quad \text{for} \quad \frac{p_z^2}{gB} < \frac{1}{2}, \quad (4.41)$$

$$z = i\beta_2(p_z) + K(1/2) \quad \text{for} \quad \frac{1}{2} < \frac{p_z^2}{gB} < 1, \quad (4.42)$$

$$z = \beta_3(p_z) + iK(1/2) \quad \text{for} \quad 1 < \frac{p_z^2}{gB} < \frac{3}{2}, \quad (4.43)$$

$$z = i\beta_4(p_z) \quad \text{for} \quad \frac{p_z^2}{gB} > \frac{3}{2}, \quad (4.44)$$

where $\beta_i \in [0, K(1/2)]$ for all four regimes. The different regimes correspond to two stable and two unstable bands: The lowest band $p_z^2 < gB/2$ corresponds to the Nielsen-Olesen instability, whereas the third band $gB < p_z^2 < 3gB/2$ corresponds to a parametric resonance instability [124]. Outside these momentum regions all modes are stable.

The corresponding growth rates and oscillation frequencies for all bands are shown in Fig. 4.2. The modes which are subject to the Nielsen-Olesen instability show no oscillatory behavior, whereas modes which are amplified by the parametric resonance instability follow the oscillation of the macroscopic field $\mathcal{A}(t)$. The stable band in between interpolates between the two oscillation frequencies, while at higher momenta $p_z^2 \gg gB$ the free field limit $\omega(p_z) = p_z$ is approached. Concerning the growth rates one observes that the Nielsen-Olesen instability exhibits the dominant growth rate when compared to the parametric resonance band. When comparing the analytic results for the growth rate to lattice simulations discussed below, we find that the analytic prediction is somewhat larger and extends to higher momenta. As mentioned above, this is a consequence of the approximation in Eq. (4.31). However, the lattice data can

be accurately described after a rescaling of the magnetic field amplitude B to reproduce the correct average amplitude \bar{B} in Eq. (4.32).

4.1.2 Classical-statistical lattice simulations

We now turn to the results of classical-statistical lattice simulations, which enable us to verify the robustness of the above approximations and study the dynamics of the instability also beyond the linear instability regime. We employ the initial conditions in Eq. (4.4) supplemented by a small noise to trigger the growth of non-equilibrium instabilities. In Fig. 4.3, we show the time evolution of the different gauge field components $|A_i^a(t, p_z, \vec{p}_T = 0)|^2$ for different longitudinal momenta $p_z = 0$, $p_z = 0.48 (g^2\epsilon)^{1/4}$ and $p_z = 1.2 (g^2\epsilon)^{1/4}$ in each panel.³ Already at first sight, one observes the emergence of different dynamical regimes, as a characteristic feature of the non-equilibrium dynamics of instabilities in many different systems [42, 52, 53]:

Starting at very early times, the homogeneous background field is contained in the A_x^2 and A_y^3 components, which initially have a large amplitude that oscillates in time. The growth of primary instabilities is clearly seen in the components A_x^2 , A_x^3 , A_y^2 and A_y^3 , which show the fastest growth of primary instabilities at early times. One also observes that for the A_x^3 and A_y^2 components modes with vanishing longitudinal momentum $p_z = 0$ exhibit the fastest growth rates without showing any oscillatory behavior. This is a clear manifestation of the Nielsen-Olesen type instability. The presence of the subleading parametric resonance instability can also be observed from Fig. 4.3. For instance, the A_y^2 mode with momentum $p_z = 1.2 (g^2\epsilon)^{1/4}$ shows a slow exponential growth with characteristic oscillations that match the behavior of the background field. This is precisely the signature of the second resonance band discussed in Sec. 4.1.1.

At later times one observes significant deviations from the linear instability regime and a large range of modes becomes unstable throughout all gauge field components. Though there is a delayed set-in of the instability for these modes, the modes are able to catch-up due to the substantial speed-up encountered in this regime. This behavior can be attributed to non-linear self-interactions of unstable gauge field modes and is a generic phenomenon of the non-equilibrium dynamics of self-interacting systems undergoing an instability [42, 52, 53]. Since this feature manifests itself in a similar way in scalar quantum field theories, we will discuss the dynamics of this non-linear regime in more detail in Sec. 4.2, by the example of a parametric resonance instability in expanding scalar theories.

Finally, the growth of instabilities saturates and the system encounters a much slower dy-

³Note that at early times $(g^2\epsilon)^{1/4} \simeq \sqrt{g\bar{B}}$, since the contributions of the fluctuations to the energy density are very small.

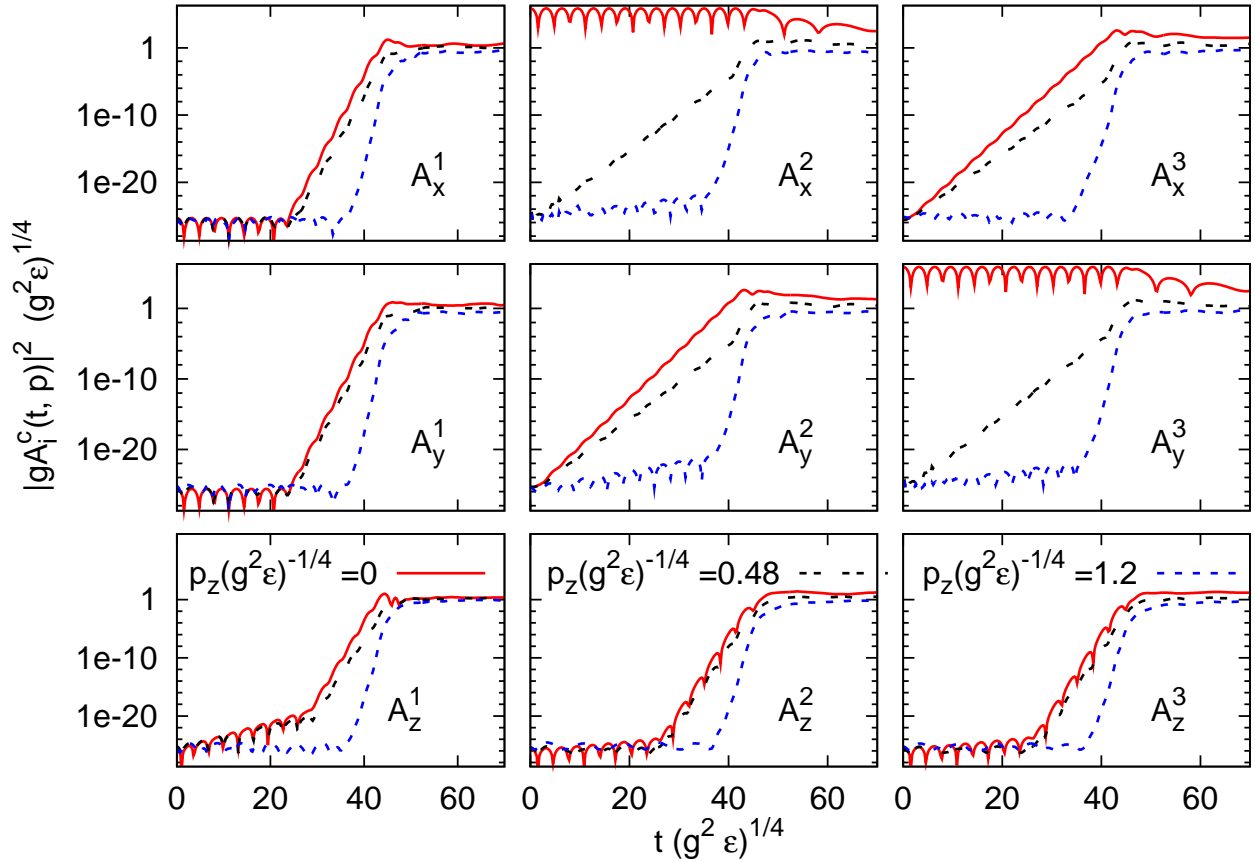


Figure 4.3: Time evolution of the individual gauge field components $A_i^a(t, p_z)$. Each panel shows the time evolution of three different Fourier coefficients whose momenta p_z are parallel to the z -axis.

namics. It is interesting to note, that in this regime also the amplitude of the background fields A_x^2 and A_y^3 decreases and becomes of the same order as the zero modes of the other gauge field components. The instability of the coherent gauge-field configurations therefore leads to a decay into a large number of incoherent particle-like excitations which start to dominate the energy density of the system. Accordingly, the ensuing state shares characteristic properties, with the over-populated initial conditions discussed in Chapter 3 and one can identify plasma instabilities as a mechanism to generate over-occupation.

4.2 Parametric resonance in expanding scalar field theories

In this section we leave the Yang-Mills sector and study the non-equilibrium dynamics of instabilities in anisotropically expanding systems by the example of parametric resonance in a real valued N -component scalar field theory. In addition to a transparent discussion of the effects of the longitudinal expansion in Sec. 4.2.1, we will analyze the emergence of different dynamical regimes due to the non-linear self-interaction of unstable modes in Sec. 4.2.2 and compare our findings to classical-statistical lattice simulations in Sec. 4.2.3.

We consider a theory with quartic interaction defined by the classical action

$$S[\varphi] = \int d^4x \sqrt{-g(x)} \left[\frac{g^{\mu\nu}(x)}{2} \partial_\mu \varphi_a \partial_\nu \varphi_a - \frac{m^2}{2} \varphi_a \varphi_a - \frac{\lambda(\varphi_a \varphi_a)^2}{4!N} \right], \quad (4.45)$$

with the self-coupling λ for $a = 1, \dots, N$ component fields $\varphi_a(x)$. To implement the longitudinal expansion, we consider boost invariant initial conditions along the longitudinal direction and employ the co-moving space time variables $x^\mu = (\tau, x^1, x^2, \eta)$ to describe the evolution. In accordance with the discussion in Sec. 2.3, the covariant metric tensor in (τ, η) coordinates is given by $g_{\mu\nu}(x) = \text{diag}(1, -1, -1, -\tau^2)$, whereas the contravariant metric tensor follows as $g^{\mu\nu}(x) = \text{diag}(1, -1, -1, -1/\tau^2)$ and the metric determinant is $g(x) = \det g_{\mu\nu}(x) = -\tau^2$.

We are interested in the time evolution of the corresponding quantum field theory for a given density matrix $\rho_D(\tau_0)$ specified at initial (proper) time τ_0 . The expectation values of Heisenberg field operators $\hat{\phi}_a(\tau, x_T, \eta)$ are then given by

$$\langle \hat{\phi}(\tau, x_T, \eta) \rangle \equiv \text{tr}[\rho_D(\tau_0) \hat{\phi}(\tau, x_T, \eta)] \quad (4.46)$$

and equivalently for products of field operators, which determine the correlation functions. We will consider the time-evolution in the forward light-cone ($\tau_0 > 0$) for spatially homogeneous expectation values.⁴ We employ Gaussian initial conditions, which can be conveniently formulated in terms of the macroscopic field

$$\phi_a(\tau) = \langle \hat{\phi}_a(\tau, x_T, \eta) \rangle \quad (4.47)$$

⁴By spatially homogeneous we mean homogeneous in the transverse plane and homogeneous in longitudinal rapidity at given proper time.

as well as the statistical two-point correlation function

$$F_{ab}(\tau, \tau', x_T - x'_T, \eta - \eta') = \frac{1}{2} \left\langle \left\{ \hat{\phi}_a(\tau, x_T, \eta), \hat{\phi}_b(\tau', x'_T, \eta') \right\} \right\rangle - \phi_a(\tau) \phi_b(\tau') \quad (4.48)$$

and their derivatives at initial (proper) time τ_0 . By use of the $O(N)$ symmetry in the field components, we can always take the homogeneous background field to point in the $a = 1$ direction, and we will denote

$$\phi_a(\tau) = \phi(\tau) \delta_{a1}. \quad (4.49)$$

We consider the statistical fluctuations to be diagonal in the field components, such that we can always decompose $F_{ab} = \text{diag}(F_{\parallel}, F_{\perp}, \dots, F_{\perp})$, where the subscripts longitudinal and transverse indicate the orientation with respect to the homogeneous background field.

To study the dynamics of the parametric resonance instability, we consider a weakly coupled theory ($\lambda \ll 1$) with a parametrically large background field

$$\phi(\tau_0) = \sqrt{\frac{6N}{\lambda}} \sigma_0, \quad \partial_{\tau} \phi(\tau)|_{\tau=\tau_0} = -\frac{1}{3\tau_0} \phi(\tau_0), \quad (4.50)$$

and small statistical fluctuations

$$\begin{aligned} F(\tau, \tau', p_T, \nu)|_{\tau=\tau'=\tau_0} &= \frac{\sigma_0}{2\tilde{\omega}_p} e^{-\tilde{\omega}_p/\sigma_0}, \\ \partial_{\tau} F(\tau, \tau', p_T, \nu)|_{\tau=\tau'=\tau_0} &= -\frac{F(\tau_0, \tau_0, p_T, \nu)}{3\tau_0}, \\ \partial_{\tau} \partial_{\tau'} F(\theta, \theta', p_T, \nu)|_{\tau=\tau'=\tau_0} &= \frac{F(\tau_0, \tau_0, p_T, \nu)}{9\tau_0^2} + \frac{\tilde{\omega}_p \sigma_0}{2} e^{-\tilde{\omega}_p/\sigma_0}, \end{aligned} \quad (4.51)$$

where we employ $\tilde{\omega}_p^{\perp} = \sqrt{p_T^2 + \nu^2/\tau_0^2 + \sigma_0^2}$ for transverse modes and $\tilde{\omega}_p^{\parallel} = \sqrt{p_T^2 + \nu^2/\tau_0^2 + 3\sigma_0^2}$ for longitudinal modes. The derivatives in Eqns. (4.50) and (4.51) are chosen to mimic an initial free-streaming behavior and σ_0 denotes the rescaled initial field amplitude. We will employ the typical set of parameters $m^2 = 0$, $\sigma_0 \tau_0 = 5$, $N = 4$ and $\lambda = 10^{-4}$ for our estimates and numerical simulations presented in this section, such that the spectral shape of the statistical fluctuations in Eq. (4.51) will be of little relevance since the magnitude is very small compared to the initial macroscopic field squared.

4.2.1 Linear instability regime and generalized conformal time

Since the initial background field ϕ is large and statistical fluctuations F are initially small, it is sufficient to consider the linearized evolution equations for the small fluctuations at the initial stage of the evolution. Since the classical theory and the quantum theory agree to this (mean-

field) order [40, 41], the quantum evolution at sufficiently early times is accurately described by the classical equations of motion for the background field and the linearized equations of motion for small fluctuations around the field expectation value.⁵

Dynamics of the background field

In this linear instability regime the evolution equation for the macroscopic field follows directly from the stationarity of the classical action in Eq. (4.45) and takes the form of the equation of motion of a damped anharmonic oscillator

$$\left[\partial_\tau^2 + \frac{1}{\tau} \partial_\tau + m^2 + \frac{\lambda}{6N} \phi^2(\tau) \right] \phi(\tau) = 0. \quad (4.52)$$

The damping term characterized by a first-order time derivative arises due to the longitudinal expansion and represents the dilution of the system. In order to solve Eq. (4.52) analytically, we perform a change in the time variable as well as a rescaling of the fields by introducing the variables

$$\sigma_0 d\tau = \left(\frac{a(\tau)}{a(\tau_0)} \right)^{1/3} d\theta, \quad \tilde{\phi} = \left(\frac{a(\tau)}{a(\tau_0)} \right)^{1/3} \frac{\phi}{\sigma_0} \quad (4.53)$$

with the generalized scale factor $a(\tau) = \tau$ in the case of a one-dimensional Bjorken expansion. This can be seen as a generalization of the concept of conformal time to anisotropically expanding systems. For the one-dimensional expansion the scale factor $a(\tau)$ enters the above definition of conformal time with exponent $1/3$, whereas in the isotropically expanding case one would use $d/3$ for d spatial dimensions instead [125]. The new dimensionless time-variable θ is explicitly given by

$$\theta(\tau) - \theta_0 = \frac{3}{2} \sigma_0 \tau_0 \left[\left(\frac{\tau}{\tau_0} \right)^{2/3} - 1 \right], \quad (4.54)$$

and we will refer to it as 'conformal time' in analogy to the isotropic case. The evolution equation of the macroscopic field in terms of the new variables reads

$$\left[\partial_\theta^2 + \tilde{m}^2(\theta) + \frac{\lambda}{6N} \tilde{\phi}^2(\theta) \right] \tilde{\phi}(\theta) = 0, \quad (4.55)$$

where we introduced the time-dependent effective 'mass term'

$$\tilde{m}^2(\theta) = \frac{m^2}{\sigma_0^2} \left(\frac{a(\theta)}{a(\theta_0)} \right)^{2/3} + \frac{2}{9} \left(\frac{a'(\theta)}{a(\theta)} \right)^2 - \frac{1}{3} \frac{a''(\theta)}{a(\theta)}. \quad (4.56)$$

⁵The direct verification of this statement will be provided in Sec. 4.2.2, where we discuss the non-linear evolution and the impact of quantum fluctuations.

Here primes denote derivatives with respect to θ , which are explicitly given by

$$\frac{a(\theta)}{a(\theta_0)} = \left(\frac{2\theta}{3\sigma_0\tau_0} \right)^{3/2}, \quad \frac{a'(\theta)}{a(\theta_0)} = \frac{1}{\sigma_0\tau_0} \left(\frac{2\theta}{3\sigma_0\tau_0} \right)^{1/2}, \quad \frac{a''(\theta)}{a(\theta_0)} = \frac{1}{3(\sigma_0\tau_0)^2} \left(\frac{2\theta}{3\sigma_0\tau_0} \right)^{-1/2}, \quad (4.57)$$

where we chose $\theta_0 = 3\sigma_0\tau_0/2$ to cancel the term on the right hand side of Eq. (4.54).

For massless scalar fields ($m^2 = 0$), the above evolution equation can be solved approximately in the limit of large initial field amplitudes $\sigma_0\tau_0 \gg 1$. According to Eq. (4.56) one then finds $\tilde{m}^2(\theta) = 1/(4\theta^2)$, which is small compared to the macroscopic field such that $\tilde{m}^2(\theta) \simeq 0$ gives an accurate description of the dynamics in this case. The evolution equation (4.55) in terms of the new variables then becomes that of an anharmonic oscillator

$$\left[\partial_\theta^2 + \frac{\lambda}{6N} \tilde{\phi}^2(\theta) \right] \tilde{\phi}(\theta) = 0, \quad (4.58)$$

and the solution is given in terms of Jacobi elliptic functions

$$\tilde{\phi}(\theta) = \sqrt{\frac{6N}{\lambda}} \operatorname{cn} \left(\theta - \theta_0; \frac{1}{2} \right), \quad (4.59)$$

for the considered initial conditions specified in Eq. (4.50). The Jacobi cosine, $\operatorname{cn}(\theta; \alpha)$, is a doubly periodic function in θ with periods $4K(\alpha)$ and $4iK(1-\alpha)$, where $K(\alpha)$ is the complete elliptic integral of the first kind [120], and the macroscopic field $\tilde{\phi}$ displays oscillations with constant period in conformal time. For the physical interpretation of this result it is insightful to express the approximate solution in Eq. (4.59) in terms of the original time and field variables according to

$$\phi(\tau) = \sigma_0 \sqrt{\frac{6N}{\lambda}} \left(\frac{\tau_0}{\tau} \right)^{1/3} \operatorname{cn} \left(\frac{3\sigma_0\tau_0}{2} \left[\left(\frac{\tau}{\tau_0} \right)^{2/3} - 1 \right]; \frac{1}{2} \right), \quad (4.60)$$

such that the macroscopic field $\phi(\tau)$ decays as $\tau^{-1/3}$, while it displays oscillatory behavior with a constant period in conformal time $\theta \propto \tau^{2/3}$. This is a direct consequence of the dilution of the system due to the longitudinal expansion. In Fig. 4.4 the analytic approximation in Eq. (4.60) is compared to the full numerical solution of Eq. (4.52) without further approximations. The excellent agreement verifies that the terms neglected in Eq. (4.58) are indeed irrelevant for this choice of parameters.

Parametric resonance instability

Equipped with an analytic solution of the background field dynamics, we can now study the dynamics of the statistical fluctuations around the macroscopic field. As outlined above, their dynamics is initially described by the linearized classical evolution equations, as long as statisti-

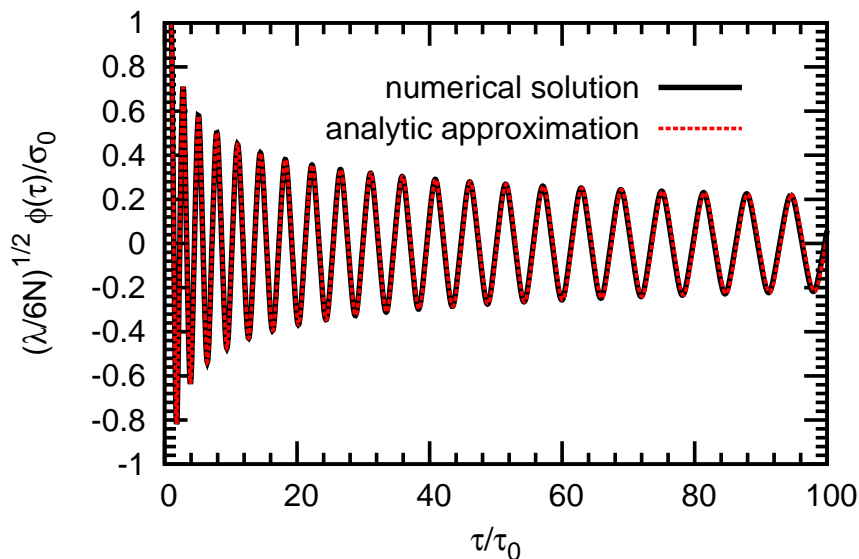


Figure 4.4: Solution to the linearized field equation (4.52) for $\sigma_0\tau_0 = 5$. The approximate analytic solution in Eq. (4.60) given by the dashed curve is practically on top of the full numerical one (solid curve). As a consequence of the longitudinal expansion, the field shows oscillations with constant period in $\tau^{2/3}$ while the amplitude of the oscillations decreases as $\tau^{-1/3}$.

cal fluctuations remain sufficiently small. The linearized equations of motion for the statistical fluctuations can be obtained by expanding the classical field equations to first order in the deviations $\delta\phi(x)$ from the homogeneous background field $\phi(\tau)$. The small fluctuations $\delta\phi(x)$ are related to the statistical two-correlation function by $F_{ab}^{cl}(\tau, \tau', \vec{x}_T - \vec{x}'_T, \eta - \eta') = \langle \delta\phi_a(x) \delta\phi_b(x') \rangle_{cl}$ in the classical-statistical field theory. Since we consider spatially homogeneous systems, it is convenient to work in Fourier space with respect to spatial coordinates, where we define the dimensionless quantity

$$F_{ab}(\tau, \tau', \vec{p}_T, \nu) = \int d^2\vec{x}_T d\eta F_{ab}(\tau, \tau', \vec{x}_T, \eta) e^{-i(\vec{p}_T \vec{x}_T + \nu\eta)}. \quad (4.61)$$

The linearized equations of motion for the statistical fluctuations then take the form

$$\begin{aligned} \left[\partial_\tau^2 + \frac{1}{\tau} \partial_\tau + p_T^2 + \frac{\nu^2}{\tau^2} + m^2 + \frac{\lambda}{6N} \phi^2(\tau) \right] F_\perp(\tau, \tau', p_T, \nu) &= 0, \\ \left[\partial_\tau^2 + \frac{1}{\tau} \partial_\tau + p_T^2 + \frac{\nu^2}{\tau^2} + m^2 + \frac{\lambda}{2N} \phi^2(\tau) \right] F_\parallel(\tau, \tau', p_T, \nu) &= 0, \end{aligned} \quad (4.62)$$

and we will verify explicitly in Sec. 4.2.2, that the linearized classical equations of motion correspond to the quantum evolution equations in the limit where all non-linear or loop corrections can be neglected.

The dynamics of the linearized evolution equations (4.62) already exhibit a rich structure due to the different scales involved in the problem. In addition to the damping term, which is characterized by the first-order time derivative and appears due to the longitudinal expansion, the other competing scales that depend differently on (proper) time τ are related to

- the macroscopic field squared $\phi^2(\tau) \sim \tau^{-2/3}$,
- the longitudinal momentum squared ν^2/τ^2 and
- the transverse 'mass' squared $m^2 + p_T^2$ which is independent of proper-time.

Hence, the interplay between the dilution and the red-shift of longitudinal momenta due to the anisotropic expansion alter the dynamics of the parametric resonance instability and induce a variety of interesting phenomena, which we will now investigate in more detail.

In order to obtain an analytic description for the time evolution of the fluctuations, we introduce conformal time variables for the statistical fluctuations according to

$$\tilde{F}(\theta, \theta', p_T, \nu) = \left(\frac{\tau(\theta)}{\tau_0} \right)^{1/3} \left(\frac{\tau'(\theta')}{\tau_0} \right)^{1/3} F(\tau, \tau', p_T, \nu). \quad (4.63)$$

Inserting the solution for the background field in Eq. (4.59), the linearized evolution equations using conformal time variables take the form

$$\begin{aligned} \left[\partial_\theta^2 + \tilde{p}^2(\theta) + \tilde{m}^2(\theta) + \text{cn}^2 \left(\theta - \theta_0; \frac{1}{2} \right) \right] \tilde{F}_\perp(\theta, \theta', p_T, \nu) &= 0, \\ \left[\partial_\theta^2 + \tilde{p}^2(\theta) + \tilde{m}^2(\theta) + 3 \text{cn}^2 \left(\theta - \theta_0; \frac{1}{2} \right) \right] \tilde{F}_\parallel(\theta, \theta', p_T, \nu) &= 0, \end{aligned} \quad (4.64)$$

and we will restrict ourselves again to the massless case, $m^2 = 0$, and approximate $\tilde{m}^2(\theta) \simeq 0$ as in Eq. (4.58) in the following. With this approximation Eq. (4.64) resembles the Jacobian form of the Lamé equation. However, a crucial difference is the explicit θ -time dependence of the (dimensionless) momentum term

$$\tilde{p}^2(\theta) \equiv \frac{2\theta}{3\sigma_0\tau_0} \frac{p_T^2}{\sigma_0^2} + \frac{9}{4} \frac{\nu^2}{\theta^2}. \quad (4.65)$$

It is thus instructive to consider first the case, where \tilde{p}^2 was not depending on θ -time. In this situation Eq. (4.64) corresponds to Lamé equations, whose analytic solutions have been discussed in Sec. 4.1.1. The dynamics is then dominated by the transverse (\tilde{F}_\perp) modes which

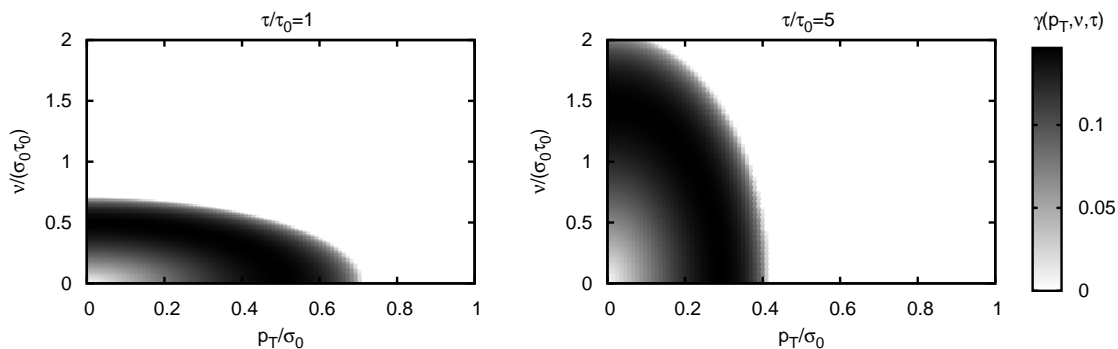


Figure 4.5: Time-dependent (dimensionless) growth rate $\gamma(p_T, \nu, \theta)$ in the transverse momentum p_T and rapidity wave number ν plane for different times. The (**left**) panel corresponds to $\tau/\tau_0 = 1$, the (**right**) panel shows $\tau/\tau_0 = 5$. The instability develops from the high p_T small ν region to the high ν small p_T region.

exhibit exponential growth in time for a resonance band of momenta

$$0 \leq \tilde{p}^2 \leq \frac{1}{2}. \quad (4.66)$$

The (dimensionless) momentum-dependent growth rate $\gamma(\tilde{p})$ is to good approximation given by

$$\gamma(\tilde{p}) \simeq \frac{4\pi e^{-\pi}}{K(1/2)} \sqrt{2\tilde{p}^2(1-2\tilde{p}^2)}, \quad (4.67)$$

which exhibits the maximum growth rate

$$\gamma_0 \simeq \frac{2\pi e^{-\pi}}{K(1/2)} \simeq 0.15, \quad \text{for} \quad \tilde{p}_0^2 \simeq \frac{1}{4}. \quad (4.68)$$

The exact analytic expressions involving Weierstrass elliptic functions are the same as in Sec. 4.1.1 and the approximation entering Eq. (4.67) is discussed in detail in Refs. [115, 124].

In the case of an anisotropically expanding system as described by Eq. (4.64), the situation is somewhat more involved due to the explicit θ -time dependence of the momentum term in Eq. (4.65). In order to extend the previous discussion to the expanding system described by Eq. (4.64), it is therefore instructive to assume that the momentum term in Eq. (4.65) varies only slowly on the characteristic time scale of one oscillation of the macroscopic field. By expanding the time dependent momentum term as $\tilde{p}^2(\theta + T_\theta) \simeq \tilde{p}^2(\theta) + \partial_\theta \tilde{p}^2(\theta) T_\theta$, where $T_\theta = 4K(1/2)$ corresponds to one period of oscillation of the macroscopic field, we find that formally this 'quasi-static' approximation corresponds to the limit $4K(1/2)|\partial_\theta \tilde{p}^2(\theta)| \ll \tilde{p}^2(\theta)$. However, for resonant modes, where the characteristic momenta are parametrically given by

$p_T \sim \sigma_0$ and $\nu \sim \sigma_0 \tau_0$, it is straightforward to verify that the above condition is approximately fulfilled whenever $\sigma_0 \tau_0 \gtrsim 4 K(1/2)$, which can easily be achieved by choice of parameters. Within this approximation the resonance band and growth rates for the expanding system can be obtained from Eqns. (4.66) and (4.67) by replacing $\tilde{p}^2 \rightarrow \tilde{p}^2(\theta)$ as given in Eq. (4.65). The time-dependence of the growth rate in this approximation then enters only through the explicit time-dependence of $\tilde{p}^2(\theta)$ and is a consequence of both the red-shift of longitudinal momenta and the dilution of the system.

The growth rate in Eq. (4.67) with time-dependent momentum terms as in Eq. (4.65) is shown in Fig. 4.5 as a function of transverse momentum p_T and longitudinal wave number ν for different times. One observes that the instability develops from the high p_T and small ν region at early times to the high ν and small p_T region at later times. We will now discuss the different phenomena that appear due to this shift of the resonance band within the 'quasi-static' approach and show that these analytic results compare well to full numerical solutions of Eq. (4.64).

The explicit θ -time dependence of the approximate resonance band criterion leads to new phenomena that are not present in the non-expanding case. In particular, a mode with fixed transverse momentum p_T and fixed ν may satisfy the resonance condition in Eq. (4.66) for a certain time window $\tau_{\text{Start}} < \tau < \tau_{\text{End}}$, while the condition may not be met outside this window. This means that modes can shift inside the resonance band, exhibit exponential growth for a certain time and then shift back out of the resonance band again so that the exponential growth stops at later times of the evolution. In particular, if $\tau_{\text{Start}} > \tau_0$ for a certain mode, this mode will exhibit a delay in the onset-time of growth. For instance, if we restrict to the case of vanishing transverse momentum, the condition in Eq. (4.66) yields the onset of exponential growth at times

$$\left(\frac{\tau_{\text{Start}}}{\tau_0} \right)^{2/3} = \frac{\sqrt{2\nu^2}}{\sigma_0 \tau_0} \quad \text{for} \quad p_T = 0, \quad (4.69)$$

and the subsequent growth continues as long as the linearized description remains valid. However, by investigating the entire momentum space one finds that there are modes which behave quite differently. For instance, modes with vanishing longitudinal momentum exhibit a resonant amplification only until the time

$$\left(\frac{\tau_{\text{End}}}{\tau_0} \right)^{2/3} = \frac{\sigma_0^2}{2p_T^2} \quad \text{for} \quad \nu = 0. \quad (4.70)$$

After the time τ_{End} these modes freeze out, such that the exponential growth stops and they

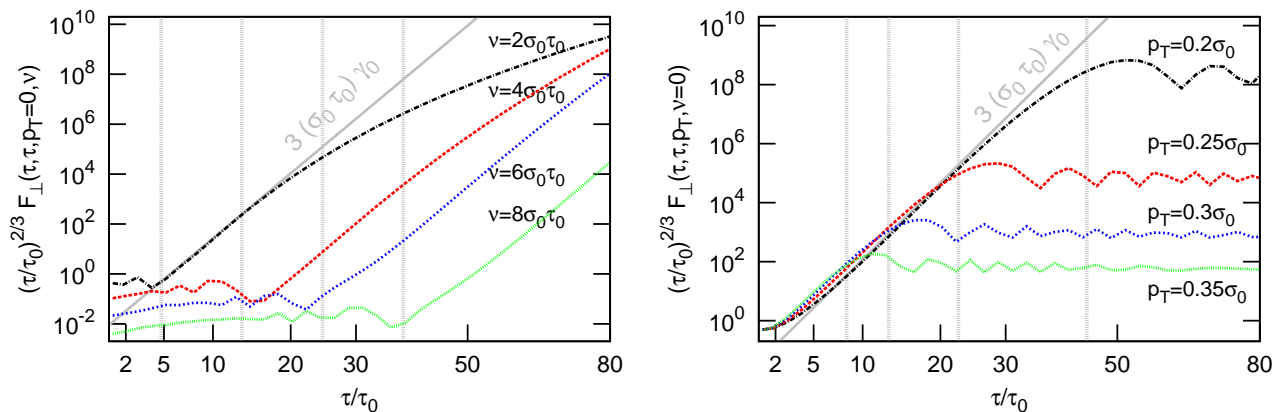


Figure 4.6: **(left)** Time evolution of the equal-time transverse fluctuations $F_{\perp}(\tau, \tau, p_T, \nu)$ from the linearized evolution equations for $p_T = 0$ and different rapidity wave numbers ν . The modes are averaged over one period of oscillation of the macroscopic field. The time axis is scaled as $(\tau/\tau_0)^{2/3}$. The vertical dashed grey lines represent the set-in time of the instability according to Eq. (4.69). The full grey line corresponds to the maximum growth rate $3\sigma_0\tau_0\gamma_0$. **(right)** Same for modes with $\nu = 0$ and different transverse momenta p_T . The vertical grey dashed lines correspond to the estimates for the freeze-out times of the instability according to Eq. (4.70).

exhibit a stable oscillatory behavior until the time when non-linear interactions between unstable modes become important. The generic situation, where neither longitudinal nor transverse momentum vanish, is discussed in detail in Appendix F and we will only present some characteristic results. By searching for real positive solutions for θ of the resonance criterion in Eq. (4.66), we find that these solutions exist for all modes satisfying the time-independent condition

$$\frac{p_T^4 \nu^2}{\sigma_0^6 \tau_0^2} \leq \frac{1}{54}. \quad (4.71)$$

Accordingly, all transverse modes (F_{\perp}) satisfying the condition (4.71) experience exponential amplification for a certain period of time. The set-in and freeze-out times for these modes correspond to times where the relation (4.66) is taken as an equality. Calling $\xi \equiv (54 p_T^4 \nu^2)/(\sigma_0^6 \tau_0^2)$ these times are given by

$$\begin{aligned} \left(\frac{\tau_{\text{Start}}}{\tau_0}\right)^{2/3} &= \frac{\sigma_0^2}{6p_T^2} \left[1 + 2 \sin \left(\frac{2}{3} \arctan \sqrt{\frac{\xi}{1-\xi}} - \frac{\pi}{6} \right) \right], \\ \left(\frac{\tau_{\text{End}}}{\tau_0}\right)^{2/3} &= \frac{\sigma_0^2}{6p_T^2} \left[1 + 2 \cos \left(\frac{2}{3} \arctan \sqrt{\frac{\xi}{1-\xi}} \right) \right], \end{aligned} \quad (4.72)$$

where $\xi \leq 1$ and, of course, $\tau_{\text{Start}} \leq \tau_{\text{End}}$ for unstable modes, which satisfy Eq. (4.71).

The phenomena of delayed set-in and freeze-out can clearly be observed in our numerical studies of the linearized evolution equations. In Fig. 4.6 we present the numerical solution of the linearized evolution equations for transverse modes $F_{\perp}(\tau, \tau, p_T, \nu)$ with different transverse and longitudinal momenta. From the right panel of Fig. 4.6 one observes that modes which are dominated by their transverse momentum exhibit an amplification at early times. However, this amplification stops once they shift out of the resonance band and we find that this behavior is indeed very well described by our analytic estimate in Eq. (4.70), indicated by the gray dashed lines. In contrast, modes which are dominated by their rapidity wave number ν , as shown in the left panel of Fig. 4.6, exhibit an amplification at later times, when they have shifted inside the resonance band. Here the set-in time of the instability is well described by Eq. (4.69) indicated by the gray dashed lines. In both cases, the modes exhibit an exponential growth in conformal time $\theta \propto \tau^{2/3}$ with a time-dependent growth-rate $\gamma(\tilde{p}(\theta)) \leq \gamma_0$ as discussed above.

Since the fluctuations exhibit an exponential growth due to the parametric resonance instability, they become large and the linear approximation underlying Eq. (4.64) breaks down once non-linear interactions of unstable modes become sizable. This gives rise to significant change of the instability dynamics, which we will now analyze in more detail.

4.2.2 Non-linear corrections and dynamical power counting

How to take into account non-linear corrections in scalar quantum field theories is well known and can be based efficiently on the two-particle irreducible (2PI) effective action [76, 77], which circumvents problems of secular time evolutions encountered in non-resummed (1PI) approximation schemes [42]. For the N -component scalar quantum field theory a non-perturbative description can be based on the $1/N$ -expansion of the 2PI effective action to next-to-leading order (NLO) [126, 127] and the evolution equations in general coordinates have been presented in Refs. [125, 128]. Here we discuss those aspects of the time evolution, which are relevant for an understanding of the non-linear amplification of instabilities. Non-linear corrections will lead to strongly enhanced 'secondary' growth rates, which are multiples of the initial 'primary' growth rates observed from the linear regime. Remarkably, this turns out to be very similar to the non-expanding case, which has been discussed extensively in the past for scalars [42, 53] as well as for non-abelian gauge theories [52].

Evolution equations

While the linear regime discussed above is entirely described in terms of the background field ϕ , defined in Eq. (4.47), and the statistical two-point function F as given by Eq. (4.48), an

important new ingredient going beyond the linear regime will be the appearance of the time-dependent spectral function

$$\rho_{ab}(\tau, \tau', x_T - x'_T, \eta - \eta') = i \left\langle \left[\hat{\phi}_a(\tau, x_T, \eta), \hat{\phi}_b(\tau', x'_T, \eta') \right] \right\rangle. \quad (4.73)$$

as an additional linearly independent correlation function in the evolution equations. Since the spectral function ρ is determined by the commutator $[\cdot, \cdot]$, it also encodes the equal-time field commutation relations of Heisenberg field operators, which in Fourier-space with respect to the transverse spatial coordinates and rapidity take the form

$$\begin{aligned} \rho_{ab}(\tau, \tau', p_T, \nu)|_{\tau=\tau'} &= 0, \\ \partial_\tau \rho_{ab}(\tau, \tau', p_T, \nu)|_{\tau=\tau'} &= \frac{\delta_{ab}}{\tau}, \\ \partial_\tau \partial_{\tau'} \rho_{ab}(\tau, \tau', p_T, \nu)|_{\tau=\tau'} &= 0. \end{aligned} \quad (4.74)$$

The τ -dependence of the commutator between the field and its conjugate momentum enters via the metric determinant $\sqrt{-g(x)} = \tau$ [125, 128]. Since the commutation relations in Eq. (4.74) are valid at all times, they also fix the initial conditions for the evolution of $\rho_{ab}(\tau, \tau', p_T, \nu)$ and by use of the $O(N)$ symmetry we can again write $\rho_{ab} = \text{diag}(\rho_{\parallel}, \rho_{\perp}, \dots, \rho_{\perp})$.

Going beyond the linear regime using, e.g., the 2PI $1/N$ -expansion to NLO the evolution equations for the background field ϕ , the statistical fluctuations $F_{\perp, \parallel}$ and the spectral functions $\rho_{\perp, \parallel}$ form a closed set of coupled integro-differential equations. The linearized evolution equations in Eq. (4.62) are generalized to their non-linear form, which for the longitudinal fluctuations take the form

$$\begin{aligned} & \left[\partial_\tau^2 + \frac{1}{\tau} \partial_\tau + p_T^2 + \frac{\nu^2}{\tau^2} + M_{\parallel}^2(\tau) + \frac{\lambda}{2N} \phi^2(\tau) \right] F_{\parallel}(\tau, \tau', p_T, \nu) \\ &= - \int_{\tau_0}^{\tau} d\tau'' \tau'' \Sigma_{\parallel}^{\rho}(\tau, \tau'', p_T, \nu) F_{\parallel}(\tau'', \tau', p_T, \nu) \\ & \quad + \int_{\tau_0}^{\tau'} d\tau'' \tau'' \Sigma_{\parallel}^F(\tau, \tau'', p_T, \nu) \rho_{\parallel}(\tau'', \tau', p_T, \nu). \end{aligned} \quad (4.75)$$

Here the effective mass term $M_{\parallel}^2 = M_{\parallel}^2[F_{\perp, \parallel}]$ and the non-zero spectral and statistical parts of the self-energy $\Sigma_{\parallel}^{\rho, F} = \Sigma_{\parallel}^{\rho, F}[\rho_{\perp, \parallel}, F_{\perp, \parallel}, \phi]$ make the evolution equations non-linear in the fluctuations.⁶ The explicit linear τ'' -term in the integrand stems from the determinant of the metric tensor for the co-moving coordinates [125, 128]. The spectral functions obey a similar equation with the characteristic 'memory integrals' over time, which for the longitudinal

⁶The spectral part, Σ^{ρ} , can be related to the imaginary part and the statistical part, Σ^F , to the real part of the self-energy for the considered theory [42].

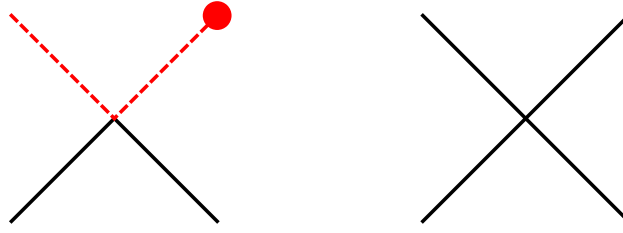


Figure 4.7: Vertices in the presence of a macroscopic field. Dashed (red) lines denote 'longitudinal' field components and solid (black) lines are associated to either longitudinal or 'transverse' components. The dot indicates a non-zero field expectation value.

components reads

$$\begin{aligned} & \left[\partial_\tau^2 + \frac{1}{\tau} \partial_\tau + p_T^2 + \frac{\nu^2}{\tau^2} + M_\parallel^2 + \frac{\lambda}{2N} \phi^2(\tau) \right] \rho_\parallel(\tau, \tau', p_T, \nu) \\ &= - \int_{\tau'}^\tau d\tau'' \tau'' \Sigma_\parallel^\rho(\tau, \tau'', p_T, \nu) \rho_\parallel(\tau'', \tau', p_T, \nu). \end{aligned} \quad (4.76)$$

The equivalent equations for the transverse components F_\perp and ρ_\perp can also be obtained from the corresponding linearized equations (4.62) by replacing m^2 with an effective mass term $M_\perp^2(F_{\perp,\parallel})$ and taking into account a non-zero right hand side. The latter is of the same form as in (4.75) and (4.76) with all longitudinal components replaced by transverse ones. At NLO in the 2PI $1/N$ expansion the remaining equation for the field ϕ can be written in the form

$$\begin{aligned} & \left[\partial_\tau^2 + \frac{1}{\tau} \partial_\tau + M_\parallel^2 + \frac{\lambda}{6N} \phi^2(\tau) \right] \phi(\tau) \\ &= - \int_{\tau_0}^\tau d\tau' \tau' \Sigma_\parallel^\rho(\tau, \tau', p_T = 0, \nu = 0)|_{\phi=0} \phi(\tau'), \end{aligned} \quad (4.77)$$

where the spectral part of the self-energy is evaluated for zero field, i.e. $\Sigma_\parallel^\rho(\rho_{\perp,\parallel}, F_{\perp,\parallel}, \phi = 0)$ [42, 53]. Of course, at even higher order in the $1/N$ expansion also terms that are non-linear in the field ϕ appear in Eq. (4.77) [126, 127].

Dynamical power counting

We will start by classifying the non-linear corrections to the evolution equations entering via the effective mass or self-energy terms $M_{\perp,\parallel}^2$, $\Sigma_{\perp,\parallel}^\rho$ and $\Sigma_{\perp,\parallel}^F$. In order to write down self-energies, it is important to note that in addition to the four-vertex proportional to λ there is an effective three-vertex due to the presence of the macroscopic field. This is visualized in the left panel of Fig. 4.7, where dashed (red) lines denote 'longitudinal' ($a = 1$) field components and solid (black) lines are associated to either longitudinal or 'transverse' ($a = 2, \dots, N$) components. A dot indicates a non-zero field expectation value $\phi(\tau)$ as in Eq. (4.49). A general non-linear

contribution to the evolution equations will then contain powers of λ , of the 'propagators' $F_{\perp,\parallel}$ and $\rho_{\perp,\parallel}$, and of the background field ϕ . Initially, the parametric dependence of the field is $\phi^2 \sim 1/\lambda$. Therefore, at not too late times a classification based on a small λ has to take this into account. Most importantly, taking $F_{\perp,\parallel}$ into account for the power counting is crucial, since F grows exponentially in time as a consequence of an instability. In contrast, the 'weight' of the spectral function $\rho_{\perp,\parallel}$ remains parametrically of order one at all times as is encoded in the equal-time commutation relations in Eq. (4.74) [53]. It is also important to note the fact that transverse fluctuations (F_{\perp}) exhibit the dominant growth in the linear regime. Consequently, contributions containing more transverse propagators (F_{\perp}) can become important earlier than those diagrams containing longitudinal propagators (F_{\parallel}) instead. For instance, an expression containing powers $\lambda^n F_{\perp}^m \phi^{2l}$ with integers n, m and l may be expected at not too late times to give sizable corrections to the linearized evolution equations once $F_{\perp} \sim 1/\lambda^{(n-l)/m}$ for typical momenta. Here n yields the suppression factor from the coupling constant, whereas m introduces the enhancement due to large fluctuations for typical momenta and l due to a large macroscopic field. The power counting can become more involved as time proceeds, and it is remarkable that one can indeed identify a sequence of characteristic time scales with corresponding growth rates.

Characteristic time scales and growth rates

To start with a simple example, we consider first one-loop 'tadpole' corrections, which are obtained by 'closing' two longitudinal or two transverse 'legs' of the four-vertex in Fig. 4.7 on the right. We emphasize already here that there are other corrections which will be of relevance before tadpoles come into play for not too large N . However, it will be convenient to express time scales in terms of the characteristic time when tadpoles become relevant, since this turns out to coincide with the time when an infinite series of self-energy corrections become sizable and all exponential growth of fluctuations stops. The tadpole corrections are mass-like and their contribution takes the form

$$\begin{aligned} M_{\perp}^2(\tau) &= m^2 + T_{\parallel}(\tau) + (N+1)T_{\perp}(\tau), \\ M_{\parallel}^2(\tau) &= m^2 + 3T_{\parallel}(\tau) + (N-1)T_{\perp}(\tau) \end{aligned} \quad (4.78)$$

for the non-linear evolution equation of the transverse (F_{\perp}) and the longitudinal fluctuations (F_{\parallel}), respectively. The one-loop tadpole integrals read

$$T_{\perp,\parallel}(\tau) = \frac{\lambda}{6N} \int^{\Lambda} \frac{d^2 p_T d\nu}{(2\pi)^3} F_{\perp,\parallel}(\tau, \tau, p_T, \nu), \quad (4.79)$$

where Λ denotes some suitable regularization that enters the renormalization procedure, which has not to be specified for the current purpose. While initially the tadpole contributions in Eq. (4.79) are suppressed by the coupling constant λ , they become sizable at later times once the fluctuations grow parametrically to $F_{\perp,\parallel}(\tau, \tau, p_T, \nu) \sim 1/\lambda$ for typical momenta p_T and ν . More precisely, for the massless case ($m^2 = 0$) the size of a tadpole contribution in Eq. (4.78) should be compared to that of the macroscopic field-squared term $\lambda\phi^2(\tau)/6N$ in Eq. (4.77), which on average is $\sigma_0^2/2 (\tau/\tau_0)^{-2/3}$ at early times. We will denote the time when both become of the same order of magnitude as τ_{nonpert} . Using that the tadpole will quickly be dominated by unstable modes entering the integral with characteristic primary growth-rate $\gamma(p_T, \nu, \theta) \leq \gamma_0$, such that

$$\left| \frac{F(\theta, \theta', p_T, \nu)}{F(\theta_0, \theta_0, p_T, \nu)} \right| \leq \exp[\gamma_0(\theta + \theta' - 2\theta_0)] , \quad (4.80)$$

one obtains the estimate

$$\tau_{\text{nonpert}} \gtrsim \tau_0 \left[1 + \frac{1}{3\sigma_0\tau_0\gamma_0} \ln \left(\frac{\sigma_0^2}{2(N+1)T_{\perp}(\tau_0)} \right) \right]^{3/2} . \quad (4.81)$$

Here we used the important fact that transverse fluctuations exhibit the dominant growth in the linearized evolution equations. It is noteworthy that τ_{nonpert} is rather sensitive to the inverse of the primary growth-rate, whereas the coupling constant and the size of the initial fluctuations only enter logarithmically through $T_{\perp}(\tau_0)$ according to Eq. (4.79). In the weak coupling limit Eq. (4.81) reduces to

$$\tau_{\text{nonpert}} \stackrel{(\lambda \ll 1)}{\gtrsim} \tau_0 \left[1 + \frac{1}{3\sigma_0\tau_0\gamma_0} \ln \left(\frac{1}{\lambda} \right) \right]^{3/2} , \quad (4.82)$$

at leading logarithmic accuracy. We emphasize again that when fluctuations have grown parametrically to $\mathcal{O}(1/\lambda)$ at τ_{nonpert} , it is not only a one-loop tadpole that becomes of order one. Since there is an infinite series of self-energy contributions including arbitrarily high loop-orders that become sizable, a non-perturbative approach such as the 2PI $1/N$ expansion or classical-statistical simulation methods have to be applied. Before addressing the non-perturbative regime within the classical-statistical framework in Sec. 4.2.3, we first consider earlier times than τ_{nonpert} to discuss the non-linear amplification of instabilities. More precisely, we will focus here on a subset of diagrams of the 2PI $1/N$ expansion to NLO [126, 127], which are relevant for times $\tau \lesssim \tau_{\text{nonpert}}$.

In general, the smaller the above introduced parameter $(n-l)/m$ for a specific self-energy correction, the earlier it may be expected to play a sizable role during the non-equilibrium time

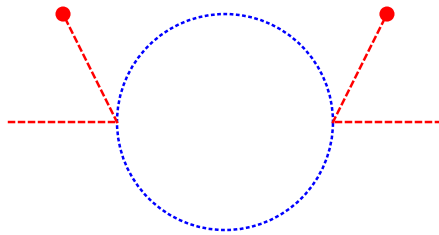


Figure 4.8: One-loop contribution to the longitudinal component of the self-energy. Transverse two-point functions are denoted by dotted (blue) lines.

evolution. For the tadpoles this parameter is one. However, there is another one-loop self-energy correction shown in Fig. 4.8 for which this parameter is $1/2$, which solely contributes to the longitudinal components of the self-energy, as indicated by the red dashed (amputated) legs. Here we denote transverse two-point functions by dotted (blue) lines. It is important to note that in this power counting scheme all other diagrams are suppressed by at least a fractional power of the coupling constant λ . Hence there exists a kinematic window where the only relevant self-energy correction originates from the diagram shown in Fig. 4.8. In the following, we will see that this leads already to a non-linear amplification of the primary instability for longitudinal fluctuations. In particular, this correction has to be taken into account when considering further corrections that become relevant at later times.

The spectral and statistical self-energies associated to Fig. 4.8 read

$$\begin{aligned}
 \Sigma_{\parallel}^{\rho}(\tau, \tau'', p_T, \nu) &\stackrel{\text{(one-loop)}}{=} -\frac{4\lambda(N-1)}{6N}\sigma(\tau)\sigma(\tau'') \\
 &\times \int \frac{d^2 q_T d\nu_q}{(2\pi)^3} \rho_{\perp}(\tau, \tau'', p_T - q_T, \nu - \nu_q) F_{\perp}(\tau, \tau'', q_T, \nu_q), \\
 \Sigma_{\parallel}^F(\tau, \tau'', p_T, \nu) &\stackrel{\text{(one-loop)}}{=} -\frac{2\lambda(N-1)}{6N}\sigma(\tau)\sigma(\tau'') \\
 &\times \int \frac{d^2 q_T d\nu_q}{(2\pi)^3} \left[F_{\perp}(\tau, \tau'', p_T - q_T, \nu - \nu_q) F_{\perp}(\tau, \tau'', q_T, \nu_q) \right. \\
 &\left. - \frac{1}{4} \rho_{\perp}(\tau, \tau'', p_T - q_T, \nu - \nu_q) \rho_{\perp}(\tau, \tau'', q_T, \nu_q) \right], \tag{4.83}
 \end{aligned}$$

which enter the memory integrals on the right-hand-side of the evolution equations (4.75), (4.76) and (4.77). We note that the $(\rho_{\perp}\rho_{\perp})$ -term in the integrand for Σ_{\parallel}^F is a genuine quantum correction, which would be absent in a classical-statistical description [40–42]. However, since $F_{\perp}F_{\perp} \gg \rho_{\perp}\rho_{\perp}$ once non-linear corrections become sizable, one can neglect the quantum part to very good accuracy. In order to make analytic progress, one can exploit the fact that the dominant contribution to the memory integrals originates from late times when fluctuations have become exponentially large [53]. Instead of considering integrals from τ_0 to τ and τ'

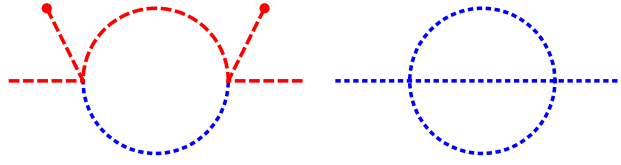


Figure 4.9: One- and two-loop contributions to the transverse components of the self-energies.

respectively, we consider the integrals only over some suitable, small interval Δ . This will be sufficient to obtain characteristic time scales to leading logarithmic accuracy. It allows us to expand the integrand around the times of interest, where at leading order one finds

$$F(\tau, \tau'', p_T, \nu) \simeq F(\tau, \tau, p_T, \nu), \quad (4.84)$$

$$\rho(\tau, \tau'', p_T, \nu) \simeq \frac{\tau - \tau''}{\tau} \simeq \frac{\tau - \tau''}{\tau''}. \quad (4.85)$$

Here we used the equal-time commutation relations in Eq. (4.74) to expand the spectral function. With these approximations one can explicitly evaluate the right-hand-side of the evolution equation (4.75) as

$$\begin{aligned} \text{RHS} &\simeq \Delta^2 \frac{\lambda(N-1)}{3N} \sigma^2(\tau) F_{\parallel}(\tau, \tau', p_T, \nu) \int \frac{d^2 q_T d\nu_q}{(2\pi)^3} F_{\perp}(\tau, \tau, q_T, \nu_q) \\ &+ \Delta^2 \frac{\lambda(N-1)}{6N} \sigma(\tau) \sigma(\tau') \int \frac{d^2 q_T d\nu_q}{(2\pi)^3} F_{\perp}(\tau, \tau', p_T - q_T, \nu - \nu_q) F_{\perp}(\tau, \tau', q_T, \nu_q). \end{aligned} \quad (4.86)$$

The first term in the above sum acts as a momentum-independent mass term similar to the tadpole term on the LHS of the evolution equation (4.75). For it to be relevant it requires $F_{\perp} \sim \mathcal{O}(1/\lambda)$ as discussed before and hence, one expects a relevant contribution starting at τ_{nonpert} . In contrast, the second term appearing in Eq. (4.86) acts as a source term for the evolution of the longitudinal fluctuations F_{\parallel} . The momentum dependence is given by the convolution of the transverse fluctuations F_{\perp} with itself. For instance, if $F_{\perp}(\tau, \tau, q_T, \nu_q)$ is peaked around some momenta p_0 and $\pm\nu_0$, the source term has its dominant contributions around $p_T = \{0, 2p_0\}$ and $\nu = \{0, \pm 2\nu_0\}$. In the presence of this strong source term, one expects F_{\parallel} to follow the source $\sim \lambda F_{\perp}^2$. In this way the primary growth of the transverse fluctuations F_{\perp} leads after some delay-time τ_{source} to a secondary stage of growth, where the longitudinal modes F_{\parallel} exhibit amplified growth-rates. In particular for the longitudinal zero-mode, i.e. $F_{\parallel}(\tau, \tau', p_T = 0, \nu = 0)$, the secondary growth-rate can be twice as large as the primary growth-rate observed for F_{\perp} . It is important to note here that the amplification occurs before tadpole corrections become important. This is due to the fact that the source term is of order λF_{\perp}^2 which only requires $F_{\perp} \sim \mathcal{O}(1/\lambda^{1/2})$ for typical momenta to yield relevant contributions. With the same approximations entering the estimate for τ_{nonpert} in Eq. (4.81)

one can estimate the associated time scale as

$$\tau_{\text{source}} \gtrsim \tau_0 \left[1 + \frac{1}{6(\sigma_0 \tau_0) \gamma_0} \ln \left(\frac{1}{2(N-1)T(\tau_0)\Delta^2} \right) \right]^{3/2}. \quad (4.87)$$

Again, in the weak coupling limit the dominant contribution arises from $\ln(\lambda^{-1})$ and Eq. (4.87) reduces to

$$\tau_{\text{source}} \stackrel{(\lambda \ll 1)}{\simeq} \frac{\tau_{\text{nonpert}}}{2^{3/2}}, \quad (4.88)$$

which is smaller than the time scale on which screening effects due to effective mass terms become relevant. Hence, there is a period of time when one expects growth of the longitudinal modes due to a non-linear amplification of the primary instability. This happens for a bound momentum region which is entirely determined by the spectral shape of the primary instability. We emphasize that the larger couplings the earlier this non-linear amplification of the instability happens.

We have seen that as a consequence of non-linear amplifications characteristic longitudinal fluctuations can be expected to become $\mathcal{O}(\lambda F_{\perp}^2)$ around the time τ_{source} . This again modifies the power counting for subsequent times, since in addition to parametrically large F_{\perp} also parametrically large F_{\parallel} enter loop corrections. In particular, this will soon after lead to sizable non-linear contributions to the evolution equation for transverse fluctuations F_{\perp} . The relevant diagrams contributing to the transverse components of the self-energies are displayed in Fig. 4.9. Assuming $F_{\parallel} \sim \mathcal{O}(\lambda F_{\perp}^2)$ for typical momenta, both depicted diagrams are $\mathcal{O}(\lambda^2 F_{\perp}^3)$. Thus one expects a relevant contribution as soon as $F_{\perp} \sim 1/\lambda^{2/3}$. The momentum-dependence of the diagrammatic contribution leads to an extension of the amplified region to higher momenta, where again multiples of the primary growth-rate appear. It is important to realize that this amplification repeats itself, i.e. the newly amplified modes together with the primarily amplified ones act as a source for other modes. In this way the instability propagates to higher and higher momentum modes for both longitudinal and transverse fluctuations. Indeed, we find that this behavior can be nicely observed from classical-statistical lattice simulations, which we will discuss now.

4.2.3 Classical-statistical lattice simulations

We will now present results of classical-statistical lattice simulations for the longitudinally expanding scalar field theory. In accordance with Sec. 2.4.2, these are obtained by numerically solving the classical field equations of motion and Monte Carlo sampling of initial conditions such that the classical-statistical ensemble averages agree with the quantum correlation func-

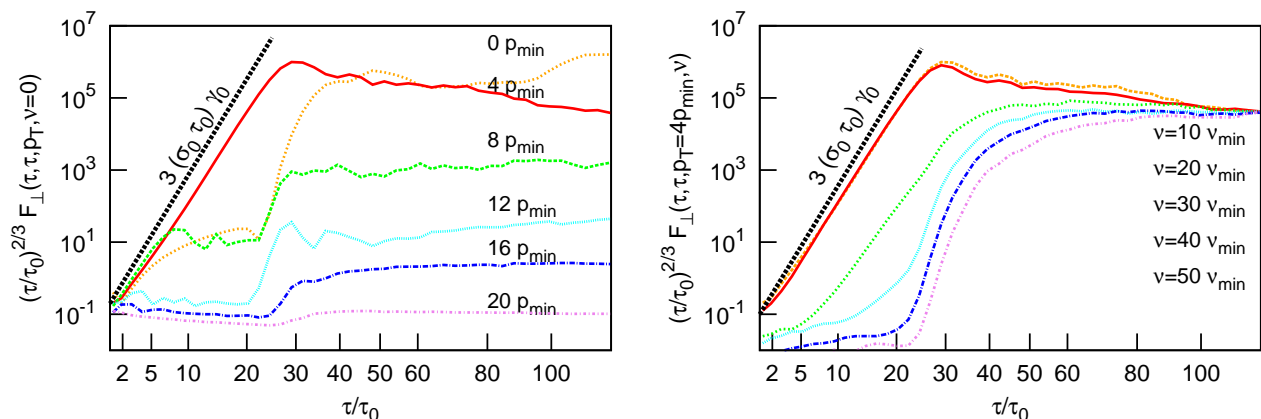


Figure 4.10: **(left)** Time evolution of transverse fluctuations with $p_T = 0, 4, 8, 12, 16, 20 p_{\min}$ and $\nu = 0$ averaged over one period of oscillation of the macroscopic field. **(right)** Same for modes with $p_T = 4 p_{\min}$ and $\nu = 0, 10, 20, 30, 40, 50 \nu_{\min}$ (top to bottom).

tions at initial time. We discretize the evolution equation for the inhomogeneous classical field on a three-dimensional lattice in transverse coordinates and rapidity with grid size $N_T^2 \times N_\eta$.⁷ The lattice spacing is chosen such that the lattice ultraviolet cut-offs $\sim 1/a_\perp$ and $\sim 1/(\tau a_\eta)$ are above all physical scales. Of course, for the expanding system this condition is time-dependent through the time-dependence of the lattice cut-off due to the red-shift of longitudinal momenta as well as through the time-dependence of physical scales due to the dilution of the system. Numerical simulations at late times are therefore computationally hard to perform and we will focus our discussion on the physics at sufficiently early times, where the parametric resonance instability is operative. The parameters are chosen as $m^2 = 0$, $\sigma_0 \tau_0 = 5$, $N = 4$ and $\lambda = 10^{-4}$ and we use $N_T = N_\eta = 128$ lattices with spacings $\sigma_0 a_\perp = 0.5$ and $a_\eta = 0.1$ in our simulations. For convenience, we will express the transverse and longitudinal momenta in terms of the smallest lattice momenta $p_{\min} = 2\sqrt{2}/(N_T a_\perp)$ and $\nu_{\min} = 2/(N_\eta a_\eta)$ respectively.

The time-evolution of transverse and longitudinal fluctuations is presented in Figs. 4.10 and 4.11 for different transverse momenta p_T and rapidity wave number ν . The right panel of Fig. 4.10 shows the transverse fluctuations for modes with different rapidity wave numbers ν and transverse momentum $p_T = 4 p_{\min}$ for which the leading primary instability occurs. From the left panel of Fig. 4.10 one observes that the primary instability occurs for a bound momentum region. The phenomenon of linear freeze-out is clearly visible. The modes with $p_T = 8 p_{\min}$ and $12 p_{\min}$, for instance, exhibit exponential growth at early times but decouple from the instability shortly. The functional form of the primary instability is well described by an exponential in $(\tau/\tau_0)^{2/3}$ with maximum growth-rate $3\sigma_0 \tau_0 \gamma_0$.

⁷Note that in contrast to gauge theories, the lattice discretization for scalar field theories is straightforward, since there is no additional symmetry which needs to be respected.

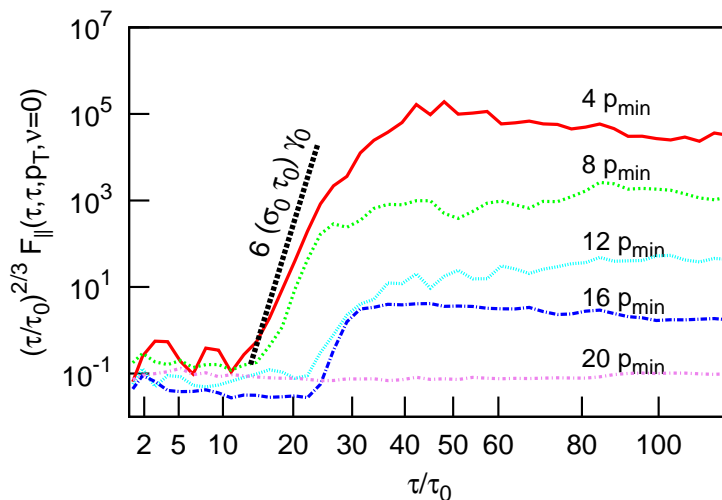


Figure 4.11: Time evolution of longitudinal fluctuations with $p_T = 4, 8, 12, 16, 20 p_{\min}$ and $\nu = 0$ averaged over one period of oscillation of the macroscopic field.

At later times, when the primary instability has been operative long enough to produce large transverse fluctuations, secondary instabilities set in for the longitudinal modes, as can be observed from Fig. 4.11. These secondary instabilities exhibit growth rates up to $6\sigma_0\tau_0\gamma_0$ as discussed in Sec. 4.2.2. The onset of these secondary instabilities is limited to a momentum region $p_T \lesssim 8 p_{\min}$ as they originate from the one-loop diagram shown in Fig. 4.8. This first non-linear amplification of the primary instability happens at times $\tau/\tau_0 \approx 15$. At later times $\tau/\tau_0 \approx 20$ the system exhibits a collective amplification of the primary instability and fluctuations begin to grow in a wide momentum range. Also modes that previously exhibited freeze-out show a second period of growth while modes with smaller primary growth-rates exhibit a significant speed-up. One can also observe from Figs. 4.10 and 4.11 how this sets off an avalanche of instabilities propagating to higher momenta. At this point of the evolution, modes with high rapidity wave number ν set in earlier as suggested by the linearized evolution equations as can be observed in Fig. 4.10. This happens because high longitudinal momenta no longer have to encounter a red-shift to become unstable, but are instead subject to the non-linear amplification.

Ultimately the growth of the instability saturates when the fluctuations become of the order of the inverse coupling $\mathcal{O}(1/\lambda)$ and the rapid dynamics of instabilities is then followed by a regime characterized by a very slow evolution. While in non-expanding systems it is well-established that the ensuing over-populated plasma exhibits a dual turbulent cascade, which drives the thermalization process at this stage of the evolution [34, 35], the situation with regard to expanding systems is further complicated by the anisotropy of the system which arises as a

consequence of the anisotropic expansion. However, since the primary focus of this work is on non-abelian gauge theories, we will not discuss the late time behavior of the expanding scalar field theory and focus on the dynamics of longitudinally expanding non-abelian plasmas instead.

4.3 Discussion

We close this chapter with a brief summary of our results and a discussion of related studies and possible future directions.

In Sec. 4.1, we analyzed the unstable dynamics of coherent non-abelian gauge fields. We obtained an approximate solution for the linear instability regime and found that in addition to a generalization of the Nielsen-Olesen instability, the system also exhibits a subleading parametric resonance instability. We also performed numerical simulations and observed that at later times, non-linear interactions of unstable modes alter the dynamics and lead to an enhanced growth of initially small fluctuations. This phenomenon is analogous to previous observations in scalar and gauge theories [52, 53]. At even later times, we found that the growth of instabilities saturates and the coherent field modes decay. The ensuing over-populated state exhibits a much slower dynamics and resembles the ones previously discussed in Chapter 3.

In Sec. 4.2, we discussed the dynamics of non-equilibrium instabilities in anisotropically expanding systems. We considered the example of the parametric resonance instability in scalar theories and found that the longitudinal expansion gives rise to a rich dynamics already in the linear instability regime. Based on analytic considerations in the framework of 2PI effective action techniques, we also discussed the emergence of “secondary instabilities” due to non-linear self-interactions. The dynamical power-counting scheme developed in this context applies in a similar way also to the non-abelian gauge theories, as will be discussed in Chapter 5. While we observed from numerical simulations that the behavior at later times is characterized by a rather slow evolution, we did not discuss the possible approach to a turbulent scaling regime.

As a final remark, we note that the expanding scalar theory has recently also attracted the interest of different authors, who extended the use of classical-statistical lattice methods beyond the range of validity of the classical-statistical approximation, in a setup which mimics more closely the situation encountered in heavy-ion collisions [129]. Most remarkably, the authors were able to demonstrate rapid isotropization of the system, although it is not clear to what extent this result is affected by the breakdown of the classical-statistical approximation for the small occupancies considered in Ref. [129]. Since powerful resummation techniques

have been developed for N -component scalar field theories [126, 127], the problem can also be studied using 2PI effective action techniques to perform numerical simulations within a genuine quantum approach. First efforts in this direction have been reported in the exploratory studies of Ref. [130]. However, since the authors could not address the problems of isotropization or wave turbulence, the late time dynamics of the expanding scalar theory remains an interesting topic for future investigations.

Chapter 5

Heavy-ion collisions at ultra-relativistic energies

In this chapter, we study the non-equilibrium dynamics of relativistic heavy-ion collisions in an idealized weak-coupling scenario. As stated in the introduction, the theoretical understanding of the thermalization process in these systems is an outstanding problem in theoretical physics and provides one of the central motivations for this work. We present an ab initio study based on Color Glass Condensate initial conditions and classical-statistical lattice gauge-theory simulations as a first principles approach to study the time evolution. We observe that the non-equilibrium evolution, starting from early times immediately after the collision of heavy nuclei, up to late times, where thermalization of the system begins to take place, is governed by different dynamical regimes which, in brief, can be characterized as follows:

- I) STRONG FIELDS ($0 < Q\tau \lesssim 1$): The initial 'Glasma' state, created immediately after the collision of heavy nuclei consists of strong chromo-electric and chromo-magnetic fields oriented in the beam direction [131–134]. The latter are characterized by large field amplitudes $\mathcal{A}_\mu^a(x) \sim \alpha_S^{-1/2}$ and a characteristic momentum scale Q , which reflect the properties of saturated nuclear wave functions prior to the collision [131–134]. On the time scale $1/Q$, the initially coherent field configurations are subject to a dephasing dynamics and form a boost invariant state characterized by large occupancies in the transverse plane [117, 135–143].
- II) PLASMA INSTABILITIES ($1 \lesssim Q\tau \lesssim \log^2(\alpha_S^{-1})$): The evolving 'Glasma' state is highly anisotropic, and thus exhibits the (chromo-) Weibel instability [44–46, 49–51, 104–113]. This leads to exponential growth of initial state vacuum fluctuations, which explicitly break the boost invariance of the system [49–51]. Once the fluctuations have grown large, non-linear amplification processes take place until saturation of the instability occurs when statistical fluctuations become of the same size as the 'Glasma' background fields. As a

result of this process, both the original 'Glasma' fields and the vacuum fluctuations of the initial state are converted to particle-like excitations, which subsequently exhibit a much slower dynamics. In this way, the Weibel instability is able to partially restore isotropy of the system, however the ensuing state still exhibits a residual order one anisotropy.

- III) TURBULENT THERMALIZATION ($\log^2(\alpha_S^{-1}) \lesssim Q\tau \lesssim \alpha_S^{-3/2}$) : The competition between interactions of strongly-correlated quasi particles and the longitudinal expansion leads again to a slow increase of the anisotropy of the system. Ultimately, the dynamics becomes independent of the details of the initial conditions and leads to the same universal attractor solution. In this regime, the plasma exhibits self-similar behavior characteristic of wave turbulence. While the physics of plasma instabilities and free streaming plays an important role for the dynamics at early times, they do not govern the universal turbulent regime. Instead, the attractor solution shows the same characteristic time-dependence as the "bottom-up" thermalization scenario, where the dynamics is governed by elastic scattering of hard excitations [29]. The dynamics proceeds in this way until at times $Q\tau \sim \alpha_S^{-3/2}$ the characteristic occupancies become of order unity and the system enters the quantum regime.
- IV) QUANTUM REGIME ($Qt \gtrsim \alpha_S^{-3/2}$): In the quantum regime, where the characteristic occupancies become of order unity, the turbulent attractor solution breaks down, since genuine quantum evolution effects can no longer be neglected. This regime has been studied in the kinetic theory framework by different authors: In the "bottom-up" scenario, inelastic processes begin to play a significant role in this regime and eventually lead to thermalization [29]. However, it is also conceivable that e.g. plasma instabilities play a role for the thermalization process at this stage of the evolution [31, 32]. Since the classical-statistical framework can no longer be applied, the study of this regime is beyond the scope of this work.

In this chapter, we present a detailed study of the non-equilibrium dynamics of the initial stages and the turbulent regime. The discussion is largely based on Refs. [144, 145] and organized in the following way: In Sec. 5.1, we introduce the theoretical framework and discuss the approximations involved to study the non-equilibrium dynamics of heavy-ion collisions at ultra-relativistic energies. In Sec. 5.2, we study the dynamics at early times, where plasma instabilities are dominant, and analyze our results within the framework of 2PI effective action techniques [42]. The turbulent regime is discussed in Sec. 5.3, where we obtain the universal scaling exponents and scaling functions and compare our findings with a kinetic theory analysis. We conclude this chapter in Sec. 5.4 with a summary of our results and a discussion of possible implications for heavy-ion collision experiments at present collider energies.

5.1 Non-equilibrium dynamics and the CGC framework

An ab initio approach to the non-equilibrium dynamics of heavy-ion collisions requires to determine the initial density matrix consisting of two incoming nuclei in the vacuum and subsequently solving the initial value problem in Quantum Chromo Dynamics. Though this is clearly beyond the scope of all present theoretical methods, one may apply suitable approximations in the combined limit of weak coupling and high collider energies, which make the problem computationally feasible.

5.1.1 The color-glass condensate approach

The dynamics of nucleus-nucleus collisions is usually discussed in terms of the light-cone coordinates $x^\pm = (t \pm z)/\sqrt{2}$, where at sufficiently high collider energies the incoming nuclei travel close to the light-cone, which is given by $x^\pm = 0$. The collision takes place around the time when $x^+ = x^- = 0$, where the center of mass of the nuclei coincide and an approximately boost invariant plasma is formed at mid-rapidity after the collision has taken place. The plasma dynamics in the forward light-cone ($x^\pm > 0$) is usually discussed in terms of the co-moving coordinates

$$\tau = \sqrt{t^2 - z^2}, \quad \eta = \text{atanh}(z/t), \quad (5.1)$$

where τ is the proper time in the longitudinal direction and η is the longitudinal rapidity. As discussed in Sec. 2.3, the metric in these coordinates takes the form $g_{\mu\nu}(x) = \text{diag}(1, -1, -1, -\tau^2)$ and we denote the metric determinant as $g(x) = \det g_{\mu\nu}(x)$. The space-time evolution of the collision and the geometry of the coordinates are illustrated in Fig. 5.1. The different colors in the forward light-cone represent the different stages of the evolution.

In the color-glass framework one considers the dynamics of the plasma at mid-rapidity ($\eta \ll \eta_{Beam}$) and the nuclear partons at high rapidities ($\eta \simeq \eta_{Beam}$) separately. In practice, this separation in high energy and low energy degrees of freedom is performed by a renormalization group procedure prescribed by the JIMWLK equations [27, 28]. In the eikonal approximation, where the trajectories of high energy degrees of freedom inside the nuclear wave functions are unaffected by the collision, the dynamics of gluons at mid-rapidity is described by the classical Yang-Mills action

$$S[A] = -\frac{1}{4} \int d^4x \sqrt{-g(x)} \mathcal{F}_{\mu\nu}^a(x) g^{\mu\alpha}(x) g^{\nu\beta}(x) \mathcal{F}_{\alpha\beta}^a(x), \quad (5.2)$$

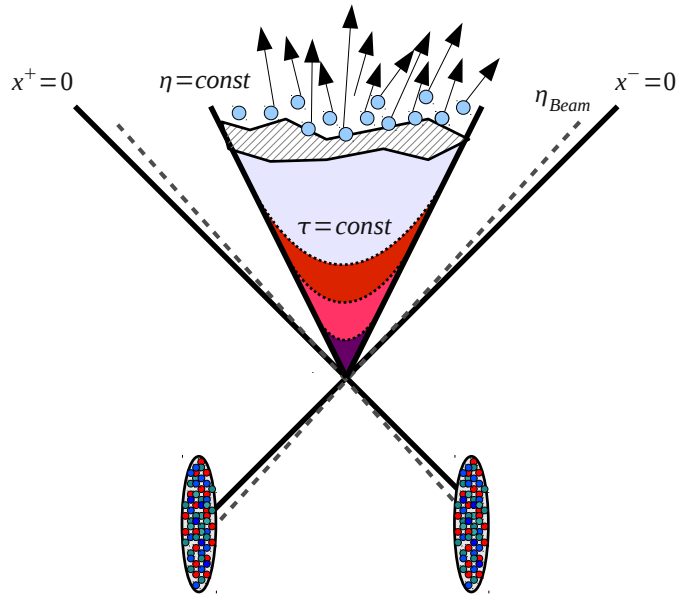


Figure 5.1: Illustration of the space time evolution of a high energy heavy-ion collision.

where, in addition, the gauge field $A_\mu^a(x)$ is coupled to an eikonal current $J_a^\mu(x)$, determined by the properties of the nuclear wave function at high rapidities. In the high energy limit, the eikonal current can be approximated as a collection of static color sources on the light-cone and takes the generic form [27, 28]

$$J_a^\mu(t, \vec{x}_\perp, z) = \delta^{\mu^+} \varrho_a^{(1)}(\vec{x}_\perp) \delta(x^-) + \delta^{\mu^-} \varrho_a^{(2)}(\vec{x}_\perp) \delta(x^+) , \quad (5.3)$$

where δ^{μ^\pm} is the Kronecker delta in light-cone coordinates. The color charge densities $\varrho_a^{(1/2)}(\vec{x}_\perp)$, where the superscript (1/2) labels the different nuclei, contain all further information about the beam energy, nuclear species and impact parameter dependence of the collision. At high collider energies, these have been conjectured to exhibit a universal behavior characterized by non-perturbatively large color charge densities $\sim 1/\sqrt{\alpha_s(Q_s)}$, up to the saturation scale Q_s in (transverse) momentum space [146–150]. Consequently, the currents in Eq. (5.3) are parametrically large, i.e. formally $\mathcal{O}(1/g)$ in powers of the coupling constant, which makes the problem inherently non-perturbative and amenable to the classical-statistical framework.

We note that, by specifying the eikonal current according to Eq. (5.3), the longitudinal geometry of the collision has effectively been reduced to the collision of two-dimensional sheets. Hence, there is no longer a longitudinal scale inherent to the problem and one obtains boost invariant field solutions at the classical level. However, quantum fluctuations explicitly break the longitudinal boost invariance of the system and are thus expected to play an important role in the space-time evolution of the collision [151]. Before we turn to a detailed discussion

of quantum fluctuations, we will briefly review the classical solution to the particle production process. We will show later, in Sec. 5.1.3, how this solution emerges naturally in the weak-coupling limit of the quantum field theory.

5.1.2 Classical solution

By neglecting quantum fluctuations for the moment, the absence of a longitudinal scale in Eq. (5.3) leads to boost-invariant solutions of the classical Yang-Mills field equations

$$\frac{\delta S[A]}{\delta A_\mu^a(x)} = -J_a^\mu(x). \quad (5.4)$$

In this classical color glass picture, the strong color-fields right after the collision are entirely determined by the continuity conditions on the light-cone ($x^\pm = 0$) [131–134]. Adapting the Fock-Schwinger gauge condition ($A_\tau = 0$), where the classical Yang-Mills action takes the form

$$S[A] = \int \tau d\tau \, d\eta \, d^2\vec{x}_\perp \left[\frac{1}{2\tau^2} (\partial_\tau A_\eta^a)^2 + \frac{1}{2} (\partial_\tau A_i^a)^2 - \frac{1}{2\tau^2} \mathcal{F}_{\eta i}^a \mathcal{F}_{\eta i}^a - \frac{1}{4} \mathcal{F}_{ij}^a \mathcal{F}_{ij}^a \right], \quad (5.5)$$

($i = 1, 2$) the initial state right after the collision can be specified at $\tau = 0^+$, where the chromo magnetic and electric fields are given by [131–134]

$$\begin{aligned} A_i(\vec{x}_\perp) &= \alpha_i^{(1)}(\vec{x}_\perp) + \alpha_i^{(2)}(\vec{x}_\perp), & A_\eta &= 0, \\ E_i &= 0, & E_\eta(\vec{x}_\perp) &= ig[\alpha_i^{(1)}(\vec{x}_\perp), \alpha_i^{(2)}(\vec{x}_\perp)]. \end{aligned} \quad (5.6)$$

Here $\alpha_i^{(1/2)}(\vec{x}_\perp)$ are pure gauge configurations which describe the Yang-Mills field outside the light-cone. They are related to the nuclear color charge densities by [131–134]

$$\begin{aligned} \alpha_i^{(N)}(\vec{x}_\perp) &= \frac{-i}{g} e^{ig\Lambda^{(N)}(\vec{x}_\perp)} \partial_i e^{-ig\Lambda^{(N)}(\vec{x}_\perp)}, \\ \partial_i \partial^i \Lambda^{(N)}(\vec{x}_\perp) &= \varrho^{(N)}(\vec{x}_\perp), \end{aligned} \quad (5.7)$$

and depend on transverse coordinates \vec{x}_\perp only. The relations (5.6) and (5.7) specify the ‘Glasma’ initial state at $\tau = 0^+$ right after the collision. At the classical level, the subsequent time evolution in the forward light-cone can be studied numerically by solving the lattice analogue of the classical evolution equations in Eq. 5.4 and has been studied extensively in the literature [135–143]. However, since the longitudinal boost invariance of the system is preserved in the classical evolution, this leads to an effectively 2+1 dimensional Yang Mills theory coupled to an adjoint scalar field [135–143]. In order to study the full glory of 3+1 dimensional Yang Mills theory, it is therefore crucial to include quantum fluctuations, which explicitly break the boost-invariance of the system.

5.1.3 Quantum fluctuations

We recall from Sec. 2.2 that, for quantum fields $A_\mu^a(x)$, the evolution equations can be formulated in terms of the expectation values of the one point function

$$\mathcal{A}_\mu^a(x) = \langle A_\mu^a(x) \rangle, \quad (5.8)$$

and the spectral and statistical two-point correlation functions, which are associated to the commutator and anti-commutator respectively according to

$$\rho_{\mu\nu}^{ab}(x, y) = i \langle [A_\mu^a(x), A_\nu^b(y)] \rangle, \quad (5.9)$$

$$F_{\mu\nu}^{ab}(x, y) = \frac{1}{2} \langle \{A_\mu^a(x), A_\nu^b(y)\} \rangle - \mathcal{A}_\mu^a(x) \mathcal{A}_\nu^b(y). \quad (5.10)$$

Here expectation values are given by the trace over the initial vacuum density matrix in the presence of the eikonal currents in Eq. (5.3). The initial density matrix is specified in the remote past ($t_0 \rightarrow -\infty$), where the background field $\mathcal{A}_\mu^a(x)$ vanishes and the statistical fluctuations $F_{\mu\nu}^{ab}(x, y)$ take the usual vacuum form (see e.g. Ref. [98]). In contrast, the initial values of the spectral function are entirely determined by the equal time commutation relations, which in temporal axial gauge ($A_0 = 0$) read

$$\begin{aligned} \rho_{\mu\nu}^{ab}(x, y)|_{x^0=y^0} &= 0, \\ \partial_{x^0} \rho_{\mu\nu}^{ab}(x, y)|_{x^0=y^0} &= -\delta^{ab} \frac{g_{\mu\nu}}{\sqrt{-g(x)}} \delta^{(3)}(\vec{x} - \vec{y}), \\ \partial_{x^0} \partial_{y^0} \rho_{\mu\nu}^{ab}(x, y)|_{x^0=y^0} &= 0, \end{aligned} \quad (5.11)$$

and are valid at all times.¹ The gauge field expectation values in Eq. (5.8) correspond to the 'Glasma' background fields, while the spectral and statistical two-point functions initially contain only quantum fluctuations of the initial vacuum state.

The evolution equations for connected one and two-point correlation functions follow from the stationarity of the two particle irreducible (2PI) effective action and form a closed set of coupled integro-differential equations [42]. The set of equations is given by the evolution equation of the macroscopic field

$$\frac{\delta S[\mathcal{A}]}{\delta \mathcal{A}_\mu^a(x)} = -J_a^\mu(x) - \frac{i}{2} \text{tr} \left[\frac{\delta G_0^{-1}[\mathcal{A}]}{\delta \mathcal{A}_\mu^a(x)} G \right] - \frac{\delta \Gamma_2[\mathcal{A}, G]}{\delta \mathcal{A}_\mu^a(x)} \quad (5.12)$$

¹Note that Eq. (5.11) is valid also for (τ, η) coordinates, when replacing $x^0 \rightarrow \tau$ and $x^3 \rightarrow \eta$ and imposing the Fock-Schwinger ($A_\tau = 0$) gauge condition.

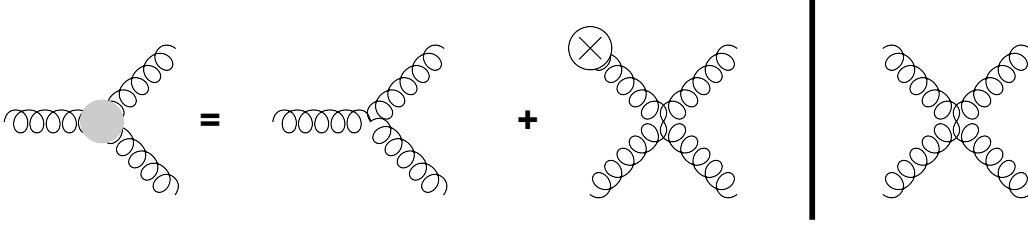


Figure 5.2: Vertices in non-abelian gauge theory in the presence of background fields. In addition to the tree-level vertices, the three-gluon-vertex receives an additional contribution. The combined three-gluon-vertex is denoted by a gray dot and the insertion of the background field is denoted a crossed circle.

and the evolution equations for spectral and statistical two point correlation functions, which can be written as [42]

$$[iG_{0,ac}^{-1,\mu\gamma}[x; \mathcal{A}] + \Pi_{ac}^{(0),\mu\gamma}(x)] \rho_{\gamma\nu}^{cb}(x, y) = - \int_{y^0}^{x^0} dz \Pi_{ac}^{(\rho),\mu\gamma}(x, z) \rho_{\gamma\nu}^{cb}(z, y), \quad (5.13)$$

$$\begin{aligned} [iG_{0,ac}^{-1,\mu\gamma}[x; \mathcal{A}] + \Pi_{ac}^{(0),\mu\gamma}(x)] F_{\gamma\nu}^{cb}(x, y) = & - \int_{-\infty}^{x^0} dz \Pi_{ac}^{(\rho),\mu\gamma}(x, z) F_{\gamma\nu}^{cb}(z, y) \\ & + \int_{-\infty}^{y^0} dz \Pi_{ac}^{(F),\mu\gamma}(x, z) \rho_{\gamma\nu}^{cb}(z, y). \end{aligned} \quad (5.14)$$

Here we denote $\int_a^b dz = \int_a^b dz^0 \int d^d z \sqrt{-g(z)}$ and $iG_{0,ab}^{-1,\mu\nu}[x; A]$ denotes the free inverse propagator

$$\begin{aligned} iG_{0,ab}^{-1,\mu\nu}[x; \mathcal{A}] = & \gamma^{-1}(x) D_{\gamma}^{ac}[x; \mathcal{A}] \gamma(x) g^{\gamma\alpha} g^{\mu\nu} D_{\alpha}^{cb}[x; \mathcal{A}] \\ & - \gamma^{-1}(x) D_{\gamma}^{ac}[x; \mathcal{A}] \gamma(x) g^{\gamma\nu} g^{\mu\alpha} D_{\alpha}^{cb}[x; \mathcal{A}] \\ & - g f^{abc} \mathcal{F}_c^{\mu\nu}[x; \mathcal{A}], \end{aligned} \quad (5.15)$$

with $\gamma(x) = \sqrt{-g(x)}$. We also introduced the (background) covariant derivative

$$D_{\mu}^{ab}[x; \mathcal{A}] = \partial_{\mu}^x \delta^{ab} + g f^{abc} \mathcal{A}_{\mu}^c(x), \quad (5.16)$$

and the background field strength

$$\mathcal{F}_{\mu\nu}^a[x; \mathcal{A}] = \partial_{\mu} \mathcal{A}_{\nu}^a(x) - \partial_{\nu} \mathcal{A}_{\mu}^a(x) + g f^{abc} \mathcal{A}_{\mu}^b(x) \mathcal{A}_{\nu}^c(x). \quad (5.17)$$

The non-zero spectral and statistical parts of the self-energy $\Pi^{(\rho/F)}[\mathcal{A}, G]$ on the right hand side and the local part $\Pi^{(0)}[G]$ on the left hand side make the evolution equations non-linear in the fluctuations. In general they contain contributions from the vertices depicted in Fig. 5.2, where in addition to the classical three gluon vertex there is a three gluon vertex associated

with the presence of the non-vanishing 'Glasma' background fields.

The explicit expressions for the derivatives on the right hand side of Eq. (5.12) and the self-energy contributions entering Eqns. (5.13) and (5.14) have been calculated to three loop order $\mathcal{O}(g^6)$ in Ref. [72] and the corresponding expressions in co-moving (τ, η) coordinates can be found in Ref. [98].

Before we turn to a more detailed discussion of the contributions on the right hand side of Eqns. (5.12), (5.13) and (5.14), it proves insightful to consider first only the leading part in a weak coupling expansion. We will see shortly how this recovers the classical solution for the 'Glasma' background fields (c.f. Sec. 5.1.2), while the leading order contributions of vacuum fluctuations of the initial state are also taken into account in terms of the connected two-point correlation functions.

In order to isolate the leading contributions in a coupling expansion, one has to take into account the strong external currents $J_a^\mu(x) \sim \mathcal{O}(1/g)$, which induce non-perturbatively large background fields $\mathcal{A}_\mu^a(x) \sim \mathcal{O}(1/g)$. In contrast, the statistical fluctuations $F_{\mu\nu}^{ab}(x, y)$ originate from initial state vacuum and are therefore $\mathcal{O}(1)$ initially. The spectral function $\rho_{\mu\nu}^{ab}(x, y)$ has to comply with the equal time commutation relations in Eq. (5.11) and is therefore parametrically $\mathcal{O}(1)$ at any time. Considering only the leading contributions in a weak coupling expansion, the evolution equation (5.12) reduces to its classical form (c.f. Eq. (5.4))

$$\frac{\delta S[\mathcal{A}]}{\delta \mathcal{A}_\mu^a(x)} = -J_a^\mu(x) , \quad (5.18)$$

and the evolution equations for the spectral and statistical two-point correlation functions at leading order read

$$iG_{0,ac}^{-1,\mu\gamma}[x; \mathcal{A}] \rho_{\gamma\nu}^{cb}(x, y) = 0 , \quad (5.19)$$

$$iG_{0,ac}^{-1,\mu\gamma}[x; \mathcal{A}] F_{\gamma\nu}^{cb}(x, y) = 0 . \quad (5.20)$$

The leading order part thus corresponds to an inhomogeneous mean-field approximation, where sub-leading contributions are suppressed by at least a factor of g^2 relative to the leading contribution.

It is important to realize that at this order the evolution of the 'Glasma' background fields (\mathcal{A}) decouples from that of the fluctuations (F/ρ), i.e. there is no back-reaction from the fluctuations on the 'Glasma' background fields. Therefore the dynamics of the background fields

remains unchanged, with respect to the classical evolution equations and one recovers the solutions discussed in Sec. 5.1.2. In addition, the evolution of vacuum fluctuations of the initial state is taken into account by Eqns. (5.19) and (5.20) to linear order in the fluctuations. We note that, to this order in the coupling constant, the quantum field theory is well known to agree with the classical-statistical theory [40, 41] and Eqns. (5.19, 5.20) can equivalently be obtained by considering the linearized classical evolution equations for small fluctuations (see e.g. Ref. [151]).² The same result has also been obtained using resummed perturbation theory in Refs. [152–154].

The linear approximation in Eqns. (5.19) and (5.20) yields a major simplification to Eqns. (5.13) and (5.14), as one can solve the linear equations (5.19) and (5.20) for a given evolution of the ‘Glasma’ background field. This feature has been exploited in Ref. [151] to evolve the fluctuations from the remote past to the forward light-cone and obtain analytic results for the spectrum of initial fluctuations at time $\tau = 0^+$ right after the collision.

In turn, the range of validity of the approximation is limited to the domain where fluctuations remain parametrically small. This is, however, not the case in the forward light-cone ($\tau > 0$), where Eqns. (5.19) and (5.20) exhibit plasma instabilities associated to exponential growth of statistical fluctuations [49–51]. In this regime statistical fluctuations will become parametrically large and thus strongly modify the naive power counting. Moreover, since the approximation underlying Eqns. (5.19) and (5.20) is not energy conserving, one encounters exponential divergences when stressing Eqns. (5.19) and (5.20) beyond their range of validity [92, 155]. It is therefore crucial to include the self-energy corrections in Eqns. (5.13) and (5.14), which naturally cure the divergences of the linearized evolution equations.

In practice, this can be efficiently achieved within the classical-statistical framework introduced in Sec. 2.4, which, phrased in the language of expectation values, resums an infinite subset of self-energy diagrams [40, 41]. More precisely, the strategy proposed in Ref. [151] is to employ the linearized evolution equations (5.19) and (5.20) only outside the forward light-cone, to obtain analytic expressions for the ‘Glasma’ background field as well as for the spectrum of statistical fluctuations at $\tau = 0^+$, while switching to a classical-statistical description in the forward light-cone ($\tau > 0$). Since the classical-statistical theory is well-defined by its own right,³ this cures the unphysical divergences of Eqns. (5.19) and (5.20) by the inclusion of non-linear interactions. Most remarkably, the classical-statistical framework allows to calculate observ-

²This can be seen immediately by solving Eq. (5.20) in terms of mode functions $F(x, y) = \delta A(x)\delta A(y)$, which then individually satisfy the linearized classical evolution equations $iG_0^{-1}[x; A] \delta A(x) = 0$.

³Strictly speaking, the classical-statistical theory requires an ultraviolet cutoff to regulate the Rayleigh-Jeans divergence. In practice this cut-off is introduced by the lattice discretization.

ables in a manifestly gauge invariant way, which is in general not guaranteed within a different approximation scheme [72, 156, 157].

5.2 The unstable Glasma

We will now study the non-equilibrium dynamics of the 'Glasma', created immediately after the collision of heavy nuclei, using classical-statistical lattice gauge theory techniques introduced in Sec. 2.4.

5.2.1 Initial conditions

The initial conditions are specified at time $\tau = 0^+$ right after the collision, according to the CGC picture discussed in Sec. 5.1. In accordance with previous works [49–51], we adapt the McLerran-Venugopalan (MV) saturation model as a simple parametrization of the saturated nuclear wave functions [158–161]. In this model, the color charge densities of the colliding nuclei are given by uncorrelated Gaussian configurations according to⁴

$$\langle \varrho_a^{(A)}(\vec{x}_\perp) \varrho_b^{(B)}(\vec{y}_\perp) \rangle = \frac{Q^2}{g^2} \delta^{AB} \delta_{ab} \delta^{(2)}(\vec{x}_\perp - \vec{y}_\perp), \quad (5.21)$$

and we impose an additional color neutrality constraint on the color charge densities such that the global color charge vanishes separately for each nucleus, i.e.

$$\int d^2\vec{x}_\perp \varrho_a^{(1/2)}(\vec{x}_\perp) = 0 \quad \forall \quad a. \quad (5.22)$$

In addition to the parametrically large 'Glasma' background fields $\mathcal{A}_\mu^a(x) \sim 1/g$, which are determined by the color charge densities as discussed in Sec. 5.1, we also include vacuum fluctuations of the initial state, which explicitly break boost invariance. Instead of including the full spectrum of vacuum fluctuations (c.f. Ref. [151]), we follow earlier works and use a somewhat simpler parametrization [49–51]. This is well justified at very weak coupling, where the details of the initial spectrum of fluctuations quickly become irrelevant, since plasma instabilities naturally select the modes which exhibit the fastest primary growth. In accordance with previous works [49–51], the statistical fluctuations are then initialized as

$$\begin{aligned} F_{\mu\nu}^{ab}(x, y) \Big|_{\tau=\tau'=0} &= 0, \\ \partial_\tau F_{\mu\nu}^{ab}(x, y) \Big|_{\tau=\tau'=0} &= 0, \\ \partial_\tau \partial_{\tau'} F_{\mu\nu}^{ab}(x, y) \Big|_{\tau=\tau'=0} &= \langle \delta E_\mu^a(x_\perp, \eta_x) \delta E_\nu^b(y_\perp, \eta_y) \rangle, \end{aligned} \quad (5.23)$$

⁴Note that, in the literature on the MV model, this is usually stated in terms of the MV model parameter $g^2\mu$, which is identical to the scale Q in our notation [158–161].

with

$$\delta E_i^a(\vec{x}_\perp, \eta) = \partial_\eta h(\eta) e_i^a(\vec{x}_\perp) \quad (5.24)$$

$$\delta E_\eta(\vec{x}_\perp, \eta) = -h(\eta) D_i[x; \mathcal{A}] e_i^a(\vec{x}_\perp), \quad (5.25)$$

such that $\delta E_\mu^a(x)$ yields an additive contribution to the 'Glasma' background field $E_\mu^a(x)$ at initial time. The advantage of this construction is that the Gauss constraint is satisfied explicitly for generic functions $h(\eta)$ and $e_i^a(\vec{x}_\perp)$. In the numerical simulations we choose

$$\langle e_i^a(\vec{p}_T) e_j^b(\vec{q}_T) \rangle = \delta_{ij} \delta^{ab} \delta^{(2)}(\vec{p}_T + \vec{q}_T), \quad (5.26)$$

$$\langle h(\nu) h(\nu') \rangle = e^{-2b|\nu|} \delta(\nu + \nu'), \quad (5.27)$$

where p_T and ν are the Fourier coefficients with respect to transverse coordinates and rapidity. Here b is a (small) number, which regulates the ultraviolet divergence and we will employ $b = 0.01$ in the following. The lattice implementation of the above initial conditions is straightforward and explained in detail in App. G. If not stated otherwise we perform simulations on $N_T = 16$, $N_\eta = 1024$ and $N_T = 32$, $N_\eta = 128$ lattices and we employ the set of parameters $Q N_\perp a_\perp = 22.6$, $N_\eta a_\eta = 1.6$ in accordance with Ref. [49, 50].

Since the statistical fluctuations are parametrically of order one at initial time $\tau = 0^+$, they are initially suppressed by a factor of g^2 relative to the (squared) 'Glasma' background field. Moreover, since the coupling constant can be scaled out of the classical equations of motion, the entire coupling dependence of our results is therefore contained in the initial conditions.

5.2.2 Plasma instabilities and non-linear dynamics

We will now study the non-equilibrium dynamics of the 'Glasma' in the presence of boost non-invariant fluctuations. While the existence of a Weibel type instability in this setup has been established in previous simulations [49–51], we will focus on the non-linear regime where unstable modes have grown large enough to significantly alter the dynamics.

In contrast to the linear regime, where the initial size of boost non-invariant fluctuations is irrelevant for the dynamics of unstable modes, it is clear that for the non-linear regime the size of the initial fluctuations matters. As discussed above, the ratio of the initial amplitude of fluctuations compared to the amplitude of the (squared) background field is parametrically of the order of the coupling constant g^2 . We will study this dependence below, where we consider different values of g^2 , which in the classical-statistical setup simply correspond to different initial conditions. We note however, that it is important to restrict the analysis to weak coupling

($g^2 \ll 1$), where classical-statistical methods are expected to provide an accurate description of the quantum dynamics on sufficiently large time scales.

In order to analyze the dynamics of QCD plasma instabilities, we follow Refs. [49–51] and study the time evolution of the gauge-invariant, equal time pressure-pressure correlation function

$$\Pi_L^2(\tau, \nu) = (N_\eta a_\eta)^{-1} \int d\eta d\eta' \langle P_L(\tau, \vec{x}_\perp, \eta) P_L(\tau, \vec{y}_\perp, \eta') \rangle_T e^{-i\nu(\eta-\eta')}. \quad (5.28)$$

Here $P_L(x)$ denotes the longitudinal pressure as a function of space and time arguments $(\tau, \vec{x}_\perp, \eta)$ as introduced in Sec. 2.4 and $\langle \dots \rangle_T$ denotes average over transverse coordinates and classical-statistical ensemble averages over typically ten to twenty different initial conditions. Spectral information is contained in the dependence on the rapidity wave number ν , which corresponds to the Fourier conjugate with respect to relative rapidity.

The time evolution of the correlation function $\Pi_L(\tau, \nu)$ is shown in Fig. 5.3 for different rapidity wave numbers ν . In order to achieve a clear separation of different time scales, we chose a very small value of the coupling constant $g = 10^{-10}$. From Fig. 5.3 one immediately observes a sequence of different dynamical regimes which can be characterized as follows:

DEPHASING: At very early times $\sqrt{Q\tau} \lesssim 2$ one observes a period of rapid initial growth, which is presumably caused by the dephasing dynamics of the 'Glasma' background fields, that takes place on the same time scale [51, 135–143].⁵ However at weak coupling, i.e. for sufficiently small fluctuations relative to the 'Glasma' background fields, this constitutes a rather small effect as the unstable modes exhibit their dominant growth at later times.

WEIBEL INSTABILITY: This rapid initial period is followed by a regime where the (chromo-) Weibel instability is operative and modes with non-zero rapidity wave number exhibit exponential amplification. The instability sets in with a delay for higher momentum modes and the functional form is well described by an exponential of the form $\exp[\Gamma(\nu)\sqrt{Q\tau}]$, with the momentum dependent growth rate $\Gamma(\nu)$, as seen for $\nu = 4, 12$ in Fig. 5.3. In order to obtain the relevant growth rates and set-in times, we fit a set of continuous, piecewise linear functions to the modes displayed in Fig. 5.3. The results of this analysis are shown in Fig. 5.4 as a function of rapidity wave number ν . From the left panel of Fig. 5.4 one observes that the primary set-in times follow a linear behavior, as reported in Ref. [49, 50]. The primary growth rates are shown in the right panel of Fig. 5.4. One observes that modes with small rapidity wave number exhibit

⁵See also Ref. [117] for an analytic discussion.

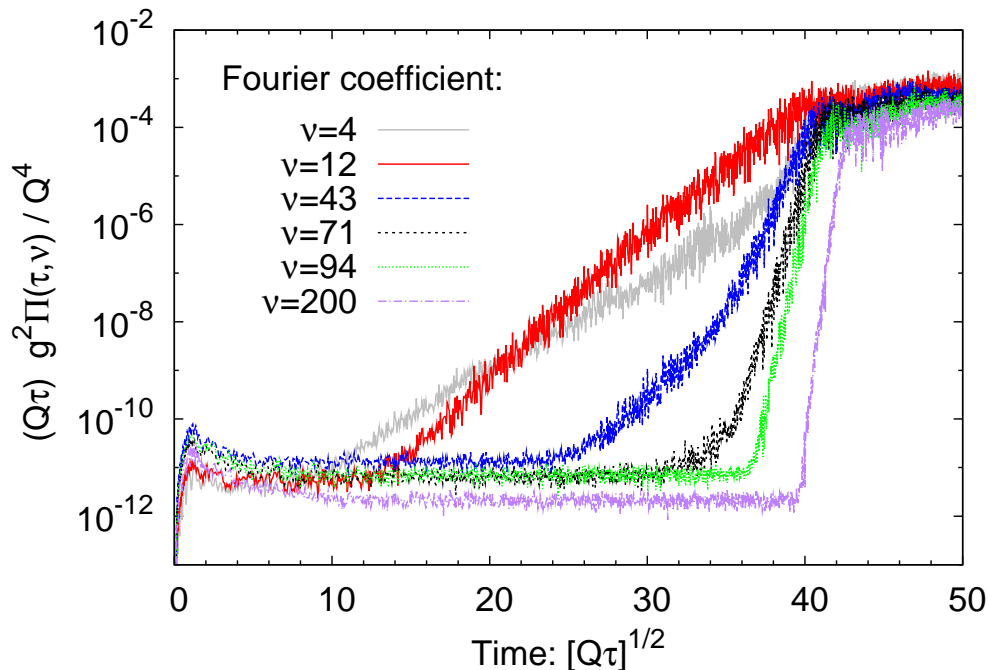


Figure 5.3: Time evolution of the pressure-pressure correlator $\Pi_L(\tau, \nu)$ for different rapidity wave numbers ν . Once the initial fluctuations have grown larger one observes the emergence of secondary instabilities, associated with much larger growth rates. Subsequently the instability propagates towards higher momenta until saturation occurs and the system exhibits a much slower dynamics.

smaller growth rates as compared to modes with higher rapidity wave number. At large ν the primary growth rates become approximately constant. The numerical values are compatible with the results reported in Ref. [49, 50], where characteristic growth rates were obtained from a convolution of the spectrum.

NON-LINEAR AMPLIFICATION: While the primary instability continues to set-in for higher momentum modes, one observes from Fig. 5.3 that at later times modes with intermediate ($\nu = 43, 71$) and small ($\nu = 4$) rapidity wave numbers suddenly exhibit much higher growth rates than previously observed. This change in the dynamics becomes evident when shortly after modes with even higher rapidity wave numbers ($\nu = 94, 200$) exhibit even stronger growth rates, such that the spectrum of unstable modes extends quickly towards the ultraviolet and the instability propagates towards higher momenta. This is precisely the signature of secondary instabilities, where non-linear self-interactions among unstable modes give rise to an amplification of the primary instability.

While the amplification occurs initially only in a small momentum region, it quickly prop-

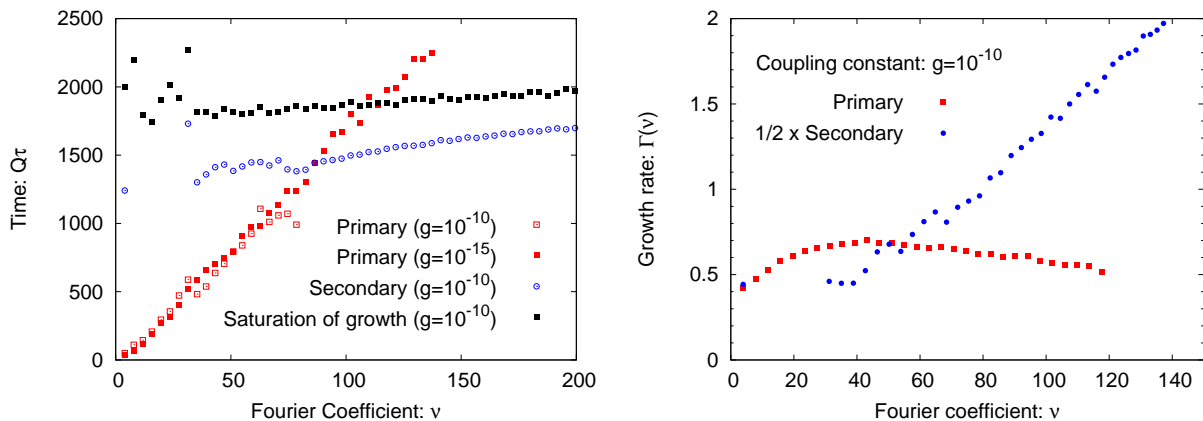


Figure 5.4: **(left)** Set in times of primary and secondary instabilities as a function of rapidity wave number ν . Once secondary instabilities set in, the growth quickly extends to higher rapidity wave numbers. **(right)** Growth rates $\Gamma(\nu)$ as a function of rapidity wave number ν for primary and secondary instabilities.

agates out towards higher momenta. This can be seen in the left panel of Fig. 5.4, where we show the set-in times of primary and secondary growth for two different values of the coupling constant g . One also observes from Fig. 5.4 that for modes with large rapidity wave number $\nu > \nu_c$ secondary instabilities set-in before the primary instability, such that the growth of high ν modes is solely due to non-linear effects. The numerical value of ν_c depends, of course, on the coupling constant, which yields the size of the initial fluctuations relative to the 'Glasma' background fields. While Fig. 5.4 shows that the set-in time for primary instabilities is independent of the coupling constant, we find that secondary instabilities set in at later times for smaller values of the coupling constant. We will confirm the non-linear origin of this phenomenon below, where we present an analytic approach to the non-linear dynamics and investigate the coupling dependence in our simulations.

SATURATION: The growth of primary and secondary instabilities in Fig. 5.3 continues until at some point saturation of the instability sets in and the system has reached non-perturbatively large occupancies. In this regime, we observe that the process of non-linear amplification continues for a short time, even after the growth of the leading primary modes has already saturated. This has a significant impact also on bulk observables such as the ratio of longitudinal pressure to energy density, which we investigate in more detail below.

5.2.3 Dynamical power counting and non-linear dynamics

In view of the striking similarity with the results presented in Chapter 4 in the context of scalar quantum field theories, it appears intuitive to apply a similar analysis to the 'Glasma' dynamics. We will thus turn back to the analytic discussion and analyze the structure of the

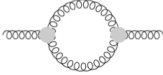
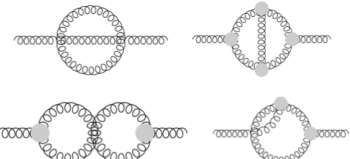
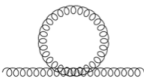
Dynamical power counting		
$\Pi^{(F)}$: one loop  $g^2 F^2, \beta = 1$	$\Pi^{(F)}$: two loop  $g^4 F^3(\rho), \beta = 4/3$	$\Pi^{(0)}$ (local)  $g^2 F, \beta = 2$

Table 5.1: Self energy diagrams to two loop order (g^4). The value β corresponds to the classification in the dynamical power-counting scheme. The one-loop diagram in the left panel yields the first relevant correction, while diagrams with higher values of β become important only at later times.

self-energy corrections in Eqns. (5.13) and (5.14) in the presence of plasma instabilities. Since the associated power counting is similar to the one introduced in Sec. 4.2, in the context of scalar field theories, we will not present all details of the calculation here and refer the interested reader to Ref. [144] instead.

In the dynamical power counting scheme, the self-energy corrections in Eqns. (5.13) and (5.14) can be classified according to powers of the coupling constant g as well as powers of the 'Glasma' background fields $\mathcal{A}_\mu^a(x)$ and the statistical fluctuations $F_{\mu\nu}^{ab}(x, y)$. For a generic self-energy contribution containing powers $g^n F^m A^l \rho^k$, the integers n, m and l yield the suppression factor from the coupling constant (n) as well as the enhancement due to parametrically large 'Glasma' background fields (l) and parametrically large fluctuations (m). The parametric 'weight' of the spectral function (k) remains of order one at all times as encoded in the equal-time commutation relations.

Since the 'Glasma' fields are parametrically large $A_\mu^a(x) \sim 1/g$, one expects a sizable $\mathcal{O}(1)$ self-energy correction once fluctuations have grown as large as $F_{\mu\nu}^{ab}(x, y) \sim 1/g^{(n-l)/m}$ for characteristic modes. The hierarchy emerging from a classification of diagrams in terms of $\beta = (n-l)/m$ is shown in Tab. 5.1. The one loop diagram shown in the left panel contains two three gluon vertices, which give rise to a suppression factor g^2 ($(n-l) = 2$). On the other hand the diagram is enhanced by two statistical propagators in the loop ($m = 2$) and we can classify the overall contribution as $\mathcal{O}(g^2 F^2)$. Similarly, one can analyze the two loop diagrams and the tadpole diagram also depicted in Tab. 5.1. The tadpole diagram contains a suppression factor g^2 from the four gluon vertex ($n = 2, l = 0$) and one statistical propagator ($m = 1$), such that the overall contribution can be classified as $\mathcal{O}(g^2 F)$. The two loop diagrams are of order g^4 ($n-l = 4$) in the coupling constant and contain at most three statistical propagators ($m = 3$).

The overall contribution is thus $\mathcal{O}(g^4 F^3)$ in the dynamical power counting.

The classification in terms of $\beta = (n - l)/m$ shows that the only diagram yielding a contribution to $\beta = 1$ is the one-loop diagram in the left panel of Tab. 5.1. The leading contribution of higher order loop diagrams can be classified as $\beta = 2L/(L + 1)$, where $L \geq 1$ is the number of loops. The tadpole diagram yields $\beta = 2$. Finally, there are self-energy contributions containing powers of the spectral function instead of statistical propagators, which give rise to even higher values of $\beta \geq 2$. In view of the discussion on quantum versus classical-statistical dynamics, we note that this class of diagrams correspond to the genuine quantum corrections, which are not included in the classical-statistical field theory [40, 41]. Since these are highly suppressed at weak coupling, we obtain a direct verification that the classical-statistical framework indeed provides a reliable approximation in this regime.

In analogy to the discussion in Sec. 4.2, this hierarchy of self-energy diagrams determines the on-set of non-linear corrections to the linear instability regime: Since the one-loop diagram in the left panel of Tab. 5.1 is of leading order $\mathcal{O}(g^2 F^2)$ in the dynamical power counting, the contribution of this diagram becomes of $\mathcal{O}(1)$ once statistical fluctuations have grown as large as $\mathcal{O}(1/g)$, whereas all higher order self-energy corrections are still suppressed by at least a fractional power of the coupling constant at this point of the evolution.

Similar to the discussion in Sec. 4.2, the one-loop correction induces a non-linear amplification of the primary instability. The analysis proceeds along similar lines as in Sec. 4.2 and suggests that these secondary instabilities emerge, with growth rates twice as large as the primary ones [144]. If we compare the rates of primary and secondary growth, as shown in the right panel of Fig. 5.4, we find that this is indeed the case for modes with intermediate ν , which exhibit the earliest non-linear amplification. Subsequently, modes with larger values of ν exhibit even higher growth rates, which can be attributed to multiple amplification processes as well as higher order self-energy corrections, which become important at later times of the evolution.

Since the growth of fluctuations in the linear instability regime can be parametrized according to

$$F_{\mu\nu}^{ab}(\tau, \tau', \vec{x}_T, \vec{y}_T, \nu) \propto \exp[\Gamma(\nu)(\sqrt{Q\tau} + \sqrt{Q\tau'})], \quad (5.29)$$

for characteristic modes, we can immediately determine the parametric dependence of the onset

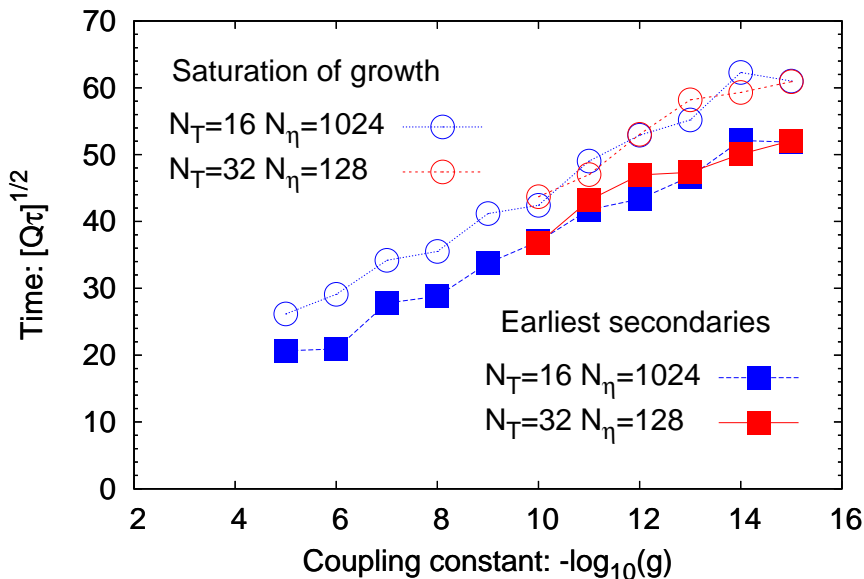


Figure 5.5: Set in times of secondary instabilities and time scale for the saturation of growth as a function of the coupling constant g . Since the coupling constant reflects the size of initial fluctuations relative to the 'Glasma' background fields, one observes a logarithmic dependence in accordance with the analytic discussion.

time of secondary instabilities according to

$$\sqrt{Q\tau_{\text{Secondary}}} \sim \sqrt{Q\tau_{\text{SetIn}}} + \frac{1}{2\Gamma_0} \ln(g^{-2}), \quad (5.30)$$

to leading logarithmic accuracy. Here τ_{SetIn} characterizes the set-in time of primary instabilities and Γ_0 is the characteristic growth rate of primary instabilities. The sub-leading corrections are associated to the spectral distribution of growth rates and set-in times and the spectral distribution of statistical fluctuations in the initial state. The logarithmic dependence on the coupling constant stems from the fact that, the magnitude of non-linear contributions depends exponentially on time according to Eq. (5.29), whereas the dependence on the coupling constant just enters as a power. We also note that this behavior is completely analogous to the discussion in Sec. 4.2, in the context of an expanding scalar field theory.

5.2.4 Coupling dependence

We will now study the dependence of our simulation results on the value of the coupling constant g . Since the range of validity of classical-statistical simulations is confined to the weak coupling regime, we vary the coupling constant g in the range of 10^{-15} to 10^{-5} , for which the classical-statistical framework safely applies. The qualitative behavior is the same as discussed above for all values of g under consideration, i.e. we observe primary instabilities followed by

non-linear amplification and subsequent saturation of the growth. Due to the non-linear origin of these phenomena, the time scales for the set in of secondary instabilities and the saturation of growth depend, of course, on the coupling constant, since the latter characterizes the initial amplitude of fluctuations relative to the 'Glasma' background fields.

The results of our analysis are summarized in Fig. 5.5, where we show the characteristic set-in times of secondary instabilities as well as the time scale when saturation of the instability occurs as a function of the coupling constant g . The (weak) logarithmic dependence observed in Fig. 5.5, can be attributed to the fact that, at early times, the magnitude of non-linear contributions grows exponentially in time according to $\exp[2\Gamma_0\sqrt{Q\tau}]$, whereas the dependence on the coupling constant is just a power. This is in qualitative agreement with the estimate in Eq. (5.30), obtained within the dynamical power counting scheme.

Similarly, one observes from Fig. 5.5, that the time scale for the saturation of exponential growth to occur exhibits the same parametric dependence. Since the latter determines the transition to a new dynamical regime, where the rapid dynamics of instabilities is followed by a very slow evolution, this constitutes one of the central results of the present discussion.

5.2.5 Saturated regime

We will now turn to a more detailed discussion of the saturated regime, and first analyze the evolution of bulk observables, such as the ratio of longitudinal pressure to transverse pressure of the system. While initially the system is extremely anisotropic, one naturally expects plasma instabilities to drive the system towards isotropy [44, 45]. However throughout the evolution, there is a competition between interactions, which tend to isotropize the system, and the longitudinal expansion, which drives the system away from isotropy, that makes the problem highly non-trivial.

In order to analyze this behavior within our simulations, we study the ratio of longitudinal pressure to transverse pressure of the system. The challenge in this analysis comes from the fact that the relevant ultraviolet cutoff associated with longitudinal momentum $\pi/(\tau a_\eta)$ decreases with (proper) time, such that at some point physical scales can no longer be resolved on the lattice. Moreover, a large rapidity cutoff π/a_η can cause severe problems at early times: Since the associated modes initially correspond to large longitudinal momenta, they yield a significant contribution to physical observables and a proper renormalization scheme might be needed to ensure convergent results. We address this problem by choosing the coupling constant g very small, such that the overall contribution of fluctuations to the energy density is less than a percent even for the largest cutoffs under consideration. We then vary the lattice spacing a_η

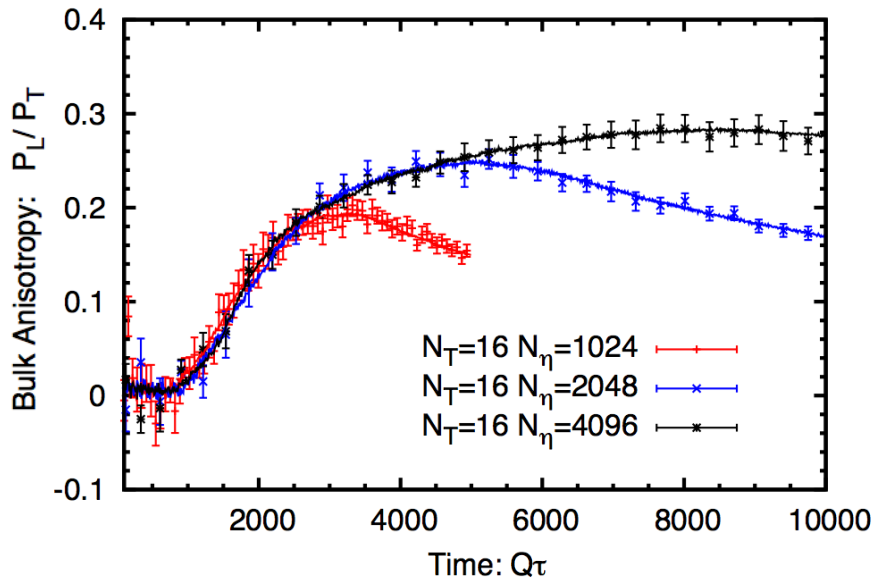


Figure 5.6: Ratio of longitudinal and transverse pressure as a function of time. The different curves correspond to different values of the lattice spacing. One observes a remaining order one anisotropy over a large time scale.

while keeping the size of the system $N_\eta a_\eta$ fixed to study the sensitivity to the lattice cutoff.⁶

The results are presented in Fig. 5.6, where we show the ratio of longitudinal and transverse pressure as a function of time. The results are insensitive of the longitudinal discretization, as long as the lattice spacing a_η is sufficiently small. While at early times the longitudinal pressure of the system is consistent with zero, we observe a clear rise of the longitudinal pressure towards later times. In the saturated regime the trend towards isotropization slows down dramatically and the system exhibits a remaining order one anisotropy over a large time scale. Since, in contrast to earlier expectations [44, 45], plasma instabilities are clearly not able to isotropize the system, we will now turn to a more detailed study of the evolution at later times.

⁶Note that, in response to our analysis, a new algorithm has recently been proposed in Ref. [162] to address this problem.

5.3 Turbulent thermalization

In this section, we will address the dynamics of the system at later times $Q\tau \gtrsim \log^2(\alpha_S^{-1})$, subsequent to the regime of plasma instabilities. This regime has been subject to several studies in the framework of kinetic theory, and different scenarios have been developed to describe the thermalization process at weak coupling [29–32]. However, since the available parametric estimates allow for different types of solutions of the employed kinetic equations, further progress relies on the ability to identify the correct attractor solution in this regime [23]. Since classical-statistical lattice gauge theory and kinetic theory have an overlapping range of validity [68, 163], real time lattice simulations can be used to unambiguously determine the solution from first principles.

In view of the discussion in Chapter 3, this is also the regime, where one expects to observe universal features of the evolution. However, since the longitudinal expansion leads to a dilution of the system and renders the plasma anisotropic on large time scales, it is by no means obvious, how the concepts developed in Chapter 3 apply in this situation. Nevertheless, we will discover shortly, that the dynamics at late times is indeed governed by a universal attractor, which exhibits a self-similar evolution characteristic of wave turbulence [34].

5.3.1 Initial conditions

Since we will be interested in universal features of the evolution, it is clear that the details of the initial conditions quickly become irrelevant for the evolution at late times. Nevertheless, it is important to connect to the discussion in Sec. 5.2, where we studied the non-equilibrium dynamics of the preceding ‘Glasma’ stage: In accordance with the discussion in the literature [30, 32], we expect that at later times of the evolution $Q\tau_0 \sim \log^2(\alpha_S^{-1})$, the plasma can be described in terms of quasi-particle excitations, which result from the preceding decay of the unstable ‘Glasma’ fields. The ensuing over-populated plasma can then be characterized in terms of the gluon distribution function $f(\vec{p}_T, p_z, \tau_0)$, which describes the mode occupancy averaged over spin and color degrees of freedom. Instead of simulating the entire evolution of the system, starting from the early ‘Glasma’ stages, we will employ a more general set of initial conditions according to the distribution

$$f(\vec{p}_T, p_z, \tau_0) = \frac{n_0}{2g^2} \Theta\left(Q - \sqrt{\vec{p}_T^2 + (\xi_0 p_z)^2}\right), \quad (5.31)$$

which describes the overpopulation of gluon modes up to the momentum Q at times $Q\tau_0 \sim \log^2(\alpha_S^{-1})$ after the collision of heavy nuclei. The parameter n_0 can be used to adjust the initial

occupancy, while ξ_0 parametrizes the residual anisotropy in momentum space.

In order to investigate a preferably large range of initial conditions, we will vary the parameters n_0 and ξ_0 and study their effect on the evolution. In a first step, the initial time is chosen as $Q\tau_0 = 100$ to minimize discretization errors, while accessing sufficiently late times $\tau \gg \tau_0$ in order to observe universal aspects of the evolution.⁷ We will verify later, that varying the initial time in a range $Q\tau_0 = 20 - 1000$ only affects the transient evolution but does not change the universal properties at later times.

The Gaussian initial conditions in Eq. (5.31) can be implemented in a straightforward way: We impose the Coulomb type gauge condition $\partial_i A_i + \tau^{-2} \partial_\eta A_\eta = 0$ at initial time τ_0 and initialize the fields as a superposition of transversely polarized gluon modes according to

$$\begin{aligned} A_\mu^a(\tau_0, \eta, \vec{x}_T) &= \sum_\lambda \int \frac{d^2 \vec{k}_T}{(2\pi)^2} \frac{d\nu}{2\pi} \sqrt{f(\vec{k}_T, \nu, \tau_0)} \left[c_{\lambda,a}^{\vec{k}_T\nu} \xi_{\mu,a}^{(\lambda)\vec{k}_T\nu+}(\tau_0) e^{i\vec{k}_T \vec{x}_T} e^{i\nu\eta} + c.c. \right], \\ E_a^\mu(\tau_0, \eta, \vec{x}_T) &= -\tau_0 g^{\mu\nu} \sum_\lambda \int \frac{d^2 \vec{k}_T}{(2\pi)^2} \frac{d\nu}{2\pi} \sqrt{f(\vec{k}_T, \nu, \tau_0)} \left[c_{\lambda,a}^{\vec{k}_T\nu} \dot{\xi}_{\nu,a}^{(\lambda)\vec{k}_T\nu+}(\tau_0) e^{i\vec{k}_T \vec{x}_T} e^{i\nu\eta} + c.c. \right]. \end{aligned} \quad (5.32)$$

Here $\xi_{\mu,a}^{(\lambda)\vec{k}_T\nu+}(\tau)$ denote the (time dependent) transverse polarization vectors in the non-interacting theory, given in Appendix C, *c.c.* denotes complex conjugation and the complex Gaussian random numbers $c_{\lambda,a}^{\vec{k}_T\nu}$ satisfy the relations

$$\langle c_{\lambda,a}^{\vec{k}_T\nu} c_{\lambda',b}^{*\vec{k}'_T\nu'} \rangle = \delta_{\lambda\lambda'} \delta_{ab} (2\pi)^3 \delta^{(2)}(\vec{k}_T - \vec{k}'_T) \delta(\nu - \nu'), \quad (5.33)$$

whereas $\langle c_{\lambda,a}^{\vec{k}_T\nu} c_{\lambda',b}^{\vec{k}'_T\nu'} \rangle = \langle c_{\lambda,a}^{*\vec{k}_T\nu} c_{\lambda',b}^{*\vec{k}'_T\nu'} \rangle = 0$ as usual. We note that by use of the relations in Sec. 2.4, this reproduces the occupation number in Eq. (5.31) at initial time $\tau = \tau_0$. We also verified explicitly, that the occupation number is conserved throughout the time evolution in the non-interacting theory.⁸

5.3.2 Universal scaling

In order to connect to the discussion in Sec. 5.2, we first study the evolution of the bulk anisotropy of the system. In Fig. 5.7 we show the ratio of longitudinal to transverse pressure of

⁷In view of the parametric estimate $Q\tau_0 \sim \log^2(\alpha_s^{-1})$, this corresponds to gauge couplings on the order of 10^{-4} .

⁸This can be achieved by initializing only a non-vanishing $a = 1$ component in our simulations, whereas all other components vanish identically. In this case, one recovers a (compact) $U(1)$ theory.

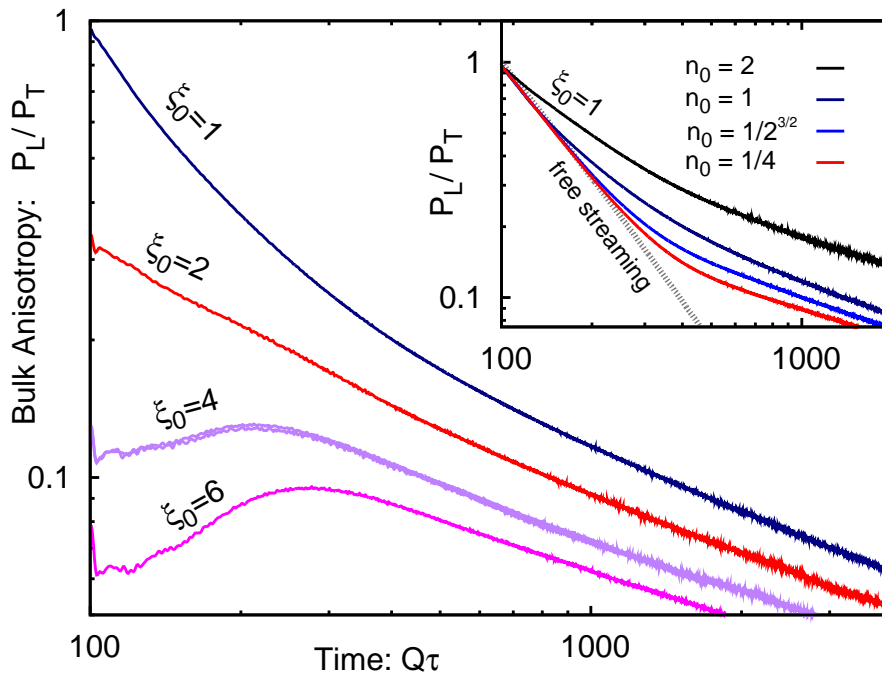


Figure 5.7: Ratio of longitudinal to transverse pressure as a function of time for different initial anisotropies ξ_0 and fixed initial occupancy $n_0 = 1$. The inset shows the same quantity for initially isotropic systems ($\xi_0 = 1$) and different initial occupancies n_0 along with the free streaming (dashed) curve.

the system P_L/P_T as a function of time. The curves in the main graph are for different initial anisotropies ξ_0 and fixed initial occupancy $n_0 = 1$. The curve for $\xi_0 = 1$ corresponds to an initially isotropic system, whereas for higher initial anisotropies $\xi_0 = 4, 6$ the observed behavior at early times smoothly matches onto the ‘Glasma’ evolution discussed in Sec. 5.2.

Starting from an isotropic initial distribution ($\xi_0 = 1$), the system is seen to become more and more anisotropic with time as a consequence of the longitudinal expansion. Indeed, the early-time behavior is governed by free streaming, whereas at later times the anisotropy of the system increases more slowly as a consequence of interactions. This feature is elaborated further in the inset, where the free streaming (dashed) curve is shown for comparison, along with results for different initial occupancies n_0 and fixed $\xi_0 = 1$. One observes that initially more dilute systems ($n_0 < 1$) exhibit a longer period of free-streaming behavior, while at late times a similar scaling behavior can be observed. For strong initial anisotropy, such as for $\xi_0 = 4$ and 6, there is a short transient regime where P_L/P_T increases due to plasma instabilities. Most remarkably, this does not affect the evolution at later times: After the transient regime all curves show very similar scaling with time, irrespective of the choice of initial conditions.

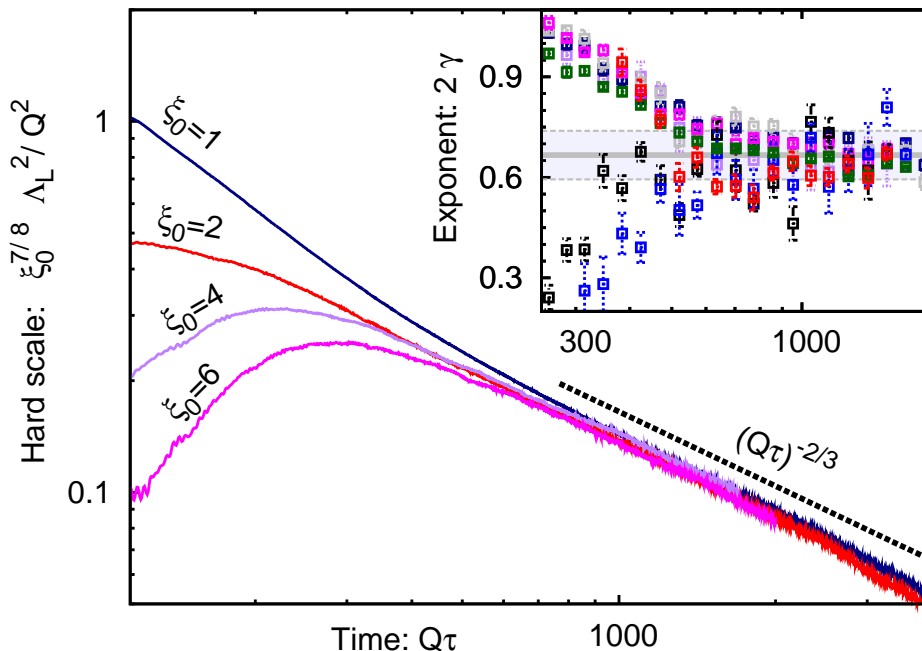


Figure 5.8: Time evolution of the characteristic longitudinal momentum scale for different initial anisotropies ξ_0 . The inset shows the scaling exponent extracted for different initial conditions and lattice discretizations. The average $2\gamma = 0.67 \pm 0.07$ is indicated by gray lines.

In order to analyze this behavior in more detail, we study the time evolution of the transverse and longitudinal hard momentum scales Λ_T and Λ_L , which characterize the typical transverse and longitudinal momenta of hard excitations. These gauge-invariant observables can be computed from longitudinal and transverse projections of the square of the covariant derivative of field strengths divided by the energy density (c.f. Sec. 2.4). The perturbative expression for Λ_L^2 – considering only the abelian parts of the field strength tensor and the covariant derivative – is given by (c.f. Eq. (2.85))

$$\Lambda_L^2(\tau) \simeq \frac{\int d^2 p_T \int dp_z p_z^2 \omega_p f(p_T, p_z, \tau)}{\int d^2 p_T \int dp_z \omega_p f(p_T, p_z, \tau)}. \quad (5.34)$$

and similarly for Λ_T^2 , as discussed in Appendix E. An advantage of the hard scale observables, compared to the components of the stress energy tensor, is that they generally probe harder excitations of the system. This concerns in particular the longitudinal components: While the longitudinal pressure P_L is dominated by excitations with relatively small transverse momenta, the longitudinal and transverse hard scales Λ_L and Λ_T probe the system at the same characteristic momentum scale and thus allow for a straightforward interpretation in terms of a kinetic description.

The time evolution of the longitudinal hard scale Λ_L^2 is shown in Fig. 5.8, for different initial anisotropies ξ_0 and fixed initial occupancy $n_0 = 1$, where we rescaled the vertical axis by a factor of $\xi_0^{7/8}$, to illustrate the universal character of the evolution. After the transient regime, for $Q\tau \gtrsim 650$ one clearly observes the emergence of a universal power-law dependence. This universal behavior of the hard scales can be characterized in terms of the scaling exponents γ and β as

$$\Lambda_L^2(\tau) \propto (Q\tau)^{-2\gamma}, \quad \Lambda_T^2(\tau) \propto (Q\tau)^{-2\beta}. \quad (5.35)$$

Comparison to the dashed curve $\propto (Q\tau)^{-2/3}$ in Fig. 5.8 indicates an approximate value of $\gamma \simeq 1/3$. This has to be seen in contrast to a free-streaming system, where one obtains $\gamma = 1$ due to the red-shift of longitudinal momenta.⁹ Therefore, the observed value of $\gamma \simeq 1/3$ can only be explained due to strong interactions of the system, which continuously increase the longitudinal momenta of excitations relative to the free streaming behavior. Hence, the observed behavior is a direct verification of the fact that the system remains strongly interacting throughout the entire evolution.

In order to determine the scaling exponent γ more precisely, we first divide the data in Fig. 5.8 in logarithmic equidistant time bins and then locally extract the scaling exponent from the logarithmic derivative. The result is shown in the inset of Fig. 5.8, where we present the extracted scaling exponent of Λ_L^2 as a function of time for a set of four different initial conditions in the range $\xi_0 = 1 - 6$ and $n_0 = 0.25 - 1$. To check for a possible further dependence on lattice discretizations, we also display results from the evolution for $\xi_0 = n_0 = 1$ using four different lattices in the range $N_T = 256 - 512$, $N_\eta = 1024 - 4096$ with $Qa_\perp = 0.5 - 1$ and $a_\eta = (0.625 - 2.5) \cdot 10^{-3}$. After the transient regime, where the local exponents are quite different for different initial conditions and subject to large error bars, one observes a clear convergence towards a single value at later times. By averaging over all data points for $Q\tau \gtrsim 650$ we obtain the estimate $2\gamma = 0.67 \pm 0.07$, as indicated by the gray band in Fig. 5.8.

In Fig. 5.9 we show the time evolution of the characteristic transverse momentum scale Λ_T for different initial occupancies n_0 and fixed initial anisotropy $\xi_0 = 1$. After an initial hardening, one observes that in the scaling regime, for $Q\tau \gtrsim 650$ the characteristic transverse momentum scale Λ_T stays approximately constant in time. This corresponds to $\beta \simeq 0$, which we investigate in the inset of Fig. 5.9, where the local scaling exponent 2β is plotted as a function of time. Indeed, the local scaling exponent extracted from our data approaches zero monotonically with $|\beta| < 0.04$ for $Q\tau \gtrsim 650$. In general, we observe that the errors are not dominated by the finite lattice size but rather by the remaining dependence on the initial conditions for the available

⁹Note that in the free-streaming case, the scaling behavior arises not due to universality, but simply due to the absence of interactions.

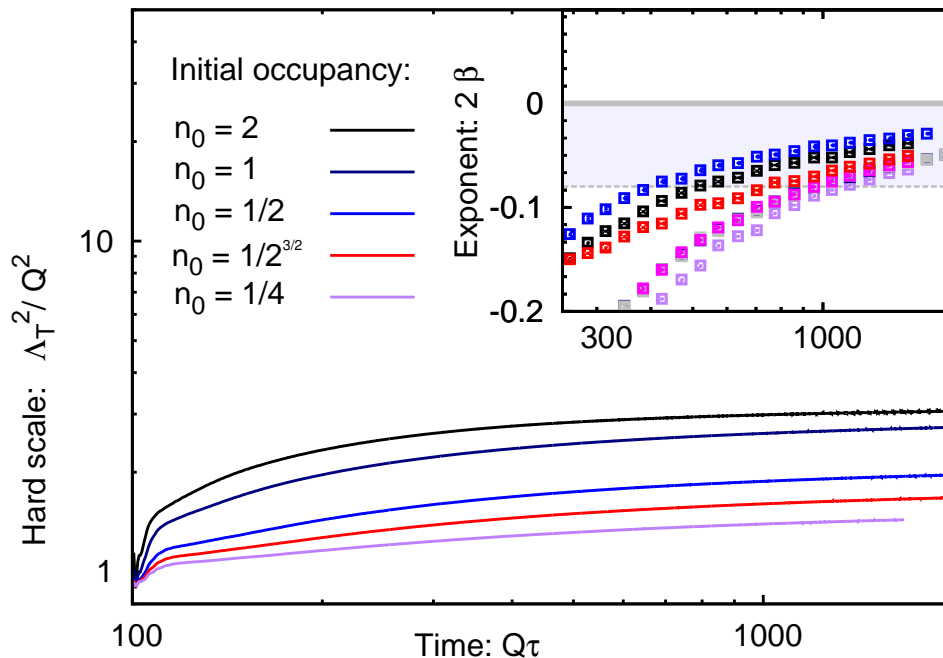


Figure 5.9: Time evolution of the characteristic transverse momentum scale for different initial occupancies n_0 . The curves show an approximately constant behavior in the scaling regime. The inset shows the scaling exponent extracted for different initial conditions and lattice discretizations. The scaling exponent 2β approaches zero monotonically.

finite times. This is remarkable, given the fact, that one is dealing with a dynamical three scale problem, characterized by the hard momentum scales Λ_T and Λ_L , as well as the soft Debye scale, which is relevant also for the physics of plasma instabilities [31, 32]. We have checked explicitly that in our simulations, all scales are properly resolved on the large lattices.

We will now also consider variations of the initial time and first study the dynamics for a smaller value of $Q\tau_0 = 20$. This strengthens the role of the longitudinal expansion, since the initial expansion rate $\sim 1/\tau_0$ increases relative to the initial interaction rate $\sim Q^{-1}$. The results are presented in Fig. (5.10), where we show the ratio of the longitudinal to transverse hard scale Λ_L^2/Λ_T^2 as a function of time. The curves in the main graph correspond to different values of the initial anisotropy ξ_0 for fixed initial occupancy $n_0 = 2$. The inset shows the variation of the initial occupancy n_0 for a fixed value of $\xi_0 = 1$, corresponding to initially isotropic systems. At early times, one observes a faster decrease of the hard scale ratio, which follows the free-streaming behavior for sufficiently small occupancies. Nevertheless, one clearly observes the universal scaling behavior at later times. We also extracted the scaling exponents 2γ and 2β using the same analysis technique introduced above. While we observe a smaller residual dependence on the initial conditions, the lattice discretization becomes more

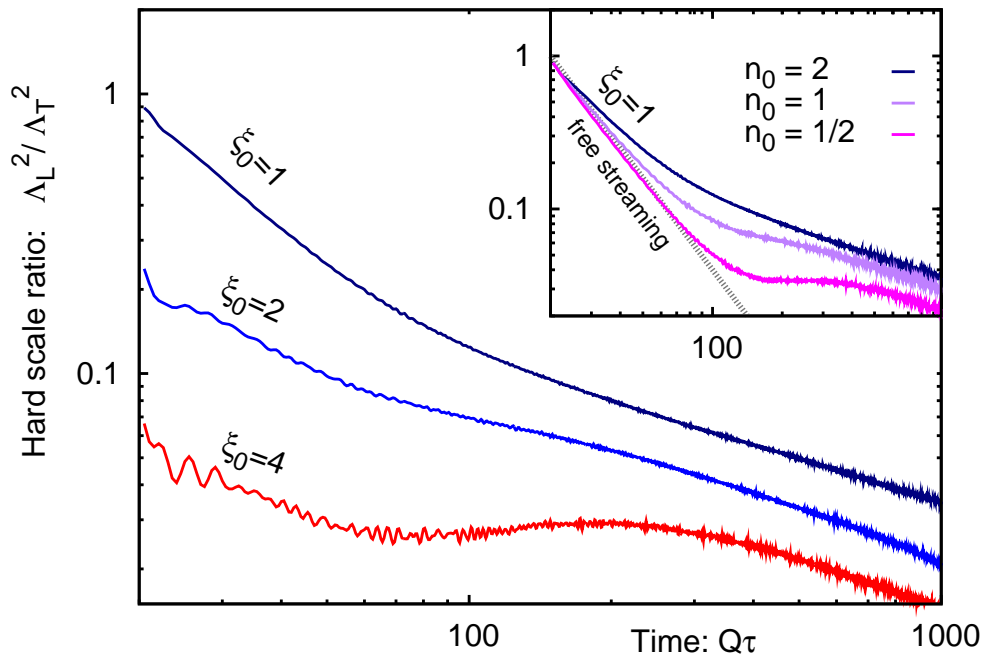


Figure 5.10: Time evolution of the ratio of the longitudinal hard scale to the transverse hard scale for different initial anisotropies ξ_0 and initial occupancy $n_0 = 2$. The inset shows the same quantity for initially isotropic systems ($\xi_0 = 1$) and different initial occupancies n_0 . Note that, in contrast to Figs. 5.8 and 5.9, the initial time is chosen as $Q\tau_0 = 20$, which increases the relative strength of the longitudinal expansion. However, after the transient regime, for $Q\tau \gtrsim 250$ one still observes the same universal scaling behavior.

problematic in this case due to the stronger expansion. The scaling exponents in this case are given by $2\gamma = 0.57 \pm 0.7$ and $|\beta| \lesssim 0.025$, which agree with the previous estimates within errors.

It is also interesting to study the case $Q\tau_0 \gg 1$, where the interaction rate $\sim Q$ is initially much larger than the expansion rate $\sim 1/\tau_0$. In this situation one expects to recover the results for non-expanding systems (c.f. Chapter 3) at early times $\sim Q^{-1}$, whereas at later times $\sim \tau_0$, the expansion starts to play an important role and one expects a transition to the universal scaling solution for expanding systems. In order to investigate this behavior in more detail, we chose a large value of $Q\tau_0 = 1000$, to achieve a clear separation between different time scales. The results are presented in Fig. 5.11. In the top panel, we show the evolution of the longitudinal and transverse hard scales as a function of time. At early times, $(\tau - \tau_0) \lesssim \tau_0$ one observes an approximate scaling of $\Lambda_T^2 \propto (\tau - \tau_0)^{2/7}$ as previously observed for non-expanding systems [88, 91]. This is indicated by the gray dashed line. At later times $(\tau - \tau_0) \gtrsim \tau_0$ the transverse hard scale Λ_T^2 becomes approximately constant in time, whereas the longitudinal hard scale Λ_L^2 exhibits an approximate $(\tau - \tau_0)^{-2/3}$ scaling, characteristic of the attractor solu-

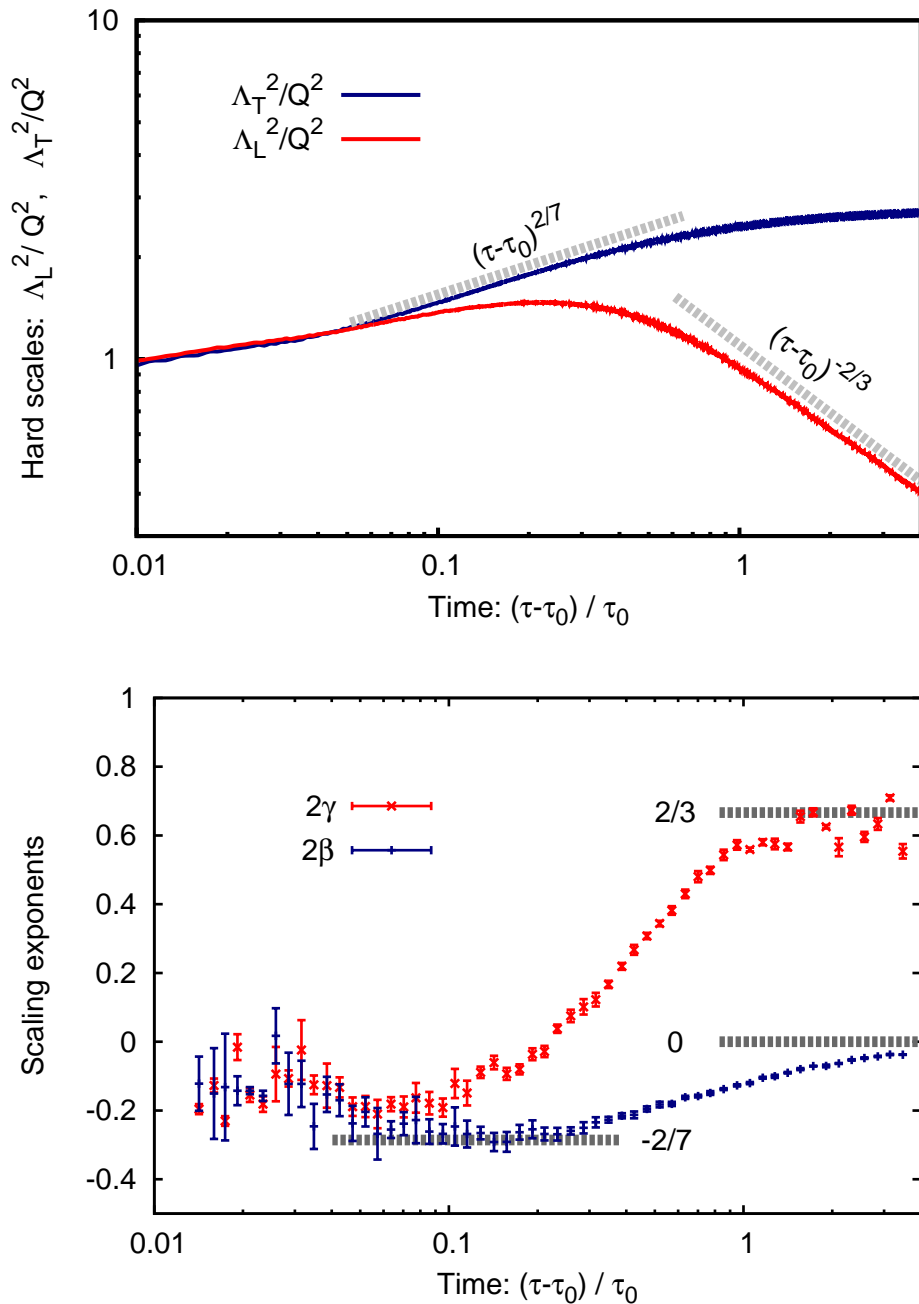


Figure 5.11: **(top)** Time evolution of the transverse and longitudinal hard scales, for slowly expanding systems ($Q\tau_0 = 1000$). One observes a transient regime where the transverse hard scale Λ_T^2 shows an approximate $(\tau - \tau_0)^{2/7}$ scaling, as indicated by the gray (dashed) line. At later times, Λ_T^2 becomes approximately constant, whereas Λ_L^2 exhibits the characteristic $(\tau - \tau_0)^{-2/3}$ scaling. **(bottom)** The lower panel shows the local scaling exponents 2β and 2γ , associated to the evolution of Λ_T^2 and Λ_L^2 respectively. One clearly observes the emergence of different scaling regimes.

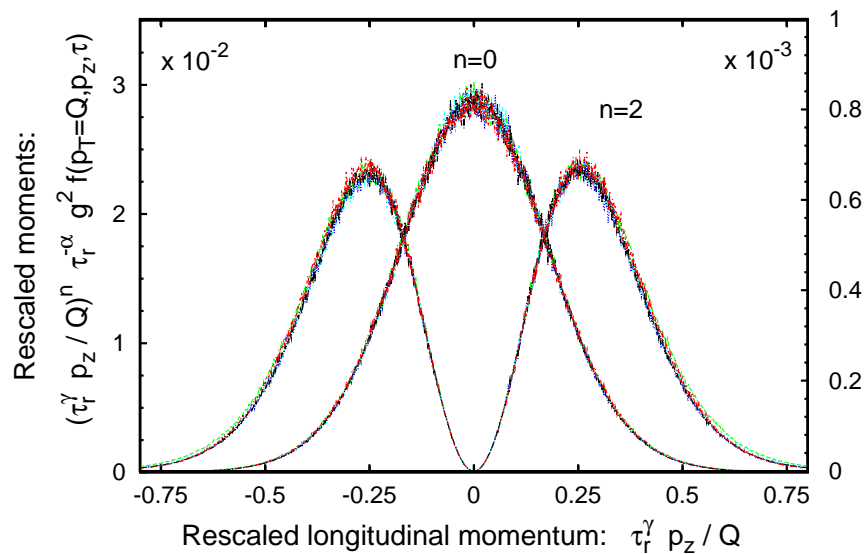


Figure 5.12: Rescaled moments of the distribution function as a function of the rescaled longitudinal momentum. The rescaled data for different times all collapse onto a single curve.

tion for longitudinally expanding systems.¹⁰ This transition between the different attractors is elaborated in the lower panel of Fig. 5.11, where we show the scaling exponents 2β and 2γ as a function of time. One observes a transient regime, where the 'static box' exponent $2\beta \simeq -2/7$ is realized. The behavior at late times is similar to the one observed in Figs. 5.8 and 5.9. One observes the scaling exponent $2\gamma \simeq 2/3$ for the longitudinal hard scale, whereas the exponent 2β for the transverse hard scale approaches zero monotonically from below.

5.3.3 Self-similarity

So far we have only considered gauge invariant observables to characterize the evolution of the different scales of the problem. However, a striking property of turbulent phenomena is the fact that these systems exhibit a self-similar evolution in time [34, 91]. To analyze this behavior, we will now study the time evolution of the gluon distribution function $f(p_T, p_z, \tau)$, which we extract from gauge fixed equal time correlation functions as discussed in Sec. 2.4. In terms of the gluon distribution function $f(p_T, p_z, \tau)$, a self-similar evolution has to fulfill the condition

$$f(p_T, p_z, \tau) = \tau^\alpha f_S(\tau^\beta p_T, \tau^\gamma p_z), \quad (5.36)$$

where f_S denotes a *stationary* distribution independent of time. The scaling exponents α , β and γ are universal, as is the stationary scaling function up to amplitude normalizations. The

¹⁰Note that at late times $\tau \gg \tau_0$ this corresponds also to scaling in $Q\tau^{-2/3}$ as observed in Fig. 5.8.

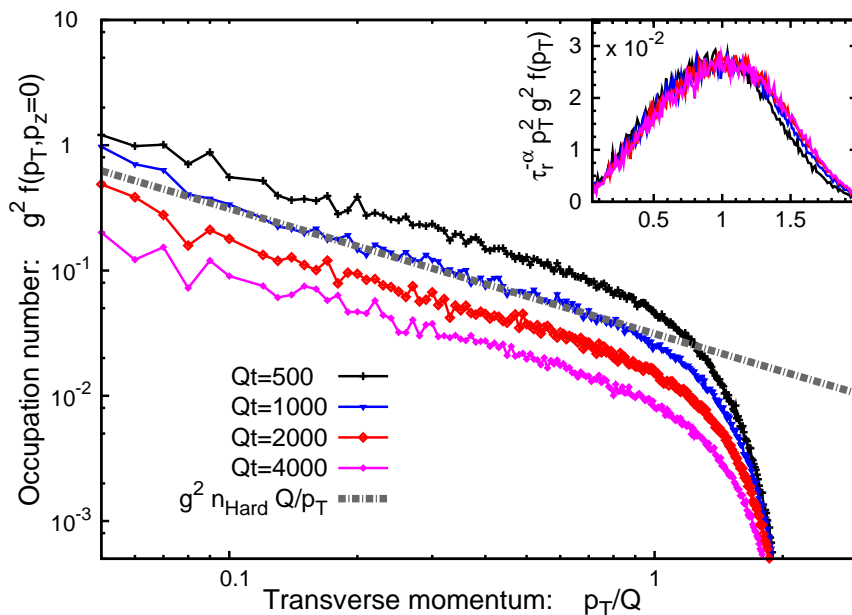


Figure 5.13: Dependence of the gluon distribution function on transverse momentum p_T for $p_z = 0$ at different times. The inset shows the self-similar evolution for the rescaled second moment of the distribution as a function of transverse momentum p_T for vanishing longitudinal momentum $p_z = 0$.

scaling exponents β and γ agree with the previous definition in Eq. (5.35), as can be verified by evaluating the perturbative expression for the hard scales in Eq. (5.34). Hence, the parametrization in Eq. (5.36) effectively amounts to measuring momenta in units of the characteristic momentum scales Λ_T and Λ_L respectively, as can directly be observed from Eq. (5.35).

In order to investigate the emergence of a self-similar scaling solution in our simulations, we study the time evolution of the gluon distribution function. Fig. 5.12 shows the rescaled zeroth and second moment of the gluon distribution as a function of rescaled longitudinal momentum $\tau_r^\gamma p_z$ for transverse momenta $p_T = Q$. Here we used $\tau_r \equiv Q\tau/10^3$ as the reference time and employed the scaling exponents $\alpha = -0.8$ and $\gamma = 0.28$. The rescaled data for different times in the range from $Q\tau = 750$ to 4000 is seen to collapse onto a single curve. This is a striking manifestation of self-similarity.

Fig. 5.13 displays the distribution, now as a function of transverse momentum p_T for vanishing longitudinal momentum ($p_z = 0$) at different times. The spectrum can be characterized as a thermal-like $1/p_T$ power-law over a large range of transverse momenta $p_T \lesssim \Lambda_T$ with a rapid fall-off for $p_T \gtrsim \Lambda_T$. Indeed, the position of Λ_T is seen to remain approximately constant

in time and the spectrum exhibits a self-similar evolution with a decreasing amplitude

$$n_{\text{Hard}}(\tau) = f(p_T = Q, p_z = 0, \tau) . \quad (5.37)$$

In the inset of Fig. 5.13, the rescaled second moment of the distribution, $\tau_r^{-\alpha} p_T^2 f(p_T, p_z = 0, \tau)$, is shown on a linear scale. Again, the results at different times nicely collapse onto a single curve to good accuracy.

In order to determine the scaling exponent α , we have employed a simultaneous least squares fit to self-similar behavior of the zeroth to fourth moment of the distribution function. Here it is advantageous to estimate the combination $\alpha - \gamma$, to reduce the covariance with the fit of γ , which can be determined independently from the analysis of the hard scales. Our data shows that $\alpha - \gamma = -1 - \Delta$ with a monotonically decreasing $\Delta < 0.13$ for $Q\tau \gtrsim 650$. Taking into account our above estimate for γ , this leads to $\alpha = -0.67 \pm 0.04 - \Delta$. Comparing the statistical uncertainty to the systematic error Δ , one observes that the dominant source of error is again the fact that the scaling limit is only approximately realized for the available finite times.

5.3.4 Analytic approach to turbulence

We will now provide a simple explanation of the characteristic scaling behavior observed in our simulations. In the framework of kinetic theory, the time evolution of the gluon distribution is described by a Boltzmann equation of the form [29, 30, 32]

$$\left[\partial_\tau - \frac{p_z}{\tau} \partial_{p_z} \right] f(p_T, p_z, \tau) = C[p_T, p_z, \tau; f] , \quad (5.38)$$

with a generic collision term $C[p_T, p_z, \tau; f]$ for $n \leftrightarrow m$ scattering processes. Here the additional term on the left hand side of Eq. (5.38) represents the red-shift of longitudinal momenta and thus captures the effects of the longitudinal expansion of the system. We follow here the standard turbulence analysis [34], for a self-similar evolution of the type given by Eq. (5.36). In this analysis, the scaling behavior of the collision integral

$$C[p_T, p_z, \tau; f] = \tau^\mu C[\tau^\beta p_T, \tau^\gamma p_z; f_S] \quad (5.39)$$

is described in terms of the exponent $\mu = \mu(\alpha, \beta, \gamma)$, whose precise form depends on the underlying interaction. Substituting this form into the Boltzmann equation (5.38), one finds that the fixed point solution $f_S(p_T, p_z)$ satisfies the relation

$$\alpha f_S(p_T, p_z) + \beta p_T \partial_{p_T} f_S(p_T, p_z) + (\gamma - 1) p_z \partial_{p_z} f_S(p_T, p_z) = C[p_T, p_z; f_S] , \quad (5.40)$$

with the scaling condition,

$$\alpha - 1 = \mu(\alpha, \beta, \gamma) . \quad (5.41)$$

As previously argued by Baier, Mueller, Schiff and Son in the “bottom-up” scenario (henceforth labeled BMSS) [29], the interaction of hard excitations is dominated by elastic scattering with small momentum transfer, as long as their occupancies are large ($n_{\text{Hard}} \gg 1$). The dominant effect of these collisions on the particle distribution $f(p_T, p_z, \tau)$ is to broaden the longitudinal momentum distribution by multiple incoherent small-angle scatterings. This broadening of the gluon distribution in longitudinal momentum may be characterized by a collision integral of the Fokker-Planck type,

$$C^{(\text{elast})}[p_T, p_z; f] = \hat{q} \partial_{p_z}^2 f(p_T, p_z, \tau) , \quad (5.42)$$

where the momentum diffusion parameter \hat{q} in this expression is parametrically given by [30, 31]

$$\hat{q} \sim \alpha_S^2 \int \frac{d^2 p_T}{(2\pi)^2} \int \frac{dp_z}{2\pi} f^2(p_T, p_z, \tau) \quad (5.43)$$

in the limit of high occupancies. This approximation is supposed to describe the dominant physics relevant for the overall scaling with time, which enters the scaling relation (5.41) considered in the following. However, it does not have to be an accurate approximation for the solution of the fixed-point equation (5.40), which in general requires more detailed information about the momentum dependence of the collision integral.¹¹

The scaling properties of the collision integral in Eq. (5.42) lead to $\mu(\alpha, \beta, \gamma) = 3\alpha - 2\beta + \gamma$ for the self-similar distribution as in Eq. (5.36). The scaling relation in Eq. (5.41) obtained from the Boltzmann equation then takes the form

$$2\alpha - 2\beta + \gamma + 1 = 0 . \quad (\text{Small angle scattering}) \quad (5.44)$$

Since the elastic scattering kernel in Eq. (5.42) is particle number conserving, a further scaling relation is obtained from integrating the distribution function over p_T and rapidity wave numbers $\nu = \tau p_z$. By use of the scaling form in Eq. (5.36), this constraint leads to the scaling

¹¹This can already be observed from the discussion in Chapter 3 in Minkowski space, where the small angle approximation reproduces the correct scaling in time, while it fails to describe the spectral properties of the fixed point correctly [87, 88, 91].

relation

$$\alpha - 2\beta - \gamma + 1 = 0. \quad (\text{Particle Number conservation}) \quad (5.45)$$

A corresponding scaling relation can be extracted from energy conservation. Taking into account that the mode energy behaves as $\omega_p \simeq p_T$ in the anisotropic scaling limit, this yields the condition

$$\alpha - 3\beta - \gamma + 1 = 0. \quad (\text{Energy conservation}) \quad (5.46)$$

The scaling exponents α, β, γ are then completely determined by the three scaling relations for particle number conservation, energy conservation and small-angle elastic scattering as incorporated in the BMSS kinetic approach. This yields the set of scaling exponents

$$\alpha = -2/3, \quad \beta = 0, \quad \gamma = 1/3, \quad (5.47)$$

as the final result, which is in excellent agreement with our lattice simulation results.

The above fixed point solution has the remarkable property, that both energy and particle number are conserved in a single turbulent cascade. In particular, this is in contrast to non-expanding isotropic systems, where enforcing both particle number and energy conservation for a single cascade, leads to the scaling relations

$$\begin{aligned} \alpha - 3\beta &= 0, & (\text{Particle number conservation}) \\ \alpha - 4\beta &= 0, & (\text{Energy conservation}) \end{aligned} \quad (5.48)$$

where we set $\beta = \gamma$ for isotropic systems.¹² Since the Eqns. (5.48) do not allow for non-trivial solutions, there is no single turbulent cascade conserving both energy and particle number. Instead, a dual cascade emerges in the situation, where both particle number and energy conservation apply [35]. In contrast, in the longitudinally expanding case, the anisotropy of the system allows for different scaling exponents $\beta \neq \gamma$, which lead to non-trivial solutions of the corresponding scaling relations in Eqns. (5.45) and (5.46). In this context, it is also interesting to observe that the exponent $\beta = 0$ is entirely fixed by enforcing both conservation laws, without further knowledge about the underlying dynamics. We therefore expect the exponent $\beta = 0$ to appear also for a larger class of systems, which are dominated by elastic interactions and undergo a longitudinal expansion.¹³

¹²Note that, the relations in Eq. (5.48) can then directly be obtained from Eqns. (5.45) and (5.46) by dropping the additional summand 1, which appears solely due to the longitudinal expansion.

¹³This includes in particular $O(N)$ symmetric scalar quantum field theories, where inelastic processes are

5.3.5 The attractor

Besides the BMSS scenario, alternative thermalization scenarios at weak coupling with different attractor solutions have been proposed in the literature. In the (KM) scenario [32], it is argued that plasma instabilities play a key role for the entire evolution since they lead to a more efficient process to increase the longitudinal momenta of hard excitations. The evolution in the KM scenario can be characterized by the scaling exponents,

$$\alpha = -7/8, \quad \beta = 0, \quad \gamma = 1/8, \quad (\text{KM scenario}) \quad (5.49)$$

such that the characteristic longitudinal momenta decrease much slower as compared to the BMSS evolution. In the (BGLMV) scenario [30] elastic scattering and transient Bose-Einstein condensation is argued to generate an attractor with fixed anisotropy parameter δ_s . The evolution in this case proceeds with the scaling exponents

$$\alpha = -(3 - \delta_s)/7, \quad \beta = (1 + 2\delta_s)/7, \quad \gamma = (1 + 2\delta_s)/7, \quad (\text{BGLMV scenario}) \quad (5.50)$$

such that the momentum space anisotropy of the system Λ_L/Λ_T remains constant in time.

In order to clearly distinguish between the different attractor scenarios, we investigate the evolution of the plasma in the occupancy–anisotropy plane, originally introduced in Refs. [31, 32]. Our findings are compactly summarized in Fig. 5.14, where we compare the observed time evolution to the different attractor scenarios. The horizontal axis shows the characteristic occupancy n_{Hard} as defined in Eq. (5.37), in the classical regime of occupancies $n_{\text{Hard}} \gtrsim 1$. The vertical axis shows the momentum-space anisotropy, which can be characterized in terms of the ratio of typical longitudinal momenta Λ_L to the typical transverse momenta Λ_T . The gray lines in Fig. 5.14 indicate the different attractor scenarios, while the blue lines show a projection of our simulation results to the anisotropy-occupancy plane for different initial conditions, indicated by blue dots. One clearly observes the attractor property, such that ultimately all curves exhibit a similar evolution along the diagonal. This is in very good agreement with the above analytic discussion of the BMSS kinetic equation in the high-occupancy regime.

By extrapolating our results to later times, we can also estimate the time scale to enter the quantum regime, where the characteristic occupancies n_{Hard} become of order unity. Since initially the occupancy is parametrically given by $n_{\text{Hard}} \sim \alpha_S^{-1}$, and subsequently decreases as $n_{\text{Hard}} \propto (Q\tau)^{-2/3}$, this leads to the estimate

$$\tau_{\text{Quantum}} \sim Q^{-1} \alpha_S^{-3/2}, \quad (5.51)$$

highly suppressed compared to elastic scattering [43].

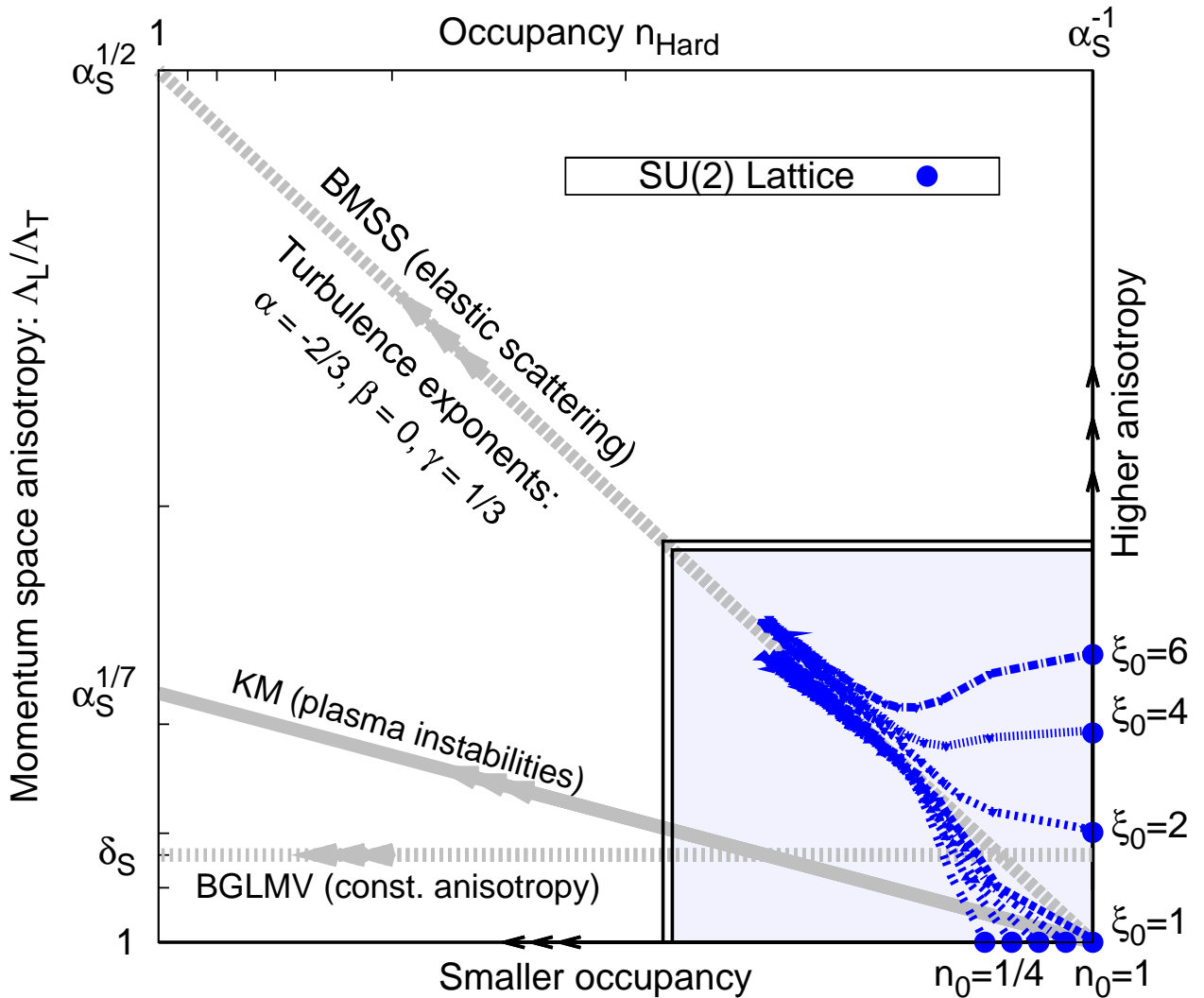


Figure 5.14: Evolution in the occupancy–anisotropy plane. Indicated are the attractor solutions proposed in (BMSS) [29], (KM) [32] and (BGLMV) [30]. The blue lines show the results of classical-statistical lattice simulations for different initial conditions.

in accordance with the original “bottom-up” thermalization scenario [29]. In the quantum regime $Q\tau \gtrsim \alpha_S^{-3/2}$, the classical-statistical framework can no longer be applied and modifications of the above kinetic equations need to be considered. While different scenarios of how thermalization is completed in the quantum regime have been developed based on kinetic descriptions [29, 32], it remains an open question how to address the quantum dynamics in non-abelian gauge theories from a first principles approach.

5.4 Discussion

We close this chapter with a brief summary of our results and a discussion of possible implications for relativistic heavy-ion collisions at RHIC and LHC energies. As outlined in the introduction, this has been a major motivation for this investigation.

We have studied the non-equilibrium dynamics of relativistic heavy-ion collisions, in an idealized weak coupling setup, using classical-statistical real time lattice simulations as a first principle approach. We have established the fact that the dynamics of the system is governed by different time scales, which lead to different dynamical regimes.

While at very early times $Q\tau \lesssim \log(\alpha_S^{-1})$, plasma instabilities trigger the exponential growth of vacuum fluctuations and partially isotropize the system, we discovered that, at later times $\log(\alpha_S^{-1}) \lesssim Q\tau \lesssim \alpha_S^{-3/2}$, the system exhibits the universal self-similar dynamics characteristic of wave turbulence. We obtained the universal scaling exponents and scaling functions and compared our results to different thermalization scenarios proposed in the literature [29, 30, 32].

We found that, while the physics of plasma instabilities and free-streaming characterize the approach to the universal attractor, the self-similar dynamics of the turbulent regime can be described entirely in terms of elastic scattering as incorporated in the “bottom-up” thermalization scenario [29].

The competition between elastic scattering and the longitudinal expansion in this regime leads to an increase of the anisotropy of the system up to a time scale $Q\tau \sim \alpha_S^{-3/2}$, when the system becomes dilute and quantum corrections can no longer be neglected. Since the classical-statistical framework can no longer be applied in this ‘quantum regime’, further progress at weak coupling relies on the ability to include quantum corrections dynamically in the non-equilibrium evolution. This is an outstanding problem in theoretical physics.

In view of relativistic heavy-ion collision experiments at RHIC and LHC energies, we note that for realistic values of α_S , the dynamics takes place on much shorter time scales where details of the initial conditions may be essential. Since the time for the approach to the universal attractor is controlled by the initial conditions, it will be interesting to explore how and on what time scales the results with more realistic initial conditions [151, 164–166] converge to the universal dynamics discussed in Sec. 5.3. Nevertheless, the paradigm of fast thermalization remains very puzzling from a weak coupling perspective, since no isotropization is observed in the classical regime.

However, in view of the enormous success of hydrodynamic models in terms of describing a vast amount of data at RHIC and LHC, we note that there has recently been a great effort in relaxing some of the underlying assumptions. In particular, in anisotropic hydrodynamic descriptions [167–171], we observe that the essential ingredient is no longer isotropization or thermalization but rather the existence of an anisotropic attractor solution. If the concepts developed here are applicable in heavy-ion collisions at RHIC and LHC energies, non-equilibrium wave turbulence and attendant phenomena may be playing a larger role in the dynamics of the Quark Gluon plasma than earlier conceived.

In addition to bulk observables, which have a limited sensitivity to the early time dynamics, it might also be interesting to consider possible signatures of turbulent non-equilibrium phenomena in different observables, such as e.g. electromagnetic probes. Some exploratory studies in this direction have recently been reported in Ref. [172], however based on the BGLMV thermalization scenario [30].

Chapter 6

Conclusion

In this chapter we summarize our main results and provide a perspective on future research directions for the study of non-abelian gauge theories out-of-equilibrium. We also refer to Sections 3.6, 4.3 and 5.4 at the end of the respective chapters for a more specific discussion of several aspects.

The central motivation of this work has been to identify the mechanism underlying the thermalization process of weakly coupled non-abelian plasmas and thus to contribute towards a better understanding of the non-equilibrium dynamics of relativistic heavy-ion collisions.

To approach this question, we first investigated the thermalization process of non-abelian plasmas in Minkowski space. We established by first principle simulations in the classical-statistical framework, that the thermalization process at weak coupling is driven by a turbulent cascade, which transports energy towards the ultraviolet. The dynamics in the turbulent regime is described by a self-similar evolution in time characteristic of a non-thermal fixed point and we obtained the universal scaling exponents associated to the spectral distribution and the dynamical evolution at late times. The dynamical scaling exponents are found to agree with a kinetic theory analysis of elastic and inelastic scattering processes and qualitatively confirm the results of Refs. [30, 31]. However, the spectral exponent of the power-law is clearly non-thermal and found to be consistent with the value $3/2$ at early times. In analogy to previous observations in scalar field theories [34, 35], we argued that this exponent can be attributed to an effective $2 \leftrightarrow (1 + \text{soft})$ interaction in the presence of a large number of very soft excitations of the system. The spectral exponent observed at late times is found to be consistent with the value $4/3$ originally proposed in Ref. [87] and can be explained by ordinary elastic interactions. While the dynamical evolution clearly shows that inelastic processes are as important as elastic processes throughout the evolution, it would be interesting to explore to what extent the spectral exponent $4/3$ is also compatible with inelastic interactions.

In Chapter 4 we studied the non-equilibrium dynamics of instabilities for the example of two different systems. In addition to a generalization of the Nielsen-Olesen instability, we discovered the phenomenon of parametric resonance in non-abelian gauge theories. As a generic feature of non-equilibrium instabilities, we also discussed the emergence of “secondary instabilities” [52, 53] for the example of an anisotropically expanding scalar theory. We found that the dynamical power counting developed in this context, applies in a similar way also to the dynamics of the non-equilibrium ‘Glasma’ state formed in heavy-ion collisions at ultra-relativistic energies.

The central result of this work concerns the dynamics of anisotropically expanding non-abelian plasmas phenomenologically relevant to relativistic heavy-ion collisions. While the physics of plasma instabilities and free streaming is found to govern the early stages of the evolution, we observed that the dynamics at late times is again characterized by a universal turbulent attractor. Most remarkably, the dynamical scaling exponents, which determine the self-similar evolution in the turbulent regime, can already be explained in terms of ordinary elastic scattering processes. We are thus able to confirm the onset of the “bottom-up” thermalization scenario [29] from first principle lattice simulations. Moreover, the discovery of turbulence has interesting consequences for the interpretation of our results. Since turbulence exhibits universal phenomena, characteristic features of the non-equilibrium evolution may also be observed in systems at different energy scales. This perspective opens up the possibility for several studies of both experimental and theoretical nature, which may help to clarify the situation in relativistic heavy-ion collisions in the future.

Since the classical-statistical framework can no longer be applied in the quantum regime, this approach can not be used to follow the dynamics of the system up to complete thermalization. Future progress in an *ab initio* understanding of the late-time thermalization process therefore crucially relies on the ability to include quantum evolution effects. A possible way would be to employ e.g. a kinetic description, which is of course valid also in the quantum regime. In this context, the results obtained in this work should serve as a benchmark for the employed kinetic equations in the classical regime. A major breakthrough would be achieved by computing the time evolution in the quantum regime in a non-perturbative way. The framework of real-time stochastic quantization may provide a way to address this problem in the future [173, 174].

The ultimate goal will be to extend the range of validity of present weak-coupling techniques to larger values of the coupling constant, to provide an *ab initio* description of heavy-ion collisions at RHIC and the LHC. In this context, we expect quantum effects to become even more important. Of course, studies at more realistic values of the coupling constant should also

include quarks, since these are no longer parametrically suppressed as in the idealized weak coupling limit. In the present setup, this could be achieved in a straightforward way by use of low-cost dynamical fermions [59–63] and would allow to study also the chemical evolution of the non-equilibrium plasma. Despite the present limitations, it is nevertheless interesting to speculate about the phenomenological consequences of our results. In view of the paradigm of fast thermalization, we carefully note that – at least within our idealized weak-coupling setup – we observe no evidence for a fast isotropization of the system. However, since the results obtained in the strong coupling limit also indicate the importance of anisotropies at the transition to the hydrodynamic regime [24–26], a re-thinking of this paradigm may also be considered. In this context, it will be extremely important to understand the actual sensitivity of experimental observables to the anisotropy of the system. First studies in this direction have already been reported [167–171].

Acknowledgement

It is my great pleasure to thank all the people who supported me in this project over the past three years:

First of all, I would like to thank my advisor Jürgen Berges, for giving me the opportunity to work on this exciting topic. I really appreciated all the support and encouragement he provided through many insightful discussions throughout this work and it has been a great pleasure for me to work with him. I would also like to thank him for the numerous opportunities to participate in international conferences and workshops, from which I benefited enormously.

I would like to thank Raju Venugopalan for many interesting discussions, which triggered important aspects of this work. In particular, I am grateful for the invitation to visit BNL as well as the kind hospitality during my stay and looking forward to future collaboration.

I thank Dénes Sexty for the great collaboration as well as his unlimited support with all my questions. In particular, I am indebted to Dénes for kindly sharing his expertise in numerical computations.

I also had the pleasure to collaborate with Kirill Boguslavski during his Bachelor and Master thesis and gratefully acknowledge our discussions and his contributions to this work. In particular, I am indebted to Kirill for his patience in checking many calculations as well as his proofreading of this document.

A special thanks is dedicated to all my present and former colleagues David Mesterhazy, Daniil Gelfand, Thorsten Zöller, Kirill Boguslavski, Valentin Kasper, Jan Stockemer, Lutz Goergen, Jean-Sebastien Gagnon, Florian Hebenstreit, Dénes Sexty and Lethicia Palhares for many stimulating discussions and providing such a friendly and productive work environment. I really enjoyed working with all of you!

I would like to thank Thomas Epelbaum, for very useful discussions in particular during our common stay at BNL. I would also like to thank Jean-Paul Blaizot, Francois Gelis, Alekski Kurkela, Larry McLerran and Guy Moore for many interesting discussions during conferences and workshops as well as for the opportunity to visit their institutions.

I would like to thank my parents Sabine and Eberhard Schlichting for supporting me during the entire time of my studies. Finally, I would like to express my gratitude towards my girlfriend Caroline Robin for all her support. Thank you!

I apologize to everyone who might feel forgotten.

Appendix A

Identities for the $SU(2)$ gauge group

In this appendix we provide selected identities for the $SU(2)$ gauge group, useful for the numerical implementation. In our convention, the generators of the $SU(2)$ gauge group are represented as traceless hermitian matrices, which can then be related to the Pauli matrices by

$$\Gamma^a = \sigma^a/2 \tag{A.1}$$

where $a = 1, 2, 3$. The Pauli matrices σ^a are explicitly given by

$$\sigma^1 = \begin{pmatrix} 0 & 1 \\ 1 & 0 \end{pmatrix}, \quad \sigma^2 = \begin{pmatrix} 0 & -i \\ i & 0 \end{pmatrix}, \quad \sigma^3 = \begin{pmatrix} 1 & 0 \\ 0 & -1 \end{pmatrix}. \tag{A.2}$$

The generators Γ^a satisfy the relations

$$\Gamma^a \Gamma^b = \frac{1}{4} \delta^{ab} + \frac{i}{2} f^{abc} \Gamma^c, \quad [\Gamma^a, \Gamma^b] = i f^{abc} \Gamma^c, \quad \{\Gamma^a, \Gamma^b\} = \frac{1}{2} \delta^{ab} \tag{A.3}$$

where δ^{ab} denotes the Kronecker delta and $f^{abc} = \epsilon^{abc}$, with the Levi-Civita symbol ϵ^{abc} , are the structure constants.

In view of the numerical implementation, the $SU(2)$ matrices U and U^\dagger can then conveniently be expressed as

$$U = u_0 \mathbb{1} + i u_a \sigma^a, \quad U^\dagger = u_0 \mathbb{1} - i u_a \sigma^a, \tag{A.4}$$

with real coefficient u_0, u_a constrained by $\det(U) = 1$ such that

$$u_0^2 + u_a u^a = 1. \tag{A.5}$$

In particular, the group elements $U \in SU(2)$ given by the exponential of the generators

$\exp[i\alpha^a\Gamma^a]$ can be calculated according to

$$U = \exp[i\alpha^a\Gamma^a] = \cos(a/2)\mathbb{1} + 2i \frac{\sin(a/2)}{a} \alpha^a\Gamma^a, \quad (\text{A.6})$$

where $a = \sqrt{\alpha_a\alpha^a}$, such that the corresponding coefficients u_0 and u_a are given by

$$u_0 = \cos(a/2), \quad u_a = \frac{\sin(a/2)}{a} \alpha^a. \quad (\text{A.7})$$

The relation (A.6) can also be inverted in order to obtain the coefficients α^a as

$$\alpha^a = \log_{SU(2)}[U] = 2 \frac{\text{atan2}(\sqrt{u_b u^b}, u_0)}{\sqrt{u_b u^b}} u^a. \quad (\text{A.8})$$

We also note that traces of $SU(2)$ matrices are in this notation given by

$$\text{tr}[U] = 2u_0, \quad \text{tr}[i\Gamma^a U] = -u^a. \quad (\text{A.9})$$

Appendix B

Occupation numbers and generalized Coulomb gauge on the lattice

In this appendix we discuss the procedure to compute gauge dependent quantities within the framework of classical-statistical lattice simulations. Since for practical purposes the Fock-Schwinger gauge ($A_\tau = 0$) needs to be employed throughout the entire time evolution, we focus here on fixing the residual gauge freedom to perform time independent gauge transformations. In this context it is of great advantage to choose the residual gauge freedom such that there is a clear interpretation of the physical degrees of freedom. Here we employ the generalized Coulomb gauge condition, which in the continuum takes the form

$$\tau^{-2} \partial_\eta A_\eta(x) + \sum_i \partial_i A_i(x) = 0 . \quad (\text{B.1})$$

We emphasize that the gauge condition in Eq. (B.1) can only be fixed once at an arbitrary time $\tau = \tau_0$ and does in general not hold for times $\tau \neq \tau_0$.¹ This is different in actual Coulomb gauge, where the gauge condition in Eq. (B.1) is employed at all times at the expense of a non-vanishing temporal component A_τ of the gauge field. However, it can easily be shown that equal-time correlation functions of the spatial components of the gauge fields are the same as in actual Coulomb gauge. In particular, since this gauge provides a clear interpretation of the physical degrees of freedom of the system (c.f. Appendix C), we can safely use this prescription to develop a quasi-particle picture. The advantage of this procedure is that the gauge condition in Eq. (B.1) can be employed at any time τ_0 , using only time independent gauge transformations. In practice, this implies that gauge dependent quantities at different times τ_0, τ_1, \dots are effectively calculated in different gauges; however the physical interpretation of the quantities

¹Note that, due to the explicit time dependence of Eq. (B.1) this is already not the case for the free theory. However, even in Minkowski space, where the corresponding Coulomb type gauge condition is time independent, Eq. (B.1) will in general not be satisfied at times $t \neq t_0$ due to the interactions of different momentum modes.

manifestly remains the same.

After these preliminary remarks, we will now discuss how the gauge condition can be employed in classical-statistical lattice simulations. The general procedure turns out to be very similar to Landau gauge fixing in standard vacuum or thermal equilibrium lattice QCD and can be formulated as a minimization procedure of the gauge fixing potential [89]

$$\mathcal{E}_U[G] = \frac{1}{6N_T^2 N_\eta} \sum_{\vec{x}_{T,\eta}} \left\{ \frac{a_\perp^2}{\tau^2 a_\eta^2} \text{tr}[\mathbb{1} - G(x)U_\eta(x)G^\dagger(x + \hat{\eta})] + \sum_i \text{tr}[\mathbb{1} - G(x)U_i(x)G^\dagger(x + \hat{i})] \right\}, \quad (\text{B.2})$$

with respect to time independent gauge transformations $G(x) \in SU(2)$. By variation of the gauge fixing potential in Eq. (B.2) with respect to infinitesimal gauge transformations around a local minimum $G(x)$ according to $G(x) \rightarrow [\mathbb{1} + i\alpha_a(x)\Gamma^a]G(x)$, it is straightforward to verify that the local minima²

$$\left. \frac{\delta \mathcal{E}_U[G]}{\delta \alpha_a(x)} \right|_{\alpha=0} = 0, \quad (\text{B.3})$$

satisfy the relation

$$\frac{a_\perp^2}{\tau^2 a_\eta^2} \text{tr}[i\Gamma^a(U_\eta^{(G)}(x) - U_\eta^{(G)}(x - \hat{\eta}))] + \sum_i \text{tr}[i\Gamma^a(U_i^{(G)}(x) - U_i^{(G)}(x - \hat{i}))] = 0, \quad (\text{B.4})$$

where $U_\mu^{(G)}(x)$ denotes the gauge transformed link variables $U_\mu^{(G)}(x) = G(x)U_\mu(x)G^\dagger(x + \hat{\mu})$ as discussed in Sec. 2.4. Since the expressions of the form $\text{tr}[i\Gamma^a U_\mu(x)]$ can be related to the gauge fields to leading order in lattice spacing, Eq. (B.4) is the lattice analogue of the Coulomb gauge condition in Eq. (B.1) in the continuum theory.

In practice, the minimization of the gauge fixing potential in Eq. (B.2), with respect to time independent gauge transformations $G(x) \in SU(2)$ can be achieved by a variety of different algorithms (see e.g. Ref. [89] for a review). Here we use the Fourier acceleration technique, where the gauge transformations $G(x)$ are iteratively updated according to

$$G_{\text{New}}(x) = \exp[i\mathcal{R}^a(x)\Gamma^a] G_{\text{Old}}(x), \quad (\text{B.5})$$

²Note that we will only consider local minima of the gauge fixing potential. The issue of identifying the global minimum of the gauge fixing potential in Eq. (B.2), usually referred to as 'Minimal Coulomb gauge', is related to the presence of Gribov copies and primarily affects the infrared sector (see e.g. Ref. [175]). Since we expect our interpretation in terms of quasi-particle excitations to break down in the infrared, this will not affect the discussion.

with

$$\mathcal{R}^a(x) = \alpha \left[\mathcal{F}^{-1} \left(\frac{p_{\text{Max}}^2}{p^2} \right) \mathcal{F} \right] \left\{ \frac{a_{\perp}^2}{\tau^2 a_{\eta}^2} \text{tr}[i\Gamma^a(U_{\eta}^{(G)}(x) - U_{\eta}^{(G)}(x - \hat{\eta}))] + \sum_i \text{tr}[i\Gamma^a(U_i^{(G)}(x) - U_i^{(G)}(x - \hat{i}))] \right\} \quad (\text{B.6})$$

until the gauge condition in Eq. (B.4) is globally satisfied to a given accuracy. Here \mathcal{F} and \mathcal{F}^{-1} denote the fast Fourier transform and the inverse fast Fourier transform respectively and the factor p_{Max}^2/p^2 corresponds to the ratio of the maximal lattice momentum to the lattice momentum. The parameter α can be tuned to optimize the convergence of the algorithm and we typically use on the order of thousand iterations with $\alpha = 0.005 - 0.025$ depending on the spatial lattice size.

We then perform the gauge transformation of the link variables to extract the lattice gauge fields by use of Eq. (A.8) according to

$$\begin{aligned} (ga_{\perp}) A_i^a(x + \hat{i}/2) &= \log_{SU(2)} \left[G(x) U_i(x) G^{\dagger}(x + \hat{i}) \right] , \\ (ga_{\eta}) A_{\eta}^a(x + \hat{\eta}/2) &= \log_{SU(2)} \left[G(x) U_{\eta}(x) G^{\dagger}(x + \hat{\eta}) \right] . \end{aligned} \quad (\text{B.7})$$

Similarly, one can extract the electric fields from the time-like plaquette variables according to

$$\begin{aligned} (ga_{\perp}) E_a^i(x + \hat{i}/2 + \hat{\tau}/2) &= \left(\frac{\tau}{a_{\tau}} \right) \log_{SU(2)} \left[G(x) U_{\tau i}(x) G^{\dagger}(x) \right] , \\ (ga_{\perp}^2) E_a^{\eta}(x + \hat{\eta}/2 + \hat{\tau}/2) &= \left(\frac{a_{\perp}^2}{a_{\tau} \tau a_{\eta}} \right) \log_{SU(2)} \left[G(x) U_{\tau \eta}(x) G^{\dagger}(x) \right] . \end{aligned} \quad (\text{B.8})$$

Finally, we perform a fast Fourier transformation of the fields in Eqns. (B.7,B.8) and evaluate the gluon distribution function $f(\vec{p}_T, p_z, \tau)$ according to Eq. (2.87), where we identify the longitudinal momentum at mid-rapidity as $p_z = \nu/\tau$ in the final step.

Appendix C

Free field solutions in co-moving coordinates

In this appendix we determine the basis of free solutions to the Yang-Mills evolution equations in τ, η coordinates. Since the solutions are labeled in terms of transverse momentum \vec{p}_T and conjugate rapidity momentum ν we will denote the set of linearly independent solutions by

$$a_\mu^{(\lambda)\vec{p}_T\nu\pm}(x) = \xi_\mu^{(\lambda)\vec{p}_T\nu\pm}(\tau) e^{i(\vec{p}_T\vec{x}_T+\nu\eta)} , \quad (\text{C.1})$$

where the index $\lambda = 1, 2, 3$ labels the different polarizations, the index \pm denotes the positive and negative frequency solutions and $\xi_\mu^{(\lambda)\vec{p}_T\nu\pm}(\tau)$ denote the time-dependent polarization vectors. Here we suppressed the color indices, since the free solutions display a diagonal structure in color space. The starting point of our discussion are the evolution equations, which in Fock-Schwinger ($a_\tau = 0$) gauge take the form [151]

$$\begin{aligned} \partial_\tau \tau \partial_\tau a_i + \tau(p_\perp^2 + \tau^{-2}\nu^2)a_i - \tau p_i p_j a_j - \tau^{-1}\nu p_i a_\eta &= 0 , \\ \partial_\tau \tau^{-1} \partial_\tau a_\eta + \tau^{-1} p_\perp^2 a_\eta - \tau^{-1} p_i a_i &= 0 , \end{aligned} \quad (\text{C.2})$$

where $p_\perp^2 = p_x^2 + p_y^2$ and summation over the transverse Lorenz index $i = x, y$ is implied. In addition to the above evolution equations, the solutions are required to satisfy the (abelian) Gauss law constraint, which takes the form

$$p_i \tau \partial_\tau a_i + \nu \tau^{-1} \partial_\tau a_\eta = 0 . \quad (\text{C.3})$$

In general there are five linearly independent solutions to the set of equations (C.2), taking into account the Gauss law constraint (C.3). However the remaining gauge freedom to perform time independent gauge transformations allows us to eliminate one of the solutions, such that we are left with four linearly independent solutions, which correspond to the negative and

positive frequency solutions of the two transverse polarizations. We will exploit this fact and fix the remaining gauge freedom by implementing the Coulomb type gauge condition

$$\left[p_i a_i + \tau^{-2} \nu a_\eta \right]_{\tau=\tau_0} = 0 , \quad (\text{C.4})$$

at arbitrary time τ_0 . To see how this gauge fixing reduces the number of solutions, we first consider a solution of the type

$$\xi_\mu^{(3)\vec{p}_{T\nu}}(\tau) = \begin{pmatrix} p_x \\ p_y \\ \nu \end{pmatrix} \xi^{(3)\vec{p}_{T\nu}}(\tau) . \quad (\text{C.5})$$

The Gauss law constraint and the evolution equations then imply that $\partial_\tau \xi^{(3)\vec{p}_{T\nu}}(\tau) = 0$, and hence $\xi^{(3)\vec{p}_{T\nu}}(\tau) = \xi^{(3)\vec{p}_{T\nu}}$ is a constant in time. However the gauge fixing condition (C.4) implies that $\xi^{(3)\vec{p}_{T\nu}}(\tau_0) = 0$ vanishes such that this solution is eliminated by the choice of the gauge. We are therefore left with four physical solutions, which correspond to the positive and negative frequency solutions for the two transverse polarizations.

C.1 First set of physical solutions

In order to construct the first set of physical solutions, we chose the ansatz

$$\xi_\mu^{(1)\vec{p}_{T\nu}}(\tau) = \begin{pmatrix} -p_y \\ p_x \\ 0 \end{pmatrix} \xi^{(1)\vec{p}_{T\nu}}(\tau) , \quad (\text{C.6})$$

which complies with the Gauss law constraint by construction. The evolution equation for $a^{(1)\vec{p}_{T\nu}}(\tau)$ follows from Eq. (C.2) and reads

$$\left[\tau^{-1} \partial_\tau \tau \partial_\tau + p_\perp^2 + \frac{\nu^2}{\tau^2} \right] \xi^{(1)\vec{p}_{T\nu}}(\tau) = 0 . \quad (\text{C.7})$$

This equation is known as the Bessel equation and the general solution can be expressed in terms of Hankel functions as

$$\xi^{(1)\vec{p}_{T\nu}}(\tau) = c_1 H_{i\nu}^{(1)}(p_\perp \tau) + c_2 H_{i\nu}^{(2)}(p_\perp \tau) , \quad (\text{C.8})$$

such that there are two linearly independent solutions. For each solution, the constants c_1 and c_2 can be fixed to yield the correct normalization and asymptotic behavior of the solution in terms of positive and negative frequency components. This is discussed in more detail below, where we obtain the final and correctly normalized result.

C.2 Second set of physical solutions

The second set of solutions can be written in the general form

$$\xi_\mu^{(2)\bar{p}T\nu}(\tau) = \begin{pmatrix} \nu p_x / (p_\perp^2 \tau_0^2) R_\perp^{\bar{p}T\nu}(\tau) \\ \nu p_y / (p_\perp^2 \tau_0^2) R_\perp^{\bar{p}T\nu}(\tau) \\ -R_\eta^{\bar{p}T\nu}(\tau) \end{pmatrix}, \quad (\text{C.9})$$

where the gauge condition (C.4) implies $R_\eta^{\bar{p}T\nu}(\tau_0) = R_\perp^{\bar{p}T\nu}(\tau_0)$ at the time τ_0 , where the residual gauge freedom is fixed. Moreover the Gauss law constraint yields the relation

$$\nu \left[\tau \tau_0^{-2} \partial_\tau R_\perp^{\bar{p}T\nu}(\tau) - \tau^{-1} \partial_\tau R_\eta^{\bar{p}T\nu}(\tau) \right] = 0, \quad (\text{C.10})$$

such that

$$\partial_\tau R_\eta^{\bar{p}T\nu}(\tau) = \frac{\tau^2}{\tau_0^2} \partial_\tau R_\perp^{\bar{p}T\nu}(\tau), \quad (\text{C.11})$$

which can be used to eliminate $R_\eta^{\bar{p}T\nu}(\tau)$ in favor of $R_\perp^{\bar{p}T\nu}(\tau)$. The dynamic equations for $R_\eta^{\bar{p}T\nu}(\tau)$ and $R_\perp^{\bar{p}T\nu}(\tau)$ follow from the evolution equations (C.2) and take the form

$$\partial_\tau \tau \partial_\tau R_\perp^{\bar{p}T\nu}(\tau) + \frac{\nu^2}{\tau} R_\perp^{\bar{p}T\nu}(\tau) + \frac{(p_\perp^2 \tau_0^2)}{\tau} R_\eta^{\bar{p}T\nu}(\tau) = 0, \quad (\text{C.12})$$

$$\partial_\tau \tau^{-1} \partial_\tau R_\eta^{\bar{p}T\nu}(\tau) + \tau^{-1} p_\perp^2 R_\eta^{\bar{p}T\nu}(\tau) + \tau^{-1} \frac{\nu^2}{\tau_0^2} R_\perp^{\bar{p}T\nu}(\tau) = 0. \quad (\text{C.13})$$

In order to decouple the evolution equations, it is convenient to multiply the equations by appropriate factors of τ and subsequently differentiate with respect to τ . By use of the relation (C.11), this yields the set of equations

$$\left[\tau^{-1} \partial_\tau \tau \partial_\tau + p_\perp^2 + \frac{\nu^2}{\tau^2} \right] \tau \partial_\tau R_\perp^{\bar{p}T\nu}(\tau) = 0 \quad (\text{C.14})$$

$$\left[\tau^{-1} \partial_\tau \tau \partial_\tau + p_\perp^2 + \frac{\nu^2}{\tau^2} \right] \tau^{-1} \partial_\tau R_\eta^{\bar{p}T\nu}(\tau) = 0, \quad (\text{C.15})$$

which are equivalent after the Gauss constraint (C.11) is taken into account. It is important to note that by transforming the set of second order differential equations (C.12) into the third order differential equation (C.14), we have introduced an additional free parameter to the general solution. We will fix this parameter by requiring the solutions of (C.14) to satisfy the

original evolution equations (C.12). The general solution of the above equations takes the form

$$R_{\perp}^{\vec{p}T\nu}(\tau) = R_{\tau_0}^{\vec{p}T\nu} + \int_{\tau_0}^{\tau} d\tau' \tau'^{-1} \left[c_1 H_{i\nu}^{(1)}(p_{\perp}\tau') + c_2 H_{i\nu}^{(2)}(p_{\perp}\tau') \right], \quad (\text{C.16})$$

$$R_{\eta}^{\vec{p}T\nu}(\tau) = R_{\tau_0}^{\vec{p}T\nu} + \int_{\tau_0}^{\tau} d\tau' \frac{\tau'}{\tau_0^2} \left[c_1 H_{i\nu}^{(1)}(p_{\perp}\tau') + c_2 H_{i\nu}^{(2)}(p_{\perp}\tau') \right], \quad (\text{C.17})$$

where we have taken into account the Gauss law constraint to ensure that the constants c_1 and c_2 are the same for $R_{\perp}^{\vec{p}T\nu}(\tau)$ and $R_{\eta}^{\vec{p}T\nu}(\tau)$ and the gauge condition which ensures that the integration constant $R_{\tau_0}^{\vec{p}T\nu}$ takes the same value. The value of the constant $R_{\tau_0}^{\vec{p}T\nu}$ is fixed by requiring the solution to satisfy the original coupled set of second order differential equations. By inserting the solutions (C.16,C.17) in the evolution equations (C.12) we obtain the condition

$$\begin{aligned} & \partial_{\tau} \left[c_1 H_{i\nu}^{(1)}(p_{\perp}\tau) + c_2 H_{i\nu}^{(2)}(p_{\perp}\tau) \right] + \tau^{-1} \left[\nu^2 + p_{\perp}^2 \tau_0^2 \right] R_{\tau_0}^{\vec{p}T\nu} \\ & + \tau^{-1} \int_{\tau_0}^{\tau} d\tau' \tau' \left[\frac{\nu^2}{\tau'^2} + p_{\perp}^2 \right] \left[c_1 H_{i\nu}^{(1)}(p_{\perp}\tau') + c_2 H_{i\nu}^{(2)}(p_{\perp}\tau') \right] = 0, \end{aligned} \quad (\text{C.18})$$

and by use of the Bessel equation, we can rewrite the integrand as

$$\left[\frac{\nu^2}{\tau^2} + p_{\perp}^2 \right] H_{i\nu}^{(1/2)}(p_{\perp}\tau) = -\tau^{-1} \partial_{\tau} \tau \partial_{\tau} H_{i\nu}^{(1/2)}(p_{\perp}\tau), \quad (\text{C.19})$$

such that the powers of time under the integral cancel and we are left with the integration of a total derivative. We can then perform the time integration and find that the term from the upper bound of the integral cancels the first derivative term in Eq. (C.18). In this way Eq. (C.18) reduces to

$$\left[\nu^2 + p_{\perp}^2 \tau_0^2 \right] R_{\tau_0}^{\vec{p}T\nu} + \tau_0 \partial_{\tau} \left[c_1 H_{i\nu}^{(1)}(p_{\perp}\tau) + c_2 H_{i\nu}^{(2)}(p_{\perp}\tau) \right] \Big|_{\tau=\tau_0} = 0, \quad (\text{C.20})$$

which fixes the constant to be

$$R_{\tau_0}^{\vec{p}T\nu} = -\frac{p_{\perp} \tau_0 \left[c_1 H'_{i\nu}{}^{(1)}(p_{\perp}\tau_0) + c_2 H'_{i\nu}{}^{(2)}(p_{\perp}\tau_0) \right]}{\nu^2 + p_{\perp}^2 \tau_0^2}, \quad (\text{C.21})$$

where $H'_{i\nu}{}^{(1/2)}(x) = \partial_x H_{i\nu}^{(1/2)}(x)$ denotes the first derivative of the function evaluated at the respective argument. The first and second set of solutions are then both characterized by two free parameters, which we will fix in the following to obtain the correctly normalized positive and negative frequency solutions.

C.3 Normalization and asymptotic behavior

In the previous section we have determined the orthogonal solutions to the free evolution equations in τ, η coordinates. In order to determine the normalization of the solutions it is important to realize that all solutions to the evolution equations (C.2) conserve the scalar product [151]

$$(a|b) = -i \int d^2 \vec{x}_T d\eta \tau g^{\mu\nu} [a_\mu^*(x) \partial_\tau b_\nu(x) - b_\nu(x) \partial_\tau a_\mu^*(x)] . \quad (\text{C.22})$$

This can be checked explicitly by use of the equations of motion (C.2) and the relation can be used to properly normalize the solutions [151].

Normalization of the first set of solutions

The first set of physical solutions takes the general form

$$\xi_\mu^{(1)\vec{p}_T\nu}(x) = \begin{pmatrix} -p_y \\ p_x \\ 0 \end{pmatrix} [c_1 H_{i\nu}^{(1)}(p_\perp \tau) + c_2 H_{i\nu}^{(2)}(p_\perp \tau)] , \quad (\text{C.23})$$

and according to Ref. [151] the positive and negative frequency solution corresponds to the parts involving only the Hankel functions of the second and first kind respectively. If we focus on the positive and negative frequency parts $a^{(1)\vec{p}_T\nu^\pm}$, with $c_1^+ = 0$ and $c_2^- = 0$, the scalar products between the solutions take the form

$$(a^{(1)\vec{p}_T\nu^+} | a^{(1)\vec{p}'_T\nu'^+}) = i\tau (2\pi)^3 \delta^2(\vec{p}_T - \vec{p}'_T) \delta(\nu - \nu') p_\perp^2 |c_2^+|^2 H_{i\nu}^{(2)*}(p_\perp \tau) \overleftrightarrow{\partial}_\tau H_{i\nu}^{(2)}(p_\perp \tau) , \quad (\text{C.24})$$

$$(a^{(1)\vec{p}_T\nu^-} | a^{(1)\vec{p}'_T\nu'^-}) = i\tau (2\pi)^3 \delta^2(\vec{p}_T - \vec{p}'_T) \delta(\nu - \nu') p_\perp^2 |c_1^-|^2 H_{i\nu}^{(1)*}(p_\perp \tau) \overleftrightarrow{\partial}_\tau H_{i\nu}^{(1)}(p_\perp \tau) , \quad (\text{C.25})$$

$$(a^{(1)\vec{p}_T\nu^+} | a^{(1)\vec{p}'_T\nu'^-}) = i\tau (2\pi)^3 \delta^2(\vec{p}_T - \vec{p}'_T) \delta(\nu - \nu') p_\perp^2 (c_2^+)^* c_1^- H_{i\nu}^{(2)*}(p_\perp \tau) \overleftrightarrow{\partial}_\tau H_{i\nu}^{(1)}(p_\perp \tau) . \quad (\text{C.26})$$

and by use of the identities (D.7, D.8) for the Hankel functions and their derivatives, we can evaluate the above expressions explicitly. With the choice of parameters

$$c_2^+ = \frac{\sqrt{\pi} e^{\frac{\pi\nu}{2}}}{2p_\perp} , \quad c_1^- = \frac{\sqrt{\pi} e^{-\frac{\pi\nu}{2}}}{2p_\perp} , \quad (\text{C.27})$$

we obtain the usual normalization properties

$$(a^{(1)\vec{p}_T\nu+}|a^{(1)\vec{p}'_T\nu'+}) = (2\pi)^3\delta^2(\vec{p}_T - \vec{p}'_T)\delta(\nu - \nu') , \quad (\text{C.28})$$

$$(a^{(1)\vec{p}_T\nu-}|a^{(1)\vec{p}'_T\nu'-}) = - (2\pi)^3\delta^2(\vec{p}_T - \vec{p}'_T)\delta(\nu - \nu') , \quad (\text{C.29})$$

$$(a^{(1)\vec{p}_T\nu+}|a^{(1)\vec{p}'_T\nu'-}) = 0 , \quad (\text{C.30})$$

and the first set of final solutions takes the final form

$$\xi_\mu^{(1)\vec{p}_T\nu\pm}(x) = \frac{\sqrt{\pi} e^{\pm\pi\nu/2}}{2p_\perp} \begin{pmatrix} -p_y \\ p_x \\ 0 \end{pmatrix} H_{i\nu}^{(2/1)}(p_\perp\tau) . \quad (\text{C.31})$$

Normalization of the second set of solutions

The second set of solutions can be normalized in a similar way, by considering again the scalar product (C.22), between the different solutions. In Ref. [151] it is argued that the positive and negative frequency solutions are again the ones which involve only Hankel functions of the second and first kind respectively. The positive and negative frequency solutions then take the form

$$\xi_\mu^{(2)\vec{p}_T\nu\pm}(x) = \begin{pmatrix} \nu p_x/(p_\perp^2\tau_0^2) R_\perp^{\vec{p}_T\nu\pm}(\tau) \\ \nu p_y/(p_\perp^2\tau_0^2) R_\perp^{\vec{p}_T\nu\pm}(\tau) \\ -R_\eta^{\vec{p}_T\nu\pm}(\tau) \end{pmatrix} , \quad (\text{C.32})$$

where the time dependence is given by

$$R_\perp^{\vec{p}_T\nu\pm}(\tau) = -\frac{p_\perp\tau_0}{\nu^2 + p_\perp^2\tau_0^2} c_{2/1}^\pm H_{i\nu}^{(2/1)}(p_\perp\tau_0) + \int_{\tau_0}^\tau d\tau' \tau'^{-1} c_{2/1}^\pm H_{i\nu}^{(2/1)}(p_\perp\tau') , \quad (\text{C.33})$$

$$R_\eta^{\vec{p}_T\nu\pm}(\tau) = -\frac{p_\perp\tau_0}{\nu^2 + p_\perp^2\tau_0^2} c_{2/1}^\pm H_{i\nu}^{(2/1)}(p_\perp\tau_0) + \int_{\tau_0}^\tau d\tau' \frac{\tau'}{\tau_0^2} c_{2/1}^\pm H_{i\nu}^{(2/1)}(p_\perp\tau') . \quad (\text{C.34})$$

Since the scalar product is constant in time we can without loss of generality evaluate it at the time $\tau = \tau_0$, when the gauge condition (C.4) applies. The scalar products between the different

solutions then take the form

$$(a^{(2)\vec{p}_T\nu+}|a^{(2)\vec{p}'_T\nu'+}) = i\tau_0 (2\pi)^3 \delta^2(\vec{p}_T - \vec{p}'_T) \delta(\nu - \nu') \frac{|c_2^+|^2}{\tau_0^3(p_\perp \tau_0)} \left[H_{i\nu}^{(2)*}(x) \overleftrightarrow{\partial}_x H_{i\nu}^{(2)}(x) \right] \Big|_{x=p_\perp \tau_0}, \quad (\text{C.35})$$

$$(a^{(2)\vec{p}_T\nu-}|a^{(2)\vec{p}'_T\nu'-}) = i\tau_0 (2\pi)^3 \delta^2(\vec{p}_T - \vec{p}'_T) \delta(\nu - \nu') \frac{|c_1^-|^2}{\tau_0^3(p_\perp \tau_0)} \left[H_{i\nu}^{(1)*}(x) \overleftrightarrow{\partial}_x H_{i\nu}^{(1)}(x) \right] \Big|_{x=p_\perp \tau_0}, \quad (\text{C.36})$$

$$(a^{(2)\vec{p}_T\nu+}|a^{(2)\vec{p}'_T\nu'-}) = i\tau_0 (2\pi)^3 \delta^2(\vec{p}_T - \vec{p}'_T) \delta(\nu - \nu') \frac{(c_2^+)^* c_1^-}{\tau_0^3(p_\perp \tau_0)} \left[H_{i\nu}^{(2)*}(x) \overleftrightarrow{\partial}_x H_{i\nu}^{(1)}(x) \right] \Big|_{x=p_\perp \tau_0}, \quad (\text{C.37})$$

where again we can evaluate the terms involving Hankel functions and their derivatives by use of the relations (D.7, D.8). With the choice of parameters

$$c_2^+ = \tau_0 \frac{\sqrt{\pi} e^{\frac{\pi\nu}{2}}}{2} p_\perp \tau_0, \quad (\text{C.38})$$

$$c_1^- = \tau_0 \frac{\sqrt{\pi} e^{-\frac{\pi\nu}{2}}}{2} p_\perp \tau_0, \quad (\text{C.39})$$

the solutions then satisfy the usual relations for the scalar product

$$(a^{(2)\vec{p}_T\nu+}|a^{(2)\vec{p}'_T\nu'+}) = (2\pi)^3 \delta^2(\vec{p}_T - \vec{p}'_T) \delta(\nu - \nu'), \quad (\text{C.40})$$

$$(a^{(2)\vec{p}_T\nu-}|a^{(2)\vec{p}'_T\nu'-}) = - (2\pi)^3 \delta^2(\vec{p}_T - \vec{p}'_T) \delta(\nu - \nu'), \quad (\text{C.41})$$

$$(a^{(2)\vec{p}_T\nu+}|a^{(2)\vec{p}'_T\nu'-}) = 0. \quad (\text{C.42})$$

The orthogonality of the solutions $a^{(2)\vec{p}_T\nu\pm}$ and $a^{(1)\vec{p}_T\nu\pm}$, in the sense that the scalar product of any combination of the two vanishes, follows directly from the structure of the polarization vectors. To complete the construction of the orthonormal basis of free modes in generalized Coulomb gauge, we have to consider also the cases where either ν or p_\perp vanishes. We find that the previous set of solutions is well behaved in the limit $\nu \rightarrow 0$, whereas in the case $p_\perp \rightarrow 0$ it is more convenient to consider a different parametrization.

C.4 Special case: Zero transverse momentum

In the case of vanishing transverse momentum, the Coulomb gauge condition (C.4) along with the Gauss constraint (C.3) imply that the physical solutions are of the form

$$\xi_{\mu}^{(1)\nu, \vec{p}_T=0}(\tau) = \begin{pmatrix} 1 \\ 0 \\ 0 \end{pmatrix} \xi^{\nu}(\tau), \quad \xi_{\mu}^{(2)\nu, \vec{p}_T=0}(\tau) = \begin{pmatrix} 0 \\ 1 \\ 0 \end{pmatrix} \xi^{\nu}(\tau). \quad (\text{C.43})$$

The time dependence of the function $\xi^{\nu}(\tau)$ is governed by the evolution equation (C.2), which in this case takes the form

$$\left[\tau^{-1} \partial_{\tau} \tau \partial_{\tau} + \frac{\nu^2}{\tau^2} \right] \xi^{\nu}(\tau) = 0. \quad (\text{C.44})$$

This equation has the general solution

$$\xi^{\nu}(\tau) = c_1 \left(\frac{\tau}{\tau_0} \right)^{i\nu} + c_2 \left(\frac{\tau}{\tau_0} \right)^{-i\nu}, \quad (\text{C.45})$$

and the positive and negative frequency solutions are given by $c_1^+ = c_2^- = 0$. With the appropriate normalization the solutions take the final form

$$\xi^{\nu+}(\tau) = \frac{1}{\sqrt{2\nu}} \left(\frac{\tau}{\tau_0} \right)^{-i\nu}, \quad \xi^{\nu-}(\tau) = \frac{1}{\sqrt{2\nu}} \left(\frac{\tau}{\tau_0} \right)^{i\nu}, \quad (\text{C.46})$$

and the scalar product between the solutions satisfies the usual relations

$$(a^{(1/2)\nu, \vec{p}_T=0+} | a^{(1/2)\nu, \vec{p}_T+}) = (2\pi)^3 \delta^2(\vec{p}_T) \delta(\nu - \nu'), \quad (\text{C.47})$$

$$(a^{(1/2)\nu, \vec{p}_T=0-} | a^{(1/2)\nu, \vec{p}_T-}) = - (2\pi)^3 \delta^2(\vec{p}_T) \delta(\nu - \nu'), \quad (\text{C.48})$$

$$(a^{(1/2)\nu, \vec{p}_T=0+} | a^{(1/2)\nu, \vec{p}_T-}) = 0, \quad (\text{C.49})$$

while the two sets of solutions $a^{(1)\nu, \vec{p}_T=0\pm}$ and $a^{(2)\nu, \vec{p}_T=0\pm}$ are orthogonal as can directly be observed from the polarization structure.

Appendix D

Hankel functions

The Hankel functions are two linearly independent solutions of the Bessel equation

$$\left[\tau^{-1} \partial_\tau \tau \partial_\tau + \frac{\nu^2}{\tau^2} + p_\perp^2 \right] H_{i\nu}^{(1/2)}(p_\perp \tau) = 0 , \quad (\text{D.1})$$

with the asymptotic behavior

$$\lim_{x \rightarrow \infty} H_{i\nu}^{(2)}(x) = \sqrt{\frac{2}{\pi x}} e^{-i(x-\pi/4)} e^{-\pi\nu/2} , \quad (\text{D.2})$$

$$\lim_{x \rightarrow \infty} H_{i\nu}^{(1)}(x) = \sqrt{\frac{2}{\pi x}} e^{i(x-\pi/4)} e^{\pi\nu/2} , \quad (\text{D.3})$$

such that the two solutions are related to each other by complex conjugation

$$H_{i\nu}^{(2)*}(x) = e^{-\pi\nu} H_{i\nu}^{(1)}(x) , \quad H_{i\nu}^{(1)*}(x) = e^{\pi\nu} H_{i\nu}^{(2)}(x) . \quad (\text{D.4})$$

There is also an integral representation of the Hankel functions, which reads

$$\begin{aligned} H_{i\nu}^{(2)}(x) &= \frac{-ie^{-\frac{\pi\nu}{2}}}{\pi} \int_{-\infty}^{\infty} d\eta e^{-ix \cosh \eta - i\nu\eta} , \\ H_{i\nu}^{(1)}(x) &= \frac{ie^{\frac{\pi\nu}{2}}}{\pi} \int_{-\infty}^{\infty} d\eta e^{ix \cosh \eta + i\nu\eta} . \end{aligned} \quad (\text{D.5})$$

D.1 Orthogonality relations

Introducing the shorthand notation

$$A \overleftrightarrow{\partial}_x B = A \partial_x B - B \partial_x A \quad (\text{D.6})$$

the Hankel functions of the first and second kind obey the following identities

$$\begin{aligned} H_{i\nu}^{(2)*}(x) \overleftrightarrow{\partial}_x H_{i\nu}^{(2)}(x) &= -\frac{4i e^{-\pi\nu}}{\pi x}, \\ H_{i\nu}^{(1)*}(x) \overleftrightarrow{\partial}_x H_{i\nu}^{(1)}(x) &= \frac{4i e^{+\pi\nu}}{\pi x}, \end{aligned} \quad (\text{D.7})$$

whereas the terms involving Hankel functions of both kinds vanish

$$\begin{aligned} H_{i\nu}^{(2)*}(x) \overleftrightarrow{\partial}_x H_{i\nu}^{(1)}(x) &= 0, \\ H_{i\nu}^{(1)*}(x) \overleftrightarrow{\partial}_x H_{i\nu}^{(2)}(x) &= 0, \end{aligned} \quad (\text{D.8})$$

since the two solutions are mutually orthogonal solutions of the Bessel equation. The identities (D.8) can easily be verified by use of the identity (D.4). The identities (D.7) follow from the fact that solutions of the Bessel equation conserve the expression

$$H_{i\nu}^{(1/2)*}(x) \partial_x x \partial_x H_{i\nu}^{(1/2)}(x) - H_{i\nu}^{(1/2)}(x) \partial_x x \partial_x H_{i\nu}^{(1/2)*}(x) = 0. \quad (\text{D.9})$$

Moreover, since the left hand side is a total derivative, this implies that the expression

$$\left[x H_{i\nu}^{(1/2)*}(x) \overleftrightarrow{\partial}_x H_{i\nu}^{(1/2)}(x) \right]_{x=x_0} = \left[x H_{i\nu}^{(1/2)*}(x) \overleftrightarrow{\partial}_x H_{i\nu}^{(1/2)}(x) \right]_{x=x_1} \quad (\text{D.10})$$

is constant in time. We can then use the asymptotic forms in order to evaluate the constants. In this way one obtains

$$\begin{aligned} \left[x H_{i\nu}^{(2)*}(x) \overleftrightarrow{\partial}_x H_{i\nu}^{(2)}(x) \right]_{x \rightarrow \infty} &= -4i \frac{e^{-\pi\nu}}{\pi} \\ \left[x H_{i\nu}^{(1)*}(x) \overleftrightarrow{\partial}_x H_{i\nu}^{(1)}(x) \right]_{x \rightarrow \infty} &= 4i \frac{e^{\pi\nu}}{\pi}. \end{aligned} \quad (\text{D.11})$$

One then recovers the identity (D.7) by making use of the invariant (D.10) with the constant on the right hand side fixed by the asymptotic expression.

D.2 Numerical computation

In order to compute the polarization vectors discussed in Appendix C one needs to evaluate the Hankel functions $H_{i\nu}^{1/2}(x)$ numerically, for real values of ν and x . Since this involves in particular the calculation of Hankel functions of large imaginary order $|\nu| \gg 1$, for which no standard library exists, we discuss here how these can be computed numerically in an efficient way. The starting point is to relate the Hankel functions and their derivatives to the Bessel

function of the first kind by [176]

$$\begin{aligned} H_\alpha^{(2)}(x) &= \frac{i [J_{-\alpha}(x) - e^{i\pi\alpha} J_\alpha(x)]}{\sin(\pi\alpha)} , \\ H_\alpha^{\prime(2)}(x) &= \frac{1}{2} [H_{\alpha-1}^{(2)}(x) - H_{\alpha+1}^{(2)}(x)] . \end{aligned} \quad (\text{D.12})$$

The Bessel functions in Eq. (D.12) can be computed by use of the series expansion [176]

$$J_\alpha(x) = \sum_{k=0}^{\infty} (-1)^k \frac{(x/2)^{2k+\alpha}}{k! \Gamma(\alpha + k + 1)} \quad (\text{D.13})$$

which converges rapidly for sufficiently small x , such that one only needs to sum over the first few terms to achieve the desired accuracy. Since we will be interested in Hankel functions of complex order $\alpha = i\nu$, it is useful to note the complex characteristics of the functions involved in Eqns. (D.12,D.13). For complex numbers $z = x + iy$ with real numbers x, y and a, b these take the form [177]

$$\sin(z) = \cosh(y) \sin(x) + i \sinh(y) \cos(x) , \quad (\text{D.14})$$

$$z^{a+ib} = \exp[a \log |z| - \arg(z)b] \exp[i(b \log |z| + \arg(z)a)] . \quad (\text{D.15})$$

The Gamma function appearing in Eq. (D.13) can efficiently be evaluated in the Lanczos approximation to high numerical accuracy [178, 179]. Since the definitions of Hankel functions of imaginary order $\alpha = i\nu$ involve large/small exponentials $\exp[\pm\pi\nu]$, we find it convenient to use a specialized number format, which separately keeps track of the exponent as well as the order one prefactor. By use of Eqns. (D.12,D.13) we can then evaluate the Hankel functions and their derivatives at small values of x . In practice, we use $x = 1$ independent of the order α and keep only the first ten terms of the power series in Eq. (D.13). The values of $H_{i\nu}^{(2)}(x)$ for $x \neq 1$ can then be calculated in a straightforward way, by numerically solving the Bessel equation (D.1) using a leap-frog discretization scheme with adaptive step width. This provides an efficient method to calculate the values of the Hankel functions and their derivatives at different arguments of x for the same set of orders α .

Appendix E

Perturbative calculation of hard scales

In this appendix we compute the perturbative expressions for the gauge-invariant hard scale observables Λ_T^2 and Λ_L^2 as introduced in Sec. 2.4. In this context, we will frequently encounter the expectation values of equal-time correlation functions of the gauge fields. Since ultimately, we are interested only in gauge invariant quantities, we can evaluate all expressions in Fock-Schwinger gauge with the residual gauge freedom fixed by the generalized Coulomb gauge condition (c.f. App. C). In order to evaluate equal-time correlation functions in this gauge, we first expand the gauge fields in terms of creation and annihilation operators according to

$$\begin{aligned} \langle A_\mu^a(\tau, \vec{x}_1, \eta) A_\nu^a(\tau, \vec{x}_2, \eta') \rangle &= \int \frac{d^2 \vec{p}_T}{(2\pi)^2} \frac{d\nu}{2\pi} \int \frac{d^2 \vec{q}_T}{(2\pi)^2} \frac{d\nu'}{2\pi} \sum_{\lambda, \lambda'} \left\langle \left[\xi_\mu^{(\lambda) \vec{p}_T \nu +} \mathbf{a}_{\lambda, a}^{\vec{p}_T \nu} e^{i(\vec{p}_T \vec{x}_1 + \nu \eta)} + h.c. \right] \right. \\ &\quad \left. \times \left[\xi_\nu^{(\lambda') \vec{q}_T \nu' +} \mathbf{a}_{\lambda', a}^{\vec{q}_T \nu'} e^{i(\vec{q}_T \vec{x}_2 + \nu' \eta')} + h.c. \right] \right\rangle, \quad (\text{E.1}) \end{aligned}$$

where $h.c.$ denotes the hermitian conjugate. In order to evaluate the above expectation values, we make use of the relations

$$\begin{aligned} \langle \mathbf{a}_{\lambda, a}^{\vec{p}_T \nu} \mathbf{a}_{\lambda', b}^{\dagger \vec{q}_T \nu'} \rangle &= \delta_{ab} \delta_{\lambda \lambda'} (f(\vec{p}_T, \nu) + 1) (2\pi)^3 \delta^{(2)}(\vec{p}_T - \vec{q}_T) \delta(\nu - \nu'), \\ \langle \mathbf{a}_{\lambda, a}^{\dagger \vec{p}_T \nu} \mathbf{a}_{\lambda', b}^{\vec{q}_T \nu'} \rangle &= \delta_{ab} \delta_{\lambda \lambda'} f(\vec{p}_T, \nu) (2\pi)^3 \delta^{(2)}(\vec{p}_T - \vec{q}_T) \delta(\nu - \nu'), \end{aligned} \quad (\text{E.2})$$

whereas all other terms appearing in Eq. (E.1) vanish identically. The expression in Eq. (E.1) can then be expressed as

$$\begin{aligned} \langle A_\mu^a(\tau, \vec{x}_1, \eta) A_\nu^a(\tau, \vec{x}_2, \eta') \rangle &= (N_c^2 - 1) \int \frac{d^2 \vec{p}_T}{(2\pi)^2} \frac{d\nu}{2\pi} \left[(f(\vec{p}_T, \nu) + 1) e^{i(\vec{p}_T(\vec{x}_1 - \vec{x}_2) + \nu(\eta - \eta'))} \right. \\ &\quad \left. + f(\vec{p}_T, \nu) e^{-i(\vec{p}_T(\vec{x}_1 - \vec{x}_2) + \nu(\eta - \eta'))} \right] \Pi_{\mu\nu}^{\vec{p}_T \nu}(\tau), \quad (\text{E.3}) \end{aligned}$$

where we defined the Lorentz tensor $\Pi_{\mu\nu}^{\vec{p}_T\nu}(\tau)$ according to

$$\Pi_{\mu\nu}^{\vec{p}_T\nu}(\tau) = \sum_{\lambda} \xi_{\mu}^{(\lambda)\vec{p}_T\nu\pm}(\tau) \xi_{\nu}^{(\lambda)\vec{p}_T\nu\mp}(\tau). \quad (\text{E.4})$$

In order to evaluate this tensor, we consider the Coulomb gauge condition to be fixed at the time τ when the observables are calculated. We recall that the polarization vectors in this gauge take the form (c.f. Appendix C)

$$\begin{aligned} \xi_{\mu}^{(1)\vec{p}_T\nu,\pm}(\tau) &= \frac{\sqrt{\pi}e^{\pm\pi\nu/2}}{2p_{\perp}} \begin{pmatrix} -p_y \\ p_x \\ 0 \end{pmatrix} H_{i\nu}^{(2/1)}(p_{\perp}\tau), \\ \xi_{\mu}^{(2)\vec{p}_T\nu,\pm}(\tau) &= \frac{\sqrt{\pi}e^{\pm\pi\nu/2}}{2\tau p^2} \begin{pmatrix} \nu p_x \\ \nu p_y \\ -(p_{\perp}\tau)^2 \end{pmatrix} H_{i\nu}'^{(2/1)}(p_{\perp}\tau), \end{aligned} \quad (\text{E.5})$$

and the Lorentz tensor $\Pi_{\mu\nu}^{\vec{p}_T\nu}(\tau)$ can then be evaluated explicitly. In order to simplify the resulting tensor structure, we will approximate the behavior of the Hankel functions and their derivatives by the expansion for large time arguments

$$\left[1 + \frac{\nu^2}{x^2}\right]^{-1} H_{i\nu}'^{(2)}(x) H_{i\nu}'^{(1)}(x) \simeq H_{i\nu}^{(2)}(x) H_{i\nu}^{(1)}(x) \simeq \frac{2}{\pi x}, \quad (\text{E.6})$$

which effectively amounts to considering highly anisotropic systems, where the characteristic transverse momenta are much larger than the longitudinal momenta ($p_{\perp} \gg \nu/\tau$). Within this approximation the Lorentz tensor can then be expressed as

$$\Pi_{\mu\nu}^{\vec{p}_T\nu}(\tau) = \frac{1}{2p_{\perp}\tau} \left[-g_{\mu\nu} - \frac{p_{\mu}p_{\nu}}{p^2} \right], \quad (\text{E.7})$$

where $g_{\mu\nu} = \text{diag}(-1, -1, -\tau^2)$ denotes the spatial components of the metric tensor, the spatial momentum vector is denoted as $p_{\mu} = (\vec{p}_T, \nu)$, the transverse momentum is $p_{\perp} = |\vec{p}_T|$ and $p^2 = p_{\perp}^2 + \nu^2/\tau^2$ denotes the spatial momentum squared. In summary the equal-time correlation functions in Eq. (E.1) can then be expressed as

$$\begin{aligned} \langle A_{\mu}^a(\tau, \vec{x}_1, \eta) A_{\nu}^a(\tau, \vec{x}_2, \eta') \rangle &= (N_c^2 - 1) \int \frac{d^2\vec{p}_T}{(2\pi)^2} \frac{d\nu}{2\pi} \left(\frac{1}{2p_{\perp}\tau} \right) \left[(f(\vec{p}_T, \nu) + 1) e^{i(\vec{p}_T(\vec{x}_1 - \vec{x}_2) + \nu(\eta - \eta'))} \right. \\ &\quad \left. + f(\vec{p}_T, \nu) e^{-i(\vec{p}_T(\vec{x}_1 - \vec{x}_2) + \nu(\eta - \eta'))} \right] \left[-g_{\mu\nu} - \frac{p_{\mu}p_{\nu}}{p^2} \right], \end{aligned} \quad (\text{E.8})$$

which we will use in the following in order to evaluate the perturbative expressions for gauge invariant quantities. We will also need the expectation value of equal-time correlation functions

of time derivatives of the gauge fields, which can be calculated in a similar fashion. Here we will only present the result of this computation, which is given by

$$\begin{aligned} \langle \partial_\tau A_\mu^a(\tau, \vec{x}_1, \eta) \partial_\tau A_\nu^a(\tau, \vec{x}_2, \eta') \rangle &= (N_c^2 - 1) \int \frac{d^2 \vec{p}_T d\nu}{(2\pi)^2 2\pi} \left(\frac{1}{2p_\perp \tau} \right) \left[(f(\vec{p}_T, \nu) + 1) \right. \\ &\times \left. e^{i(\vec{p}_T(\vec{x}_1 - \vec{x}_2) + \nu(\eta - \eta'))} + f(\vec{p}_T, \nu) e^{-i(\vec{p}_T(\vec{x}_1 - \vec{x}_2) + \nu(\eta - \eta'))} \right] \left[-p^2 g_{\mu\nu} - p_\mu p_\nu \right]. \end{aligned} \quad (\text{E.9})$$

In order to evaluate the perturbative expressions for the hard scale observables, we will first evaluate the perturbative expression for the energy density. Here we will consider separately the electric and magnetic components of the energy density, which can be calculated from Eqns. (E.8, E.9) in a straightforward way. The individual components of the magnetic energy density are given by

$$\begin{aligned} \langle \mathcal{B}_x^2(\tau) \rangle &= \frac{1}{V_\perp L_\eta} \int d^2 x_\perp d\eta \langle \mathcal{F}_{y\eta}^a(x) \mathcal{F}_a^{y\eta}(x) \rangle, \\ \langle \mathcal{B}_y^2(\tau) \rangle &= \frac{1}{V_\perp L_\eta} \int d^2 x_\perp d\eta \langle \mathcal{F}_{x\eta}^a(x) \mathcal{F}_a^{x\eta}(x) \rangle, \\ \langle \mathcal{B}_\eta^2(\tau) \rangle &= \frac{1}{V_\perp L_\eta} \int d^2 x_\perp d\eta \langle \mathcal{F}_{xy}^a(x) \mathcal{F}_a^{xy}(x) \rangle, \end{aligned} \quad (\text{E.10})$$

where in the following we will consider only the abelian part of the field strength tensor. The expressions in Eq. (E.10) then reduce to

$$\begin{aligned} \langle \mathcal{B}_x^2(\tau) \rangle &= \frac{1}{V_T L_\eta} \int d^2 x_\perp d\eta \Delta_{y\eta}^{\mu\nu}(x_1, x_2) \langle A_\mu^a(x_1) A_\nu^a(x_2) \rangle \Big|_{x_1=x_2=x}, \\ \langle \mathcal{B}_y^2(\tau) \rangle &= \frac{1}{V_T L_\eta} \int d^2 x_\perp d\eta \Delta_{x\eta}^{\mu\nu}(x_1, x_2) \langle A_\mu^a(x_1) A_\nu^a(x_2) \rangle \Big|_{x_1=x_2=x}, \\ \langle \mathcal{B}_\eta^2(\tau) \rangle &= \frac{1}{V_T L_\eta} \int d^2 x_\perp d\eta \Delta_{xy}^{\mu\nu}(x_1, x_2) \langle A_\mu^a(x_1) A_\nu^a(x_2) \rangle \Big|_{x_1=x_2=x}, \end{aligned} \quad (\text{E.11})$$

where the differential operator $\Delta_{\alpha\beta}^{\mu\nu}(x_1, x_2)$ is given by

$$\Delta_{\alpha\beta}^{\mu\nu}(x_1, x_2) = \partial_\alpha^{x_1} \partial_{x_2}^\alpha g^{\mu\beta} \delta_\beta^\nu + \partial_\beta^{x_1} \partial_{x_2}^\beta g^{\mu\alpha} \delta_\alpha^\nu - 2\partial_\alpha^{x_1} \partial_\beta^{x_2} g^{\mu\beta} g^{\nu\alpha}, \quad (\text{E.12})$$

(no summation over α, β) where δ_{β}^{α} denote the Kronecker symbol. By use of Eq. (E.8) for the equal time correlation functions in Coulomb gauge, one then obtains the final result

$$\begin{aligned}
\langle \mathcal{B}_x^2(\tau) \rangle &= N_g \int \frac{d^2 \vec{p}_T}{(2\pi)^2} \frac{d\nu}{2\pi} \frac{p_y^2 + \nu^2/\tau^2}{2p_{\perp}\tau} [f(p) + 1/2], \\
\langle \mathcal{B}_y^2(\tau) \rangle &= N_g \int \frac{d^2 \vec{p}_T}{(2\pi)^2} \frac{d\nu}{2\pi} \frac{p_x^2 + \nu^2/\tau^2}{2p_{\perp}\tau} [f(p) + 1/2], \\
\langle \mathcal{B}_{\eta}^2(\tau) \rangle &= N_g \int \frac{d^2 \vec{p}_T}{(2\pi)^2} \frac{d\nu}{2\pi} \frac{p_{\perp}^2}{2p_{\perp}\tau} [f(p) + 1/2],
\end{aligned} \tag{E.13}$$

where $N_g = 2(N_c^2 - 1)$ is the number of transverse gluons. Similarly, one can evaluate the electric components of the energy density

$$\begin{aligned}
\langle \mathcal{E}_x^2(\tau) \rangle &= \frac{1}{V_T L_{\eta}} \int d^2 x_{\perp} d\eta \frac{[E_a^x(x)]^2}{\tau^2}, \\
\langle \mathcal{E}_y^2(\tau) \rangle &= \frac{1}{V_T L_{\eta}} \int d^2 x_{\perp} d\eta \frac{[E_a^y(x)]^2}{\tau^2}, \\
\langle \mathcal{E}_{\eta}^2(\tau) \rangle &= \frac{1}{V_T L_{\eta}} \int d^2 x_{\perp} d\eta [E_a^{\eta}(x)]^2,
\end{aligned} \tag{E.14}$$

according to

$$\begin{aligned}
\langle \mathcal{E}_x^2(\tau) \rangle &= N_g \int \frac{d^2 \vec{p}_T}{(2\pi)^2} \frac{d\nu}{2\pi} \frac{p_y^2 + \nu^2/\tau^2}{2p_{\perp}\tau} [f(p) + 1/2], \\
\langle \mathcal{E}_y^2(\tau) \rangle &= N_g \int \frac{d^2 \vec{p}_T}{(2\pi)^2} \frac{d\nu}{2\pi} \frac{p_x^2 + \nu^2/\tau^2}{2p_{\perp}\tau} [f(p) + 1/2], \\
\langle \mathcal{E}_{\eta}^2(\tau) \rangle &= N_g \int \frac{d^2 \vec{p}_T}{(2\pi)^2} \frac{d\nu}{2\pi} \frac{p_{\perp}^2}{2p_{\perp}\tau} [f(p) + 1/2],
\end{aligned} \tag{E.15}$$

such that the overall energy density $\epsilon(\tau)$ is given by (c.f. Eqns. (2.79,2.81))

$$\epsilon(\tau) = 2N_g \int \frac{d^2 \vec{p}_T}{(2\pi)^2} \frac{d\nu}{2\pi} \frac{p^2}{2p_{\perp}\tau} [f(p) + 1/2]. \tag{E.16}$$

We note that the factor in the denominator has the interpretation of the mode energy $\omega_p \simeq p_{\perp}$ in the limit of highly anisotropic systems, where the characteristic transverse momenta are much larger than the characteristic longitudinal momenta. Since this limit enters the approximation in Eq. (E.6), we can also replace this factor to obtain the usual relativistic normalization. By absorbing the additional factor of τ into the integration over the longitudinal momentum $p_z = \nu/\tau$, one then recovers the standard textbook relations.

In order to evaluate the perturbative expressions for the gauge invariant hard scale observables Λ_T^2 and Λ_L^2 , we also have to consider covariant derivatives of the field strength tensor according to (c.f. Eq. (2.82))

$$\langle \mathcal{H}_\mu^\mu(\tau) \rangle = \frac{1}{V_\perp L_\eta} \int d^2 \vec{x}_\perp d\eta \langle D_\alpha^{ab}(x) \mathcal{F}_b^{\alpha\mu}(x) D_{ac}^\beta(x) \mathcal{F}_{\beta\mu}^c(x) \rangle, \quad (\text{E.17})$$

(no summation over μ) where summation over spatial Lorentz indices $\alpha, \beta = x, y, \eta$ is implied. We proceed as previously and consider only the abelian part of the covariant derivative and the field strength tensor, such that the expression in Eq. (E.17) reduces to

$$\langle \mathcal{H}_\mu^\mu(\tau) \rangle = \frac{1}{V_\perp L_\eta} \int d^2 x_\perp d\eta \Gamma_\mu^{\mu,\gamma\delta}(x_1, x_2) \langle A_\gamma^a(x_1) A_\delta^a(x_2) \rangle \Big|_{x_1=x_2=x} \quad (\text{E.18})$$

where we introduced the derivative operator

$$\Gamma_\mu^{\mu,\gamma\delta}(x_1, x_2) = [\partial_\alpha \partial^\alpha g^{\mu\gamma} - \partial_\alpha g^{\mu\nu} \partial_\nu g^{\alpha\gamma}]_{x_1} [\partial_\beta \partial^\beta \delta_\mu^\delta - g^{\beta\delta} \partial_\beta \partial_\mu]_{x_2}. \quad (\text{E.19})$$

Since the second parts of the derivatives are of the form $\partial^\gamma A_\gamma(x)$, they do not contribute in the generalized Coulomb gauge. With this simplification, the above expression can then be evaluated explicitly according to

$$\begin{aligned} \langle \mathcal{H}_x^x(\tau) \rangle &= N_g \int \frac{d^2 \vec{p}_T}{(2\pi)^2} \frac{d\nu}{2\pi} \frac{p^2 [p_y^2 + \nu^2/\tau^2]}{2p_\perp \tau} [f(p) + 1/2], \\ \langle \mathcal{H}_y^y(\tau) \rangle &= N_g \int \frac{d^2 \vec{p}_T}{(2\pi)^2} \frac{d\nu}{2\pi} \frac{p^2 [p_x^2 + \nu^2/\tau^2]}{2p_\perp \tau} [f(p) + 1/2], \\ \langle \mathcal{H}_\eta^\eta(\tau) \rangle &= N_g \int \frac{d^2 \vec{p}_T}{(2\pi)^2} \frac{d\nu}{2\pi} \frac{p^2 p_\perp^2}{2p_\perp \tau} [f(p) + 1/2]. \end{aligned} \quad (\text{E.20})$$

Combining the results in Eqns. (E.16) and (E.20), we obtain the final result (c.f. Eqns. (2.84,2.85))

$$\Lambda_T^2(\tau) \simeq \frac{\int d^2 \vec{p}_T dp_z p_\perp^2/2 \omega_p f(\vec{p}_T, p_z, \tau)}{\int d^2 \vec{p}_T dp_z \omega_p f(\vec{p}_T, p_z, \tau)}, \quad \Lambda_L^2(\tau) \simeq \frac{\int d^2 \vec{p}_T dp_z p_z^2 \omega_p f(\vec{p}_T, p_z, \tau)}{\int d^2 \vec{p}_T dp_z \omega_p f(\vec{p}_T, p_z, \tau)}, \quad (\text{E.21})$$

where in the last step, we explicitly used $\omega_p \simeq p_T$ as the relativistic quasi-particle energy in the limit $p_T \gg \nu/\tau$.

Appendix F

Set-in and freeze-out times in the parametric resonance instability

Here we investigate the instability criterion for the parametric resonance instability discussed in Sec. 4.2 for generic modes with transverse momentum p_T and rapidity wave number ν . In accordance with Eqns. (4.65) and (4.66), the condition for modes to be contained in the unstable resonance band takes the form

$$\frac{2\theta}{3(\sigma_0\tau_0)} \frac{p_T^2}{\sigma_0^2} + \frac{9\nu^2}{4\theta^2} \leq \frac{1}{2}, \quad (\text{F.1})$$

and we are only interested in the solutions $\theta > 0$, which characterize the on-set and freeze-out of instabilities relevant for the initial value problem. Before considering the generic case $p_T \neq 0$ and $\nu \neq 0$ we consider briefly the special cases where one of the two vanishes. For vanishing transverse momentum the condition is satisfied if

$$\theta \geq \frac{\sqrt{18}}{2} \nu, \quad (\text{F.2})$$

which suggests that exponential growth sets in with a delay. In contrast for vanishing ν unstable growth is limited to the time when

$$\theta \leq (\sigma_0\tau_0) \frac{3\sigma_0^2}{4p_T^2}, \quad (\text{F.3})$$

suggesting that exponential growth stops for later times. For the generic case, Eq. (F.1) can be solved graphically. First we rescale $\theta'/\theta = 2/(3\sigma_0\tau_0) p_T^2/\sigma_0^2$ yielding

$$\frac{\nu^2 p_T^4}{\sigma_0^4 (\sigma_0\tau_0)^2} \frac{1}{\theta'^2} \leq \frac{1}{2} - \theta'. \quad (\text{F.4})$$

This suggests that the existence of an unstable window only depends on the value of $p_T^4 \nu^2 / (\sigma_0^4 (\sigma_0 \tau_0)^2)$, whereas the precise time also depends on p_T^2 / σ_0^2 . The existence of real solutions is visualized in Fig. F.1, where we show the left hand side and the right hand side of Eq. (F.4) for different values of $p_T^4 \nu^2 / (\sigma_0^4 (\sigma_0 \tau_0)^2)$. One observes that one solution is always real and negative and therefore not relevant for the study of the initial value problem. The other solutions are real for $\nu^2 p_T^4 < \sigma_0^4 (\sigma_0 \tau_0)^2 / 54$. In this case the solutions are given by

$$\theta'_{Start} = \frac{1}{6} [1 - e^{-i\pi/3} / \alpha - e^{i\pi/3} \alpha] , \quad (\text{F.5})$$

$$\theta'_{End} = \frac{1}{6} [1 + 1/\alpha + \alpha] , \quad (\text{F.6})$$

$$\alpha = \left(1 - 2\beta + \sqrt{4\beta(\beta - 1)} \right)^{1/3} , \quad (\text{F.7})$$

$$\beta = 54 \frac{p_T^4 \nu^2}{\sigma_0^4 (\sigma_0 \tau_0)^2} . \quad (\text{F.8})$$

The solution is real if and only if $|\alpha| = 1$. Indeed this is the case for resonant modes, i.e. modes with $\beta < 1$. We can exploit this fact to rewrite the solution for the starting and ending times as

$$\theta'_{Start} = \frac{1}{6} (1 + 2 \sin(\phi/3 - \pi/6)) \quad (\text{F.9})$$

$$\theta'_{End} = \frac{1}{6} (1 + 2 \cos(\phi/3)) \quad (\text{F.10})$$

$$\phi = 2 \arctan \left(\sqrt{\frac{1}{\beta^{-1} - 1}} \right) \quad (\text{F.11})$$

which is manifestly real. We also note that $\phi \in (0, \pi)$ for modes satisfying Eq. (F.4) and therefore $\theta'_{Start} \leq \theta'_{End}$ as suggested by the naming.

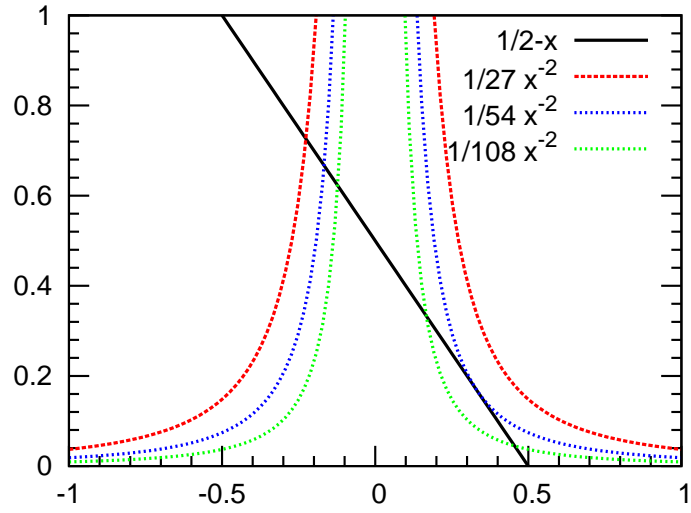


Figure F.1: Visualization of Eq. (F.4) for different values of $p_T^4 \nu^2 / (\sigma_0^4 (\sigma_0 \tau_0)^2)$. There is always one negative solution which is irrelevant for the initial value problem. If $p_T^4 \nu^2 / (\sigma_0^4 (\sigma_0 \tau_0)^2)$ is smaller than the critical value of $1/54$ there are two positive solutions corresponding to the set-in and freeze-out times of the primary instability.

Appendix G

CGC initial conditions on the lattice

In this appendix, we describe the lattice implementation of the color-glass initial conditions discussed in Sec. 5.2. We first generate $2(N_c^2 - 1)$ sets of uncorrelated Gaussian random numbers associated to the color-charge densities of the two incoming nuclei. This is done in coordinate space, where for every position in the transverse plane we initialize

$$\rho_a^{(A)}(\vec{x}_\perp) = \left(\frac{Q}{g}\right) \frac{\xi_a^{(A)}(\vec{x}_\perp) - R_a^{(A)}}{N_T a_\perp} . \quad (\text{G.1})$$

Here $a = 1, \dots, N_c^2 - 1$, labels the different color components, $A = 1, 2$ labels the different nuclei, $\xi_a^{(A)}(\vec{x}_\perp)$ denote Gaussian random numbers and the subtraction of the overall color charge $R_a^{(A)} = N_T^{-2} \sum_{\vec{x}_\perp} \xi_a^{(A)}(\vec{x}_\perp)$ ensures the overall color neutrality constraint.

In order to obtain the initial gauge links and electric fields in the forward light cone, the result is then Fourier transformed to (transverse) momentum space, where we solve the Laplace equation

$$\Lambda_a^{(A)}(\vec{p}_T) = -\frac{\rho_a^{(A)}(\vec{p}_T)}{\vec{p}_T^2} . \quad (\text{G.2})$$

The result is Fourier transformed back to obtain the solution of the Laplace equation in coordinate space. We then proceed by calculating the pure gauge solutions $U^{(1/2)}(\vec{x}_\perp)$ according to

$$U_i^{(A)}(\vec{x}_\perp) = V^{(A)}(\vec{x}_\perp) V^{\dagger(A)}(\vec{x}_\perp + \hat{i}) , \quad (\text{G.3})$$

$$V^{(A)}(\vec{x}_\perp) = \exp[ig \Lambda_a^{(A)}(\vec{x}_\perp) \Gamma^a] . \quad (\text{G.4})$$

The link variables $U_\mu(\vec{x}_\perp, \eta, \tau = 0^+)$ at initial time $\tau = 0^+$ can then be obtained as [50, 51]

$$U_i(\vec{x}_\perp, \eta, \tau = 0^+) = \left[U_i^{(1)}(\vec{x}_\perp) + U_i^{(2)}(\vec{x}_\perp) \right] \left[U_i^{\dagger(1)}(\vec{x}_\perp) + U_i^{\dagger(2)}(\vec{x}_\perp) \right]^{-1}, \quad (\text{G.5})$$

whereas $U_\eta(\vec{x}_\perp, \eta, \tau = 0^+) = \mathbb{1}$. Similarly, the (dimensionless) electric field variables $\tilde{E}_\mu^a(x_\perp, \eta, \tau = 0^+)$ at initial time are given by $\tilde{E}_i^a(x_\perp, \eta, \tau = 0^+) = 0$, while the longitudinal component is given by [50]

$$\begin{aligned} \tilde{E}_\eta^a(\vec{x}_\perp, \eta, \tau = 0^+) &= 2\text{Re} \text{tr} \left[i\Gamma^a \sum_{i=1,2} U_i^{(2)}(\vec{x}_\perp) - U_i^{(2)}(\vec{x}_\perp - \hat{i}) \right. \\ &\quad \left. + U_i^{(1)}(\vec{x}_\perp) U_i^\dagger(\vec{x}_\perp) - U_i^\dagger(\vec{x}_\perp - \hat{i}) U_i^{(1)}(\vec{x}_\perp - \hat{i}) \right]. \end{aligned} \quad (\text{G.6})$$

In order to generate the fluctuations, which explicitly break the boost invariance of the system we first sample the functions $h(\nu)$ and $e_i^a(\vec{p}_\perp)$ in momentum space according to

$$h(\nu) = e^{-b|\nu|} \xi(\nu) \sqrt{N_\eta a_\eta}, \quad e_i^a(\vec{p}_\perp) = \xi_i^a(\vec{p}_\perp) (N_\perp a_\perp) \quad (\text{G.7})$$

where $\xi_i^a(\vec{p}_\perp)$ and $\xi(\nu)$ are uncorrelated Gaussian random numbers. After performing a Fourier transform to coordinate space, the (dimensionless) electric field fluctuations $\delta E_\mu^a(\vec{x}_\perp, \eta, \tau = 0^+)$ can then be calculated as

$$\delta \tilde{E}_i^a(\vec{x}_\perp, \eta, \tau = 0^+) = (g a_\perp) e_i^a(\vec{x}_\perp) \frac{h(\eta) - h(\eta - \hat{\eta})}{a_\eta}, \quad (\text{G.8})$$

$$\delta \tilde{E}_\eta^a(\vec{x}_\perp, \eta, \tau = 0^+) = -h(\eta) \text{tr} \left[i\Gamma^a \sum_{j=1,2} \mathcal{D}_j(x) \right], \quad (\text{G.9})$$

where $\mathcal{D}_j(x)$ denotes the covariant derivative of the transverse electric fields according to

$$\mathcal{D}_j(\vec{x}_\perp, \eta, \tau = 0^+) = \exp[ig a_\perp e_j^a(\vec{x}_\perp)] - U_j^\dagger(x - \hat{j}) \exp[ig a_\perp e_j^a(\vec{x}_\perp - \hat{j})] U_j(x - \hat{j}). \quad (\text{G.10})$$

The electric field variables in our simulations are then initialized as the sum of the two contributions $\tilde{E}_\mu^a(x_\perp, \eta, \tau = 0^+)$ and $\delta \tilde{E}_\mu^a(x_\perp, \eta, \tau = 0^+)$.

Bibliography

- [1] D.J. GROSS and F. WILCZEK. “*Ultraviolet Behavior of Nonabelian Gauge Theories*“. Phys.Rev.Lett. **30** (1973), 1343–1346. DOI: [10.1103/PhysRevLett.30.1343](https://doi.org/10.1103/PhysRevLett.30.1343).
- [2] H. D. POLITZER. “*Reliable Perturbative Results for Strong Interactions?*“ Phys.Rev.Lett. **30** (1973), 1346–1349. DOI: [10.1103/PhysRevLett.30.1346](https://doi.org/10.1103/PhysRevLett.30.1346).
- [3] J. BERINGER et al. “*Review of Particle Physics (RPP)*“. Phys.Rev. **D86** (2012), 010001. DOI: [10.1103/PhysRevD.86.010001](https://doi.org/10.1103/PhysRevD.86.010001).
- [4] Y. AOKI, G. ENDRODI, Z. FODOR, S.D. KATZ, and K.K. SZABO. “*The Order of the quantum chromodynamics transition predicted by the standard model of particle physics*“. Nature **443** (2006), 675–678. DOI: [10.1038/nature05120](https://doi.org/10.1038/nature05120). arXiv: [hep-lat/0611014](https://arxiv.org/abs/hep-lat/0611014) [[hep-lat](#)].
- [5] Y. AOKI, Z. FODOR, S.D. KATZ, and K.K. SZABO. “*The QCD transition temperature: Results with physical masses in the continuum limit*“. Phys.Lett. **B643** (2006), 46–54. DOI: [10.1016/j.physletb.2006.10.021](https://doi.org/10.1016/j.physletb.2006.10.021). arXiv: [hep-lat/0609068](https://arxiv.org/abs/hep-lat/0609068) [[hep-lat](#)].
- [6] Y. AOKI, SZ. BORSANYI, S. DURR, Z FODOR, S. D. KATZ, et al. “*The QCD transition temperature: results with physical masses in the continuum limit II.*“ JHEP **0906** (2009), 088. DOI: [10.1088/1126-6708/2009/06/088](https://doi.org/10.1088/1126-6708/2009/06/088). arXiv: [0903.4155](https://arxiv.org/abs/0903.4155) [[hep-lat](#)].
- [7] A. BAZAVOV, T. BHATTACHARYA, M. CHENG, N.H. CHRIST, C. DETAR, et al. “*Equation of state and QCD transition at finite temperature*“. Phys.Rev. **D80** (2009), 014504. DOI: [10.1103/PhysRevD.80.014504](https://doi.org/10.1103/PhysRevD.80.014504). arXiv: [0903.4379](https://arxiv.org/abs/0903.4379) [[hep-lat](#)].
- [8] P. DE FORCRAND. “*Simulating QCD at finite density*“. PoS **LAT2009** (2009), 010. arXiv: [1005.0539](https://arxiv.org/abs/1005.0539) [[hep-lat](#)].
- [9] G. AARTS. “*Complex Langevin dynamics and other approaches at finite chemical potential*“. PoS **LATTICE2012** (2012), 017. arXiv: [1302.3028](https://arxiv.org/abs/1302.3028) [[hep-lat](#)].
- [10] J. M. PAWLOWSKI. “*The QCD phase diagram: Results and challenges*“. AIP Conf.Proc. **1343** (2011), 75–80. DOI: [10.1063/1.3574945](https://doi.org/10.1063/1.3574945). arXiv: [1012.5075](https://arxiv.org/abs/1012.5075) [[hep-ph](#)].

- [11] K. ADCOX et al. “*Formation of dense partonic matter in relativistic nucleus-nucleus collisions at RHIC: Experimental evaluation by the PHENIX collaboration*“. Nucl.Phys. **A757** (2005), 184–283. DOI: [10.1016/j.nuclphysa.2005.03.086](https://doi.org/10.1016/j.nuclphysa.2005.03.086). arXiv: [nucl-ex/0410003](https://arxiv.org/abs/nucl-ex/0410003) [nucl-ex].
- [12] J. ADAMS et al. “*Experimental and theoretical challenges in the search for the quark gluon plasma: The STAR Collaboration’s critical assessment of the evidence from RHIC collisions*“. Nucl.Phys. **A757** (2005), 102–183. DOI: [10.1016/j.nuclphysa.2005.03.085](https://doi.org/10.1016/j.nuclphysa.2005.03.085). arXiv: [nucl-ex/0501009](https://arxiv.org/abs/nucl-ex/0501009) [nucl-ex].
- [13] I. ARSENE et al. “*Quark gluon plasma and color glass condensate at RHIC? The Perspective from the BRAHMS experiment*“. Nucl.Phys. **A757** (2005), 1–27. DOI: [10.1016/j.nuclphysa.2005.02.130](https://doi.org/10.1016/j.nuclphysa.2005.02.130). arXiv: [nucl-ex/0410020](https://arxiv.org/abs/nucl-ex/0410020) [nucl-ex].
- [14] B.B. BACK, M.D. BAKER, M. BALLINTIJN, D.S. BARTON, B. BECKER, et al. “*The PHOBOS perspective on discoveries at RHIC*“. Nucl.Phys. **A757** (2005), 28–101. DOI: [10.1016/j.nuclphysa.2005.03.084](https://doi.org/10.1016/j.nuclphysa.2005.03.084). arXiv: [nucl-ex/0410022](https://arxiv.org/abs/nucl-ex/0410022) [nucl-ex].
- [15] J. SCHUKRAFT. “*First Results from the ALICE experiment at the LHC*“. Nucl.Phys. **A862-863** (2011), 78–84. DOI: [10.1016/j.nuclphysa.2011.05.023](https://doi.org/10.1016/j.nuclphysa.2011.05.023). arXiv: [1103.3474](https://arxiv.org/abs/1103.3474) [hep-ex].
- [16] U. W. HEINZ. “*Towards the Little Bang Standard Model*“ (2013). arXiv: [1304.3634](https://arxiv.org/abs/1304.3634) [nucl-th].
- [17] D. TEANEY, J. LAURET, and E. V. SHURYAK. “*Flow at the SPS and RHIC as a quark gluon plasma signature*“. Phys.Rev.Lett. **86** (2001), 4783–4786. DOI: [10.1103/PhysRevLett.86.4783](https://doi.org/10.1103/PhysRevLett.86.4783). arXiv: [nucl-th/0011058](https://arxiv.org/abs/nucl-th/0011058) [nucl-th].
- [18] U. W. HEINZ and P. F. KOLB. “*Early thermalization at RHIC*“. Nucl.Phys. **A702** (2002), 269–280. DOI: [10.1016/S0375-9474\(02\)00714-5](https://doi.org/10.1016/S0375-9474(02)00714-5). arXiv: [hep-ph/0111075](https://arxiv.org/abs/hep-ph/0111075) [hep-ph].
- [19] P. F. KOLB and R. RAPP. “*Transverse flow and hadrochemistry in Au+Au collisions at $(S(NN))^{1/2} = 200$ -GeV*“. Phys.Rev. **C67** (2003), 044903. DOI: [10.1103/PhysRevC.67.044903](https://doi.org/10.1103/PhysRevC.67.044903). arXiv: [hep-ph/0210222](https://arxiv.org/abs/hep-ph/0210222) [hep-ph].
- [20] U. W. HEINZ. “*Thermalization at RHIC*“. AIP Conf.Proc. **739** (2005), 163–180. DOI: [10.1063/1.1843595](https://doi.org/10.1063/1.1843595). arXiv: [nucl-th/0407067](https://arxiv.org/abs/nucl-th/0407067) [nucl-th].
- [21] E. V. SHURYAK. “*What RHIC experiments and theory tell us about properties of quark-gluon plasma?*“ Nucl.Phys. **A750** (2005), 64–83. DOI: [10.1016/j.nuclphysa.2004.10.022](https://doi.org/10.1016/j.nuclphysa.2004.10.022). arXiv: [hep-ph/0405066](https://arxiv.org/abs/hep-ph/0405066) [hep-ph].

- [22] P. ROMATSCHKE and U. ROMATSCHKE. “*Viscosity Information from Relativistic Nuclear Collisions: How Perfect is the Fluid Observed at RHIC?*“ Phys.Rev.Lett. **99** (2007), 172301. DOI: [10.1103/PhysRevLett.99.172301](https://doi.org/10.1103/PhysRevLett.99.172301). arXiv: [0706.1522](https://arxiv.org/abs/0706.1522) [nucl-th].
- [23] J. BERGES, J.-P. BLAIZOT, and F. GELIS. “*EMMI Rapid Reaction Task Force on ‘Thermalization in Non-abelian Plasmas’*“. J.Phys. **G39** (2012), 085115. DOI: [10.1088/0954-3899/39/8/085115](https://doi.org/10.1088/0954-3899/39/8/085115). arXiv: [1203.2042](https://arxiv.org/abs/1203.2042) [hep-ph].
- [24] M. P. HELLER, P. SUROWKA, R. LOGANAYAGAM, M. SPALINSKI, and S. E. VAZQUEZ. “*Consistent Holographic Description of Boost-Invariant Plasma*“. Phys.Rev.Lett. **102** (2009), 041601. DOI: [10.1103/PhysRevLett.102.041601](https://doi.org/10.1103/PhysRevLett.102.041601). arXiv: [0805.3774](https://arxiv.org/abs/0805.3774) [hep-th].
- [25] G. BEUF, M. P. HELLER, R. A. JANIK, and R. PESCHANSKI. “*Boost-invariant early time dynamics from AdS/CFT*“. JHEP **0910** (2009), 043. DOI: [10.1088/1126-6708/2009/10/043](https://doi.org/10.1088/1126-6708/2009/10/043). arXiv: [0906.4423](https://arxiv.org/abs/0906.4423) [hep-th].
- [26] M. P. HELLER, R. A. JANIK, and P. WITASZCZYK. “*The characteristics of thermalization of boost-invariant plasma from holography*“. Phys.Rev.Lett. **108** (2012), 201602. DOI: [10.1103/PhysRevLett.108.201602](https://doi.org/10.1103/PhysRevLett.108.201602). arXiv: [1103.3452](https://arxiv.org/abs/1103.3452) [hep-th].
- [27] E. IANCU and R. VENUGOPALAN. “*The Color glass condensate and high-energy scattering in QCD*“ (2003). arXiv: [hep-ph/0303204](https://arxiv.org/abs/hep-ph/0303204) [hep-ph].
- [28] F. GELIS, E. IANCU, J. JALILIAN-MARIAN, and R. VENUGOPALAN. “*The Color Glass Condensate*“. Ann.Rev.Nucl.Part.Sci. **60** (2010), 463–489. DOI: [10.1146/annurev.nucl.010909.083629](https://doi.org/10.1146/annurev.nucl.010909.083629). arXiv: [1002.0333](https://arxiv.org/abs/1002.0333) [hep-ph].
- [29] R. BAIER, A. H. MUELLER, D. SCHIFF, and D. T. SON. “*‘Bottom up’ thermalization in heavy ion collisions*“. Phys.Lett. **B502** (2001), 51–58. DOI: [10.1016/S0370-2693\(01\)00191-5](https://doi.org/10.1016/S0370-2693(01)00191-5). arXiv: [hep-ph/0009237](https://arxiv.org/abs/hep-ph/0009237) [hep-ph].
- [30] J.-P. BLAIZOT, F. GELIS, J.-F. LIAO, L. MCLERRAN, and R. VENUGOPALAN. “*Bose–Einstein Condensation and Thermalization of the Quark Gluon Plasma*“. Nucl.Phys. **A873** (2012), 68–80. DOI: [10.1016/j.nuclphysa.2011.10.005](https://doi.org/10.1016/j.nuclphysa.2011.10.005). arXiv: [1107.5296](https://arxiv.org/abs/1107.5296) [hep-ph].
- [31] A. KURKELA and G. D. MOORE. “*Thermalization in Weakly Coupled Nonabelian Plasmas*“. JHEP **1112** (2011), 044. DOI: [10.1007/JHEP12\(2011\)044](https://doi.org/10.1007/JHEP12(2011)044). arXiv: [1107.5050](https://arxiv.org/abs/1107.5050) [hep-ph].
- [32] A. KURKELA and G. D. MOORE. “*Bjorken Flow, Plasma Instabilities, and Thermalization*“. JHEP **1111** (2011), 120. DOI: [10.1007/JHEP11\(2011\)120](https://doi.org/10.1007/JHEP11(2011)120). arXiv: [1108.4684](https://arxiv.org/abs/1108.4684) [hep-ph].

- [33] J. BERGES, A. ROTHKOPF, and J. SCHMIDT. “*Non-thermal fixed points: Effective weak-coupling for strongly correlated systems far from equilibrium*“. Phys.Rev.Lett. **101** (2008), 041603. DOI: [10.1103/PhysRevLett.101.041603](https://doi.org/10.1103/PhysRevLett.101.041603). arXiv: [0803.0131](https://arxiv.org/abs/0803.0131) [hep-ph].
- [34] R. MICHA and I. I. TKACHEV. “*Turbulent thermalization*“. Phys.Rev. **D70** (2004), 043538. DOI: [10.1103/PhysRevD.70.043538](https://doi.org/10.1103/PhysRevD.70.043538). arXiv: [hep-ph/0403101](https://arxiv.org/abs/hep-ph/0403101) [hep-ph].
- [35] J. BERGES and D. SEXTY. “*Strong versus weak wave-turbulence in relativistic field theory*“. Phys.Rev. **D83** (2011), 085004. DOI: [10.1103/PhysRevD.83.085004](https://doi.org/10.1103/PhysRevD.83.085004). arXiv: [1012.5944](https://arxiv.org/abs/1012.5944) [hep-ph].
- [36] B. NOWAK, J. SCHOLE, D. SEXTY, and T. GASENZER. “*Nonthermal fixed points, vortex statistics, and superfluid turbulence in an ultracold Bose gas*“. Phys.Rev. **A85** (2012), 043627. DOI: [10.1103/PhysRevA.85.043627](https://doi.org/10.1103/PhysRevA.85.043627). arXiv: [1111.6127](https://arxiv.org/abs/1111.6127) [cond-mat.quant-gas].
- [37] V.E. ZAKHAROV, V.S. LVOV, and G. FALKOVICH. *Kolmogorov spectra of turbulence*. Springer series in nonlinear dynamics Bd. 1. Springer-Verlag, 1992.
- [38] U. FRISCH and A.N. KOLMOGOROV. *Turbulence*: Cambridge University Press, 1995.
- [39] S. NAZARENKO. *Wave Turbulence*. Lecture Notes in Physics. Springer, 2011.
- [40] G. AARTS and J. BERGES. “*Classical aspects of quantum fields far from equilibrium*“. Phys.Rev.Lett. **88** (2002), 041603. DOI: [10.1103/PhysRevLett.88.041603](https://doi.org/10.1103/PhysRevLett.88.041603). arXiv: [hep-ph/0107129](https://arxiv.org/abs/hep-ph/0107129) [hep-ph].
- [41] J. BERGES and T. GASENZER. “*Quantum versus classical statistical dynamics of an ultracold Bose gas*“. Phys.Rev. **A76** (2007), 033604. DOI: [10.1103/PhysRevA.76.033604](https://doi.org/10.1103/PhysRevA.76.033604). arXiv: [cond-mat/0703163](https://arxiv.org/abs/cond-mat/0703163) [cond-mat.other].
- [42] J. BERGES. “*Introduction to nonequilibrium quantum field theory*“. AIP Conf.Proc. **739** (2005), 3–62. DOI: [10.1063/1.1843591](https://doi.org/10.1063/1.1843591). arXiv: [hep-ph/0409233](https://arxiv.org/abs/hep-ph/0409233) [hep-ph].
- [43] J. BERGES and D. SEXTY. “*Bose condensation far from equilibrium*“. Phys.Rev.Lett. **108** (2012), 161601. DOI: [10.1103/PhysRevLett.108.161601](https://doi.org/10.1103/PhysRevLett.108.161601). arXiv: [1201.0687](https://arxiv.org/abs/1201.0687) [hep-ph].
- [44] S. MROWCZYNSKI. “*Plasma instability at the initial stage of ultrarelativistic heavy ion collisions*“. Phys.Lett. **B314** (1993), 118–121. DOI: [10.1016/0370-2693\(93\)91330-P](https://doi.org/10.1016/0370-2693(93)91330-P).
- [45] P. B. ARNOLD, J. LENAGHAN, G. D. MOORE, and L. G. YAFFE. “*Apparent thermalization due to plasma instabilities in quark-gluon plasma*“. Phys.Rev.Lett. **94** (2005), 072302. DOI: [10.1103/PhysRevLett.94.072302](https://doi.org/10.1103/PhysRevLett.94.072302). arXiv: [nuc1-th/0409068](https://arxiv.org/abs/nuc1-th/0409068) [nuc1-th].
- [46] E. S. WEIBEL. “*Spontaneously Growing Transverse Waves in a Plasma Due to an Anisotropic Velocity Distribution*“. Phys.Rev.Lett. **2** (1959), 83–84. DOI: [10.1103/PhysRevLett.2.83](https://doi.org/10.1103/PhysRevLett.2.83).

- [47] N.K. NIELSEN and P. OLESEN. “*An Unstable Yang-Mills Field Mode*“. Nucl.Phys. **B144** (1978), 376. DOI: [10.1016/0550-3213\(78\)90377-2](https://doi.org/10.1016/0550-3213(78)90377-2).
- [48] S.-J. CHANG and N. WEISS. “*Instability of constant Yang-Mills Fields*“. Phys.Rev. **D20** (1979), 869. DOI: [10.1103/PhysRevD.20.869](https://doi.org/10.1103/PhysRevD.20.869).
- [49] P. ROMATSCHKE and R. VENUGOPALAN. “*Collective non-Abelian instabilities in a melting color glass condensate*“. Phys.Rev.Lett. **96** (2006), 062302. DOI: [10.1103/PhysRevLett.96.062302](https://doi.org/10.1103/PhysRevLett.96.062302). arXiv: [hep-ph/0510121](https://arxiv.org/abs/hep-ph/0510121) [hep-ph].
- [50] P. ROMATSCHKE and R. VENUGOPALAN. “*The Unstable Glasma*“. Phys.Rev. **D74** (2006), 045011. DOI: [10.1103/PhysRevD.74.045011](https://doi.org/10.1103/PhysRevD.74.045011). arXiv: [hep-ph/0605045](https://arxiv.org/abs/hep-ph/0605045) [hep-ph].
- [51] K. FUKUSHIMA and F. GELIS. “*The evolving Glasma*“. Nucl.Phys. **A874** (2012), 108–129. DOI: [10.1016/j.nuclphysa.2011.11.003](https://doi.org/10.1016/j.nuclphysa.2011.11.003). arXiv: [1106.1396](https://arxiv.org/abs/1106.1396) [hep-ph].
- [52] J. BERGES, S. SCHEFFLER, and D. SEXTY. “*Bottom-up isotropization in classical-statistical lattice gauge theory*“. Phys.Rev. **D77** (2008), 034504. DOI: [10.1103/PhysRevD.77.034504](https://doi.org/10.1103/PhysRevD.77.034504). arXiv: [0712.3514](https://arxiv.org/abs/0712.3514) [hep-ph].
- [53] J. BERGES and J. SERREAU. “*Parametric resonance in quantum field theory*“. Phys.Rev.Lett. **91** (2003), 111601. DOI: [10.1103/PhysRevLett.91.111601](https://doi.org/10.1103/PhysRevLett.91.111601). arXiv: [hep-ph/0208070](https://arxiv.org/abs/hep-ph/0208070) [hep-ph].
- [54] M. LEBELLAC. *Quantum and statistical field theory*. Oxford science publications. Oxford University Press, 1991.
- [55] S. WEINBERG. *The Quantum Theory of Fields*. The Quantum Theory of Fields 3 Volume Hardback Set Bd. 2. Cambridge University Press, 1996.
- [56] J. ZINN-JUSTIN. *Quantum Field Theory and Critical Phenomena*. The International Series of Monographs on Physics Series. Clarendon Press, 2002.
- [57] V.P. NAIR. *Quantum Field Theory: A Modern Perspective*. Graduate Texts in Contemporary Physics. Springer, 2005.
- [58] C. ITZYKSON and J.B. ZUBER. *Quantum Field Theory*. Dover books on physics. Dover Publications, Incorporated, 2012.
- [59] SZ. BORSANYI and M. HINDMARSH. “*Low-cost fermions in classical field simulations*“. Phys.Rev. **D79** (2009), 065010. DOI: [10.1103/PhysRevD.79.065010](https://doi.org/10.1103/PhysRevD.79.065010). arXiv: [0809.4711](https://arxiv.org/abs/0809.4711) [hep-ph].
- [60] J. BERGES, D. GELFAND, and J. PRUSCHKE. “*Quantum theory of fermion production after inflation*“. Phys.Rev.Lett. **107** (2011), 061301. DOI: [10.1103/PhysRevLett.107.061301](https://doi.org/10.1103/PhysRevLett.107.061301). arXiv: [1012.4632](https://arxiv.org/abs/1012.4632) [hep-ph].

- [61] P. M. SAFFIN and A. TRANBERG. “*Real-time Fermions for Baryogenesis Simulations*“. JHEP **1107** (2011), 066. DOI: [10.1007/JHEP07\(2011\)066](https://doi.org/10.1007/JHEP07(2011)066). arXiv: [1105.5546](https://arxiv.org/abs/1105.5546) [hep-ph].
- [62] P. M. SAFFIN and A. TRANBERG. “*Dynamical simulations of electroweak baryogenesis with fermions*“. JHEP **1202** (2012), 102. DOI: [10.1007/JHEP02\(2012\)102](https://doi.org/10.1007/JHEP02(2012)102). arXiv: [1111.7136](https://arxiv.org/abs/1111.7136) [hep-ph].
- [63] F. HEBENSTREIT, J. BERGES, and D. GELFAND. “*Simulating fermion production in 1+1 dimensional QED*“ (2013). arXiv: [1302.5537](https://arxiv.org/abs/1302.5537) [hep-ph].
- [64] J. BERGES, D. GELFAND, S. SCHEFFLER, and D. SEXTY. “*Simulating plasma instabilities in $SU(3)$ gauge theory*“. Phys.Lett. **B677** (2009), 210–213. DOI: [10.1016/j.physletb.2009.05.008](https://doi.org/10.1016/j.physletb.2009.05.008). arXiv: [0812.3859](https://arxiv.org/abs/0812.3859) [hep-ph].
- [65] A. IPP, A. REBHAN, and M. STRICKLAND. “*Non-Abelian plasma instabilities: $SU(3)$ vs. $SU(2)$* “. Phys.Rev. **D84** (2011), 056003. DOI: [10.1103/PhysRevD.84.056003](https://doi.org/10.1103/PhysRevD.84.056003). arXiv: [1012.0298](https://arxiv.org/abs/1012.0298) [hep-ph].
- [66] J. BERGES and D. MESTERHAZY. “*Introduction to the nonequilibrium functional renormalization group*“. Nucl.Phys.Proc.Suppl. **228** (2012), 37–60. DOI: [10.1016/j.nuclphysbps.2012.06.003](https://doi.org/10.1016/j.nuclphysbps.2012.06.003). arXiv: [1204.1489](https://arxiv.org/abs/1204.1489) [hep-ph].
- [67] J.-P. BLAIZOT and E. IANCU. “*The Quark gluon plasma: Collective dynamics and hard thermal loops*“. Phys.Rept. **359** (2002), 355–528. DOI: [10.1016/S0370-1573\(01\)00061-8](https://doi.org/10.1016/S0370-1573(01)00061-8). arXiv: [hep-ph/0101103](https://arxiv.org/abs/hep-ph/0101103) [hep-ph].
- [68] S. JEON. “*The Boltzmann equation in classical and quantum field theory*“. Phys.Rev. **C72** (2005), 014907. DOI: [10.1103/PhysRevC.72.014907](https://doi.org/10.1103/PhysRevC.72.014907). arXiv: [hep-ph/0412121](https://arxiv.org/abs/hep-ph/0412121) [hep-ph].
- [69] E.A. CALZETTA and B.L.B. HU. *Nonequilibrium Quantum Field Theory*. Cambridge Monographs on Mathematical Physics. Cambridge University Press, 2008.
- [70] V.N. GRIBOV. “*Quantization of Nonabelian Gauge Theories*“. Nucl.Phys. **B139** (1978), 1. DOI: [10.1016/0550-3213\(78\)90175-X](https://doi.org/10.1016/0550-3213(78)90175-X).
- [71] D. ZWANZIGER. “*Nonperturbative Landau gauge and infrared critical exponents in QCD*“. Phys.Rev. **D65** (2002), 094039. DOI: [10.1103/PhysRevD.65.094039](https://doi.org/10.1103/PhysRevD.65.094039). arXiv: [hep-th/0109224](https://arxiv.org/abs/hep-th/0109224) [hep-th].
- [72] J. BERGES. “ *N -particle irreducible effective action techniques for gauge theories*“. Phys.Rev. **D70** (2004), 105010. DOI: [10.1103/PhysRevD.70.105010](https://doi.org/10.1103/PhysRevD.70.105010). arXiv: [hep-ph/0401172](https://arxiv.org/abs/hep-ph/0401172) [hep-ph].
- [73] T. ZOELLER. “Nonequilibrium Formulation of Abelian Gauge Theories”. PhD thesis. Tech. Univ. Darmstadt, 2013.

- [74] R. KUBO. “*Statistical mechanical theory of irreversible processes. 1. General theory and simple applications in magnetic and conduction problems*“. J.Phys.Soc.Jap. **12** (1957), 570–586.
- [75] P. C. MARTIN and J. S. SCHWINGER. “*Theory of many particle systems. 1.*“ Phys.Rev. **115** (1959), 1342–1373. DOI: [10.1103/PhysRev.115.1342](https://doi.org/10.1103/PhysRev.115.1342).
- [76] G. BAYM. “*Selfconsistent approximation in many body systems*“. Phys.Rev. **127** (1962), 1391–1401. DOI: [10.1103/PhysRev.127.1391](https://doi.org/10.1103/PhysRev.127.1391).
- [77] J. M. CORNWALL, R. JACKIW, and E. TOMBOULIS. “*Effective Action for Composite Operators*“. Phys.Rev. **D10** (1974), 2428–2445. DOI: [10.1103/PhysRevD.10.2428](https://doi.org/10.1103/PhysRevD.10.2428).
- [78] H. GIES. “*Introduction to the functional RG and applications to gauge theories*“. Lect.Notes Phys. **852** (2012), 287–348. DOI: [10.1007/978-3-642-27320-9_6](https://doi.org/10.1007/978-3-642-27320-9_6). arXiv: [hep-ph/0611146](https://arxiv.org/abs/hep-ph/0611146) [hep-ph].
- [79] J. M. PAWLOWSKI. “*Aspects of the functional renormalisation group*“. Annals Phys. **322** (2007), 2831–2915. DOI: [10.1016/j.aop.2007.01.007](https://doi.org/10.1016/j.aop.2007.01.007). arXiv: [hep-th/0512261](https://arxiv.org/abs/hep-th/0512261) [hep-th].
- [80] C. S. FISCHER. “*Infrared properties of QCD from Dyson-Schwinger equations*“. J.Phys. **G32** (2006), R253–R291. DOI: [10.1088/0954-3899/32/8/R02](https://doi.org/10.1088/0954-3899/32/8/R02). arXiv: [hep-ph/0605173](https://arxiv.org/abs/hep-ph/0605173) [hep-ph].
- [81] S. WEINBERG. *Gravitation and cosmology: principles and applications of the general theory of relativity*. Wiley, 1972.
- [82] C. GATtringER and C.B. LANG. *Quantum Chromodynamics on the Lattice: An Introductory Presentation*. Lecture Notes in Physics. Springer, 2009.
- [83] J. B. KOGUT and L. SUSSKIND. “*Hamiltonian Formulation of Wilson’s Lattice Gauge Theories*“. Phys.Rev. **D11** (1975), 395. DOI: [10.1103/PhysRevD.11.395](https://doi.org/10.1103/PhysRevD.11.395).
- [84] K. G. WILSON. “*Confinement of Quarks*“. Phys.Rev. **D10** (1974), 2445–2459. DOI: [10.1103/PhysRevD.10.2445](https://doi.org/10.1103/PhysRevD.10.2445).
- [85] K. SYMANZIK. “*Continuum Limit and Improved Action in Lattice Theories. 1. Principles and ϕ^4 Theory*“. Nucl.Phys. **B226** (1983), 187. DOI: [10.1016/0550-3213\(83\)90468-6](https://doi.org/10.1016/0550-3213(83)90468-6).
- [86] S. SCHEFFLER. “*Plasma Instabilities and Turbulence in Non-Abelian Gauge Theories*“. PhD thesis. Tech. Univ. Darmstadt, 2010.
- [87] J. BERGES, S. SCHEFFLER, and D. SEXTY. “*Turbulence in nonabelian gauge theory*“. Phys.Lett. **B681** (2009), 362–366. DOI: [10.1016/j.physletb.2009.10.032](https://doi.org/10.1016/j.physletb.2009.10.032). arXiv: [0811.4293](https://arxiv.org/abs/0811.4293) [hep-ph].

- [88] A. KURKELA and G. D. MOORE. “*UV Cascade in Classical Yang-Mills Theory*“. Phys.Rev. **D86** (2012), 056008. DOI: [10.1103/PhysRevD.86.056008](https://doi.org/10.1103/PhysRevD.86.056008). arXiv: [1207.1663](https://arxiv.org/abs/1207.1663) [hep-ph].
- [89] A. CUCCHIERI and T. MENDES. “*Critical slowing down in $SU(2)$ Landau gauge fixing algorithms*“. Nucl.Phys. **B471** (1996), 263–292. DOI: [10.1016/0550-3213\(96\)00177-0](https://doi.org/10.1016/0550-3213(96)00177-0). arXiv: [hep-lat/9511020](https://arxiv.org/abs/hep-lat/9511020) [hep-lat].
- [90] J. BERGES, S. SCHLICHTING, and D. SEXTY. “*Over-populated gauge fields on the lattice*“. Phys.Rev. **D86** (2012), 074006. DOI: [10.1103/PhysRevD.86.074006](https://doi.org/10.1103/PhysRevD.86.074006). arXiv: [1203.4646](https://arxiv.org/abs/1203.4646) [hep-ph].
- [91] S. SCHLICHTING. “*Turbulent thermalization of weakly coupled non-abelian plasmas*“. Phys.Rev. **D86** (2012), 065008. DOI: [10.1103/PhysRevD.86.065008](https://doi.org/10.1103/PhysRevD.86.065008). arXiv: [1207.1450](https://arxiv.org/abs/1207.1450) [hep-ph].
- [92] T. EPELBAUM and F. GELIS. “*Role of quantum fluctuations in a system with strong fields: Spectral properties and Thermalization*“. Nucl.Phys. **A872** (2011), 210–244. DOI: [10.1016/j.nuclphysa.2011.09.019](https://doi.org/10.1016/j.nuclphysa.2011.09.019). arXiv: [1107.0668](https://arxiv.org/abs/1107.0668) [hep-ph].
- [93] K. DUSLING, T. EPELBAUM, F. GELIS, and R. VENUGOPALAN. “*Initial state and thermalization*“ (2012). arXiv: [1207.5401](https://arxiv.org/abs/1207.5401) [hep-ph].
- [94] M.H. ANDERSON, J.R. ENSHER, M.R. MATTHEWS, C.E. WIEMAN, and E.A. CORNELL. “*Observation of Bose-Einstein condensation in a dilute atomic vapor*“. Science **269** (1995), 198–201.
- [95] K.B. DAVIS, M.-O. MEWES, M.R. ANDREWS, N.J. VAN DRUTEN, D.S. DURFEE, D.M. KURN, and W. KETTERLE. “*Bose-Einstein condensation in a gas of sodium atoms*“. Phys.Rev.Lett. **75** (1995), 3969–3973. DOI: [10.1103/PhysRevLett.75.3969](https://doi.org/10.1103/PhysRevLett.75.3969).
- [96] J. BERGES and G. HOFFMEISTER. “*Nonthermal fixed points and the functional renormalization group*“. Nucl.Phys. **B813** (2009), 383–407. DOI: [10.1016/j.nuclphysb.2008.12.017](https://doi.org/10.1016/j.nuclphysb.2008.12.017). arXiv: [0809.5208](https://arxiv.org/abs/0809.5208) [hep-th].
- [97] E. BRAATEN and R. D. PISARSKI. “*Soft Amplitudes in Hot Gauge Theories: A General Analysis*“. Nucl.Phys. **B337** (1990), 569. DOI: [10.1016/0550-3213\(90\)90508-B](https://doi.org/10.1016/0550-3213(90)90508-B).
- [98] Y. HATTA and A. NISHIYAMA. “*Towards thermalization in heavy-ion collisions: CGC meets the 2PI formalism*“. Nucl.Phys. **A873** (2012), 47–67. DOI: [10.1016/j.nuclphysa.2011.10.007](https://doi.org/10.1016/j.nuclphysa.2011.10.007). arXiv: [1108.0818](https://arxiv.org/abs/1108.0818) [hep-ph].
- [99] H. BETHE and W. HEITLER. “*On the Stopping of fast particles and on the creation of positive electrons*“. Proc.Roy.Soc.Lond. **A146** (1934), 83–112.

- [100] F. A. BERENDS, R. KLEISS, P. DE CAUSMAECKER, R. GASTMANS, and T. T. WU. “*Single Bremsstrahlung Processes in Gauge Theories*“. Phys.Lett. **B103** (1981), 124. DOI: [10.1016/0370-2693\(81\)90685-7](https://doi.org/10.1016/0370-2693(81)90685-7).
- [101] P. B. ARNOLD, G. D. MOORE, and L. G. YAFFE. “*Effective kinetic theory for high temperature gauge theories*“. JHEP **0301** (2003), 030. arXiv: [hep-ph/0209353](https://arxiv.org/abs/hep-ph/0209353) [[hep-ph](#)].
- [102] D.V. SEMIKOZ and I.I. TKACHEV. “*Kinetics of Bose condensation*“. Phys.Rev.Lett. **74** (1995), 3093–3097. DOI: [10.1103/PhysRevLett.74.3093](https://doi.org/10.1103/PhysRevLett.74.3093). arXiv: [hep-ph/9409202](https://arxiv.org/abs/hep-ph/9409202) [[hep-ph](#)].
- [103] D.V. SEMIKOZ and I.I. TKACHEV. “*Condensation of bosons in kinetic regime*“. Phys.Rev. **D55** (1997), 489–502. DOI: [10.1103/PhysRevD.55.489](https://doi.org/10.1103/PhysRevD.55.489). arXiv: [hep-ph/9507306](https://arxiv.org/abs/hep-ph/9507306) [[hep-ph](#)].
- [104] J. RANDRUP and S. MROWCZYNSKI. “*Chromodynamic Weibel instabilities in relativistic nuclear collisions*“. Phys.Rev. **C68** (2003), 034909. DOI: [10.1103/PhysRevC.68.034909](https://doi.org/10.1103/PhysRevC.68.034909). arXiv: [nucl-th/0303021](https://arxiv.org/abs/nuc1-th/0303021) [[nucl-th](#)].
- [105] P. B. ARNOLD, J. LENAGHAN, and G. D. MOORE. “*QCD plasma instabilities and bottom up thermalization*“. JHEP **0308** (2003), 002. arXiv: [hep-ph/0307325](https://arxiv.org/abs/hep-ph/0307325) [[hep-ph](#)].
- [106] P. ROMATSCHKE and M. STRICKLAND. “*Collective modes of an anisotropic quark gluon plasma*“. Phys.Rev. **D68** (2003), 036004. DOI: [10.1103/PhysRevD.68.036004](https://doi.org/10.1103/PhysRevD.68.036004). arXiv: [hep-ph/0304092](https://arxiv.org/abs/hep-ph/0304092) [[hep-ph](#)].
- [107] P. ROMATSCHKE and M. STRICKLAND. “*Collective modes of an anisotropic quark-gluon plasma II*“. Phys.Rev. **D70** (2004), 116006. DOI: [10.1103/PhysRevD.70.116006](https://doi.org/10.1103/PhysRevD.70.116006). arXiv: [hep-ph/0406188](https://arxiv.org/abs/hep-ph/0406188) [[hep-ph](#)].
- [108] A. REBHAN, P. ROMATSCHKE, and M. STRICKLAND. “*Hard-loop dynamics of non-Abelian plasma instabilities*“. Phys.Rev.Lett. **94** (2005), 102303. DOI: [10.1103/PhysRevLett.94.102303](https://doi.org/10.1103/PhysRevLett.94.102303). arXiv: [hep-ph/0412016](https://arxiv.org/abs/hep-ph/0412016) [[hep-ph](#)].
- [109] A. REBHAN, P. ROMATSCHKE, and M. STRICKLAND. “*Dynamics of quark-gluon-plasma instabilities in discretized hard-loop approximation*“. JHEP **0509** (2005), 041. DOI: [10.1088/1126-6708/2005/09/041](https://doi.org/10.1088/1126-6708/2005/09/041). arXiv: [hep-ph/0505261](https://arxiv.org/abs/hep-ph/0505261) [[hep-ph](#)].
- [110] P. ROMATSCHKE and A. REBHAN. “*Plasma Instabilities in an Anisotropically Expanding Geometry*“. Phys.Rev.Lett. **97** (2006), 252301. DOI: [10.1103/PhysRevLett.97.252301](https://doi.org/10.1103/PhysRevLett.97.252301). arXiv: [hep-ph/0605064](https://arxiv.org/abs/hep-ph/0605064) [[hep-ph](#)].
- [111] D. BODEKER and K. RUMMUKAINEN. “*Non-abelian plasma instabilities for strong anisotropy*“. JHEP **0707** (2007), 022. DOI: [10.1088/1126-6708/2007/07/022](https://doi.org/10.1088/1126-6708/2007/07/022). arXiv: [0705.0180](https://arxiv.org/abs/0705.0180) [[hep-ph](#)].

- [112] A. REBHAN, M. STRICKLAND, and M. ATTEMS. “*Instabilities of an anisotropically expanding non-Abelian plasma: 1D+3V discretized hard-loop simulations*“. Phys.Rev. **D78** (2008), 045023. DOI: [10.1103/PhysRevD.78.045023](https://doi.org/10.1103/PhysRevD.78.045023). arXiv: [0802.1714](https://arxiv.org/abs/0802.1714) [hep-ph].
- [113] M. ATTEMS, A. REBHAN, and M. STRICKLAND. “*Instabilities of an anisotropically expanding non-Abelian plasma: 3D+3V discretized hard-loop simulations*“. Phys.Rev. **D87** (2013), 025010. DOI: [10.1103/PhysRevD.87.025010](https://doi.org/10.1103/PhysRevD.87.025010). arXiv: [1207.5795](https://arxiv.org/abs/1207.5795) [hep-ph].
- [114] J. BERGES, S. SCHEFFLER, S. SCHLICHTING, and D. SEXTY. “*Out of equilibrium dynamics of coherent non-abelian gauge fields*“. Phys.Rev. **D85** (2012), 034507. DOI: [10.1103/PhysRevD.85.034507](https://doi.org/10.1103/PhysRevD.85.034507). arXiv: [1111.2751](https://arxiv.org/abs/1111.2751) [hep-ph].
- [115] J. BERGES, K. BOGUSLAVSKI, and S. SCHLICHTING. “*Nonlinear amplification of instabilities with longitudinal expansion*“. Phys.Rev. **D85** (2012), 076005. DOI: [10.1103/PhysRevD.85.076005](https://doi.org/10.1103/PhysRevD.85.076005). arXiv: [1201.3582](https://arxiv.org/abs/1201.3582) [hep-ph].
- [116] A. IWAZAKI. “*Decay of Color Gauge Fields in Heavy Ion Collisions and Nielsen-Olesen Instability*“. Prog.Theor.Phys. **121** (2009), 809–822. DOI: [10.1143/PTP.121.809](https://doi.org/10.1143/PTP.121.809). arXiv: [0803.0188](https://arxiv.org/abs/0803.0188) [hep-ph].
- [117] H. FUJII and K. ITAKURA. “*Expanding color flux tubes and instabilities*“. Nucl.Phys. **A809** (2008), 88–109. DOI: [10.1016/j.nuclphysa.2008.05.016](https://doi.org/10.1016/j.nuclphysa.2008.05.016). arXiv: [0803.0410](https://arxiv.org/abs/0803.0410) [hep-ph].
- [118] H. FUJII, K. ITAKURA, and A. IWAZAKI. “*Instabilities in non-expanding glasma*“. Nucl.Phys. **A828** (2009), 178–190. DOI: [10.1016/j.nuclphysa.2009.06.020](https://doi.org/10.1016/j.nuclphysa.2009.06.020). arXiv: [0903.2930](https://arxiv.org/abs/0903.2930) [hep-ph].
- [119] T. N. TUDRON. “*Instability of constant Yang-Mills fields generated by constant gauge potentials*“. Phys.Rev. **D22** (1980), 2566. DOI: [10.1103/PhysRevD.22.2566](https://doi.org/10.1103/PhysRevD.22.2566).
- [120] M. ABRAMOWITZ and I.A. STEGUN. *Handbook of Mathematical Functions: With Formulas, Graphs, and Mathematical Tables*. Applied mathematics series. Dover Publications, Incorporated, 1964.
- [121] S. G. MATINYAN, G.K. SAVVIDY, and N.G. TER-ARUTUNIAN SAVVIDY. “*Classical Yang-Mills mechanics. Non-linear color oscillations*“. Sov.Phys.JETP **53** (1981), 421–425.
- [122] L. KOFMAN, A. D. LINDE, and A. A. STAROBINSKY. “*Reheating after inflation*“. Phys.Rev.Lett. **73** (1994), 3195–3198. DOI: [10.1103/PhysRevLett.73.3195](https://doi.org/10.1103/PhysRevLett.73.3195). arXiv: [hep-th/9405187](https://arxiv.org/abs/hep-th/9405187) [hep-th].
- [123] E.L. INCE. *Ordinary differential equations*. Dover Books on Mathematics Series. Dover Publications, Incorporated, 1956.

- [124] D. BOYANOVSKY, H.J. DE VEGA, R. HOLMAN, and J.F.J. SALGADO. “*Analytic and numerical study of preheating dynamics*“. Phys.Rev. **D54** (1996), 7570–7598. DOI: [10.1103/PhysRevD.54.7570](https://doi.org/10.1103/PhysRevD.54.7570). arXiv: [hep-ph/9608205](https://arxiv.org/abs/hep-ph/9608205) [hep-ph].
- [125] A. TRANBERG. “*Quantum field thermalization in expanding backgrounds*“. JHEP **0811** (2008), 037. DOI: [10.1088/1126-6708/2008/11/037](https://doi.org/10.1088/1126-6708/2008/11/037). arXiv: [0806.3158](https://arxiv.org/abs/0806.3158) [hep-ph].
- [126] J. BERGES. “*Controlled nonperturbative dynamics of quantum fields out-of-equilibrium*“. Nucl.Phys. **A699** (2002), 847–886. DOI: [10.1016/S0375-9474\(01\)01295-7](https://doi.org/10.1016/S0375-9474(01)01295-7). arXiv: [hep-ph/0105311](https://arxiv.org/abs/hep-ph/0105311) [hep-ph].
- [127] G. AARTS, D. AHRENSMEIER, R. BAIER, J. BERGES, and J. SERREAU. “*Far from equilibrium dynamics with broken symmetries from the 2PI - 1/N expansion*“. Phys.Rev. **D66** (2002), 045008. DOI: [10.1103/PhysRevD.66.045008](https://doi.org/10.1103/PhysRevD.66.045008). arXiv: [hep-ph/0201308](https://arxiv.org/abs/hep-ph/0201308) [hep-ph].
- [128] J. BERGES and S. ROTH. “*Topological defect formation from 2PI effective action techniques*“. Nucl.Phys. **B847** (2011), 197–219. DOI: [10.1016/j.nuclphysb.2011.01.024](https://doi.org/10.1016/j.nuclphysb.2011.01.024). arXiv: [1012.1212](https://arxiv.org/abs/1012.1212) [hep-ph].
- [129] K. DUSLING, T. EPELBAUM, F. GELIS, and R. VENUGOPALAN. “*Instability induced pressure isotropization in a longitudinally expanding system*“. Phys.Rev. **D86** (2012), 085040. DOI: [10.1103/PhysRevD.86.085040](https://doi.org/10.1103/PhysRevD.86.085040). arXiv: [1206.3336](https://arxiv.org/abs/1206.3336) [hep-ph].
- [130] Y. HATTA and A. NISHIYAMA. “*Nonequilibrium 2PI evolution of the $O(N)$ model with longitudinal expansion*“. Phys.Rev. **D86** (2012), 076002. DOI: [10.1103/PhysRevD.86.076002](https://doi.org/10.1103/PhysRevD.86.076002). arXiv: [1206.4743](https://arxiv.org/abs/1206.4743) [hep-ph].
- [131] A. KOVNER, L. D. MCLERRAN, and H. WEIGERT. “*Gluon production from nonAbelian Weizsacker-Williams fields in nucleus-nucleus collisions*“. Phys.Rev. **D52** (1995), 6231–6237. DOI: [10.1103/PhysRevD.52.6231](https://doi.org/10.1103/PhysRevD.52.6231). arXiv: [hep-ph/9502289](https://arxiv.org/abs/hep-ph/9502289) [hep-ph].
- [132] A. KOVNER, L. D. MCLERRAN, and H. WEIGERT. “*Gluon production at high transverse momentum in the McLerran-Venugopalan model of nuclear structure functions*“. Phys.Rev. **D52** (1995), 3809–3814. DOI: [10.1103/PhysRevD.52.3809](https://doi.org/10.1103/PhysRevD.52.3809). arXiv: [hep-ph/9505320](https://arxiv.org/abs/hep-ph/9505320) [hep-ph].
- [133] M. GYULASSY and L. D. MCLERRAN. “*Yang-Mills radiation in ultrarelativistic nuclear collisions*“. Phys.Rev. **C56** (1997), 2219–2228. DOI: [10.1103/PhysRevC.56.2219](https://doi.org/10.1103/PhysRevC.56.2219). arXiv: [nucl-th/9704034](https://arxiv.org/abs/nucl-th/9704034) [nucl-th].
- [134] K. FUKUSHIMA, F. GELIS, and L. D. MCLERRAN. “*Initial Singularity of the Little Bang*“. Nucl.Phys. **A786** (2007), 107–130. DOI: [10.1016/j.nuclphysa.2007.01.086](https://doi.org/10.1016/j.nuclphysa.2007.01.086). arXiv: [hep-ph/0610416](https://arxiv.org/abs/hep-ph/0610416) [hep-ph].

- [135] A. KRASNITZ and R. VENUGOPALAN. “*Nonperturbative computation of gluon minijet production in nuclear collisions at very high-energies*“. Nucl.Phys. **B557** (1999), 237. DOI: [10.1016/S0550-3213\(99\)00366-1](https://doi.org/10.1016/S0550-3213(99)00366-1). arXiv: [hep-ph/9809433](https://arxiv.org/abs/hep-ph/9809433) [hep-ph].
- [136] A. KRASNITZ and R. VENUGOPALAN. “*The Initial energy density of gluons produced in very high-energy nuclear collisions*“. Phys.Rev.Lett. **84** (2000), 4309–4312. DOI: [10.1103/PhysRevLett.84.4309](https://doi.org/10.1103/PhysRevLett.84.4309). arXiv: [hep-ph/9909203](https://arxiv.org/abs/hep-ph/9909203) [hep-ph].
- [137] A. KRASNITZ and R. VENUGOPALAN. “*The Initial gluon multiplicity in heavy ion collisions*“. Phys.Rev.Lett. **86** (2001), 1717–1720. DOI: [10.1103/PhysRevLett.86.1717](https://doi.org/10.1103/PhysRevLett.86.1717). arXiv: [hep-ph/0007108](https://arxiv.org/abs/hep-ph/0007108) [hep-ph].
- [138] A. KRASNITZ, Y. NARA, and R. VENUGOPALAN. “*Coherent gluon production in very high-energy heavy ion collisions*“. Phys.Rev.Lett. **87** (2001), 192302. DOI: [10.1103/PhysRevLett.87.192302](https://doi.org/10.1103/PhysRevLett.87.192302). arXiv: [hep-ph/0108092](https://arxiv.org/abs/hep-ph/0108092) [hep-ph].
- [139] A. KRASNITZ, Y. NARA, and R. VENUGOPALAN. “*Gluon production in the color glass condensate model of collisions of ultrarelativistic finite nuclei*“. Nucl.Phys. **A717** (2003), 268–290. DOI: [10.1016/S0375-9474\(03\)00636-5](https://doi.org/10.1016/S0375-9474(03)00636-5). arXiv: [hep-ph/0209269](https://arxiv.org/abs/hep-ph/0209269) [hep-ph].
- [140] A. KRASNITZ, Y. NARA, and R. VENUGOPALAN. “*Classical gluodynamics of high-energy nuclear collisions: An Erratum and an update*“. Nucl.Phys. **A727** (2003), 427–436. DOI: [10.1016/j.nuclphysa.2003.08.004](https://doi.org/10.1016/j.nuclphysa.2003.08.004). arXiv: [hep-ph/0305112](https://arxiv.org/abs/hep-ph/0305112) [hep-ph].
- [141] T. LAPPI. “*Production of gluons in the classical field model for heavy ion collisions*“. Phys.Rev. **C67** (2003), 054903. DOI: [10.1103/PhysRevC.67.054903](https://doi.org/10.1103/PhysRevC.67.054903). arXiv: [hep-ph/0303076](https://arxiv.org/abs/hep-ph/0303076) [hep-ph].
- [142] T. LAPPI. “*Energy density of the glasma*“. Phys.Lett. **B643** (2006), 11–16. DOI: [10.1016/j.physletb.2006.10.017](https://doi.org/10.1016/j.physletb.2006.10.017). arXiv: [hep-ph/0606207](https://arxiv.org/abs/hep-ph/0606207) [hep-ph].
- [143] T. LAPPI and L. MCLERRAN. “*Some features of the glasma*“. Nucl.Phys. **A772** (2006), 200–212. DOI: [10.1016/j.nuclphysa.2006.04.001](https://doi.org/10.1016/j.nuclphysa.2006.04.001). arXiv: [hep-ph/0602189](https://arxiv.org/abs/hep-ph/0602189) [hep-ph].
- [144] J. BERGES and S. SCHLICHTING. “*The non-linear Glasma*“. Phys.Rev. **D87** (2013), 014026. DOI: [10.1103/PhysRevD.87.014026](https://doi.org/10.1103/PhysRevD.87.014026). arXiv: [1209.0817](https://arxiv.org/abs/1209.0817) [hep-ph].
- [145] J. BERGES, K. BOGUSLAVSKI, S. SCHLICHTING, and R. VENUGOPALAN. “*Turbulent thermalization of the Quark Gluon Plasma*“ (2013). arXiv: [1303.5650](https://arxiv.org/abs/1303.5650) [hep-ph].
- [146] E. IANCU and L. D. MCLERRAN. “*Saturation and universality in QCD at small x* “. Phys.Lett. **B510** (2001), 145–154. DOI: [10.1016/S0370-2693\(01\)00526-3](https://doi.org/10.1016/S0370-2693(01)00526-3). arXiv: [hep-ph/0103032](https://arxiv.org/abs/hep-ph/0103032) [hep-ph].
- [147] E. IANCU, K. ITAKURA, and L. D. MCLERRAN. “*Geometric scaling above the saturation scale*“. Nucl.Phys. **A708** (2002), 327–352. DOI: [10.1016/S0375-9474\(02\)01010-2](https://doi.org/10.1016/S0375-9474(02)01010-2). arXiv: [hep-ph/0203137](https://arxiv.org/abs/hep-ph/0203137) [hep-ph].

- [148] K. RUMMUKAINEN and H. WEIGERT. “*Universal features of JIMWLK and BK evolution at small x* “. Nucl.Phys. **A739** (2004), 183–226. DOI: [10.1016/j.nuclphysa.2004.03.219](https://doi.org/10.1016/j.nuclphysa.2004.03.219). arXiv: [hep-ph/0309306](https://arxiv.org/abs/hep-ph/0309306) [hep-ph].
- [149] E. IANCU, A. H. MUELLER, and S. MUNIER. “*Universal behavior of QCD amplitudes at high energy from general tools of statistical physics*“. Phys.Lett. **B606** (2005), 342–350. DOI: [10.1016/j.physletb.2004.12.009](https://doi.org/10.1016/j.physletb.2004.12.009). arXiv: [hep-ph/0410018](https://arxiv.org/abs/hep-ph/0410018) [hep-ph].
- [150] A. DUMITRU, J. JALILIAN-MARIAN, T. LAPPI, B. SCHENKE, and R. VENUGOPALAN. “*Renormalization group evolution of multi-gluon correlators in high energy QCD*“. Phys.Lett. **B706** (2011), 219–224. DOI: [10.1016/j.physletb.2011.11.002](https://doi.org/10.1016/j.physletb.2011.11.002). arXiv: [1108.4764](https://arxiv.org/abs/1108.4764) [hep-ph].
- [151] K. DUSLING, F. GELIS, and R. VENUGOPALAN. “*The initial spectrum of fluctuations in the little bang*“. Nucl.Phys. **A872** (2011), 161–195. DOI: [10.1016/j.nuclphysa.2011.09.012](https://doi.org/10.1016/j.nuclphysa.2011.09.012). arXiv: [1106.3927](https://arxiv.org/abs/1106.3927) [nucl-th].
- [152] F. GELIS, T. LAPPI, and R. VENUGOPALAN. “*High energy scattering in Quantum Chromodynamics*“. Int.J.Mod.Phys. **E16** (2007), 2595–2637. DOI: [10.1142/S0218301307008331](https://doi.org/10.1142/S0218301307008331). arXiv: [0708.0047](https://arxiv.org/abs/0708.0047) [hep-ph].
- [153] F. GELIS, T. LAPPI, and R. VENUGOPALAN. “*High energy factorization in nucleus-nucleus collisions. II. Multigluon correlations*“. Phys.Rev. **D78** (2008), 054020. DOI: [10.1103/PhysRevD.78.054020](https://doi.org/10.1103/PhysRevD.78.054020). arXiv: [0807.1306](https://arxiv.org/abs/0807.1306) [hep-ph].
- [154] F. GELIS, T. LAPPI, and R. VENUGOPALAN. “*High energy factorization in nucleus-nucleus collisions. 3. Long range rapidity correlations*“. Phys.Rev. **D79** (2009), 094017. DOI: [10.1103/PhysRevD.79.094017](https://doi.org/10.1103/PhysRevD.79.094017). arXiv: [0810.4829](https://arxiv.org/abs/0810.4829) [hep-ph].
- [155] K. DUSLING, T. EPELBAUM, F. GELIS, and R. VENUGOPALAN. “*Role of quantum fluctuations in a system with strong fields: Onset of hydrodynamical flow*“. Nucl.Phys. **A850** (2011), 69–109. DOI: [10.1016/j.nuclphysa.2010.11.009](https://doi.org/10.1016/j.nuclphysa.2010.11.009). arXiv: [1009.4363](https://arxiv.org/abs/1009.4363) [hep-ph].
- [156] U. REINOSA and J. SERREAU. “*2PI functional techniques for gauge theories: QED*“. Annals Phys. **325** (2010), 969–1017. DOI: [10.1016/j.aop.2009.11.005](https://doi.org/10.1016/j.aop.2009.11.005). arXiv: [0906.2881](https://arxiv.org/abs/0906.2881) [hep-ph].
- [157] URKO REINOSA and JULIEN SERREAU. “*Ward Identities for the 2PI effective action in QED*“. JHEP **0711** (2007), 097. DOI: [10.1088/1126-6708/2007/11/097](https://doi.org/10.1088/1126-6708/2007/11/097). arXiv: [0708.0971](https://arxiv.org/abs/0708.0971) [hep-th].
- [158] L. D. MCLERRAN and R. VENUGOPALAN. “*Computing quark and gluon distribution functions for very large nuclei*“. Phys.Rev. **D49** (1994), 2233–2241. DOI: [10.1103/PhysRevD.49.2233](https://doi.org/10.1103/PhysRevD.49.2233). arXiv: [hep-ph/9309289](https://arxiv.org/abs/hep-ph/9309289) [hep-ph].

- [159] L. D. McLERRAN and R. VENUGOPALAN. “*Gluon distribution functions for very large nuclei at small transverse momentum*“. Phys.Rev. **D49** (1994), 3352–3355. DOI: [10.1103/PhysRevD.49.3352](https://doi.org/10.1103/PhysRevD.49.3352). arXiv: [hep-ph/9311205](https://arxiv.org/abs/hep-ph/9311205) [hep-ph].
- [160] L. D. McLERRAN and R. VENUGOPALAN. “*Green’s functions in the color field of a large nucleus*“. Phys.Rev. **D50** (1994), 2225–2233. DOI: [10.1103/PhysRevD.50.2225](https://doi.org/10.1103/PhysRevD.50.2225). arXiv: [hep-ph/9402335](https://arxiv.org/abs/hep-ph/9402335) [hep-ph].
- [161] J. JALILIAN-MARIAN, A. KOVNER, L. D. McLERRAN, and H. WEIGERT. “*The Intrinsic glue distribution at very small x* “. Phys.Rev. **D55** (1997), 5414–5428. DOI: [10.1103/PhysRevD.55.5414](https://doi.org/10.1103/PhysRevD.55.5414). arXiv: [hep-ph/9606337](https://arxiv.org/abs/hep-ph/9606337) [hep-ph].
- [162] A. KURKELA and G. D. MOORE. “*New algorithm for classical gauge theory simulations in an expanding box*“ (2012). arXiv: [1209.4091](https://arxiv.org/abs/1209.4091) [hep-lat].
- [163] A.H. MUELLER and D.T. SON. “*On the Equivalence between the Boltzmann equation and classical field theory at large occupation numbers*“. Phys.Lett. **B582** (2004), 279–287. DOI: [10.1016/j.physletb.2003.12.047](https://doi.org/10.1016/j.physletb.2003.12.047). arXiv: [hep-ph/0212198](https://arxiv.org/abs/hep-ph/0212198) [hep-ph].
- [164] B. SCHENKE, P. TRIBEDY, and R. VENUGOPALAN. “*Fluctuating Glasma initial conditions and flow in heavy ion collisions*“. Phys.Rev.Lett. **108** (2012), 252301. DOI: [10.1103/PhysRevLett.108.252301](https://doi.org/10.1103/PhysRevLett.108.252301). arXiv: [1202.6646](https://arxiv.org/abs/1202.6646) [nucl-th].
- [165] B. SCHENKE, P. TRIBEDY, and R. VENUGOPALAN. “*Event-by-event gluon multiplicity, energy density, and eccentricities in ultrarelativistic heavy-ion collisions*“. Phys.Rev. **C86** (2012), 034908. DOI: [10.1103/PhysRevC.86.034908](https://doi.org/10.1103/PhysRevC.86.034908). arXiv: [1206.6805](https://arxiv.org/abs/1206.6805) [hep-ph].
- [166] C. GALE, S. JEON, B. SCHENKE, P. TRIBEDY, and R. VENUGOPALAN. “*Event-by-event anisotropic flow in heavy-ion collisions from combined Yang-Mills and viscous fluid dynamics*“. Phys.Rev.Lett. **110** (2013), 012302. DOI: [10.1103/PhysRevLett.110.012302](https://doi.org/10.1103/PhysRevLett.110.012302). arXiv: [1209.6330](https://arxiv.org/abs/1209.6330) [nucl-th].
- [167] M. MARTINEZ, R. RYBLEWSKI, and M. STRICKLAND. “*Boost-Invariant (2+1)-dimensional Anisotropic Hydrodynamics*“. Phys.Rev. **C85** (2012), 064913. DOI: [10.1103/PhysRevC.85.064913](https://doi.org/10.1103/PhysRevC.85.064913). arXiv: [1204.1473](https://arxiv.org/abs/1204.1473) [nucl-th].
- [168] R. RYBLEWSKI and W. FLORKOWSKI. “*Highly-anisotropic hydrodynamics in 3+1 space-time dimensions*“. Phys.Rev. **C85** (2012), 064901. DOI: [10.1103/PhysRevC.85.064901](https://doi.org/10.1103/PhysRevC.85.064901). arXiv: [1204.2624](https://arxiv.org/abs/1204.2624) [nucl-th].
- [169] W. FLORKOWSKI, R. MAJ, R. RYBLEWSKI, and M. STRICKLAND. “*Hydrodynamics of anisotropic quark and gluon fluids*“. Phys. Rev. C **87**, **034914** (2013). DOI: [10.1103/PhysRevC.87.034914](https://doi.org/10.1103/PhysRevC.87.034914). arXiv: [1209.3671](https://arxiv.org/abs/1209.3671) [nucl-th].
- [170] W. FLORKOWSKI, M. MARTINEZ, R. RYBLEWSKI, and M. STRICKLAND. “*Anisotropic hydrodynamics – basic concepts*“ (2013). arXiv: [1301.7539](https://arxiv.org/abs/1301.7539) [nucl-th].

- [171] W. FLORKOWSKI, R. RYBLEWSKI, and M. STRICKLAND. “*Anisotropic Hydrodynamics for Rapidly Expanding Systems*“ (2013). arXiv: [1304.0665 \[nucl-th\]](#).
- [172] M. CHIU, T. K. HEMMICK, V. KHACHATRYAN, A. LEONIDOV, J. LIAO, and L. D. MCLERRAN. “*Production of Photons and Dileptons in the Glasma*“. Nucl.Phys. **A900** (2013), 16–37. DOI: [10.1016/j.nuclphysa.2013.01.014](#). arXiv: [1202.3679 \[nucl-th\]](#).
- [173] J. BERGES, SZ. BORSANYI, D. SEXTY, and I.-O. STAMATESCU. “*Lattice simulations of real-time quantum fields*“. Phys.Rev. **D75** (2007), 045007. DOI: [10.1103/PhysRevD.75.045007](#). arXiv: [hep-lat/0609058 \[hep-lat\]](#).
- [174] J. BERGES and D. SEXTY. “*Real-time gauge theory simulations from stochastic quantization with optimized updating*“. Nucl.Phys. **B799** (2008), 306–329. DOI: [10.1016/j.nuclphysb.2008.01.018](#). arXiv: [0708.0779 \[hep-lat\]](#).
- [175] A. CUCCHIERI. “*Gribov copies in the minimal Landau gauge: The Influence on gluon and ghost propagators*“. Nucl.Phys. **B508** (1997), 353–370. DOI: [10.1016/S0550-3213\(97\)00629-9](#). arXiv: [hep-lat/9705005 \[hep-lat\]](#).
- [176] F.W.J. OLVER and L.C. MAXIMOM. *NIST Digital Library of Mathematical Functions*. (c.f. Eqns. 10.2.2, 10.4.8 and 10.6.1).
- [177] WOLFRAM RESEARCH. *The Wolfram functions site*.
<http://functions.wolfram.com/ElementaryFunctions/Sin/19/01/> ,
<http://functions.wolfram.com/ElementaryFunctions/Sin/19/02/> ,
<http://functions.wolfram.com/ElementaryFunctions/Power/19/01/> ,
<http://functions.wolfram.com/ElementaryFunctions/Power/19/02/>.
- [178] C. J. LANZOS. Soc. Indust. Appl. Math. Ser. B **Numer. Anal.** **1** (1964), 86–96.
- [179] Y. L. LUKE. *The Special Functions and Their Approximations: v. 1*. Mathematics in Science and Engineering Bd. 1. Elsevier Science, 1969.

Affidavit

I certify that this thesis is the result of my own work. I have only used the indicated sources and have not made unauthorised use of services of a third party. Furthermore, I have not previously presented this thesis or parts thereof to a university as part of an examination or degree.

Heidelberg, May 31, 2013

..... sgd. Sören Schlichting
(Signature)